Fatigue life modelling of anisotropic styrenic block copolymers for a prosthetic heart valve application

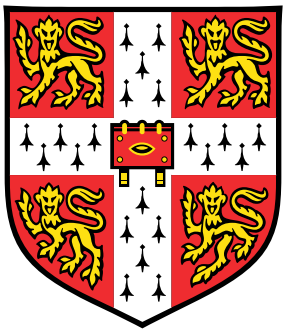

Eugenia Biral

Department of Chemical Engineering and Biotechnology
University of Cambridge

This dissertation is submitted for the degree of
Doctor of Philosophy

King's College

January 2021

Declaration

This thesis is the result of my own work and includes nothing which is the outcome of work done in collaboration except as declared in the Preface and specified in the text. I further state that no substantial part of my thesis has already been submitted, or, is being concurrently submitted for any such degree, diploma or other qualification at the University of Cambridge or any other University or similar institution except as declared in the Preface and specified in the text. It does not exceed the prescribed word limit for the relevant Degree Committee.

Eugenia Biral
January 2021

Abstract

This thesis describes a fatigue lifetime prediction model for anisotropic styrenic block copolymers. A shortlist of cylinder forming block copolymers has been tested for a flexible leaflet aortic prosthetic heart valve, designed to mimic the native structure of the aortic leaflet. Polymeric valves have the potential to overcome the limit of current available prosthesis, however no such valve is available clinically at present. Durability and calcification are among the main issues with polymeric valves designed and tested previously. The solution to these problems resides in the correct choice of material. In this study, a fatigue model was validated for anisotropic styrenic block copolymers to assist in the selection of the most durable material. The prediction is based on a unified approach of crack growth and nucleation tests. The model correctly predicted the lifetime of the material with same microstructure orientation, thickness and geometry. Material comparison based on the fatigue results highlighted the most durable material, a poly(styrene-b-butadiene-b-styrene) with 20% weight of styrene. The material was manufactured into a valve, which comfortably exceeded ISO standards for *in vitro* durability and hydrodynamic perfomance. Calcification and its effect on durability were tested. The calcification test was conducted in a simulated body fluid solution. Calcium levels on the styrenic block copolymers were significantly lower than on bovine pericardium, which is one of the materials used in clinical prosthesis. Durability of the calcified valve was not affected, indicating that the selected materials have great potential for biomedical applications. Finally, the effect of heparin coating was measured for both durability and calcification. The coating increased the level of calcification but did not affect durability in either unitensile specimens or valve prototypes.

Preface

This dissertation is submitted for the degree of Doctor of Philosophy at the University of Cambridge. It describes the research carried out in the Department of Chemical Engineering and Biotechnology between October 2016 and January 2021, under the supervision of Prof. G. Moggridge. Except where reference is made to the work of others, the contents of this dissertation are entirely original and have not been the result of collaboration.

Work described in Chapters 3 was presented at the International Rubber Conference in London (UK, September 2019), at the NanoMed / SMS / EGF 2018 International Joint Conferences in Venice (Italy, October 2018) and at the RIEG/MPG day-conference in Manchester (UK, May 2018).

The results of sections 2.2.2 and 3.3.7 and chapter 5 were published in Biomaterials science, 8 (16), 4467-4480. A patent was also filed as the result of this work: WO2020/174253 published 3rd of September 2020.

Acknowledgements

I had an unforgettable and life changing experience in Cambridge these past years and I owe it to the people that I met in my journey.

I am very grateful to my supervisor, Prof Geoff Moggridge, for his guidance, support and encouragements and for giving me the opportunity to study at the University of Cambridge. Special thanks to Drs Marta Serrani, Joanna Stasiak and Jacob Brubert, for patiently helping me and teaching me along the way.

I would like to thank King's college for funding my project and for giving me the chance to meet wonderful people, to be part of conferences and enchanting soirées. I really felt at home.

I had the fortune to visit the DuPont site in Geneva, as part of my studentship. I received training in their R&D site, for which I am very thankful.

I have very fond memories of my time spent in the office and lab, between a cup of tea and engaging conversations. I was lucky to have many friends around me in the department and college, among students and staff. They gave me the strength to face any obstacle.

There are no words that can express how grateful I am to my family. They have always believed in me and taught me to dream big.

Finally, I would like to thank Francesco for being there for me every day and every minute, for your love and kindness.

Thank you,

Eugenia

Contents

1 Introduction **1**

1.1 Background . . . 1

1.1.1 The heart and heart valves . . . 1

1.1.2 Heart valve diseases . . . 2

1.1.3 Prosthetic heart valves . . . 4

1.1.4 Polymeric prosthetic heart valves . . . 7

1.2 Aim of the research . . . 13

2 Block copolymers **15**

2.1 Introduction . . . 15

2.1.1 Applications of BCPs . . . 16

2.1.2 Synthesis of BCPs . . . 17

2.1.3 Microphase theory . . . 18

2.1.4 Styrenic block copolymer for PHV application: state of the art . . . 25

2.1.5 Achieving anisotropy . . . 27

2.2 Materials and Methods . . . 32

2.2.1 Materials . . . 32

2.2.2 Methods . . . 34

2.3 Results and Discussion . . . 41

2.3.1 Gel permeation chromatography . . . 41

2.3.2 DSC . . . 41

2.3.3 SAXS . . . 42

2.3.4 DMA . . . 48

2.3.5 Rheology and T_{ODT} . . . 51

2.3.6 Estimate of the microstructure dimensions . . . 60

2.4 Conclusions . . . 68

3 Fatigue Model **69**
3.1 Introduction . . . 69
3.1.1 Fatigue prediction models . . . 70
3.1.2 Unified fatigue model for the PHV application . . . 80
3.1.3 Finite element model for anisotropic block copolymers . . . 84
3.2 Materials and Methods . . . 86
3.2.1 Materials . . . 86
3.2.2 Methods . . . 87
3.2.3 Finite element modelling . . . 93
3.3 Results and Discussion . . . 94
3.3.1 Planar mechanical test . . . 94
3.3.2 Crack growth test . . . 95
3.3.3 Crack nucleation test . . . 105
3.3.4 Rigid stent experiment . . . 124
3.3.5 Effect of thickness on the initial crack size . . . 129
3.3.6 Transition law . . . 133
3.3.7 Polivalve . . . 138
3.4 Conclusions . . . 143

4 Calcification **145**
4.1 Introduction . . . 145
4.1.1 Mechanism of calcification for soft tissue and failure of BHV . . . 146
4.1.2 Polymer calcification . . . 148
4.1.3 Anticalcification techniques and treatments . . . 154
4.1.4 Method for calcification tests . . . 156
4.2 Materials and Methods . . . 160
4.2.1 Unitensile samples . . . 161
4.2.2 PHV samples . . . 162
4.2.3 Calcium Analysis . . . 163
4.3 Results and Discussion . . . 163
4.3.1 Atomic absorption spectroscopy . . . 163
4.3.2 Results from hydrodynamic test . . . 169
4.3.3 Results from durability test . . . 173
4.4 Conclusions . . . 175

5 *Ex vivo* hemocompatibility **177**
5.1 Introduction 177
5.2 Materials and Methods 179
5.3 Results and Discussion 181
5.4 Conclusions 181

6 Conclusions and future work **185**
6.1 Conclusions 185
6.2 Future work 188

References **190**

List of Figures

1.1 Gian Giacomo Dal Forno, "Portraits of ancient foreign students at the University of Padova - William Harvey", Palazzo Bo, Padua (on the left) [3]; cover of *"Exercitatio Anatomica de Motu Cordis et Sanguinis in Animalibus"* , the best-known work of Harvey, firstly published in 1628. Image taken from [4]. 2

1.2 Section of the human heart. The image shows the atria and ventricles and the blood vessels connecting the heart to the rest of the circulatory system. Taken from [7]. 3

1.3 Equatorial section of the human heart showing the four valves: mitral, tricuspid, aortic and pulmonary valve. Image credit: OpenStax College, Anatomy & Physiology, 2013. 3

1.4 Image of an aortic valve suffering regurgitation. The equatorial section of the heart on the right shows the weakened valve leaflets, which allow the blood to flow backwards, as indicated in the image on the left. Taken from [8]. 4

1.5 Aortic valve stenosis consist of a progressive narrowing of the aortic valve opening over time (from left to right in the picture). The result is an increased pressure within the heart, which reduces its capacity to pump blood to the rest of the body. Image adapted from [10]. 4

1.6 Mechanical valves: a- The St Jude valve, b- Medtronic Hall valve, c- Carbomedics valve and d- ON-X valve. Image adapted from [15]. . . . 5

1.7 Commercially available bioprosthetic aortic valves: a- Carpentier-Edwards PERIMOUNT™,b- Carpentier-Edwards Magna Ease™,c- Medtronic Mosaic®and d-Medtronic Hancock®. a-b:Stented pericardial bovine surgical aortic valve bioprostheses, c-d Stented porcine surgical aortic valve bioprostheses. Image adapted from reference [22]. 6

1.8 Balloon-expandable bovine pericardial tissue transcatheter bioprostheses a- Edward SAPIEN®XT, b- Edward SAPIEN®3. Self-expanding porcine pericardial tissue: c- Medtronic CoreValve®, d- Medtronic CoreValve®Evolut®, e- Symetis ACURATE neo™. Image adapted from reference [22]. 7

1.9 Polymeric aortic valves prototypes. a- the Reul-Ghista trileaflet PU valve, b- the Helmholtz Institute PU valve, c- the Reul-Haussinger PU valve, d- PU heart valve developed by the Glasgow group: Elliptohyperbolic Estane® dipcoated on a PEEK frame,e- polycarbonate urethane valves developed by ADIAM life sciences, Erkelenz, Germany, produced by a robotic droplet deposition technique,f- silicon 3D printed valves designed by ETH Zürich and SAT company, g- Foldax valve made of Siloxane Poly(urethane-urea), the valve is undergoing patient clinical trials. Image adapted from reference [19, 24, 27]. 8

1.10 Image of native aortic valve with radial elastin and circumferential collagen fibres distribution. Image taken from reference [32]. 11

1.11 Styrenic block copolymer valve prototypes manufactured in the Chemical Engineering and Biotechonology department of the University of Cambridge by the Structured material group. Valve from A to G where developed chronologically by Dr M. Serrani, Dr J. Stasiak and Dr J. Brubert. 12

1.12 Image of Polivalve: a tri-leaflet polymeric PHV manufactured in our laboratories. The leaflets and stent are made of styrenic block copolymers. 12

2.1 Generic representation of living anionic polymerization initiation [39]. 17

2.2 Linear block copolymer chain configurations possibilities. The different colours represent chemically different blocks. In this case blue corresponds to an hypothetical block A, while the orange to block B. 19

2.3 Ordered morphologies for in bulk self assembled polymer melts. Different color indicates the mesophase types. Figure obtained form reference [41]. 20

2.4 a) AB diblock copolymer equilibrium moprhologies: S,S'= BCC spheres, C,C'= hexagonally packed cylinders, G,G'=bicontinuous gyroids, L=lamellae; b) Phase diagram predicted by the self-consistent mean-field theory, f_A= volume fraction of block A, χ= Flory-Huggins interaction parameter, N = degree of polymerisation, CPS= closely packed spheres; c) experimental phase diagram for polyisoprene-block-polystyrene reported by Bates and co-workers [33], PL=perforated lamellae. Reproduced from reference [35]. 22

2.5 Illustration of possible chain arrangements in a) spheres, b) cylinders and c) lamellae mesophase configuration as f_A increases (up to $\sim$0.5). The dashed line represents the two phase interface. Figure reproduced from reference [35]. 23

2.6 Schematic representation of the regimes between weak and strong segregation limits for diblocks melt- The first row reprensets a qualititative graph of the amplitude fluctuation of local composition with increasing χN. The second row shows the correspective morphological pattern. Figure taken from reference [51]. 23

2.7 Baseline and optimised representation of the cylinders orientation obtained from Serrani *et al.* [67] computational tool. On the right is the porcine native aortic leaflet with collagen fibre architecture hiligheted. Figure adapted from reference [67]. 27

2.8 Schematic representation of section of injection moulded cylinder forming styrenic block copolymer sample. The height represent the thickness of the sample, which shows two external layer with cylinders oriented in the flow direction by shear flow, and a central layer with cylinders aligned perpendicular to the flow direction. The latter orientation is generated by the extensional flow regime related to the fountain flow effect. Figure taken from reference [65]. 29

2.9 Schemicatic representation of Colby report of scale down shear induced cylinders morphology. The white circle represent the shear induced cyliner packing while the blue circles are the second structure induced by high shear with a smaler lattice structure. Image adapted from reference [97]. 29

2.10 Mould design for a-flat sheet sample b- long unitensile sample (ISO 37 type 2) c- short unitensile sample (ASTM D638 type v). Mould a was made 1 mm thickness, mould b and c were made 0.7 mm, 1 mm and 2 mm thick. Unit measure for mould dimension is mm. 30

2.11 Unitensile sample design according to a- ASTM D638 type v and b- ISO37 type 2. 30

2.12 Mould set up in BOY22D. The pins coming out from the right side are the anchoring points of the mould plates. The injection point is in the middle of the right side (just visible). On top of the plates the attachments for the water cooling are visible and also the holes were cartridge heaters are inserted. 31

2.13 Schematic representation of the mould for compression moulding. A polymer bar is placed in the middle of the bottom plate, which is then squashed by the top plate. The side of the mould constrain the flow melt in one direction. Figure obtained from reference [5]. 31

2.14 BOY 25 E injection moulder. 32

2.15 a- valve design cad model for the rigid stent experiment; b,d- different angles of the male part; c-female part; e- complete picture of the mould. This design was used in the experiements described in chapter 3. 32

2.16 Polivalve design : a- female and male part of the alluminium mould, b- size description and prototypes of the polymer valve. Figure adapted from reference [6]. 33

2.17 Map of the styrenic cylinders orientation of the valve leaflet of Polivalve made of SEBS20. The orientation is determined by the angle vectors, their length is proportional to the inverse the full width at half maximum (FWHM) for the relevant reflection of the SAXS pattern for every point scanned in the leaflet. a- two meridional reflection indicate parallel unidirectional orientation; b- two equatorial reflection indicate unidirectional perpendicular orientation, c- four intermediate reflection at perpendicular axis show bidirectionality at spefic angles. Figure adapted from reference [6]. 33

2.18 a-SEBS chemical structure, b-SEPS chemical structure 34

2.19 Schematic representation of the z-beam axis mapping the surface of the sample in x and y directions. 38

2.20 Example of a sample grid for SAXS analysis. 39

2.21 Differential scanning calorimetry results for a-SEBS20 and b-SEPS22. The plots show a temperature ramp form -50°C to 300 °C (10°C/min), a decreasing ramp from 300°C to -50°C (25°C/min) and a third ramp up to 300°C. The test was performed on DSC Q2000 (TA instruments, DE, USA). 42

2.22 Compression moulding SEPS22 SAXS analysis: a- 2D refraction pattern, showing equatorial 1st and higher order reflections indicating highly ordered hexagonally cylinders packed in parallel direction to the melt flow; b-2 θ polar integration of the reflection pattern, the first peak is the first order reflection, followed by second order peak at $\sqrt{3}$, $\sqrt{9}$ and $\sqrt{13}$ peaks typical of an hexagonally packed pattern; c- azimuthal integration of the first order peaks, the narrow peak indicates a well oriented microstructure. Integration calculation performed by Dr. J. Stasiak. . . 43

2.23 Calculation of the d-spacing for MED500400, SEBS20 and SEPS22. d-spacing was calculated from the first reflection via polar integration applying Bragg's Law. The SAXS images are taken from Bruker Nanostar. Integration performed by Dr J. Stasiak. 44

2.24 SAXS pattern and azimuthal integration of the central narrow section of the unitensile samples for both ISO37 type 2 and ASTM D638 type v geometries. The samples were injection moulded with mould in Figure 2.10. a- SEPS22 X-ray pattern, c- SEPS22 azimuthal integration, b-SEBS20 X-ray pattern, d- SEBS20 azimuthal integration. Both images show equatorial refractions indicating parallel orientation respect to the flow direction. 45

2.25 Schematic representation of the injection moulded flat samples from mould 2.10-a of both SEBS20 (a) and SEPS22 (b). The drawings give an indication of how the samples were cut with the unitensile sample die. The red angular vector indicates the orientation pattern, the lenght of the vector is proportional to the inverse of the full width at half maximum (FWHM) for the relevant reflection. Calculation performed by Dr J. Stasiak. 46

2.26 SEBS20 samples X-ray patterns. The samples were cut from the injection moulded flat sheet in parallel (b,e) and perpendicular directions (a,c,d). The red angular vector indicates the orientation pattern, the length of the vector is proportional to the inverse of the full width at half maximum (FWHM) for the relevant reflection. Calculation performed by Dr J. Stasiak. 47

2.27 SEPS22 samples X-ray pattern. The samples were cut from the injection moulded flat sheet in parallel (a,b,c) and perpendicular direction (d).The red angular vector indicates the orientation pattern, the lenght of the vector is proportional to the inverse of the full width at half maximum (FWHM) for the relevant reflection. Calculation performed by Dr J. Stasiak. 48

2.28 Tan δ, storage and loss modulus as a function of temperature using DMA 800 (TA instruments, DE, USA). The analysis are for a-SEBS20, b-MED500400 and c- SEPS22. 50

2.29 a- Effect of ethyl branches on loss tangent for SEBS (30% styrene) b- effect of styrene content on loss tangent for SEBS (10 ethylegroup/100 C). The figure was adapted from reference [75]. The number indicates their samples nomenclature. On the β transition peak there are indications of the ethyl branches and styrene fraction. 51

2.30 Temperature ramp for SEPS22 .a-the graph represents the loss and storage modulus on the left, and the tanδ on the righ axis. The temperature ramp was perferomed between 180°C and 250°C, 10 rad/s frequency and 1% strain; b-storage modulus versus temperature for 10, 1 and 0.1 rad/s at 1% strain for SEPS22 55

2.31 Plot of loss modulus versus storage modulus for SEPS22. The data were collected for frequency sweeps at different temperatures. The tests were performed at 190°C, 210°C, 230°C and 250°C at 1% strain. The frequency sweep started at 0.1 rad/s and reached 100 rad/s. The results idenitfy a order-disorder transition temperature at around 230°, where the log G'vs log G" behaviour starts to be independent from temperature. 56

2.32 a- storage modulus vs frequency behaviour at 190°C, 210°C, 230°C and 250°C for SEPS22. Above 230°C the terminal behaviour indicates a shift towrds a disordered phase; b- dynamic viscosisty vs frequency at 190°C, 210°C, 230°C and 250°C for SEPS22, above 230°C the viscosity starts to become independet from frequency, representing a homogenoeus melt, *i.e.* a disordered phase. 57

2.33 Low frequency behaviour of storage modulus for different types of ordered microstructure. The cubic spherical phase is frequency independent. The disordered phase has a rapid decay towards terminal behaviour. The figure was adapeted from reference [78]. 58

2.34 a-Temperature ramp for SEBS20, the graph represents the loss and storage modulus at 1% strain, 1 and 10 rad/s;b- logG" vs logG" Cole-Cole plot for SEBS20 from frequency sweep (0.1-100 rad/s) performed at 190°C, 210°C, 230°C and 250°C at 1% strain. No phase transition have been detected from these analysis. 59

2.35 a- storage modulus vs frequency behaviour at 190°C, 210°C, 230°C and 250°C and 1% strain for SEBS20, the slight change of slope at low frequencies might indicate a change in microstructure configuration from cylinders to sphere; b- dynamic viscosity vs frequency at 190°C, 210°C, 230°C and 250°C at 1% strain for SEBS20. Shear thinning is shown for all temperatures investigated. 59

2.36 Temperature ramp for MED500400. The graph represents the loss and storage modulus on the left, and the tan δ on the righ axis. 10 The temperature ramp was perferomed at 10 (a) and 1 (b) rad/s frequency and 1% strain. 60

2.37 Frequency sweep for MED500400 at 1% strain. a- storage modulus vs frequency behaviour at 160°C and 250°C for MED500400, there is marked change towards disordered terminal behaviour from 160°C to 250°C; b- dynamic viscosisty vs frequency at 160°C and 250°C for MED500400,above 1rad/s the frequency is almost independet from temperature and shows a shear thinning behaviour; c- Cole-Cole plot for MED500400. 61

2.38 AFM images of SI/BS19 (a,b) and SIBS30 (c,d). The images show worm like cylinder microphase structures. The images were collected by Dr J. Stasiak. 62

2.39 Schematic representation of the hexagonal pattern of the styrene cylinders divided in 6 equilater triangles. The red circles represent the cylinders. The height of the cylinder corresponds to the d-spacing. 63

3.1 Schematic of pure shear test specimen adapted from reference [106]. . . 73
3.2 Schematic of unitensile specimen with small crack adapted from reference [106]. 74
3.3 Values of k(λ) plotted against extension ratio. The results are for different types of vulcanized rubber. Picture taken from reference [108]. . 75
3.4 Regimes of fatigue crack growth behaviour in unfilled styrene-butadiene (x) and natural rubber (o) under R=0. Plot from reference [110]. . . . 76
3.5 Diagram representing a polymer chain of n-monomer lying across the crack propagation plane. Schematic adapted from reference [111] 78
3.6 Schematic process overview of CHC™ Corline Heparin kit (Corline®,Uppsala, Sweden) coating process. The procedure was supplied by the manufacturer. 87
3.7 Pure shear specimen geometry. 87
3.8 Stable Microsystem Texture Analyser during crack growth test. 88
3.9 Unitensile samples mounted on the Stable Microsystem TA for crack nucleation test. 90
3.10 ElectroForce® DuraPulse™ (TA instruments, DE, USA). A total of 6 valves could run at the same time. 91
3.11 3D printed rigid ring for valve rigid stent experiment. a- bottom view, where the post inserts are visible;b- side view; c- top view showing extra cavity to allow the opening of the leaflets. 91
3.12 a- photo of the Pulse Duplicator of the Department of Chemical Engineering and Biotechnology (University of Cambridge, UK), the red circle indicates the polymeric valve housing; b- schematic representation of the pulse duplicator. 92
3.13 Tearing energy (kJ/m^2) versus crack growth rate (mm/cycle) for SEBS20 and SEPS22 parallel and perpendicular, MED500400 and Natural rubber. The plot for each material show the experimetnal points, the best fit, the 95% confindence band and the prediction band. 97
3.14 Crack growth slope for isotropic materials SEPS22, MED500400 and natural rubber. The dashed line represents the best fit for the experimental points. 98

3.15 MED500400 compression moulded pure shear samples after crack growth test. The material is isotropic and shows a smooth linear crack path profile. 98

3.16 Natural rubber compression moulded pure shear sample after crack growth test. 98

3.17 Crack growth slope for parallel oriented SEPS22 and SEBS20 and isotropic MED500400. The dashed line represents the best fit for the experimental points. 99

3.18 Schematic representation of the effect of molecular weight and styrene fraction on the position of the crack growth slope for styrenic block copolymers. 99

3.19 Crack growth slope for parallel and perpendicular orientation of SEPS22 and SEBS20. The dashed line represents the best fit for the experimental points. 100

3.20 Pure shear specimen samples after crack growth test, after stretching at increasing strain levels. The samples are compression moulded and cut SEBS20. a) SEBS20 with cylinders parallel to the strain direction, the blue square highlights the saw-tooth profile at low-medium strain (up to 70%) and the red square represent the higher strain (up to 100%) for which a more linear profile is noticeable; b) SEBS20 with cylinders perpendicular to the strain direction, represented by a smooth crack line. 102

3.21 Crack growth slope for parallel, perpendicular and isotropic SEPS22. The dashed line represents the best fit for the experimental points. . . . 103

3.22 Crack growth versus tearing energy profile of transition and power low regime for SEPS22 and SEBS20 parallel oriented. The vertical dashed line on the low tearing end are the calculated T_0 values, the grey box at 1 kJ/m^2 is the predicted transition tearing energy, a precise value was not calculated. The dashed line is the best fit for the experimental points. 104

3.23 Lifetime prediction model for unitensile samples with cylinders parallel and perpendicular to the strain direction. The grey box represent the SED range for the valve made of the respective material. The samples were cut with a die from an injection moulded sheet. (a)SEBS20, (b)SEPS22. Error bars represent standard deviation. 106

3.24 SEBS20 broken unitensile samples; the samples were cut from an injection moulded sheet with a ISO37-type 2 sharp cutting die. a- samples with styrene cylinders perpendicular to the strain direction b- injection moulded samples with styrene domain parallel to the strain direction. . 107

3.25 Lifetime prediction for 1 mm and 2 mm thickness unitensile specimens made of SEPS22 with cylinders oriented parallel to strain direction. Error bars represent standard deviation. 108

3.26 Lifetime prediction for 0.7 mm, 1 mm and 2 mm thickness unitensile specimens made of SEBS20 with cylinders oriented parallel to strain direction. The nucleation test for 0.7 mm samples was performed by R.Patel. Error bars represent standard deviation. 109

3.27 Left: Crack growth data for SEPS22 parallel separated in different samples thicknesses of 0.41 mm, 0.48 mm, 0.56 mm and 0.67 mm. Right: Crack growth data for SEBS20 parallel separated in different samples thicknesses of 0.67 mm, 0.7 mm and 0.92 mm. The data points fall in the same area of the plot for both cases. 110

3.28 Lifetime prediction for compression and injection moulded parallel and perpendicular SEPS22. The dashed lines represent the injection moulded prediction. Error bars represent standard deviation. 111

3.29 Lifetime prediction of 1 mm and 2 mm thick parallel oriented SEPS22 specimens. The nucleation points for short and long geometry from ISO37 type 2 and ASTM D638 type v specimen fall on the same line for the same thickness. The short 1 mm points are within the error of the prediction. 112

3.30 Orientation map and angle measurement of specimen cut form injection moulded sheet. a- SEBS20 specimens have 66% of cylinders oriented at 40° on the left, and 45° on the right, the central specimen has 62% of cylinders oriented parallel to strain; b- SEPS22 specimens have 100% cylinders oriented at a 30° angle on the left hand side, 89% parallel in the centre and 79% at a 30° angle on the right edge. 113

3.31 SEPS22 broken unitensile samples. The samples were cut with a ISO37 type 2 sharp cutting die from the injection moulded sheet . The samples are cut from specific area of the sheet to obtain different orientation of the styrene domain. a) left cut samples with unidirectional 30° orientation; b) central cut samples with bimodal styrene cylinders orientation 89% parallel and 11% perpendicular; c) right cut samples with bimodal styrene cylinders orientation 79% at 30° angle. 115
3.32 SEBS20 broken unitensile samples. The samples were cut with a ISO37-type 2 sharp cutting die from the injection moulded sheet shown in Figure 2.11. The samples are cut from specific area of the sheet to obtain different orientation of the styrene domain. a) left cut samples with bimodal styrene cylinders orientation 66% at 45° angle; a) central cut samples with bimodal styrene cylinders orientation 62% parallel and 36% perpendicular. 116
3.33 Lifetime prediction for central injection cut specimen of SEBS20. The prediction is compared to the cases of 1 mm, 2 mm parallel and 1 mm perpendicular samples for the same material. Error bars represent standard deviation. 116
3.34 Lifetime prediction for central injection cut specimen of SEPS22. The prediction is compared to the cases of 1 mm, 2 mm parallel and 1 mm perpendicular samples for the same material. Error bars represent standard deviation. 117
3.35 Lifetime prediction of coated with Corline®and ASTUTE®and uncoated SEBS20 parallel oriented samples;a- 1 mm specimen thickness;b-2 mm specimen thickness. Error bars represent standard deviation. . . 118
3.36 Lifetime prediction of coated with Corline®and ASTUTE®and uncoated SEPS22 parallel oriented samples; a- 1 mm specimen thickness;b-2 mm specimen thickness. Error bars represent standard deviation. . . 118
3.37 Crack growth results for SEBS20 parallel oriented. The experimental points for the Corline®coated samples are plotted with the results obtained from crack growth of uncoated samples. The coated data points lay withing the same prediction band. 119
3.38 Stress strain curve of parallel oriented SEPS22 (a) and SEBS20 (b) uncoated, Corline®coated and ASTUTE®coated. The plot shows engineering and real stresses. Data collected by E. Okafor, J. Allford and V. Manhas. 120

3.39 Valve durability for prototype JA and JB [6] uncoated and Corline®heparin coated. Error bars represent standard deviation. Data collected by Dr J. Stasiak. 120

3.40 Lifetime prediction of 1 mm thick SEBS20 and SEPS22 specimens.(a) perpendicular, (b) parallel orientation of the styrene domain respect to the principal strain direction. The grey box indicates the SED range for a prosthetic valve made of these materials.Error bars represent standard deviation. 122

3.41 Lifetime prediction of 1 mm thick parallel oriented SEPS22 , 0.7 mm parallel SEBS20 and 0.7 mm MED500400 specimens. The grey box indicates the SED range for a prosthetic valve made of these materials. Error bars represent standard deviation. 122

3.42 Lifetime prediction of 0.34 mm isotropic SEPS22 compared with prediction of anisotropic parallel and perpendicular 1 mm thick specimens. The grey box indicates the SED range for a prosthetic valve made of these materials.Error bars represent standard deviation. 123

3.43 Rigid stent valve prototypes made of SEBS20, SEPS22 and MED500400 from left to right. 125

3.44 SED map of the ISO37-type 2 specimen stretched at 50% strain. The figure was obtained from ABAQUS software output. 126

3.45 Comparison of maximum, medium and minimum principal stress/strain in the element with maximum SED in the valve leaflet simulation. . . . 127

3.46 Lifetime prediction of the rigid stent experiment for a-0.25 mm and 0.35 mm SEPS22 valves ,b-0.1 mm, 0.25 mm and 0.35 mm SEBS20 valves. Error bars represent standard deviation. 127

3.47 Schematic representation of the leaflet indicating where the thickness measurements were taken. 128

3.48 Thickness map in mm of the valve leaflet for the rigid stent experiment. Image produced by Dr. M. Serrani. 128

3.49 SED map of the 0.25 mm valve leaflet 3.48 for the rigid stent experiment. Image produced by Dr. M. Serrani. 129

3.50 Number of cycles to failure for the rigid stent experiment valve made of SEBS20, SEPS22 and MED500400 both uncoated and coated with Corline®and ASTUTE®coatings.Error bars represent standard deviation. 130

3.51 XPS data for a valve that underwent fatigue testing. The measurements were taken at different time for the duration of the valve. The peak area is related to the concentration of sulfur on the surface. Data collected by Dr J. Stasiak. 130

3.52 Relationship between initial crack size and part thickness for SEBS20 parallel oriented. The dashed line represent the best fit of the experimental points. Both results for unitensile samples and rigid stent experiment valve are plotted. The red triangle represent the initial crack size prediction for a 0.35 mm thick part with cylinders oreinted parallel to main strain direction. 132

3.53 Relationship between initial crack size and part thickness for SEPS22 parallel oriented. The dashed line represent the best fit of the experimental points. Prediction and 95%confidence band are also reported. Both results for unitensile samples and rigid stent experiment valve are plotted. The red triangle represent the initial crack size prediction for a 0.35 mm thick part with cylinders oreinted parallel to main strain direction. 132

3.54 Lifetime prediction based on power law and transition law for SEPS22 parallel oriented. The plot includes nucleation points for unitensile samples 1 and 2 mm thick and rigid stent valves. 135

3.55 Lifetime prediction based on power law and transition law for SEBS20 parallel oriented. The plot includes nucleation points for unitensile samples 0.7,1 and 2 mm thick. 137

3.56 Bench durability testing: A: durability of PHV prototypes with leaflets made from SEPS22 and SEBS20. Error bars represent one standard deviation. Data for J6 valves does not show any variation and represents the actual state of ongoing test. B: Durability as a function of mean leaflet thickness for J5/J6 design. Ongoing durability testing of the J6 prototype is shown by shaded markers, while finished tests are represented by unfilled markers. Figure sourced from reference [6]. . . . 140

3.57 Hydrodynamic performance of fatigued J6 valves. A Effective Orifice Area (EOA); B Fractional Regurgitation (REG). Error bars indicate variation between repeated measurements of the same valve. Figure sourced from reference [6]. 141

3.58 Measurements of hydrodynamic performance: A: Prototype J6 21 mm and Edwards Perimount 21 mm valve at peak systole (left) and diastole (right); B: Pressure and flow waveforms acquired during pulsatile tests of J6 valve: AP is aortic pressure, LVP left ventricular pressure, and AF aortic flow; C: Effective Orifice Area (EOA); D: Regurgitant fraction (REG); E: mean systolic pressure gradient ΔP. Error bars represent one standard deviation. The trend line catches the effect of leaflet thickness on hydrodynamics of 21 mm polymeric valves. Results for the J6 valve (21 mm) are circled by a dashed line; the 19 mm J6 valve selected for *in vivo* testing is represented by red markers. All data are prior to fatiguing. Figure sourced from reference [6]. 142

4.1 Complete testing apparatus for the calcification test. The big outer tank is filled with water and covered with bubble wrap to insulate the system. The instrument on the top left is the ANOVA heater set at 38°C. The inner green tank contains the calcifying solution, the green plastic stand where the static samples are hung, the bending device and some weights to prevent the floating of the green tank in the water. Picture collected by E. Okafor and J.Allford. 160

4.2 a- Picture of the bending device (collected by V. Manhas), the arrows point out the rotating cam and driving rod that move the deflector bar; b- schematic drawing of the rig showing the deflector tensile test on the uni-tensile samples depicted in blue-red lines (picture adapted from Brubert [5]). 162

4.3 a- Picture of the bending device immersed in the calcifying solution with the set of 3 stents with the valves prototypes mounted on top of the deflector; b- zoom of the picture a on the valves on attached to the stents. 163

4.4 Calcium concentration on SEBS20, SEPS22, MED500400 and Bovine pericardium tissue measured with AAS (Varian AA 240 & Spectra AA v.5.1, air/acetylene flame) after static calcification test on unitensile samples. Error bars represent standard deviation. Data collected by E. Okafor, J. Allford and V. Manhas. 164

4.5 Comparison of injection moulded samples uncalcified and samples that underwent static calcification; (a) SEPS22, (b) SEBS20. 164

4.6 Calcium concentration on unitensile samples of MED500400 uncoated, Corline®and ASTUTE®coated measured with AAS (Varian AA 240 & Spectra AA v.5.1, air/acetylene flame) after static and under-stress calcification. Error bars represent standard deviation. Data collected by E. Okafor, J. Allford and V. Manhas. 166

4.7 Calcium concentration on unitensile samples of SEBS20, SEPS22 and MED500400 Corline®and ASTUTE®coated measured with AAS (Varian AA 240 & Spectra AA v.5.1, air/acetylene flame) after static and under-stress calcification. Error bars represent standard deviation. Data collected by E. Okafor, J. Allford and V. Manhas. 167

4.8 Calcium concentration on polymeric valve leaflet of SEBS20 and MED500400 measured with AAS (Varian AA 240 & Spectra AA v.5.1, air/acetylene flame) after static and dynamic calcification. Error bars represent standard deviation. 168

4.9 a-Comparison between SEBS20 PHVs calcified dynamically and statically; the level of calcium is visibly higher for the dynamic test; b-valve prototype uncoated and not calcified. 168

4.10 Calcium concentration on polymeric valve leaflet of SEBS20, SEPS22 and MED500400 Corline coated and uncoated measured with AAS (Varian AA 240 & Spectra AA v.5.1, air/acetylene flame) after dynamic calcification. Error bars represent standard deviation. 169

4.11 Effective orifice area for MED500400, SEPS22 and SEBS20 uncoated and not calcified, uncoated and calcified, calcified and Corline® coated. The dashed line represents the minimum ISO 5840 requirements for a 19 mm valve. The measurements of pressure and flow were taken according to the instruction in section 3.2.2 for the Pulse Duplicator. Error bars represent standard deviation. 171

4.12 Regurgitation fraction for MED500400, SEPS22 and SEBS20 uncoated and not calcified, uncoated and calcified, calcified and Corline® coated. The dashed line represents the minimum ISO 5840 requirements for a 19 mm valve. The measurements of pressure and flow were taken according to the instruction in section 3.2.2 for the Pulse Duplicator. Error bars represent standard deviation. 172

4.13 Images taken from the Pulse Duplicator test during opening and closing of the valve prototypes made of MED500400, SEPS22 and SEBS20. The last line represents an SEBS20 tested after calcification. The right-hand column has highlighted in the pictures the area that remains open for the fluid to pass through during diastole. 173
4.14 Number of cycles to failure for MED500400, SEPS22 and SEBS20 uncoated and not calcified, Corline®coated and not calcified, uncoated and calcified, calcified and Corline®coated. The valves were calcified dynamically. The value n indicates the number of samples tested for each condition. The results are obtained from durability test run at 30 Hz on the Dura Pulse (TA instruments, DE, USA). Error bars represent standard deviation 174

5.1 Badimon chamber instrument: a- high and low shear chambers connected in series and positioned in a water bath at 37°C, the right side tube connects to the pump while the left one is connected to the vein of the patient to withdraw blood; b- close up from the top, showing the blood crossing the chambers; c- close set up of the three chambers in series; d- open chambers showing the channel size and the area where the polymeric sample is positioned, the two pieces on the right are closed on top of each other and inserted in the cover on the left. 180
5.2 Images obtained from the samples after blood contact in Badimon chamber, fixation and staining. The columns group, from left to right, uncoated, Corline®heparin coated and ASTUTE®heparin coated SEBS20 injection moulded samples. a-f samples subjected to high shear blood flow; g-l samples subjected to low shear blood flow. 182
5.3 Thrombus of patients obtained from Badimon chamber experiment at high (left column) and low shear (central column). Platelet rich thrombus was stained in pink and the tunica media of the aortic tissue stained in green.The images on the top row are from a patient suffering from diabetes (T2DM) while the second row is from an healthy subject. The SEM micrographs show the respective fibre mesh of the thrombus.Images adapted from reference [186]. 183

List of Tables

2.1 Injection moulding parameters for BOY 25 E for the valves prototypes. Indicated are the temperature of the mould, injection pressure and velocity, holding pressure profile with time and screw temperature (higher temperature is on the nozzle side) 35

2.2 Injection moulding parameters for BOY22D for the specimens in mould 2.10. Indicated are the temperature of the mould, injection pressure (as % of the maximum 160 bar) and velocity (as per machine specific settings), and screw temperature (higher temperature is on the nozzle side) 35

2.3 Plate temperature of heated press for compression moulding of SEBS20, SEPS22 and MED500400 36

2.4 Rheological test paramters for temperature ramp test for SEBS20, SEPS22 and MED500400 at various frequencies. 40

2.5 Rheological test paramters for strain and frequency sweep for SEBS20, SEPS22 and MED500400. 40

2.6 Measurement of molecular weight (Mw in g/mol), polidispersity index and polystyrene fraction (%wt) for SEBS20, SEBS29 and SEPS22. The results were obtained from a GPC dual detector (Viscotek GPC max VE2001). 41

2.7 Calculation of the matrix density (EB-ethylene butylene, EP-ethylene propylene), styrene volumetric fraction and cylinders diameter as a function of the matrix composition. The data shows the results for SEBS20 and SEPS22. The matrix density has been calculated using the rule of mixture : $\rho_{matrix} = \rho_1 \%m_1 + \rho_2 \%m_2$. 65

2.8 Results for SEBS20 and SEPS22 of the estimation of Young's modulus of the two domains of the block copolymers considered as matrix and fibres of a composite system, using the rule of mixture [91, 92]. The last column on the right shows the calculation of the average length of a fibre according to the Halpin-Tsai equation [93, 94]. 66

2.9 Calculation of the number of chains per cylinder of styrene and number of chains per unit cylinder volume for SEBS20 and SEPS22. V_{cyl} is the volume of one styrene cylinder, w_{cyl} is the weight of one cylinder, $Mw_{st,ch}$ is the molecular weight of a chain block of polystyrene, N_{cyl} and N_{ch} is the number of moles for a single cylinder and in one chain block respectively. The constants used are $\rho_{st} = 0.9075\ g/cm^3$, Avogadro's number $Na = 6 * 10^{23}$, $Mw_{st} = 104.15\ g/mol$. 67

3.1 Strain energy density function defined by second order equation experimental parameters and Young's modulus E (MPa) for SEPS22, SEBS20, MED500400 and Natural rubber. 95

3.2 Experimental results of the power law fitting to the crack growth results for SEPS22, SEBS20, MED500400 and natural rubber. 96

3.3 Parameters A and T_0 of the transition law for SEBS20 and SEPS22 parallel oriented. 103

3.4 Initial crack size values for parallel and perpendicular orientation of SEPS22 and SEBS20. 106

3.5 Initial crack size values for 2 mm, 1 mm and 0.7 mm thickness specimen for SEPS22, SEBS20 and MED500400. 108

3.6 Initial crack size value for compression and injection moulded SEPS22, both parallel and perpendicular. The injection moulded samples were 1 mm thick, while the compression moulded 0.55 mm thick. 110

3.7 Initial crack size for central injection cut specimen. The samples are cut from the centre of the injection moulded sheet. 114

3.8 Initial crack size for 2 mm thick SEBS20 and SEPS22 parallel oriented samples Corline®coated and uncoated. 118

3.9 Initial crack size values for parallel, perpendicular and isotropic SEPS22 specimen. The parallel and perpendicular value refer to 1 mm thick samples. The isotropic case is calculated based on solvent casted 0.34 mm specimen. 123

3.10 Experimental and finite element values of SED (MPa) for a unitensile sample (ISO37-type 2) stretched at 50% strain. 126
3.11 Initial crack size value for valve made of SEPS22 and SEBS20. Thicknesses of 0.35 mm, 0.25 mm and 0.1 mm of the leaflets were tested. . . 128
3.12 Thickness values of the leaflet (mm). The numeration respect the scheme on the left. Measurements were taken with a micrometer. 128
3.13 Transition law prediction parameters for SEPS22 parallel oriented. Three cases represented in Figure 3.54 are summarised. 136
3.14 Transition law prediction parameters for SEBS20 parallel oriented. Three cases represented in Figure 3.55 are summarised. 137

4.1 Metastable calcifying solution compositions from Golomb *et al.* [159] and Starcher *et al.* [173] (mM). 157
4.2 Calcium, phosphate and buffer composition of Bernacca *et al.* [169] study on *in vitro* dynamic calcification of bovine pericardium valves. . . 158
4.3 Ion concentration (mM) of SBF solutions compared to human blood plasma values according to Kokubo *et al.* [172]. 158
4.4 Ion concentration (mM) of modified SBF solutions by various authors. For all the solutions a Tris buffer was used, except Brubert [5], which used MOPS buffer. 159
4.5 Ion concentration (mM) of modified SBF solution. Resulting calcium concentration is equal to 100 ppm. 161
4.6 Average leaflet thickness measured for valve prototype made of SEPS22, MED500400 and SEBS20. The valve geometry is the one for the rigid stent experiment described in chapter 2 and 3. The thickness was measured in 4 different points within one leaflet and averaged with the results for the three leaflets. A digital micrometre was used. 171

List of Abbreviations

AAS	Atomic absorption spectroscopy
AF	Aortic flow
AFM	Atomic force microscopy
AP	Aortic pressure
ASTM	American Society for Testing and Materials
BCC	Body-centered cubic
BCP	Block copolymer
BHV	Bioprosthetic heart valve
CAD	Computer-aided design
CEB	Chemical Engineering and Biotechnology
CT	Computed tomography
DMA	Dynamic mechanical analysis
EDX	Energy dispersive X-ray analysis
EFS	Effective flaw size
EHBP	Ethane-1-hydroxy-1,1-bisphosphonate
EOA	Effective orifice area
EPDM	ethylene propylene diene monomer
FDA	Food and Drug Administration
FEM	Finite element modelling
FTIR	Fourier-transform infrared spectroscopy
FWHM	Full width at half maximum
GPC	Gas permeation chromatography
HAP	Hydroxyapatite
HBP	Human blood plasm
IgG	Immunoglobulin G
IgM	Immunoglobulin M

ISL	Intermediate segregation limit
ISO	International organisation for standardisation
IR	Infrared
LAP	Living anionic polymerisation
LVP	Left ventricular pressure
MQ	Milli-Q®(water)
ODT	Order-disorder transition
OOT	Order-order transition
PB	Polybutylene
PBS	Phosphate-buffered saline
PC	Polycarbonate
PCU	Polycarbonate urethane
PCUU	Polycarbonate urethane ureas
PEB	Polyethylene-butylene
PEEK	Polyether ether ketone
PEG	Polyethylene glycol
PEO	Polyethylene glycol
PEP-PEE	Poly(ethylenepropylene)-block-polyethylethylene
PEU	Poly(ester urethane)
PEUE	Poly(ether)urethane
PEUU	Poly(ester urethane) urea
PHV	Polymeric heart valve
PI	Performance index
PIB	Polyisobutylene
PIB-PU	Polyisobutylene-based polyurethanes
PIB-PUU	Polyisobutylene-based polyurethane urea
PMMA	Polymethyl methacrylate
POSS	Polyhedral oligomeric silsesquioxane
PS	Polystyrene
PSU	Polysulfone
PTFE	Polytetrafluoroethylene
PU	Polyurethane
RAFT	Reversible addition fragmentation chain transfer
REG	Regurgitant fraction

RO	Reverse osmosis (water)
SANS	Small angle neutron scattering
SAXS	Small angle X-ray scattering
SBC	Styrenic block copolymer
SBF	Simulated body fluid
SBS	Polystyrene-butadiene-styrene
SBR	styrene-butadiene rubber
SEBS	polystyrene-block-polytethylene-butylene-block-polystyrene
SED	Strain energy density
SEM	Scanning electron microscopy
SEPS	polystyrene-block-polyethylene-propylene-block-polystyrene
SIBS	Poly(styrene-b-isobutylene-b-styrene)
SIS	Styrene-isoprene block copolymer
SI/BS	polystyrene-block-polyisoprene-block-polybutadiene-block-polystyrene
Si-PUU	Siloxane poly(urethane-urea)
SSL	Strong segregation limit
TAVI	Transcatheter aortic valve implant
TEM	Transmission electron microscopy
THF	Tetrahydrofuran
TPE	Thermoplastic elastomer
UV	Ultra violet
VHD	Valvular heart diseas
WSL	Weak segregation limit
XPS	X-ray photoelectron spectroscopy

Chapter 1

Introduction

This chapter describes the background and the aim of this work. The focus of the thesis is the application of styrenic block copolymers to a polymeric prosthetic heart valve for use in the aortic position. Here I briefly describe what a heart valve is and why a new prosthesis is needed. Moreover, I describe the currently available options for heart valve replacement and new technologies developed in recent years to overcome problems with the current prostheses. Finally, I present Polivalve, a novel polymeric heart valve, and the culmination of this research.

1.1 Background

1.1.1 The heart and heart valves

The discovery of the function of the heart and the circulation of blood is usually attributed to William Harvey (1578-1657). However, in AD 157 an ancient Greek physician, Galen, discovered the pulmonary circulation as a result of assisting injured fighters. His writings reached Michael Servitus, a Spanish physician, in the 16th century, who also observed the pulmonary circulation . Nevertheless, it was only after Harvey's studies that the circulatory system was properly understood. He demonstrated that blood flows in two separate loops, that venous blood flowed to the heart and that the valves in the veins maintain a one way system [1, 2].

The heart as we now know it is shown in Figure 1.2. The heart is a muscle located in the middle compartment of the mediastinum in the chest and is the centre of the circulatory system, which consists of a network of blood vessels, such as arteries, veins, and capillaries. The heart is divided in four chambers, two atria and two ventricles. Deoxygenated blood enters from the superior vena cava into the right atrium, is pumped

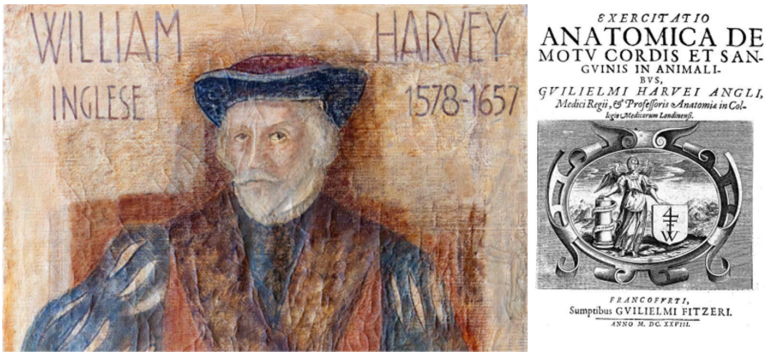

Figure 1.1: Gian Giacomo Dal Forno, "Portraits of ancient foreign students at the University of Padova - William Harvey", Palazzo Bo, Padua (on the left) [3]; cover of *"Exercitatio Anatomica de Motu Cordis et Sanguinis in Animalibus"* , the best-known work of Harvey, firstly published in 1628. Image taken from [4].

into the right ventricle and exits through the pulmonary arteries to reach the lungs, where it is oxygenated. The blood coming back from the lungs enters the left atrium through the pulmonary veins, moves to the left ventricle and is finally pumped out through the aorta to reach the rest of the circulatory system. When the atria contract to fill the ventricles it is called diastole, while when ventricles contract to pump the blood out is called systole. Diastole and systole are the two phases of the heartbeat, which happens around 100,000 times a day. Several valves are positioned in the circulatory system to ensure that the blood circulates only in one direction. Four valves are present in the heart, as shown in Figure 1.2 and 1.3.

The tricuspid valve is composed of three leaflets and sits between the right atrium and ventricle. The bicuspid mitral valve connects the left atrium to the left ventricle. In these two valves, the cusps are also attached via *chordae tendinea* to two papillary muscles projecting from the ventricular wall. The pulmonary valve separates the right ventricle from the pulmonary arteries. Finally, the aortic valve regulates the flow between the left ventricle and the aorta.

1.1.2 Heart valve diseases

The correct functioning of the heart valves is vital to maintaining blood supply to the body. Unfortunately, valvular heart diseases (VHDs) are extremely common. This report describes only aortic valve diseases, since it is the focus of the study. The most relevant diseases are regurgitation and stenosis.

Aortic regurgitation is diagnosed when the valve does not close tightly and blood

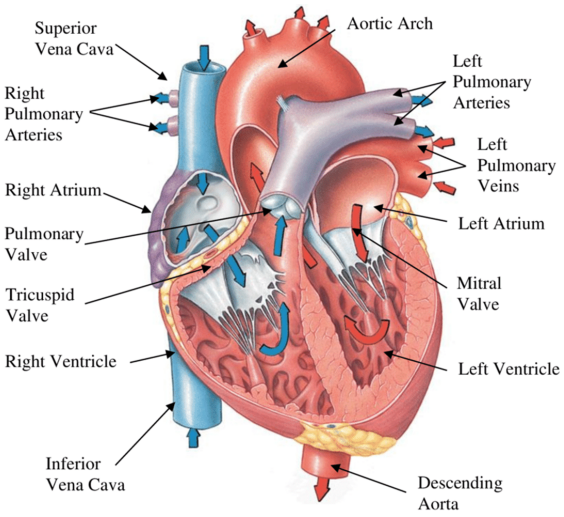

Figure 1.2: Section of the human heart. The image shows the atria and ventricles and the blood vessels connecting the heart to the rest of the circulatory system. Taken from [7].

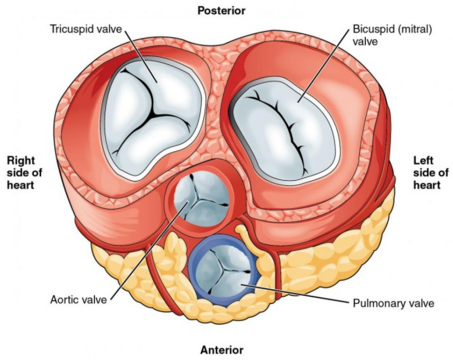

Figure 1.3: Equatorial section of the human heart showing the four valves: mitral, tricuspid, aortic and pulmonary valve. Image credit: OpenStax College, Anatomy & Physiology, 2013.

can flow backward, as shown in Figure 1.4. Aortic stenosis consists of narrowing of the opening area, due to fused or stiffer leaflets. This decreases the blood flow from the heart. Examples of different stages of stenosis are represented in Figure 1.5.

The causes of VHDs are congenital deformation, rheumatic fever or other complications such as hypertension, endocarditis and degenerative calcification [9]. Aortic stenosis affects around 4% of over-65 year olds in the western world and, every year, around 6,000 patients in the UK and 60,000 in the USA undergo heart valve replacement surgery. VHDs account for 10-20% of the cardiac procedures in the USA [9, 11]. This number is predicted to rise in the future years, due to increasing population age. Nearly 21% of the world population is predicted to be over 60 years old by 2050 and

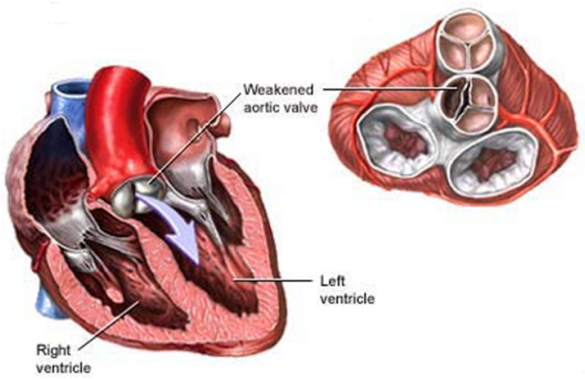

Figure 1.4: Image of an aortic valve suffering regurgitation. The equatorial section of the heart on the right shows the weakened valve leaflets, which allow the blood to flow backwards, as indicated in the image on the left. Taken from [8].

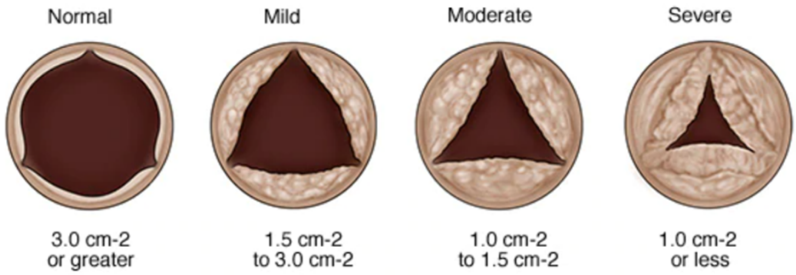

Figure 1.5: Aortic valve stenosis consist of a progressive narrowing of the aortic valve opening over time (from left to right in the picture). The result is an increased pressure within the heart, which reduces its capacity to pump blood to the rest of the body. Image adapted from [10].

the number of necessary heart valve replacement is expected to triple to nearly 900,000 worldwide [11, 12].

Valve repair is the current preferred method to treat patients with severe VHDs. However, a large number of valves cannot be repaired and require replacement [11]. Valve replacement has significantly improved the life expectancy of the patients; however many complications associated with artificial heart valves remain.

1.1.3 Prosthetic heart valves

In the last 60 years, over 80 models of artificial prostheses have been developed [12]. Two types of prosthesis are commercially available for replacement surgery: mechanical and bioprosthetic valves. Each has advantages and disadvantages. The main complications related to PHVs are the following: thrombosis and thromboembolism,

anticoagulant related haemorrhage, pannus overgrowth over the prosthesis, infections, paravalvular leaks and valve failure due to material fatigue or chemical attack [13].

The choice of the ideal combination of operation and prosthesis must be made together by the patient, cardiologist, and surgeon. Research is focusing on overcoming these complications and extending the life expectancy and quality of life of patients with artificial PHVs. Novel technologies include polymeric valves, tissue engineering, biodegradable materials and hydrogels. Manufacturing techniques, like addictive manufacturing and electrospinning, are also receiving increasing attention [16].

Mechanical valves

The first valve implanted was a mechanical valve in 1952 (ball and cage valve [14]). Mechanical valves are made of rigid material (elastic modulus higher than 1GPa) and are formed of one or two leaflets. Current valves are made of stainless steel, titanium or pyrolytic carbon for the housing coating, with leaflets made of graphite coated in pyrolytic carbon. Figure 1.6 shows some examples of commercial mechanical valves [16, 18, 19].

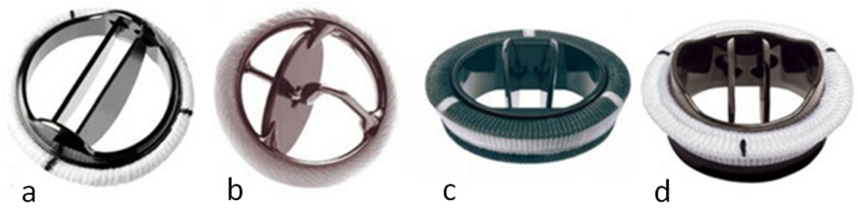

Figure 1.6: Mechanical valves: a- The St Jude valve, b- Medtronic Hall valve, c- Carbomedics valve and d- ON-X valve. Image adapted from [15].

The most dangerous complications of mechanical valves are thromboembolism and haemorrhage. Patients with mechanical valves require life-long anticoagulant treatment, which creates the risk of bleeding and major trauma [12, 16, 18]. The hemodynamics of these valves is the cause of these complications. High shear stresses are produced by blood flow jets. The jets form because the blood flow is obstructed and forced to go around the stiff tilting disk in the orifice area. Therefore, platelets are activated, and the coagulation cascade is started. Furthermore, areas of flow recirculation form around the discs, where flow stagnation and separation promotes deposition of damaged cells increasing the probability of thrombus formation [13, 20]. Other complications are infective endocarditis, risk of failure or separation of valvular components, which may embolise [20]. Despite these drawbacks, mechanical valves provide lifelong

durability and are the most suitable valves for young patients [12].

Bioprosthetic valves

Bioprosthetic valves are manufactured either from animal-derived tissue (xenograft) or human-derived tissue (homograft) [21]. The latter have very limited availability, despite being the most biocompatible option among mechanical and bioprosthetic valves. Xenograft valves are typically made of porcine aortic tissue or bovine pericardium [20, 21]. The valves are tricuspid, as are native aortic valve, and the tissue is stitched onto a frame or stent made of metal or plastic and covered with synthetic fabric, as shown in Figure 1.7. The geometry allows for optimal hydrodynamic performance, and the surfaces have good thrombo-resistance in comparison to mechanical valves. Hence, the risk of thromboembolism is significantly reduced, and very rarely is anticoagulant treatment needed [21, 22].

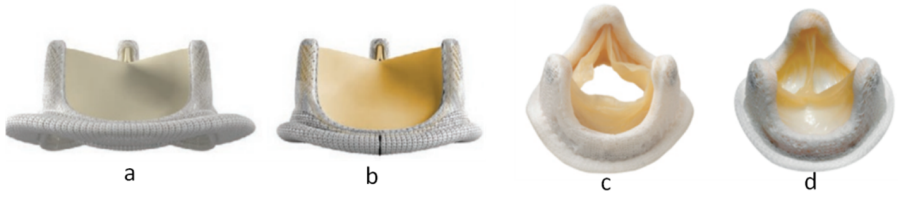

Figure 1.7: Commercially available bioprosthetic aortic valves: a- Carpentier-Edwards PERIMOUNT™,b- Carpentier-Edwards Magna Ease™,c- Medtronic Mosaic®and d-Medtronic Hancock®. a-b:Stented pericardial bovine surgical aortic valve bioprostheses, c-d Stented porcine surgical aortic valve bioprostheses. Image adapted from reference [22].

The low host immunological response has been attributed to the decellularization of the tissue. However, the process leads to deterioration of the mechanical properties of the material. To solve this issue, the valves are treated with chemical crosslinking agents, such as glutaraldehyde, to increase durability. Despite this, xenograft bioprostheses are afflicted by relatively short lifetimes (10-15 years), mainly due to tissue deterioration and calcification [16, 20]. These valves are mostly recommended for older patients. Today, the most used bioprosthesis are porcine and bovine glutaraldehyde-treated stented valves (Figure 1.7).

The new frontier of bioprosthetic valves is the transcatheter aortic valve implant (TAVI). This type of valve requires minimally invasive operation, avoiding risky and traumatic open-heart surgery. A valve with stent is collapsed inside a catheter, which enters either through the femoral artery or, with a small incision in the chest, through

a large artery or direct into the left ventricle. Once the valve is in place it is expanded and pushes the damaged native valve out of the way. Figure 1.8 shows examples of commercially available TAVI valves, both balloon-expandable and self-expandable. In the last few years, there has been a trend towards the expansion of indications for TAVI, to include intermediate and low-risk groups; and implantation numbers are increasing. In Germany, more than 15,000 TAVI procedures were performed in 2016. Recent studies are investigating the risks and benefits of TAVI for low-risk patients [23]. Long durability remains still a key concern for this type of valves, but the benefit of minimally invasive surgery makes them the most attractive prosthesis for many patients at present.

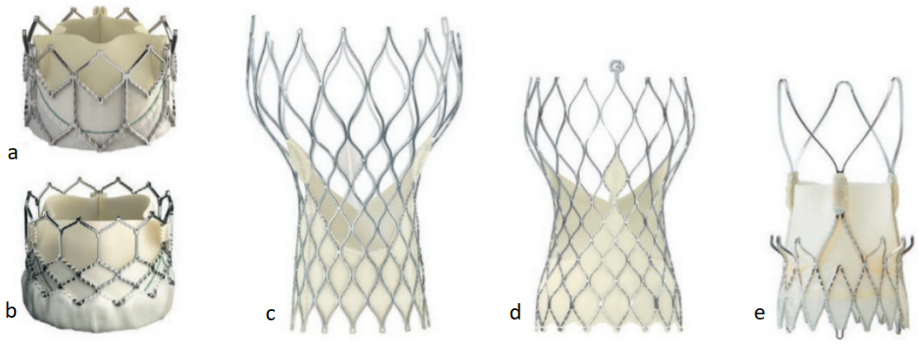

Figure 1.8: Balloon-expandable bovine pericardial tissue transcatheter bioprostheses a- Edward SAPIEN®XT, b- Edward SAPIEN®3. Self-expanding porcine pericardial tissue: c- Medtronic CoreValve®, d- Medtronic CoreValve®Evolut®, e- Symetis ACURATE neo™. Image adapted from reference [22].

1.1.4 Polymeric prosthetic heart valves

The first studies on the application of polymers to PHVs date back to the 1950s [17]. Polymers, elastomers in particular, have the potential to overcome the limitations of the other types of prosthesis. Soft tricuspid polymeric valves have optimal hydrodynamics and are less prone to calcification than bioprostheses. Moreover, they can be easily manufactured and so available at a low cost. The production of a bioprosthesis takes 40 days, in a facility requiring 150 skilled employees. In contrast, a polymeric valve can take a maximum of few hours to make, even with the most complicated polymeric manufacturing technique.

Despite these advantages, no polymeric valve is clinically available for surgery at present. The critical part is the selection of a suitable candidate material able to retain

mechanical integrity over repeated loading and unloading cycles, good biocompatibility and chemical stability. Standards for valve performance are described in ISO 10993-2018, for safety and biocompatibility of materials intended for medical devices, and ISO 5840-2015, for cardiovascular prosthesis general requirements. The ISO 5840-2015 specifies hydrodynamic standards, such as opening area and regurgitation threshold, and durability, which should reach a minimum of 200 million cycles (5 years equivalent).

Polymeric materials that have received most attention are polysiloxane (silicone), polytetrafluoroethylene (PTFE), poly(styrene-b-isobutylene-b-styrene) (SIBS) and polyurethane (PU) [16, 19].

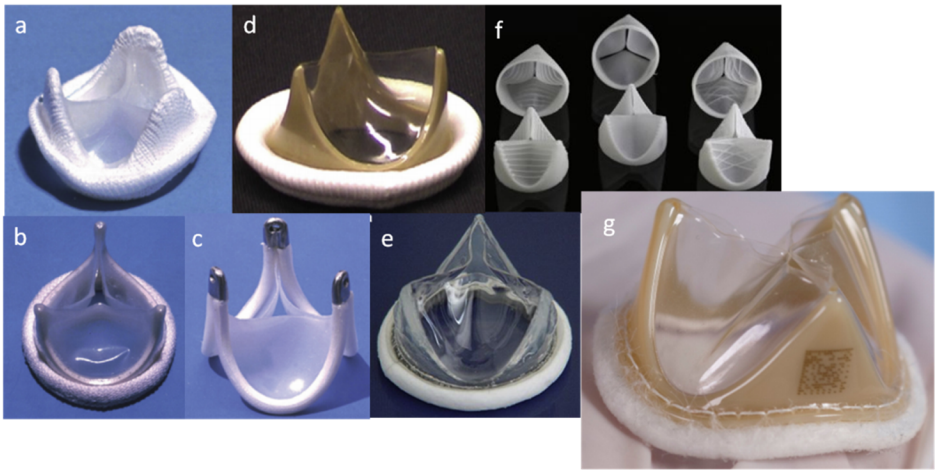

Figure 1.9: Polymeric aortic valves prototypes. a- the Reul-Ghista trileaflet PU valve, b- the Helmholtz Institute PU valve, c- the Reul-Haussinger PU valve, d- PU heart valve developed by the Glasgow group: Ellipto-hyperbolic Estane® dipcoated on a PEEK frame,e- polycarbonate urethane valves developed by ADIAM life sciences, Erkelenz, Germany, produced by a robotic droplet deposition technique,f- silicon 3D printed valves designed by ETH Zürich and SAT company, g- Foldax valve made of Siloxane Poly(urethane-urea), the valve is undergoing patient clinical trials. Image adapted from reference [19, 24, 27].

Polysiloxane

Polysiloxanes, commonly referred as silicones, are used in many medical devices for their excellent biostability and biocompatibility. The first silicone valve was developed in the late 1950's and it was among the first flexible leaflets PHVs prototypes (Silastic 50, Ellay Rubber Company). The valve had 0.38 mm thick leaflets housed in a silicone cylinder. However, the valve did not achieve long-term durability in a subcoronary

model. Later versions were made from different silicones with a variety of leaflet thicknesses. Some valves showed poor durability and in some emboli were noted in some patients. Silicone has not been used since the 1980s [19]. Recently, Coulter *et al.* [24] designed a 3D printed silicone valve (Figure 1.9-f). The structure is inspired by the anisotropic aortic valve tissue and it showed good hydrodynamic performance. Data on durability are not available.

PTFE and ePTFE

PTFE (Teflon®) and expanded PTFE (ePTFE, *i.e.* Gore-Tex®) have a good reputation for inertness and low surface energy, which usually correspond to good biocompatibility and make them an optimal candidate for medical applications. For example, ePTFE is used in the construction of artificial *chordae tendineae* in mitral valve repair.

Braunwald and Morrow in 1965, reported the first clinical trial of a flexible tricuspid Teflon fabric valve. At the end of the trial the valve had become stiffer and calcific deposits were found [25]. All further prototypes made of PTFE or ePTFE exhibited low resistance to thromboembolism and calcification, leaflets tending to become stiff, resulting in increased regurgitation [16, 19].

Polyurethane

Polyurethane (PU) has been extensively studied for valve application. The main concern with this class of material is hydrolytic or oxidative degradation. Several changes over the years brought significant improvement to the hydrolytically unstable polyester soft segment of PUs. Among the new formulations are polycarbonate urethane ureas (PCUUs), polycarbonate-based materials containing polyhedral oligomeric silsequioxane nanoparticles (POSS) and those that contain polysiloxane soft segments (PSUs), such as siloxane poly(urethane-urea) [19].

The first PU valves made of Estane (BF Goodrich) resulted in high mortality in animal trial, with fibrin deposition leading to stenosis and emboli [16].

In the 1980s, valves made of Biomer, a segmented PEUU from Ethicon and DuPont Lycra Spandex had low regurgitation, but showed serious calcification and thrombosis in a large animal model. After the 80s, leaders in the PU research for valves were two groups, one based in Aachen, Germany and the other in Glasgow, Scotland [19].

Figures 1.9-a-b-c show the valve prototypes made by the group of Reul in Aachen. The valves were made of a polyether/silicone based polyurethane and subsequently an aliphatic PCU (ENKA 1025/1 or ENKA/AKZO). *In vitro* durability reached between

400 and 650 million cycles for the first valve group, and up to 1000 million cycles for the PCU valve in accelerated *in vitro* tests. However, mitral implants in young calves showed extensive thrombotic deposits and calcification related to the surface roughness of the cusps [19].

Wheatley, in Glasgow, worked with a variety of polyurethanes, such as PEU (Estane, Figure 1.9-d) a PEUU (Lycra) and polysiloxane soft segment-based polyurethane (Elast-Eon). Geometry and leaflet thickness optimisation lead to satisfactory hydrodynamics and durability (up to 800 million cycles for PEUU valves). However, calcification was present in both *in vivo* (6-month sheep mitral model) and *in vitro* dynamic test for PEU and PEUU valves. On the other hand, Elast-Eon did not show evidence of thrombus formation, fibrin deposition or calcification in the *in vivo*-model. However, some evidence of hydrolysis degradation has been observed in Elast-Eon [19]. A different study on Elast-Eon valves showed high shear and velocity at the leakage jet during diastole, increasing the risk of thrombosis [26].

Very recently, a siloxane poly(urethane-urea) (SiPUU) valve, Foldax [27] (Figure 1.9-g), underwent an early feasibility human study, and it is to date the first polymer heart valves approved by the Food and Drug Administration (FDA) for human clinical trials. (SiPUU) was developed by incorporating a macrodiol linked with a diisocyanate to enhance mixing of hard and soft segments in PU. The material has low dynamic modulus, high tensile strength and minimal creep. It also showed excellent biocompatibility, which was tested as per ISO 10993 standard, demonstrating no observable toxicity. After an *ex vivo* AV shunt thrombogenicity experiment, the material had a minimum level of platelet attachment and thrombus formation. Chronic ovine implantations of a (SiPUU) valve revealed the same thrombogenicity as a clinical standard tissue-based valve. The valve was manufactured by dip coating, using a robotic arm; the prototypes' bench testing showed excellent durability, up to 600 million cycles. [28, 29].

SIBS

Poly(styrene-b-isobutylene-b-styrene), produced by Innovia, was selected to overcome the degradation problem of PU, since it has no reactive pendant group [30]. SIBS valves implanted in sheep failed due to calcification, creep and material failure. Nevertheless, the material was highly inert and there was no evidence of biodegradation [164]. Furthermore, the valve showed no enhanced thrombogenicity in a ventricular assist device, compared to mechanical or bioprosthetic valves [31].

The issue of the poor durability and creep was solved by using a crosslinked version of SIBS, xSIBS. Prototypes made of the latter material showed improved hydrodynamics and reduced thrombogenicity [16, 19].

Polivalve

At the Structured material group, based at the Department of Chemical Engineering and Biotechnology of the University of Cambridge (Cambridge, UK), we have developed a new valve design: Polivalve.

Polivalve is a flexible tri-leaflet polymeric valve designed for aortic implantation. The valve mimics the structure of the native valve leaflet. Collagen and elastin form a highly anisotropic microstructure in the native leaflet (Figure 1.10). The mechanical performance of the leaflet is dominated by tough collagen in areas of high stress and elastin in low stress domains. The leaflet is stiffer in the circumferential direction compared to the radial one. The aortic leaflet has a radial elastic modulus of 1.3 MPa for collagen and 0.04 MPa for elastin, while the modulus for the circumferential direction is 11.9 MPa and 0.36 MPa for collagen and elastin respectively [16]. Hence, block copolymers able to exhibit anisotropic mechanical properties were studied.

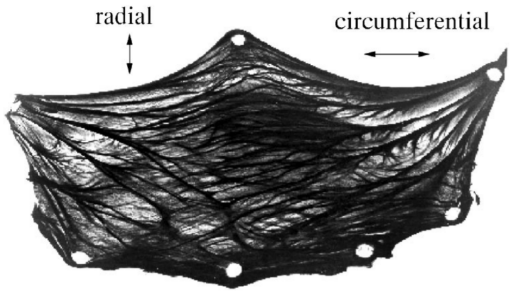

Figure 1.10: Image of native aortic valve with radial elastin and circumferential collagen fibres distribution. Image taken from reference [32].

This class of thermoplastic elastomers self-assemble into different microstructure according to composition, molecular weight and block compatibility. The polymers selected for this study form cylinders of styrene in an elastomeric matrix. The cylinders can be shear-oriented during moulding processes to give the desired anisotropic structure.

In the past 7 years, several styrenic block copolymers (SBCs) were shortlisted and tested to achieve the requirement of the ISO 5840-2015 standard for durability, hydrodynamics and biocompatibility. Figure 1.11 shows the prototypes designed over the

years by the Structured material group. The geometry has been optimized to minimise the stresses in the leaflets and reach optimal hydrodynamics and maximise durability.

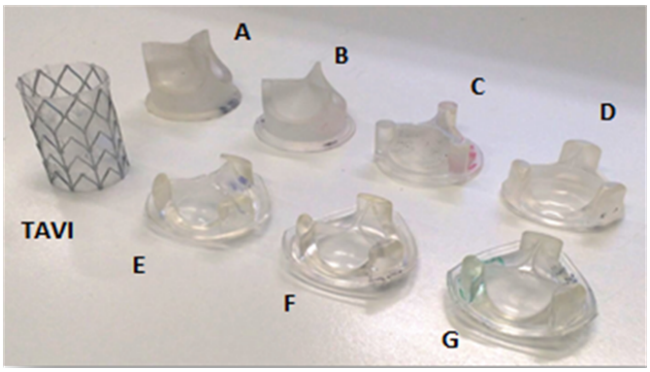

Figure 1.11: Styrenic block copolymer valve prototypes manufactured in the Chemical Engineering and Biotechonology department of the University of Cambridge by the Structured material group. Valve from A to G where developed chronologically by Dr M. Serrani, Dr J. Stasiak and Dr J. Brubert.

The final prototype is shown in Figure 1.12. Polivalve has already undergone a preliminary *in vivo* feasibility evaluation [6].

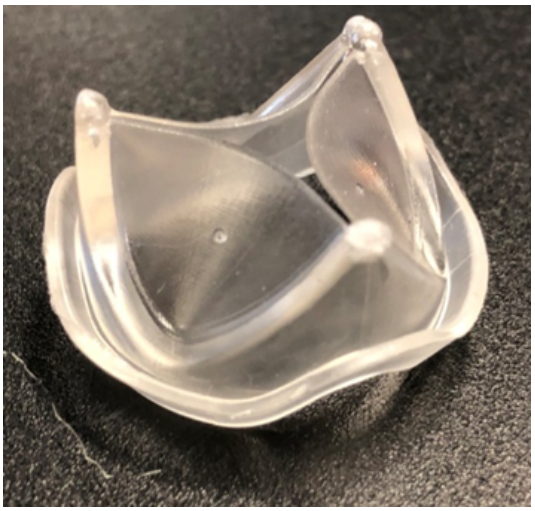

Figure 1.12: Image of Polivalve: a tri-leaflet polymeric PHV manufactured in our laboratories. The leaflets and stent are made of styrenic block copolymers.

As demonstrated in the previous sections, the most critical part in the design of PHVs is the selection of the material. Previously used polymers failed because of poor durability, calcification and thrombogenicity.

This study focuses on the fatigue properties of anisotropic styrenic block copolymers and the application of a lifetime prediction model for these materials. This model

guided in the selection of the most durable SBC for the valve application. Moreover, I investigated the calcification tendency of the material *in vitro* in a simulated-body-fluid assay. Finally, I present the results of an *ex vivo* hemocompatibility test on the shortlisted material for Polivalve.

1.2 Aim of the research

The aim of this research is the understanding of the fatigue behaviour of anisotropic styrenic block copolymers, with application to a flexible leaflet aortic valve prosthesis. A selection of SBCs was characterised in order to investigate the relation between morphology, microstructure and fatigue properties. Furthermore, the effect of heparin coating and calcification on fatigue resistance was investigated. A lifetime prediction model was validated for anisotropic specimens and valve prototypes based on the combination of crack growth and crack nucleation tests.

The thesis is structured in the following chapters:

- Chapter 2- Block copolymers: consists of a review of general block copolymer theory, explains the concept behind anisotropy and the materials studied, describes manufacturing techniques and material characterisation via small angle X-ray scattering (SAXS), gel permeation chromatography (GPC), dynamic mechanical analysis (DMA) and rheological analysis as well as an approximation of the domain size of the microstructure of the materials.

- Chapter 3- Fatigue model: reviews fatigue theory for elastomers and describes the most important models, presents the result of the mechanical tests and the investigation of parameters influencing fatigue lifetime prediction such as orientation, thickness, heparin coating, geometry; the fatigue model is also applied to the valve geometry and finite element modelling results are discussed. Finally, the study on durability and hydrodynamic performance and an early feasibility *in vitro* test conducted on Polivalve are presented.

- Chapter 4- Calcification: this chapter reviews the main findings on the calcification tendencies of polymeric materials used for medical application and identifies the possible causes of the phenomenon; the result of an *in vitro* calcification test is presented, showing durability and calcium level of the tested specimens and valve prototypes.

- Chapter 5- *Ex vivo* hemocompatibility: describes the method and results of an ex vivo hemocompatibility test using a Badimon chamber, performed on the leaflet's material of Polivalve.

- Chapter 6- Conclusions and Future work: contains a summary of the main findings discussed in the previous chapter of this dissertation. Future works introduces ideas and suggestions for future research, to progress the development and understanding of fatigue modelling of anisotropic materials and thermoplastic elastomers in general, as well as their biocompatibility properties.

Each chapter contains an introduction presenting a review of the relevant literature, a methods and materials section, a results and discussions section and conclusions.

Chapter 2

Block copolymers

2.1 Introduction

Block copolymers are a sub-class of polymeric materials characterized by different monomer units grouped in discrete blocks along the polymer chain. They were discovered thanks to termination-free anionic polymerization, which allowed the sequential addition of monomers to linear polymer chains terminated by carbanion [33] . The blocks are chemically distinct, immiscible and connected by covalent bonds [35]. The immiscible microphases can assemble in a variety of morphologies, giving rise to a vast spectrum of thermal, mechanical, optical, electrical and other physical properties that can be tailored for specific applications [34]. Advances in BCP synthesis in the last two decades allows the manufacture of polymers with controlled molecular weight and precise macromolecular architectures. Nowadays, there are remarkably precise statistical theories able to describe and predict domain shapes, dimensions, connectivity and ordered symmetry of many types of block copolymers [34, 35, 36].

The category of block copolymers includes several molecular architectures, such as diblocks, triblocks, starblocks, graft blocks and multiblocks, each containing a multitude of structural variations [37]. BCPs can be distinguished between self assembly in bulk or in solution [35]. The first group received the most attention initially, being the first BCPs discovered. BCPs in solution represent a new frontier for research, with their field of application rapidly expanding to include drug delivery, soft nanolithography and synthesis of porous materials. Among BCPs in bulk, thermoplastic elastomers are the most studied and exploited group. Their growing popularity is due to the outstanding elastic properties, shape memory features and good processability [36].

TPEs make use of the synergistic combination of rubbery and rigid segments. The rigid segments act as physical crosslinking, anchoring the rubbery chains. The result is similar elasticity to conventional rubbers and the same processability as thermoplastics using standard industrial techniques, such as injection moulding and melt extrusion [38]. Furthermore, one unique characteristic of BCPs is their ability to show anisotropic physical properties, generated by the orientation of microdomains [40]. This feature is the key for the application of BCPs in polymeric prosthetic heart valves, as will be explained in section 2.1.4 .

This chapter introduces the main BCP application and morphology studies, with a particular focus on bulk linear block copolymers and TPEs. The main focus of this research is anisotropic styrenic block copolymers for PHV application. The materials selected have been characterized with gel permeation chromatography (GPC), dynamic mechanical analysis (DMA), rheology and small angle X-ray scattering (SAXS) to understand the viscoelastic properties and mictrustructure morphology. The results and main findings are summerised in this chapter.

2.1.1 Applications of BCPs

Common applications for BCPs are found in many commodities, such as adhesives, sealants, automotive, wire, paving, high impact plastics, foams and oil additives [38, 41]. In general, BCPs are added to common plastic commodities (*i.e.* polystyrene) to enhance or modify certain properties, such as toughness or surface roughness [41, 34]. BCPs are also added to asphalts mix to reduce cracking and rutting at low and high temperature, taking advantage of their high-temperature resilience and low-temperature flexibility. Nowadays, sports equipments where fatigue resistance, energy damping and immunity to temperature variations, such as ski boots or running shoes, use BCPs [42]. TPEs enable low cost manufacturing of a myriad of recyclable, flexible, thermoformed, creep resistant and durable products. Classic examples of applications are gaskets, cable insulation, protective headgear and piping systems [42]. Common box adhesives are made of linear triblock to achieve pressure sensitive adhesion. In automotives, they are often used in bumpers, tires, CVJ boots and internal car components. Also medical devices, such as stents, catheters, wound drain and tubing are made of TPEs.

Novel fields of applications for BCPs are biomaterials, microelectronics, biomedicine and catalysts [43]. Membranes for batteries and fuel cells, catalyst supports/scaffolds, actuators, and self-healing or shape-memory systems represent new opportunities for

material designs [42]. A more recent opportunity for BCPs is nanolitography for patterning of semiconductors, production of ultradense arrays of metal as well as condensation and isolation of magnetic storage media [42, 50].

For polymer self assembled in solution, the majority of research has focused on aqueous self-assembly. In recent years there have been significant efforts to study also BCPs assembly in organic solvents, ionic liquids, supercritical solvents and mixed solvents [42]. Amphilic BCPs are applied as micelles for drug delivery, soft nanolitography with directed self assembly technique and mesoporous structures [38, 42].

2.1.2 Synthesis of BCPs

The BCPs studied in this work are commercially available polymer grades. The lack of control on the manufacturing side is compensated by the achievement of ISO standard requirements for medical grades materials. Hence, the following section only briefly introduces the main manufacturing methods for TPEs. The main strategies for TPEs synthesis can be divided in two classes: addition by living polymerization and radical polymerization [38, 42].

Living anionic polymerization (LAP) is a widely exploited method for BCPs industrial production. The process for this type of polymerization is characterized by quantitative conversion without chain transfer and/or chemical termination. It is currently the best method for the synthesis of well-defined BCPs made of vinyl monomers (*i.e.* styrene, dienes, (meth)acrylates, vinyl pyridines, acrylonitriles, siloxanes). This method allows more efficient control over the molecular weight, architecture, composition and functionality compared to radical polymerisation [38].

Figure 2.1 shows a schematic representation of the reaction for LAP. The initiation step consists of a nucleophilic attack on a monomer resulting in carbanion. The reaction can be initiated by several different compounds, among them alkali metal salts, bases, and organometalic derivatives such as alkyl, aryl, alkoxy, amino, and cyano. For example, alkyl lithium compounds are frequently used to polymerize diene-styrene copolymers [39].

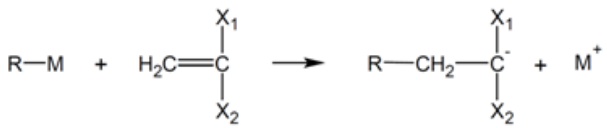

Figure 2.1: Generic representation of living anionic polymerization initiation [39].

LAP allows for sequential growth of block-copolymers because the reactive part of the chain remains so even if the monomers are all consumed. The main condition for its application is that the nucleophilicity of the macroanion is high enough to initiate the second monomer. For this reason the monomers are added in order of increasing electron affinity (ex:styrene<butadiene-isoprene) [38].

The absence of transfer reactions and termination results in a narrow molecular weight distribution. Furthermore, LAP opens possibilities of molecular architectures allowing tailored BCPs for a wide range of applications [39, 38].

Radical polymerisation covers most of the monomers which do not fulfil the requirement for LAP. It is a very versatile technique, compatible with a wide spectrum of monomers. It has a high tolerance of functional groups and impurities. The general mechanism consists of keeping the terminal part of the chain active by a reversible reaction between the active and dormant species. The main techniques in radical polymerisation are: atom transfer radical polymerization, nitroxide-mediated polymerization, reversible addition fragmentation chain transfer (RAFT). These techniques give poor control over molecular weight and polydispersity, which is the reason why they are considered when LAP is not a viable solution. They are often coupled in different steps or with a macroinitiator [38].

The polymers considered in this study are produced via industrial LAP methods, which guarantee uniform composition, narrow molecular weight distribution and defined architecture.

2.1.3 Microphase theory

In the last 60 years there have been significant advances in the understanding of the physics and chemistry behind microphase formation in block copolymers. Block copolymers exhibit microphase separated structures as a consequence of the thermodynamic incompatibility of their constituent blocks and the chain connectivity of the different blocks [44].
There are several techniques available to study the microstructure of SBCs, the most relevant are SANS, SAXS and TEM [45, 48], and extensive studies have dealt with theoretical predictions of the microphase morphology. Nowadays it is possible to measure and predict the size and packing of the microdomains [33].
In this literature review, the focus is on linear BCPs self-assembled in bulk. Figure 2.2 shows a schematic representation of possible configurations for this class of BCPs. Linear block copolymer can be di or triblock, ordered in an alternating or tapered

sequence. Other BCPs configuration, such as graft or star copolymer, are getting increasing attention, however the study of these materials is beyond the scope of this work.

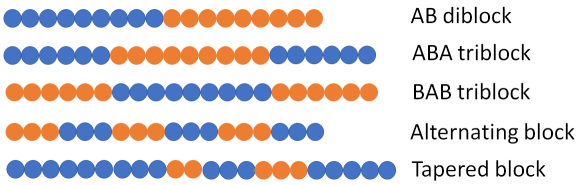

Figure 2.2: Linear block copolymer chain configurations possibilities. The different colours represent chemically different blocks. In this case blue corresponds to an hypothetical block A, while the orange to block B.

There are two competing factors in the formation of BCPs: the enthalpic contribution from the interfacial energy between two different blocks, and the entropic contribution from the stretching of the polymeric chains. The blocks conformation tends towards minimising the interfacial area between the blocks, in order to reduce the total interfacial energy. There is a limited number of possible configurations that minimises the number of unlike monomer-monomer contacts in which the BCPs can arrange [35, 50]. The equilibrium configuration depends on the block volume fraction (f), degree of polymerisation (N) and degree of block incompatibility (χ) [43].Figure 2.3 shows the 6 equilibrium configurations documented so far. The most studied phases are BCC spheres, hexagonally packed cylinders and lamellae. Only at the beginning of the 90's the hexagonally modulated lamellae, hexagonally perforated layers and bicontinuous gyroids were discovered. The new conformations are restricted to a very narrow composition range between lamellae and hexagonally packed cylinders [41].

Meier [57] presented the first of a series of papers dealing with microphase configuration of block copolymers. In his theory, he established a criterion for domain formation considering thermodynamic and molecular variables. He showed that the critical block molecular weights necessary for domain formation are much larger than that required for phase separation of a simple block mixture. This is mainly due to a considerable loss in configurational entropy due to the constraints in the spatial placement of the chains. Meier defined a relationship between the radius of a spherical microstructure and the unperturbed chain length based on the requirement that the space in the domain should be filled with uniform segment density.

Helfand *et al.* [52, 53, 54], in the same series of papers, described an equilibrium theory based on the free energy of the microdomain system in block copolymers.

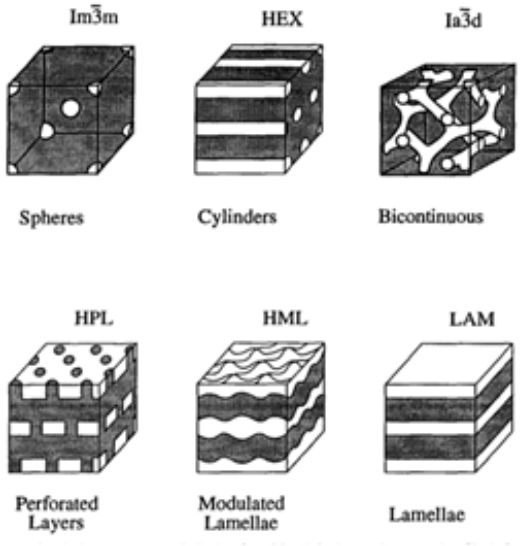

Figure 2.3: Ordered morphologies for in bulk self assembled polymer melts. Different color indicates the mesophase types. Figure obtained form reference [41].

Their objective was to determine the free energy as a function of the domain size and geometry. Minimising this energy leads to the determination of the repeat distance (d-spacing) and main lattice dimensions. Briefly, they combined the solution for homopolymer interfaces and a solution for pure microdomains where the blocks all originate at the interface. The free energy equation also considered the narrow interphase approximation [49, 53, 54], for which the interphase is considered much smaller than the domain size and simplifies the free energy balance.Their theoretical simplification was successfully compared with experimental results. The energy balance for the microdomain involves terms representing the driving force towards expansion and contraction of the domains. The full equation is reported in their paper [54]. Briefly, they defined 4 different terms. The term representing interfacial free energy is inversely proportional to d-spacing and drives towards larger phases. The term for loss of entropy due to localizing the joints of the different blocks at the interface opposes the domain growth, since it is proportional to log d. The third term represents the loss of conformational entropy correlated to the redistribution of the conformational probability of the molecules in order to fill the centre of the domains; the localization of the joints at the interfaces creates an imbalance in the chain density: since all the molecules starts at an hypothetical wall at the interface of the domain, the molecular density is higher there compared to the centre, which in a condensed system creates strong forces opposing the non-uniform density, hence the loss of conformational entropy. This term is inversely proportional to the d-spacing, in physical terms the larger the phase size

the more difficult it will be for the blocks to reach the centre of the domain. Finally, the last term is independent of d and is necessary to set the free energy at zero for a homogenous single-phase system. The model comparison with experimental results proved to be accurate in estimating the size and shape of the microdomains. Helfand and co workers [52] were among the first to develop a self consistent field theory which allowed quantitative free energy, composition profiles and chain conformation calculation. The theoretical prediction contributed to the calculation of the phase diagram and located the composition boundaries for thermodynamic stability of spheres, cylinders and lamellae.

Liber [55] proposed a different approach and tried to overcome the limitations of the Helfand-Wesserman equation [54]. He studied the onset of a microphase separation starting from a homogenous melt; in this regime the narrow interphase approximation is not valid, since the concept of an interphase is inappropriate: the monomers' concentration was theorised not to change suddenly within a short distance, but to gradually change over the microstructure period. Starting from general statistical physics relations, a free energy balance in terms of a defined ordered parameter was provided. The characterization of the phase equilibria was dependent on two main parameters: the fraction f of the monomer A in the chain, and the product χN between the polymerization index N and the Flory-Huggins interaction parameter of monomer A and B. The region of stability of different phases could be represented in a phase diagram in a χN-f plane, as shown in Figure 2.4.

Experimental evidence of a BCP's phase diagram was first obtain from SAXS, SANS and TEM of polystyrene-polydiene (mainly isoprene or butadiene) [56]. Figure 2.4 shows a theoretical phase diagram next to an experiemental one (PI-block-PS) showing remarkable similarities. The different parts of the diagram indicate the equilibrium phases and spatially homogenous disordered phase. The ordered polymer architectures represented in the diagram are: body centered cubic lattice, hexagonally packed cylinders, ordered double diamond structure and lamellae (this was first found for PS-PI [56]).

The Flory-Huggins interaction parameter is commonly described as the non-ideal enthalpic part of the mixing-free energy, which is the free-energy cost of contacts between monomer A and B per monomer unit [34]. The interaction parameter depends on the monomers selected and has a temperature dependence that can be written as: $\chi = \alpha T^{-1} + \beta$, where α and β are constants for given values of composition and architectural constraints [33].

At lower temperature, the interaction parameter is larger and the contact between

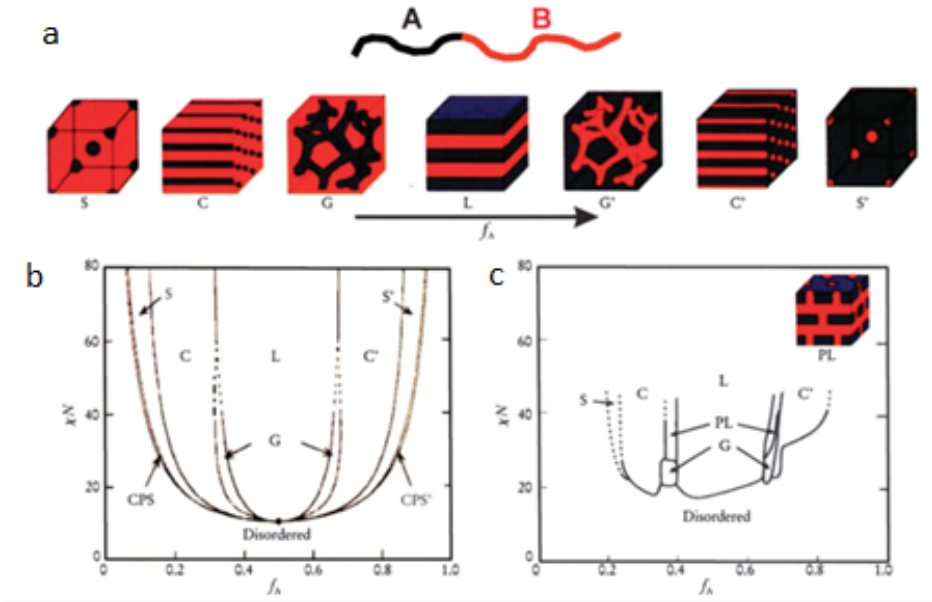

Figure 2.4: a) AB diblock copolymer equilibrium moprhologies: S,S'= BCC spheres, C,C'= hexagonally packed cylinders, G,G'=bicontinuous gyroids, L=lamellae; b) Phase diagram predicted by the self-consistent mean-field theory, f_A= volume fraction of block A, χ= Flory-Huggins interaction parameter, N = degree of polymerisation, CPS= closely packed spheres; c) experimental phase diagram for polyisoprene-block-polystyrene reported by Bates and co-workers [33], PL=perforated lamellae. Reproduced from reference [35].

monomers A and B is reduced, which, if N is large enough, is accomplished by loss of translational and configurational entropy, i.e. local ordering [33]. The transition between ordered phase, known as order-order transition (OOT), is represented by the vertical lines, which reflect the fact that it does not generally happen by changing temperature alone [56].

Figure 2.5 shows the mechanism for morphology transition from spherical to cylindrical and lamellae. When f_A is low, the blocks of A aggregate into spheres surrounded by block B matrix. The latter represents the most energetically favourable configuration, since it minimises the interfacial area. With increasing f_A , both the *corona* volume of the B block and the curvature of the interface decrease. As a consequence the chains rearrange to reduce their stretching and produce a morphological transition to cylinders and then lamellae, with even higher f_A [35].

Furthermore, it is evident from the graph that if χ or N are lowered enough, entropic factors dominate leading to microphase disordering [33, 35]. The transition towards disordering is defined as an order-disorder transition (ODT).

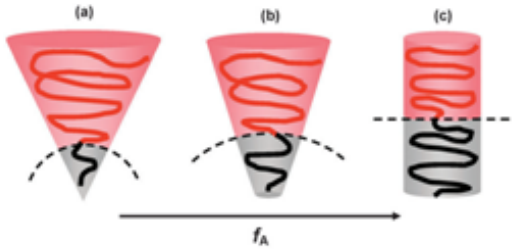

Figure 2.5: Illustration of possible chain arrangements in a) spheres, b) cylinders and c) lamellae mesophase configuration as f_A increases (up to ∼0.5). The dashed line represents the two phase interface. Figure reproduced from reference [35].

It has been pointed out that the entropic and enthalpic contribution to the free energy scale as N^{-1} and χ respectively. Hence the product χN is the leading parameter determining the phase state [33]. It is commonly assumed that the composition f_A primarly dictates ordered-state symmetry, interfacial curvature and microdomain shape [37].

The variation of the product χN has been theoretically divided into three main so called segregation limits, where segregation refers to the different phases [56]. Figure 2.6 shows the phase state development with increasing χN from left to right.

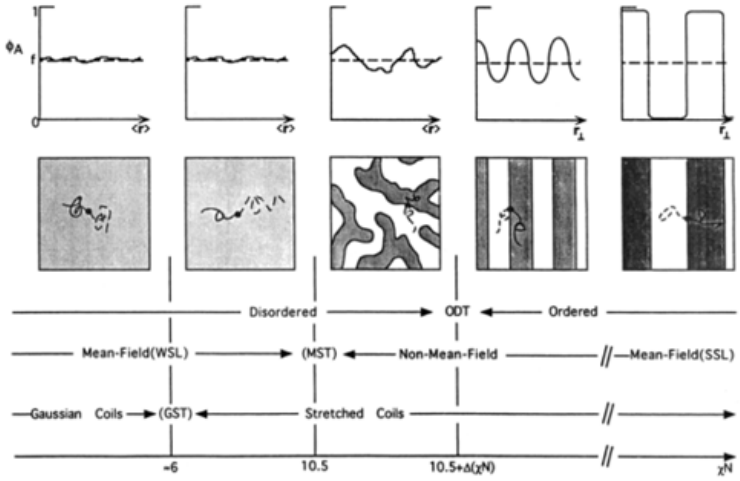

Figure 2.6: Schematic representation of the regimes between weak and strong segregation limits for diblocks melt- The first row reprensets a qualititative graph of the amplitude fluctuation of local composition with increasing χN. The second row shows the correspective morphological pattern. Figure taken from reference [51].

When χN<< 1 the material is in the weak segregation limit (WSL). In this regime

the chain statistics are unperturbed because of weak A-B interactions (Gaussian coils) and there are infinitesimally small deviations in local composition around the uniform average value f. The material is in a disordered state and still described by the mean field theory [33, 37, 41]. WSL is characterised by nearly sinusoidal composition profiles and the domain period is predicted to scale as $d \sim N^{1/2}$ [58].

When the amplitude of the composition profile starts to grow with increasing χN, the regime moves to the intermediate segregation limit (ISL), where additional Fourier components are required to describe the composition profile and free energy. The individual chains are extended compared to their unperturbed Gaussian dimension. The cross-over happens before ODT because of finite amplitude fluctuations in the composition which causes chain polarization and a shift of the ODT to higher χN compared to the one predicted by mean field theory [52, 55] . WSL can be theoretically achieved for N$\rightarrow +\infty$, however realistic systems tend to show ISL characteristics during the transition. Modelling of composition fluctuations near ODT are essential for a realistic description of the collective diffusion mechanism in the transition region. ODT is a fluctuation-induced phase transition, so we can anticipate some influence of fluctuations on the ordered state near the point of disordering [37, 41].

SANS and rheology measurements showed that as diblocks were heated towards T_{ODT} the lamellae softened, and composition fluctuations and conformational asymmetry drove the lamellae to distort. It was demonstrated that in the disordered state composition fluctuation effects decrease with increasing chain size (N) [59]. Rosedale *et al.* [60] demonstrated the influence of composition fluctuation on the rheological properties near the ODT and confirm it is a first order transition. Properties above and below strong first order transition, such as melting or freezing, are not affected by the proximity of the transition, while they found that weakly first order ODT is driven by fluctuations.

Near χN $\sim$10 the composition profile starts to saturate and separate into nearly pure blocks, leading to well defined interfaces and significantly stretched chains, which constitutes the Strong segregation limit (SSL). There is no sharp transition between ISL and SSL, the latter could also manifest at χN above 50 [41]. The system tends to minimise the interfacial area where the interaction energy is localized, but can do so only under the constraint of incompressibility and with an entropic penalty due to extended chain configurations. The result of these opposing forces is a perturbed chain configuration and microdomain period that scale as $d \sim aN^{2/3}\chi^{1/6}$. This has been verified by SAXS and TEM on polystyrene-polydiene block copolymers [33, 37, 41, 58]. The SSL regime manifests in the different equilibrium morpholgies represented in the

phase diagram, while the WSL better models the ODT. Helfand theory predicted the SSL equilibrium region, while Liebler in his theory described the WSL.

Libler's [55] main field theory demonstrated that the phase diagram prediction has a critical point for f=0.5 and that the order-disorder transition boundary curve converges at that point, as shown in the phase diagram (Figure 2.4). A series of studies investigated the effect of composition fluctuations around the critical point presented by Libler [56, 59, 60, 61, 62]. Rosedale *et al.* [60] observed that the amplitude of the fluctuations increased with decreasing temperature, which means higher unfavourable mixing. They explained how the segregation of the BCPs is constrained by the molecular dimension and fluctuations are responsible for the unfavourable segment-segment interaction relieve.

Almdal *et al.* [56] studied a series of asymetric PEP-PEE diblock copolymers near the critical composition point (f=0.65) in different parts of the phase diagram. SANS and rheological measurements showed a transition from lamella to disordered state which passed through two intermediate ordered phases, different from the hexagonally packed cylinders and BCC spheres predicted by the mean-field theory. They questioned the universality of the phase diagram based only on χN and f, marking the importance of the study of fluctuations in composition.

2.1.4 Styrenic block copolymer for PHV application: state of the art

Brubert *et al.* [5, 64] conducted a thorough material search for the flexible polymeric prosthetic heart valve application. They developed a performance index for the valve leaflets, able to assist with the identification of the correct candidate to support the mechanical loading during the opening and closing of the valve.

The parameters for the performance index calculation are the flexibility and curvature of the leaflets, which have to bend significantly in order to open, and the maximum stress supported by the material during valve closure. The index is described as follow:

$$PI = min \frac{E}{\sigma_{max}^3} \tag{2.1}$$

where E is the materials' Young's modulus and σ_{max} is the maximum stress.

Moreover, the materials shortlisted had to be hemocompatible, which means reduced inflammation and thrombogenicity, and biostable, *i.e.* resistant to hydrolysis and oxidation. Among the materials investigated, a group of styrenic block copolymers

(SBC) showed excellent performance and were considered for further development of the flexible PHV: SIS30, SIBS30, SEBS20, SEBS29 and SEPS22 [64]. This group of SBCs self assemble into hexagonally packed cylinders, the local orientation of which can be controlled using the material rheological properties, mould design and moulding parameters, such as temperature and injection rate. The advantage of using these materials is the anisotropic properties achieved with uniform orientation of the cylinders. The final goal is to mimic the native biological tissue material of the leaflets, which are formed of highly anisotropic layers of collagen fibres. The fibrosa and ventricular layers of the native leaflets are composed of circumferentially oriented fibres to better sustain stress during loading. A third layer is present, mainly composed of radially oriented elastin fibres, the function of which is to maintain the desired collagen fibres' configuration during and after loading. Circumferential modulus of the native leaflet is 10 times higher than the modulus for the radial direction (14.5 vs 1.5 MPa) [65]. The main function of the leaflet tissue is to maintain mechanical stresses and remain resilient for a large number of stress cycles [66].

Stasiak *et al.* [66] showed that, under SAXS, the cylinders in the hexagonally packed alignment of SIBS30 fragment during stress loading and completely recover the spacing between cylinders during unloading. Microdomains parallel to the applied strain were fragmented from stress transfer by the surrounding matrix. Elongation and fragmentation were demonstrated to happen simultaneously. The perpendicular direction of cylinders with respect to strain showed segments pulled apart by the stretch of the matrix, no fragmentation being observed. The d-spacing increased and recovered over many stress cycles.

These findings confirmed that the hexagonally packed cylindrical SBCs could be a very promising solution to replicate the native leaflets. Furthermore, an engineered optimisation of the orientation within the leaflet could improve the stress distribution and extend the lifetime of the prosthesis [65].

In a subsequent study, Serrani *et al.* [67] simulated with a finite element modelling (FEM) the optimal orientation for SBCs within the leaflet. They implemented an iterative procedure to align the main axis of the cylinder along the maximum principal stress direction of the leaflet. The result was an optimised leaflet with mainly circumferential orientation of the cylinders, as shown in Figure 2.7.

In the optimised version of the leaflet they observed a decrease in the circumferential strain and an increase in the radial strain. Furthermore, the calculated strain energy density (SED) was found to be much lower for the optimised case. Reduced strain energy density is likely to improve the durability of the leaflet. Serrani and co-workers'

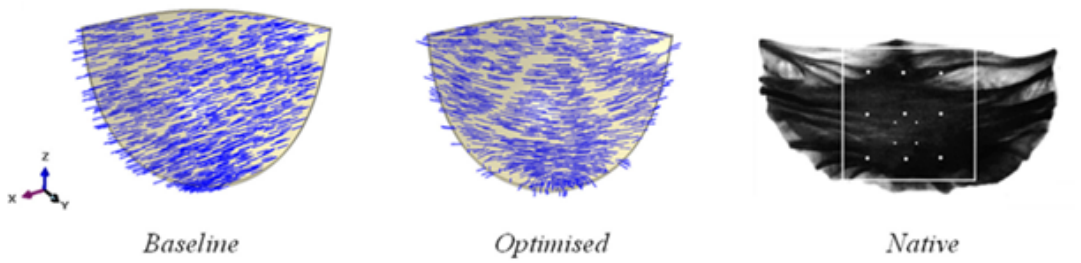

Figure 2.7: Baseline and optimised representation of the cylinders orientation obtained from Serrani *et al.* [67] computational tool. On the right is the porcine native aortic leaflet with collagen fibre architecture hiligheted. Figure adapted from reference [67].

tool has been applied for further development of valve designs and manufacturing. The optimal orientation was achieved via injection moulding by tuning the mould design. More details are presented in the following sections.

In order for a polymeric valve to reach the market, more studies are needed on the geometry and material selection side, as mentioned in the first chapter. This study focuses on SEBS and SEPS materials for leaflets and valve stents. The following sections discuss material characterisation from the point of view of morphology, orientation and viscoelastic properties.

2.1.5 Achieving anisotropy

Extrusion, injection and compression moulding are standard industrial methods able to impart long range morphology alignment of bulk BCPs through the application of a mechanical flow field [68, 69].

Flow induced micro structural alignment was first shown in 1970 and shear flow was proven to produce long range orientation in both tri and di block copolymers. The BCPs with cylinder-forming rigid domains are able to orient the cylinders along the axes parallel to the flow direction [41, 68].

For this reason, injection moulding is the technique used to manufacture the oriented prosthetic heart valves. The optimisation of the injection process can improve the degree of orientation: hence much attention was given to tuning of the moulding parameters. Among them, the most relevant to affect orientation are the temperature of the mould and polymer melts, shear rate and injection velocity. Moreover, the mechanical flow field can be conveniently controlled by mould part design and its melt delivery system (gate and runners) [68].

The orientation at the surface is the result of the combination of two opposite effects: the fountain flow, which is composed of shear flow down the cavity and elongation at the melt front, and stress relaxation after filling. Higher mould temperature is effective in increasing the degree of orientation. When the hot melt touches the cold mould the polymer solidifies in the given orientation, Fang *et al.* [68] measured a 85°C decrease in the first 0.45 s. When increasing the temperature, the melt is given more time to align with shear at the surface. Higher melt temperatures proved to improve orientation, but worked better when coupled with high mould temperature.

In theory, the optimal combination for good orientation is low viscosity, high shear rates, high temperature and high injection velocity [68]. However, several studies showed that increasing temperature, velocity and shear do not always lead to a good alignment.

The temperature range of injection moulding can influence the microphase structure. Zhao *et al.* [36] reported in a study of polystyrene-block-polyisoprene-block-polystyrene, where increasing temperature produced a change in microstructure in the polymer, from cylinders at lower temperature to BCC spheres, disordered spheres and a disordered state with increasing processing temperature.

Stasiak *et al.* [65] showed that SBCs with cylindrical microstructure have different core and skin orientation when injection moulded. The bi-directionality was stable and extended throughout the samples. The presence of different perpendicular layers, shown in Figure 2.8, is explained by the balance of shear and extensional flow in different regions of the sample during injection. In their case, the injection rate was kept at least 10 times slower than the industrial norm. The slow injection rate produced a laminar flow between the mould plates, and where the flow was fully developed the orientation was consistent.

Moreover, thinner samples, for a constant volumetric injection, had shear dominant and unidirectional orientation (higher injection rate). It was the opposite for thicker samples, where the extensional regime was dominant, and the internal layer was more evident compared to the shear oriented skin layer. They proved there is a degree of control over the ratio between shear and extensional flow induced orientation through the variation of thickness and injection rate.

In a follow-up study, Stasiak *et al.* [40] demonstrated that low strain and slow deformation rate resulted in better long range orientation in cylinders forming SBCs. Furthermore, they showed that orientation rapidly improved during the first 10 minutes of annealing without flow.

At high shear rates, Colby *et al.* [50] demonstrated that a second phase is formed,

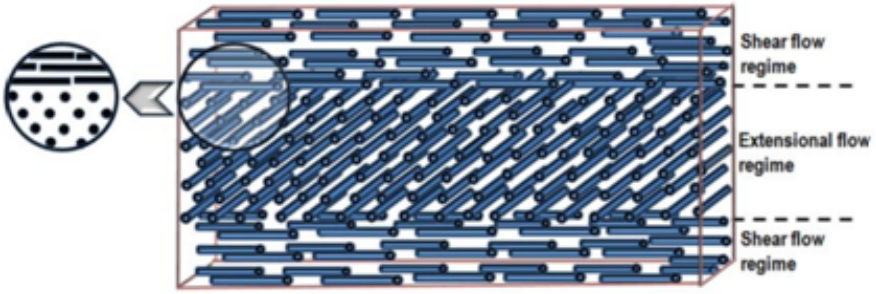

Figure 2.8: Schematic representation of section of injection moulded cylinder forming styrenic block copolymer sample. The height represent the thickness of the sample, which shows two external layer with cylinders oriented in the flow direction by shear flow, and a central layer with cylinders aligned perpendicular to the flow direction. The latter orientation is generated by the extensional flow regime related to the fountain flow effect. Figure taken from reference [65].

which appears like a scaled-down cylinders phase (smaller cylinders and distance) that fits inside the primary hexagonally packed cylinder phase, as shown in Figure 2.9.

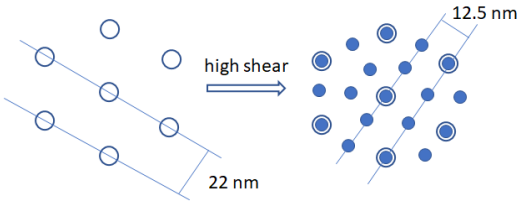

Figure 2.9: Schemicatic representation of Colby report of scale down shear induced cylinders morphology. The white circle represent the shear induced cyliner packing while the blue circles are the second structure induced by high shear with a smaler lattice structure. Image adapted from reference [97].

Higher flow alignment can also induce more fragmented polystyrene domains, since the PS is stretched during alignment [68]. Moreover, it was demonstrated that shear forces can induce both ordering (low shear) and disordering (high shear). The main theory is that the fluctuations in cylinder orientation and their relative motions under shear result in an unfavourable increase in local polymer concentration [71]. It was suggested that shear higher that the inverse relaxation time could lead to a disordering of the cylinders since they would not be able to react fast enough to the imposed shear. In addition to this, the cylinder forming microstructure disordering time also depends on the orientation angle: if the cylinders are parallel to the flow they are not affected by shear, if they are perpendicular to the flow direction they can be destroyed as soon

as strain reaches of the order of 1 (which corresponds to a distortion similar to the intercylinder spacing) [50, 69].

The strategy applied in this study to achieve optimal anisotropy takes into consideration the findings above. The moulding process was performed at high mould and melt temperature and slow injection rate. The moulds for the standard samples and valves were designed in order to create a flow field in the desired direction. Figure 2.10 shows the mould plates created for standard unitensile specimens and flat samples. Two different unitensile specimen designs were moulded, the geometry details are illustrated in Figure 2.11. The plates were fitted between thicker heated plates, using a central injection point in injection moulder BOY22 D, as shown in Figure 2.12. Plates of different thicknesses were prepared for the considered shapes.

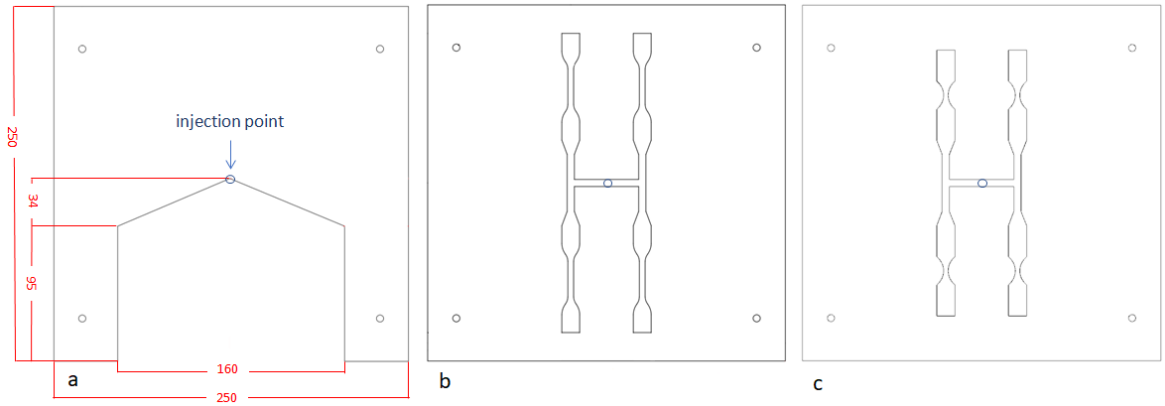

Figure 2.10: Mould design for a-flat sheet sample b- long unitensile sample (ISO 37 type 2) c- short unitensile sample (ASTM D638 type v). Mould a was made 1 mm thickness, mould b and c were made 0.7 mm, 1 mm and 2 mm thick. Unit measure for mould dimension is mm.

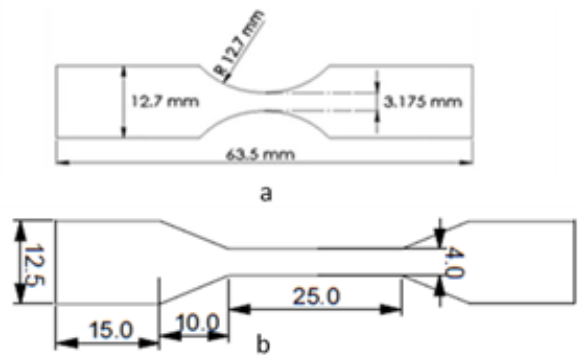

Figure 2.11: Unitensile sample design according to a- ASTM D638 type v and b-ISO37 type 2.

Compression moulding was also considered for manufacturing SBC films. The mould, represented in Figure 2.13, was designed in order to have the side walls constrain the melt flow to one direction.

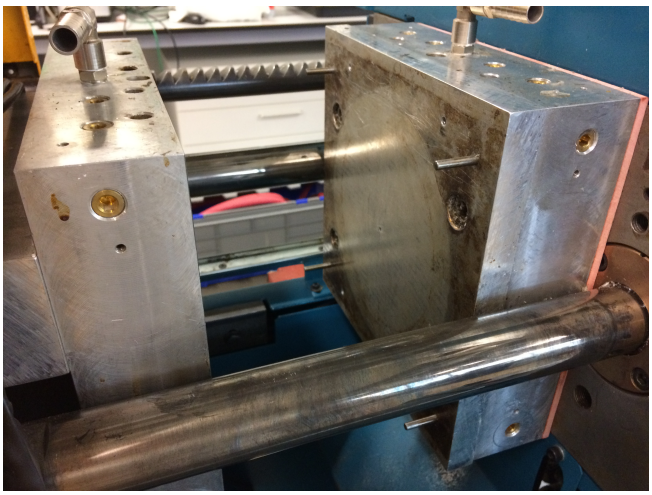

Figure 2.12: Mould set up in BOY22D. The pins coming out from the right side are the anchoring points of the mould plates. The injection point is in the middle of the right side (just visible). On top of the plates the attachments for the water cooling are visible and also the holes were cartridge heaters are inserted.

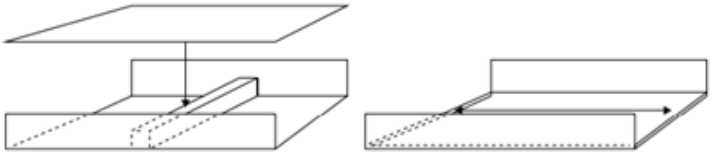

Figure 2.13: Schematic representation of the mould for compression moulding. A polymer bar is placed in the middle of the bottom plate, which is then squashed by the top plate. The side of the mould constrain the flow melt in one direction. Figure obtained from reference [5].

The valve prototypes were manufactured in BOY 25E (Figure 2.14). The mould in Figure 2.15 represents the valve used for the experiments in chapter 3, while Figure 2.16 shows the mould design and prototypes for Polivalve, described in section 3.3.7. For both cases the injection point in the mould were designed in order to achieve mostly horizontal alignment of the cylinders, as predicted to be the optimised design by Serrani *et al.* [67] (see Figure 2.7). Confirmation of successful alignment was given by a SAXS map of the leaflet, shown in Figure 2.17. More details about the injection parameters and orientations calculation are presented in the following sections.

Figure 2.14: BOY 25 E injection moulder.

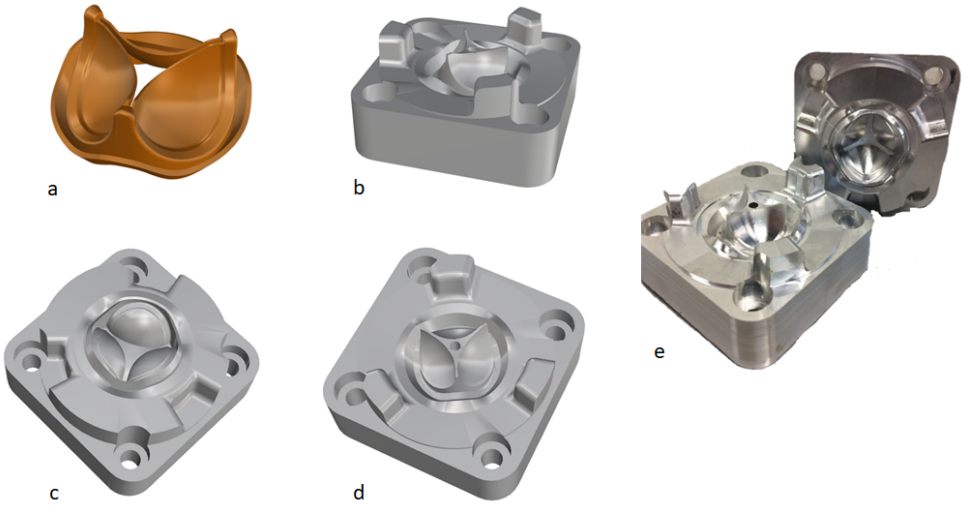

Figure 2.15: a- valve design cad model for the rigid stent experiment; b,d- different angles of the male part; c-female part; e- complete picture of the mould. This design was used in the experiements described in chapter 3.

2.2 Materials and Methods

2.2.1 Materials

The four materials investigated in this study are polystyrene-b-polytethylene-butylene-b-polystyrene (SEBS) and polystyrene-b-polyethylene-propylene-b-polystyrene (SEPS). The chemical structures are represented in Figure 2.18-a and 2.18-b respectively.

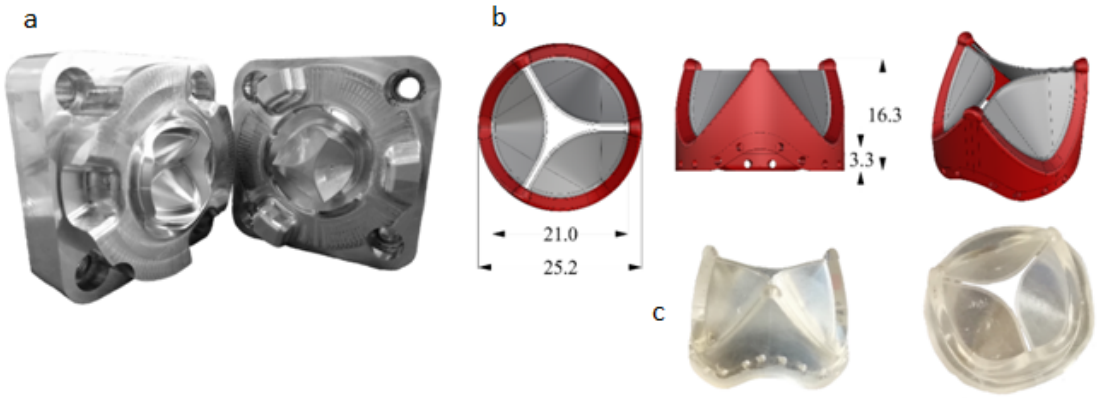

Figure 2.16: Polivalve design : a- female and male part of the alluminium mould, b- size description and prototypes of the polymer valve. Figure adapted from reference [6].

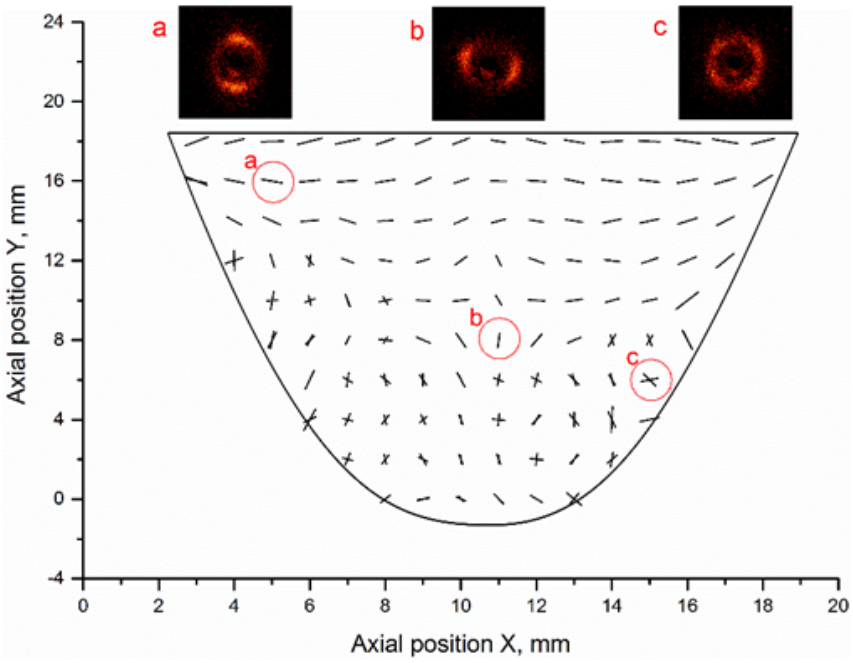

Figure 2.17: Map of the styrenic cylinders orientation of the valve leaflet of Polivalve made of SEBS20. The orientation is determined by the angle vectors, their length is proportional to the inverse the full width at half maximum (FWHM) for the relevant reflection of the SAXS pattern for every point scanned in the leaflet. a- two meridional reflection indicate parallel unidirectional orientation; b- two equatorial reflection indicate unidirectional perpendicular orientation, c- four intermediate reflection at perpendicular axis show bidirectionality at spefic angles. Figure adapted from reference [6].

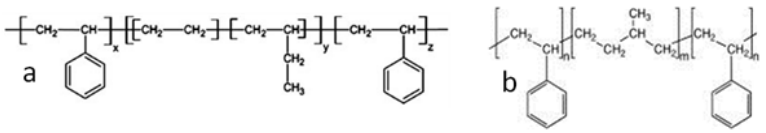

Figure 2.18: a-SEBS chemical structure, b-SEPS chemical structure

The polymers are commercially available grades, with different molecular weight and styrene fraction. The three materials investigated for the leaflets are SEBS20 (fluffy powder, G1642 H Kraton, Belgium), SEPS22 (pellets, Septon series, Kuraray, Japan) and MED500400 (pellets, Mediprene MED500400M, HexpolTPE, Sweden). The first two have hexagonal cylindrical microstructures, resulting in anisotropic mechanical properties; MED500400 is a SEBS block copolymer, but does not self assemble in cylinders, instead having isotropic mechanical properties, with a BCC spherical microstructure. SEBS29 (fluffy powder, G1650 Kraton, Belgium) was selected for the stent of Polivalve (see section 3.3.7).

2.2.2 Methods

Injection moulding

Two different injection moulders were used to produce the two standard specimens (Figure 2.12 and 2.14) and the valve prototypes. BOY 22 D (BOY Ltd, Northants, UK) was used for the manufacturing of unitensile samples and flat sheet (mould in Figure 2.10). The valve prototypes were manufactured using BOY 25 E (BOY Ltd, Northants, UK). The moulds were heated with oil in BOY 25 E and cartidge heaters in BOY 22 D. Both systems used water for cooling. Table 2.1 and 2.2 list the main injection parameters applied for the different materials and geometries. The older BOY 22 D machine had less control over the parameters, I report here the settings to input to repeat the test in the same injection moulder. Pressure and velocity were not measured accurately; the settings on the moulder panel indicated percentage on the maximum pressure or velocity, the first one is 160 bar, the second one is not specified in the manual. The holding pressure was applied for 50 seconds and it was based on the pressure set for the injection phase.

Table 2.1: Injection moulding parameters for BOY 25 E for the valves prototypes. Indicated are the temperature of the mould, injection pressure and velocity, holding pressure profile with time and screw temperature (higher temperature is on the nozzle side)

	T_{mould} (℃)	P (bar)	v (mm/sec)	P_{hold} (bar)+(s)	T_{screw} (℃)
SEBS20	160	50	15	50-30-20-10 30-40-50	190-185-170-150-130
SEPS22	160	40	12	41-39-30-8 30-50-99	185-180-170-150-130
MED500400	140	10	8	20-14-13-5 30-50-99	160-150-140-130-120

Table 2.2: Injection moulding parameters for BOY22D for the specimens in mould 2.10. Indicated are the temperature of the mould, injection pressure (as % of the maximum 160 bar) and velocity (as per machine specific settings), and screw temperature (higher temperature is on the nozzle side)

	T_{mould} (℃)	P (%)	v (%)	T_{screw} (℃)
SEBS20	175	99	99	215-210-199-160
SEPS22	160	99	45	210-190-180-150
MED500400	140	30	20	170-160-150-130

Compression moulding

The compression moulding technique was used to manufacture polymeric films, from which both pure shear and unitensile specimens were cut. The material was poured into a square mould (see Figure 2.13) which was positioned in a heated press and compressed between 5 and 10 kg on 10:16 inch dia. RAM. The processing temperatures for the different materials are listed in Table 2.3.

After 10 to 15 minutes the mould was removed from the press and placed under cold water for immediate cooling. This method achieves comparable material properties to specimens made by injection moulding. The sheets produced ranged between 0.3 and 0.7 mm thickness. The compression moulded samples possessed anisotropic mechanical properties. From the sheet, two types of specimen were cut according to cylinder orientations in parallel and perpendicular directions.

Table 2.3: Plate temperature of heated press for compression moulding of SEBS20, SEPS22 and MED500400

Material	T plate (℃)
SEBS20	200
SEPS22	190
MED500400	160

Gel permeation chromatography

The analysis was conducted using a tetra detection on a Viscotek GPCmax VE2001 GPC Solvent/Sample Module. The detectors used were refractive index, UV, viscosity and light scattering. THF was the eluent (flow 1 ml/min) at a constant temperature of 24°C. The detectors were calibrated with polystyrene standard Malvern PolyCal™Std-PS99k. The values for the refractive index increment (dn/dc) used for the calculation are 0.185 ml/g for Polystyrene and 0.072 ml/g for both Ethylene-Butylene and Ethylene-Propylene blocks.

The materials analysed were SEBS20, SEPS22 and SEBS29. MED500400 was not dissolvable in THF or Toluene, and the information for the material is restricted to that provided in the manufacturer's data sheet.

The composition of BCPs can be determined by dual detector GPC, where the two detectors are UV absorption and refractive index [72]. The technique works with one block being visible to one of the detectors, while the other is not. In this case polystyrene is the visible component. RI and UV signals are proportional to the concentration of the macromolecules, which in turn means that the area under the GPC traces are proportional to the total amount of macromolecules in the sample.

The main principle for the calculation is based on the fact that a dilute solution of two or more components passing through the detectors will have an additive response with respect to each component. This remains valid for block copolymers where the

different blocks are linked by covalent bonds and the following equation system has to be satisfied.

$$U = a_1 c_1 + a_2 c_2 \tag{2.2}$$

$$R = b_1 c_1 + b_2 c_2 \tag{2.3}$$

$$rA_U = a_1 m_1 + a_2 m_2 = r \int U dt \tag{2.4}$$

$$rA_R = b_1 m_1 + b_2 m_2 = r \int R dt \tag{2.5}$$

where U and R are the magnitudes of the UV and RI signal respectively, c is concentration, A is the area under the GPC curve integrated over time, a and b are the specific response for respectively UV and RI signal (taken from the calibration), m is the amount of homopolymer passing through the detector during time t and r is the volumetric flow of the eluent [72]. Solving the system gives the results for concentration and molecular weight.

DSC

Differential scanning calorimetry was performed to measure the glass transition temperature. DSC Q2000 (TA instruments, DE, USA) was used in the Department of Materials Science and Metallurgy (University of Cambridge,UK).

The polymer pellets/powder were weighed with a precision balance and deposited in the instrument crate. The temperature ramp went through the following steps: equilibrate -50°C , heating ramp at 10°C/min to 300°C, cooling ramp at 25°C/min to -50°C, repeat of heating ramp with the same conditions and equilibrate at 35°C.

DMA

A temperature ramp was performed on the polymeric samples using a DMA Q800 (TA instruments, DE, USA) in the Department of Materials Science and Metallurgy (University of Cambridge, UK). Small rectangles were cut from injection moulded flat sheets of polymer.

The materials tested were MED500400, SEPS22 and SEBS20. The two latter materials were cut from injection moulded sheets in order to have the styrene cylinders parallel to the strain direction. Thickness was measured at three points with an electronic micrometer, width was measured with a standard ruler and height was measured from the machine.

For all the materials tested, frequency was set at 1 Hz and strain at 1%. The temperature ramp conditions were set as follows: -60°C equilibrate, 3°C/min up to 400°C.

SAXS

Microstructure SAXS investigation took place at two different facilities. Part of the analysis was performed using Synchrothron radiation on beamline I22 at the Diamond Light Source (Harwell Science and Innovation Campus, Oxford , UK) and part on a conventional X-ray source: a Bruker Nanostar Gen7 (Department of Material Science and Metallurgy, University of Cambridge, UK) .

In both experiments multiple samples were mounted in a grid, which was positioned in order to have the beam perpendicular to the samples' surface. Hence, the beam did a z-axis scan along x and y axis to map the samples, as represented in Figure 2.19.

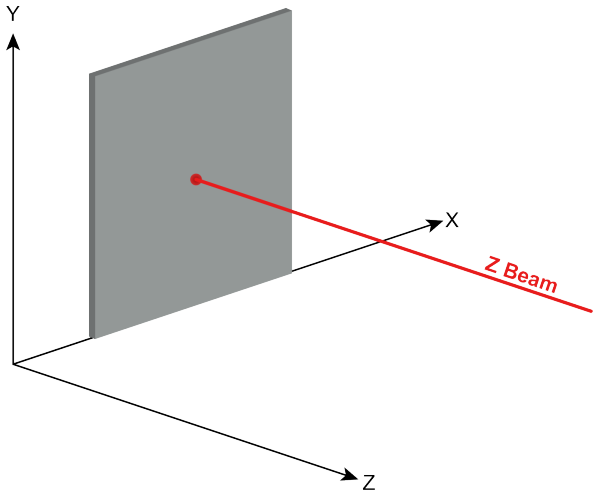

Figure 2.19: Schematic representation of the z-beam axis mapping the surface of the sample in x and y directions.

At the I22 beamline 12.4 keV (0.1 nm) beam energy was used (wavelength 1Å). The beam dimensions were 240 (H) x 60 (V) µm. There were 6 m between the sample and the RAPID 2D detector. The detector capabilities allowed remarkably short frame acquisition times (down to 10 ms). The beam mapped every 1 mm in x and y direction, taking 1 second for each acquisition.

The SAXS Bruker Nanostar had a circular beam of diameter ∼1 mm at the sample and the instrument was equipped with a 2-D detector. The sample to detector distance was set at 1060 cm and Cu Kα radiation was used (wavelength 1.54 Å). Samples were mapped every 1 mm in x and y directions, with 10 seconds for each acquisition.

The cylinders' patterns were calculated with a peak integration method developed by Dr J. Stasiak using OriginPro 9.0 (OriginLab, MA, USA). Briefly, the SAXS techniques involves X-ray radiations being scattered when passing through the crystalline structure. Bragg's law (eq.2.6) relates the scattering angle to the crystal spacing by

$$n\lambda = 2dsin\theta \tag{2.6}$$

where d is the distance between crystal planes, θ is the scattering angle, λ is the wavelength, and n is the order of the scattering peak.

One dimensional SAXS profiles are used to examine the morphology. The scattering intensity profile is plotted against 2 theta (polar integration) and the azimuthal angle (azimuthal integration). For the polar integration, the full width at half maximum (FWHM) of the peak in the scattering intensity profile is determined by the size of the crystal domain, while the area under the peak is proportional to the amount of crystal planes aligned to give constructive interference at the detector [66, 65].

In the azimuthal integration, FWHM is correlated to the degree of anisotropy, its value is inversely proportional to the degree of orientation responsible for the reflection [65]. A narrow peak indicates a well-aligned microstructure. The azimuthal integration was calculated for the first order reflection of SAXS images.

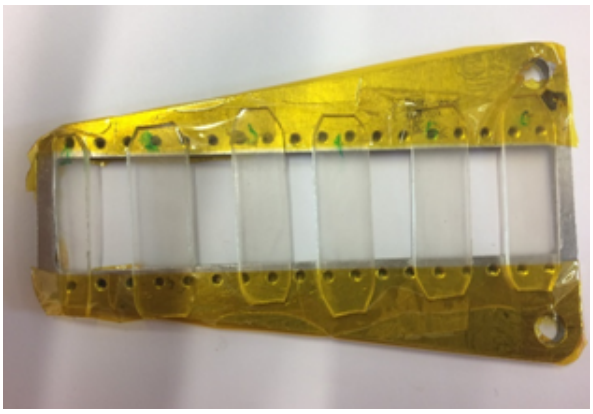

Figure 2.20: Example of a sample grid for SAXS analysis.

Rheometer

Rheological characterisation of the materials was carried out on a strain-controlled rheometer (ARES Rheometric Scientific, TA Instruments, DE, USA). The samples for the analysis were cut from an injection moulded sheet with a circular cutting die to make 25 mm diameter polymer discs. A parallel plate set up was used for the analysis.

Every material underwent a temperature ramp, a strain sweep and a frequency sweep. The test parameters for each material and test are summarised in Tables 2.4 and 2.5. Spacing between the plates was measure every run.

The strain sweep was necessary to determine the range for the linear viscoelastic response of the material so that a strain within that range could be used for the temperature ramp and frequency sweep.

Table 2.4: Rheological test paramters for temperature ramp test for SEBS20, SEPS22 and MED500400 at various frequencies.

Material	strain sweep:1-100%	
	T (℃)	Freq (rad/s)
SEBS20	190-310	10, 1
SEPS22	180-250	10, 1, 0.1
MED500400	140-250	10, 1

Table 2.5: Rheological test paramters for strain and frequency sweep for SEBS20, SEPS22 and MED500400.

Material	strain sweep:1-100%		frequency sweep:0.1-100 rad/s	
	T (℃)	Freq (rad/s)	T plate (℃)	strain (%)
SEBS20	190	10	190	1
	190	10	190	1
	210	10	210	1
	230	10	230	1
	250	10	250	1
SEPS22	190	10	190	1
	190	10	190	1
	210	10	210	1
	230	10	230	1
	250	10	250	1
MED500400	160	10	160	1
	250	10	250	1

2.3 Results and Discussion

The polymers considered in this thesis were characterised using dynamic mechanical analysis (DMA Q800, TA instruments, DE, USA), differential scanning calorimetry (DSC Q2000, TA instruments, DE, USA), gel permeation chromatography (Viscotek GPCmax) and rheology (ARES Rheometric Scientific, Ta instruments, DE, USA). Thermal properties, such as the order-disorder transition temperature (T_{ODT}) and the glass transition temperature (T_g), were assessed to inform optimisation of the injection moulding parameters. Small angle X-ray scattering was applied to assess the microstructure pattern and orientation of compression and injection moulded samples.

The aforementioned analyses concentrated on the materials destined for the leaflets of the valve (SEBS20, SEPS22 and MED500400) and, where applicable, on the parallel orientation of the hexagonally packed cylindrical styrenic domain. SEBS29 was analysed mainly to verify styrene fraction and molecular weight.

2.3.1 Gel permeation chromatography

The measurements gave accurate values for the polystyrene fraction and molecular weight, the results are summerised in Table 2.6.

Table 2.6: Measurement of molecular weight (Mw in g/mol), polidispersity index and polystyrene fraction (%wt) for SEBS20, SEBS29 and SEPS22. The results were obtained from a GPC dual detector (Viscotek GPC max VE2001).

Material	M_w (g/mol)	PI	PS fraction (%wt)
SEBS20	111327	1.072	19.6
SEPS22	71697	1.038	19.2
SEBS29	74837	1.061	28.4

As expected, the polystyrene fraction was close to the number stated in the polymer name. SEBS20 has higher molecular weight but similar PS fraction compared to SEPS22.

2.3.2 DSC

Differential scanning calorimetry indicates a phase transition manifested by sudden change in the heat flow. As shown in the Figure 2.21-a and 2.21-b, the test did not

clearly detect any thermal transition, hence I did not take this technique forward for the analysis of the materials' properties.

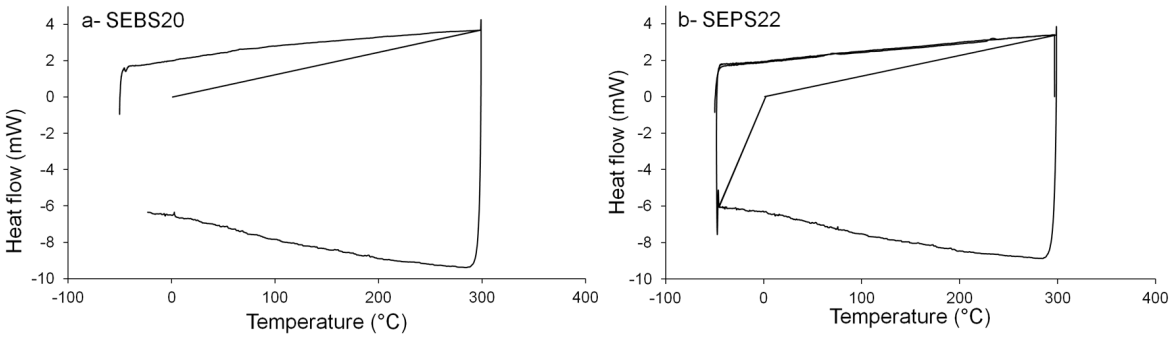

Figure 2.21: Differential scanning calorimetry results for a-SEBS20 and b-SEPS22. The plots show a temperature ramp form -50°C to 300 °C (10°C/min), a decreasing ramp from 300°C to -50°C (25°C/min) and a third ramp up to 300°C. The test was performed on DSC Q2000 (TA instruments, DE, USA).

2.3.3 SAXS

The compression and injection moulded samples were analysed using SAXS to verify the correct orientation of the cylindrical domain. The mechanical properties depend strongly on the cylinders' orientation and packing. Hence, accurate microstructure determination is essential for understanding the fatigue performances of the materials.

The SAXS patterns allowed calculation of the degree and direction of orientation and d-spacing. Figure 2.22 shows the 2D SAXS pattern for compression moulded SEPS22 and the corresponding polar and azimuthal integrations. The beam was perpendicular to the normal of the specimen surface. In general, a point pattern means an ordered microphase, while a uniform ring reflects isotropy. Moreover, a six point pattern means that the cylinders are hexagonally-packed [36]. Clear equatorial reflections are visible in the 2D pattern in Figure 2.22-a. The equatorial direction is perpendicular to the specimen normal, indicating an orientation of microdomains parallel to the flow direction. The narrow peaks in the azimuthal plot confirm this. The appearance of higher order reflections in the polar integration (Figure 2.22b) also suggests that the polymer is well oriented. Moreover, the presence of the $\sqrt{3}$ reflection (second peak in the polar integration) confirms hexagonally packed cylinders [66, 65]. From this data and using Bragg's law (2.6), an average lattice spacing of 22 nm was calculated.

The d-spacing was measured for the three candidate materials for the leaflets.

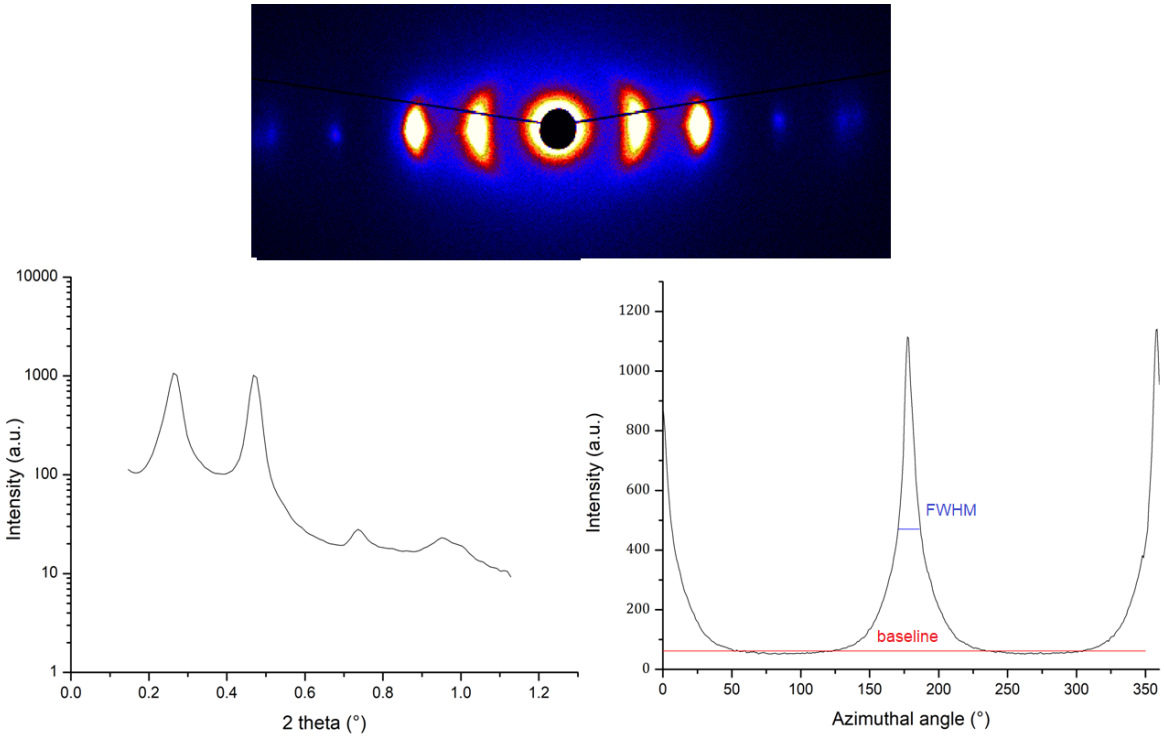

Figure 2.22: Compression moulding SEPS22 SAXS analysis: a- 2D refraction pattern, showing equatorial 1st and higher order reflections indicating highly ordered hexagonally cylinders packed in parallel direction to the melt flow; b-2 θ polar integration of the reflection pattern, the first peak is the first order reflection, followed by second order peak at $\sqrt{3}$, $\sqrt{9}$ and $\sqrt{13}$ peaks typical of an hexagonally packed pattern; c- azimuthal integration of the first order peaks, the narrow peak indicates a well oriented microstructure. Integration calculation performed by Dr. J. Stasiak.

SEBS29 was not analysed since there is no need to have orientation in the more rigid bulk part of the stent and the mould was not designed to direct the flow for a specific orientation. More details of design of the valve, which involves SEBS29, are in chapter 3. Figure 2.23 shows the first reflection for SEBS20, SEPS22 and MED500400 obtained with the Bruker Nanostar. The samples for this analysis were cut from a section of an injection moulded valve leaflet, flat injection moulded sheet and injection moulded unitensile sample, respectively. SEPS22 has a smaller d-spacing than the other two materials; furthermore the value confirms the calculation obtained with the I22 beamline. SEBS20 shows a 4 spot pattern, due to its bi-directionality. Also, MED500400 shows a bright ring reflection, indicating that there is no preferential orientation and indicating that the microphase structure could be spherical, rather than cylindrical. This result was expected since the material is softer, meaning lower styrene fraction. According to

the phase diagram, for styrene fractions lower than 18-20% the microphase should be spherical (see Figure 2.3). Moreover, from the theory the d-spacing is predicted to have a power law relationship with the molecular weight, hence MED500400 result suggests that the material has a higher molecular weight compared to the other two SBC [63]. Furthermore, the narrow channel of the unitensile sample mould should have imparted a strong flow field, which would have oriented a cylindrical forming microstructure, as shown in Figure 2.24-a and 2.24-b.

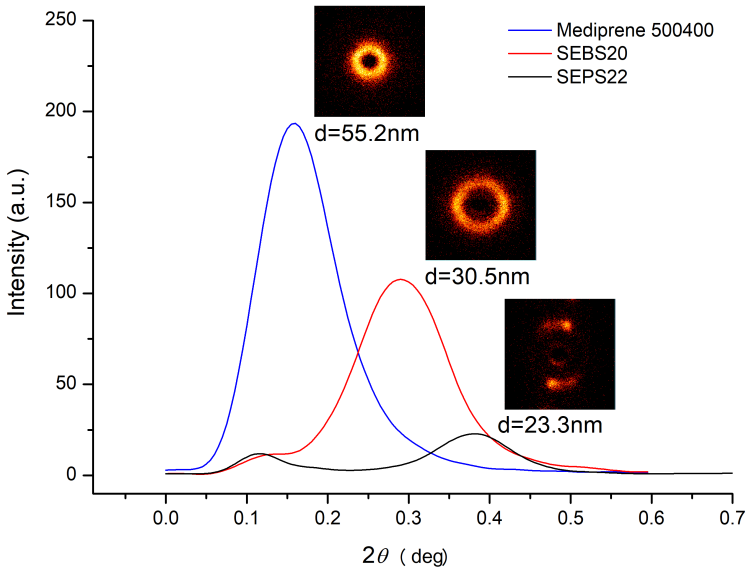

Figure 2.23: Calculation of the d-spacing for MED500400, SEBS20 and SEPS22. d-spacing was calculated from the first reflection via polar integration applying Bragg's Law. The SAXS images are taken from Bruker Nanostar. Integration performed by Dr J. Stasiak.

The two patterns represent the reflections for shape a and b of the unitensile samples (Figure 2.24) for SEPS22 and SEBS20 respectively. The samples are highly oriented in the flow direction. The reflections are meridional rather than equatorial because the samples were mounted with the long axis parallel to the table top, as shown in Figure 2.24. There is no bi-directionality, as reported by Stasiak *et al.* [65] in their injection moulded samples. The results also demonstrate that both unitensile mould shapes produce an optimal alignment in the flow direction.

Part of this study is the comparison between parallel and perpedicular orientations of the cylindrical domain relative to the strain direction. However, there is no flow field capable of producing purely perpendicularly oriented cylinders. For this reason,

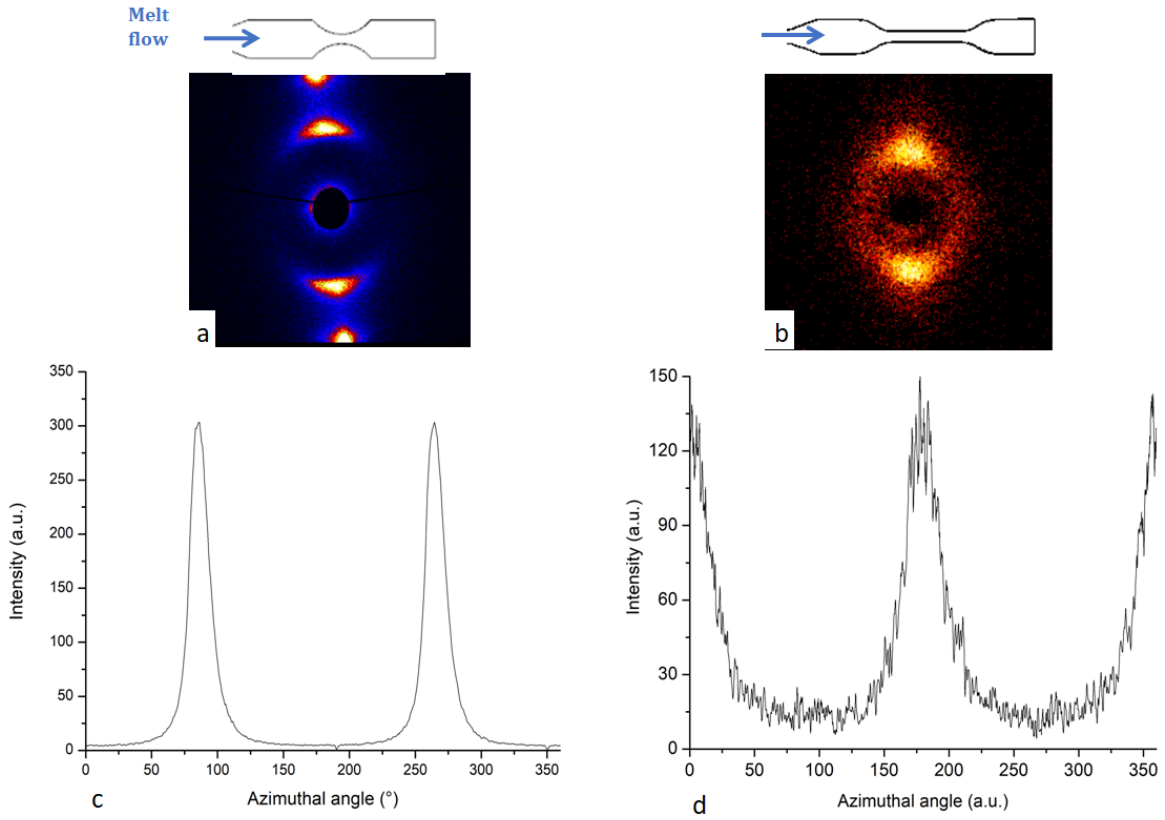

Figure 2.24: SAXS pattern and azimuthal integration of the central narrow section of the unitensile samples for both ISO37 type 2 and ASTM D638 type v geometries. The samples were injection moulded with mould in Figure 2.10. a- SEPS22 X-ray pattern, c- SEPS22 azimuthal integration, b- SEBS20 X-ray pattern, d- SEBS20 azimuthal integration. Both images show equatorial refractions indicating parallel orientation respect to the flow direction.

perpendicular samples were obtained from flat injection moulded sheets (mould 2.10-a). A cutting die for unitensile sample shapes 2.11-a was placed perpendicular to the flow direction, as it is shown in Figure 2.25-a and 2.25-b. Samples were cut starting from 1 cm below the triangular part close to the injection point. For both figures the orientation angle of alignment is represented by the angle vector (red lines) and its length is proportional to the reciprocal of FWHM for the relevant reflection [65].

The complete pattern of the flat sheet shows that the flow field was not perfectly unidirectional, but was rather radial, more so for SEBS20 then SEPS22. Moreover, the microstructure was bi-directional, with two surface layers perpendicular to the core layer, as described by Stasiak *et al.* [65] and represented in Figure 2.8. The ratio of core and surface can be considered uniform in most of the sheet, it varies within a small

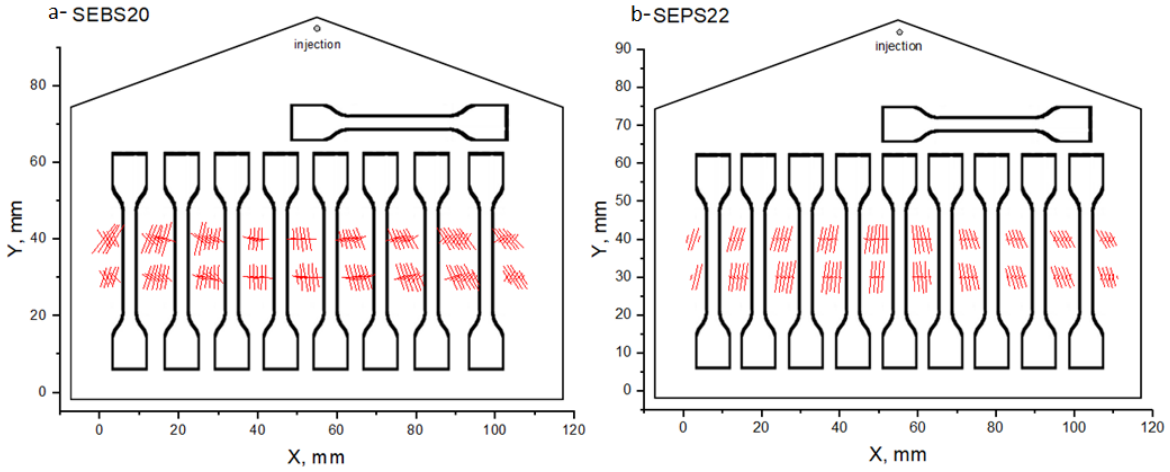

Figure 2.25: Schematic representation of the injection moulded flat samples from mould 2.10-a of both SEBS20 (a) and SEPS22 (b). The drawings give an indication of how the samples were cut with the unitensile sample die. The red angular vector indicates the orientation pattern, the lenght of the vector is proportional to the inverse of the full width at half maximum (FWHM) for the relevant reflection. Calculation performed by Dr J. Stasiak.

range (core fraction: 34 ± 2.9% for SEBS20, 13 ± 5.9% for SEPS22) . The orientation angle changed with the local flow field for both layers. SEPS22 showed a much lower core reflection intensity and a closer to uni-directional orientation (Figure 2.25-b). This difference can be explained by a combination of effects. As reported in Table 2.12, the mould temperature for SEBS20 was 10/15 degrees higher, despite this the mould took longer to fill. I observed that the melt front was faster in the middle of the mould, which developed a radial flow field. This effect is corrected when the mould is full and some material starts to flow out of the mould since the bottom is kept open to allow air to exit during injection. The longer the material takes to flow, the more likely it is for the orientation to freeze at the surface. A higher mould temperature could improve the orientation, however it was not possible with the equipment available.

It is important to emphasise that the samples in Figure 2.25 and 2.24 have the same thickness. The open mould led to some degree of bi-directionality across the section, while the unitensile specimen moulds produced unidirectional samples.

Figure 2.26 shows the specimen cut from the flat sheet for SEBS20. The bright point meridional reflection indicates the cylinders aligned with the flow (parallel). The equatorial reflections in Figure 2.26 a-c-d-e indicates perpendicular orientation with respect to the long axis of the sample. Figure 2.26 e shows both meridional and equatorial reflections, the latter corresponding to the core layer of the sample, meaning

that there is a more balanced ratio of core and surface layer. Images for samples a-b-c and d show a less bright core reflection, which is represented in a smaller vector. The majority of the domain for these samples is oriented in one direction, which makes them a good representation of the perpendicular orientation.

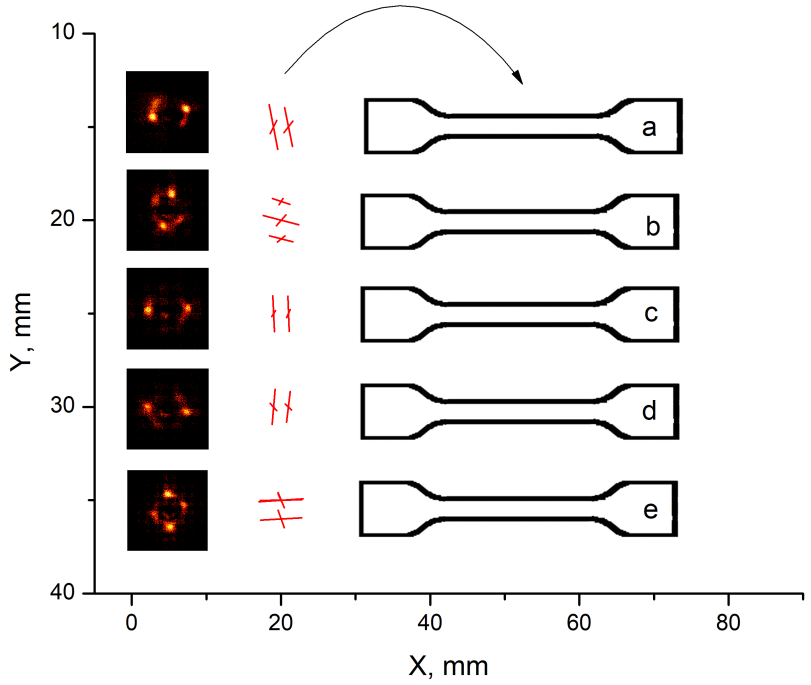

Figure 2.26: SEBS20 samples X-ray patterns. The samples were cut from the injection moulded flat sheet in parallel (b,e) and perpendicular directions (a,c,d). The red angular vector indicates the orientation pattern, the length of the vector is proportional to the inverse of the full width at half maximum (FWHM) for the relevant reflection. Calculation performed by Dr J. Stasiak.

Similar images were obtained from the unitensile samples cut parallel and perpendicular to the flow direction for SEPS22, shown in Figure 2.27. The weak reflection around the ring confirm the fraction of core perpendicular orientation calculated for the flat sample in Figure 2.25. Sample 2.27-d shows equatorial reflections at 12°±2 angle shift compared to the perfect perpendicular orientation. Subsequent samples were cut at this angle to produce more accurate orientation. Sample 2.27-d confirms (unsurprisingly) that there is no effect on the microstructure if a heparin coating is applied on the polymer (more details on the coating in chapter 3 and 4).

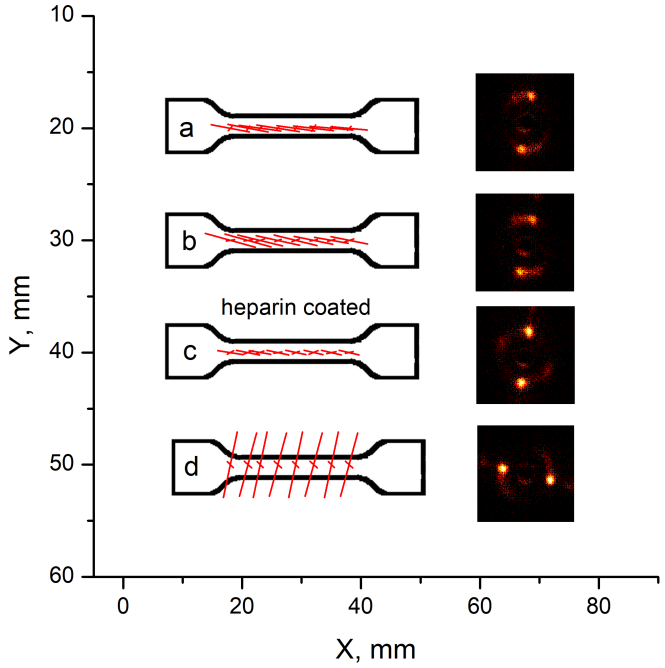

Figure 2.27: SEPS22 samples X-ray pattern. The samples were cut from the injection moulded flat sheet in parallel (a,b,c) and perpendicular direction (d).The red angular vector indicates the orientation pattern, the lenght of the vector is proportional to the inverse of the full width at half maximum (FWHM) for the relevant reflection. Calculation performed by Dr J. Stasiak.

2.3.4 DMA

The aim of the DMA test was to identify the glass transition temperatures for the BCPs considered in this work, most importantly the candidate materials for the valve leaflets. This technique in principle could also allow detection of order-disorder transition temperatures; however it was not clear in the following results.

The glass transition temperature (T_g) is the limit below which writhing thermal motions desist. The material is stiffer due to lack of long-range chain readjustments. Above the T_g, the thermal motions of the chains result in a softer, leathery state. A further increase in temperature leads first to a rubbery material, ideal for moulding and processing, and to a viscous liquid-like material at even higher temperatures. In the latter situation, the polymer chains are completely relaxed and disentangled [73].

The graphs in Figure 2.28-a to c show the viscoeleastic behaviour of the three materials SEBS20, SEPS22 and MED500400. As expected from block copolymers, more than one transition was found, indicating different mechanisms of chain movement

and phase transition. The test could not run up to 400°C because the samples broke, melted or lost their initial shape due to softening.

The tan δ is one of the parameters used in literature to identify the glass transition temperature [98]. The peak in tan δ indicates the transition point between glassy and rubbery states of the polymer. For SEBS20 there are two clear peaks in tan δ (Figure 2.28-a), identified as relaxations α and β. The higher temperature peak at 112°C is the glass transition of polystyrene, while the lower temperature peak can be identified as the secondary β transition correlated to the relaxation of the elastomeric -EB- matrix. The latter transition can be described as the intermediate glass transition temperature between the two homopolymers forming the -EB- segment. However, several studies argue that there is a composition relationship depending on the ethyl branching level in the segment: when butylene is above 50% the segment is completely amorphous and the glass transition can be computed from linear relationship with composition; for lower butylene contents the β transition is due to relaxation of chain units which are located in the interfacial region between the crystallites [74, 75].

Figure 2.29 from Sierra *et al.* [75] shows DMA response for SEBS with variation in ethyl branching fraction at constant PS fraction, and variation in PS fraction at constant E/B ratio. They pointed out that the β transition peak is broader and higher for lower styrene content (Figure 2.29-b) and also the α peak has lower intensity. Figure 2.29-a, on the other hand, shows that increasing the ethyl branching density increases the β transition peak and makes it slightly narrower. Comparing the results I obtained with those reported by Sierra *et al.*, it is reasonable to assume that the peak for the β transition of SEBS20 is broad due to some amount of crystallinity mixed with amorphous segments and that butylene is probably less than 50% (mass) of the elastomeric phase. Furthermore, the peak height for the β transition reached the same value of the 20% fraction of the SEBS studied by Sierra *et al.* [75], even though SEBS20 has double the molecular weight of their sample. The β transition for MED500400 is shifted to lower temperature, which was identified as an effect of high ethyl branches density.

The MED500400 plot shows a narrow peak in tan δ at -50°C, followed by a smooth descent. The fact that the peak is narrower compared to the β transition peak obtained for SEBS20 suggests that -EB- segments in MED500400 are completely amorphous, *i.e.* E/B ratio is lower than 1. There is a small peak at ∼112°C which is the PS glass transition, the fact that it is difficult to detect confirms the hypothesis in section 2.2.2 that MED500400 has a PS fraction between 10-18%. After this transition tan δ increases as a response to the softening and loss of initial geometry of the specimen

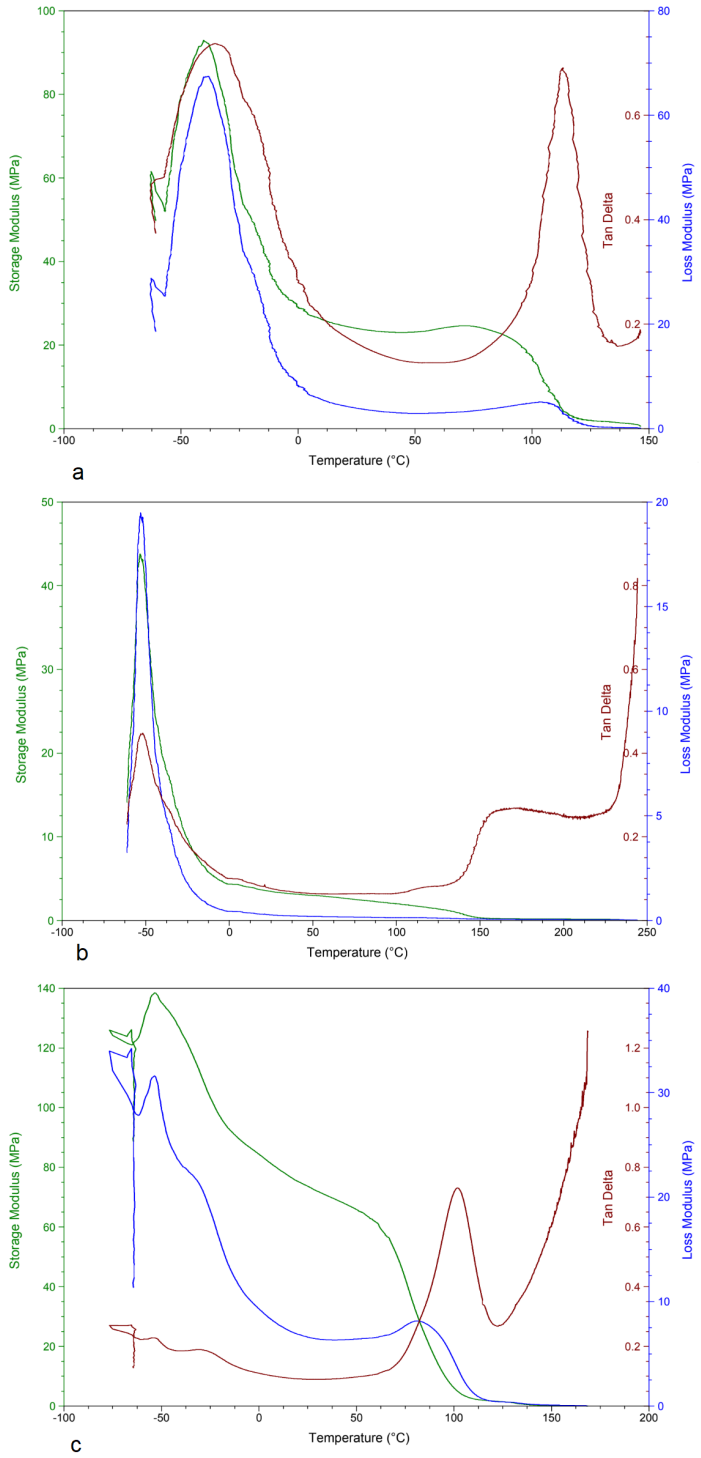

Figure 2.28: Tan δ, storage and loss modulus as a function of temperature using DMA 800 (TA instruments, DE, USA). The analysis are for a-SEBS20, b-MED500400 and c- SEPS22.

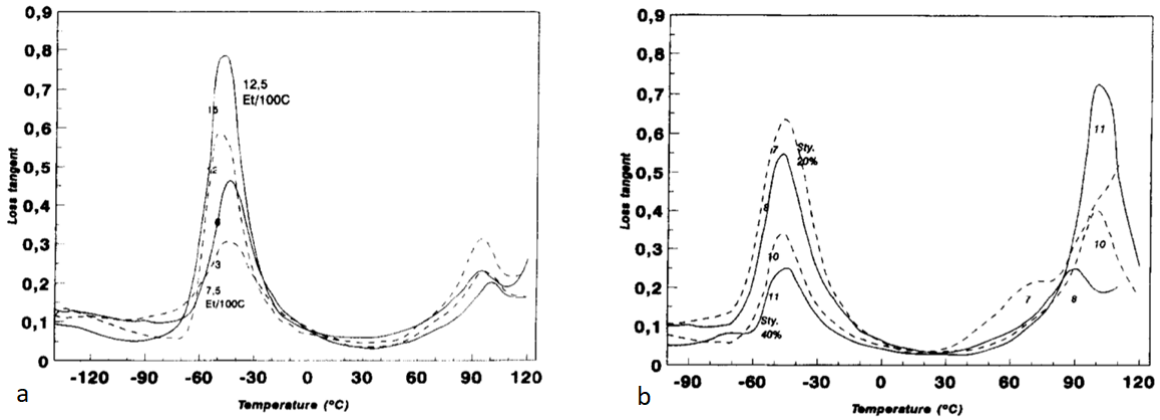

Figure 2.29: a- Effect of ethyl branches on loss tangent for SEBS (30% styrene) b- effect of styrene content on loss tangent for SEBS (10 ethylegroup/100 C). The figure was adapted from reference [75]. The number indicates their samples nomenclature. On the β transition peak there are indications of the ethyl branches and styrene fraction.

mounted in the DMA machine.

Since the width and height of the β transition peak is enhanced by branching, it is expected not to find a defined peak in tan δ at low temperatures for SEPS22, since the elastomeric ethylene-propylene segment does not have chain branches [75, 76, 99]. SEPS22 shows a tan δ peak at ∼100°C of the same height of the α transition for SEBS20, identifying the glass transition of PS. The two polymers have similar PS content, explaining this similarity. Moreover, two small peaks in tan δ are visible at -50°C and -25°C, corresponding with a peak and a shoulder respectively in both storage and loss modules. This probably signifies rubbery domain chain motions, which are still constrained by the anchorages of the glassy PS.

Further tests should be done on the perpendicular orientation of the styrenic domain compared to strain direction. This is beyond the scope of this work.

2.3.5 Rheology and T_{ODT}

Theoretical models have been applied to predict the transition temperatures. Helfand-Wesserman theory [52] sets the transition from an ordered domain to a homogenous phase to occur at the temperature at which the free energy change is zero. The narrow interphase approximation was applied to simplify the calculations. The outcome of their study was in good agreement with experimental data available at the time.

A second criterion to identify microphase separation transition (ODT) was defined according to Lieber's definition of free-energy balance. The first and second derivative

of the free energy, with respect to the order parameter, must be respectively equal and greater than zero; meaning that at equilibrium the order parameter minimises the free energy. In addition, the ODT occurs when the order parameter sets the free energy at zero [55]. The result is a χN threshold value below which the system exhibits a disordered phase. Moreover, the phase diagram obtained from the equilibrium criterion applied to Liber's free energy balance, allowed prediction of mesophase transitions (OOT) for specific value of χN for an AB di-block copolymer.

The application of these theoretical methods to the materials of this study is complicated by the lack of precise information on the parameters in the equations. The literature archive for material parameters is still lacking and proceding via theoretical methods would require a high degree of approximation. Han *et al.* [77] predicted T_{ODT} of a series of PS/PB and PS/PEB with different PB content applying Helfand-Wesserman theory. They determined the interaction parameter as a function of blend composition and temperature applying Flory-Huggins theory to experimental cloud point measurements. However, interaction parameters obtained via cloud point measurements are applicable only to polymers having the same molecular weight.

Empirical methods proved to be more reliable and simple to perform. According to several studies [56, 60, 61, 78, 79], an accurate method to identify the order-disorder transition temperature is with rheological measurements of an isochronal temperature ramp at low frequency. The method is based on the principle that ordered and disordered states are characterized by different rheological properties. The measured properties in the rheological test are loss and storage modulus. The storage modulus G' represents the stored elastic energy. It is a measure of the energy stored and recovered every cycle. The loss modulus G" quantifies the energy dissipated as heat in every sinusoidal cyclic deformation. It describes the viscous properties of the material. In general, in a temperature versus G' and G" plot of a viscoelastic test, G' is higher than G" at lower temperature. As temperature increases G' decreases until the two curves cross each other, which represents a transition from glassy to rubbery state. A third parameter that is often used in the rheological analysis is tanδ, which is the ratio of G" and G'. Tanδ is equal to one at the cross over point. When tan$\delta > 1$ the polymer acts more similar to a liquid, while for tan$\delta < 1$ the storage modulus dominates and the polymer is more rigid [73].

The discontinuity in the storage modulus (G') with temperature, less evident in the loss modulus (G"), represents the ODT temperature. The moduli suddenly drop as a consequence of disordering. The discontinuity is a direct consequence of the first-order nature of the order-disorder transition [60].

Gouinlock *et al.* [79] studied the styrene-butadiene-styrene (SBS, Shell Development Co., molecular weight 7000-43000-7000 g/mol, 25% styrene) response to rheological measurements as a function of temperature and frequency. The temperature ramp at low frequency (between 0.01 and 1 rad/s) showed a drastic discontinuity in both the elastic modulus and the dynamic viscosity, indicating strong changes in viscoelastic properties, and thus a transition to a disordered phase. Low temperature measurements showed a characteristic non-Newtonian behaviour, while at higher temperatures Newtonian behaviour occurred. The authors attributed the transition to weakening and/or loss of crosslinking structure as a consequence of increased phase miscibility and the achievement of a disruptible dispersed phase not giving a viscoelastic response. Furthermore, it was pointed out that the narrow transition implies that miscibility is the major factor, since if the phase transition was not present, the change in viscoelastic properties would be expected to be more gradual.

Han *et al.* [80] developed a different rheological technique to identify the T_{ODT} for block copolymers. The protocol uses the measurements of the loss (G") and storage (G') moduli as functions of angular frequency for isothermal conditions (Cole-Cole plot). The relationship between log G' and log G" was shown to become independent of temperature above the T_{ODT}. They investigated SIS (Kraton 1107, Shell Development Co.) and SBS (Kraton 1102, Shell Development Co.). The plot of log G' vs log G" for both polymers showed a strong temperature dependence over a range of temperatures (from 140°C up to 240°C), which is explained as the thermally induced transition from an ordered to a disordered phase. They showed that, for monodispersed flexible homopolymers, the temperature dependence of the logarithm of the loss and storage moduli is very weak. Hence, if there was no morphological change within the range of the temperature tested, virtually no temperature dependence would be expected, which is the opposite of what they observed. The sensitivity of this method depends on the deformation rate, as the authors explained. High deformation rate could disrupt and reform the network of the PS domain. They suggest maintaining a stable state at low deformation rate to investigate the T_{ODT}. In the same study, they predicted the T_{ODT} of the BCPs with Helfand-Wesserman and Leibler theories. However, they pointed out that the accuracy of these predictions very much depends on the accuracy of the relationships between temperature and the equation's parameter (interaction parameters (α) and specific volume of the block's components).

Chun *et al.* [81] applied Han's criteria to identify the ODT temperature for SEBS29 (Kraton G1650). The dynamic frequency sweep was performed up to 310°C. However, the logG' vs log G" plot did not show any temperature independence, meaning that

the T_{ODT} is higher than 310°C. They also estimated the temperature applying the Helfand-Wesserman theory, which predicted a T_{ODT} of 350°C.

However, Rosedale *et al.* [60] argue that this continuous departure from T-independent behaviour is the effect of fluctuations and should not be considerate as evidence of ODT. Fluctuations below ODT cannot be evaluated quantitatively, but G' and G" dependence are shown below ODT. At $T > T_{ODT}$ amplitudes of concentration fluctuations are small and have little influence on the low frequency properties, while when approaching T_{ODT} the amplitude of the fluctuations increases and impedes the long range motion of individual chains.

Almdal *et al.* [56] investigated poly(ethylenepropylene)-poly(ethyleethylene) (PEP-PEE) di-block copolymer using SANS. ODT and OOT were determined as discontinuities in the SANS pattern intensity and symmetry. Two OOTs were found at 91°C and 155°C and ODT was detected at 175°C. The transitions were confirmed by rheological measurements of a temperature ramp under isochronal conditions.

Sakamoto *et al.* [82] studied the ODT and OOT of polystyrene-block-polyisoprene-block-polystyrene (SIS, 18% PS, Vector 4111, Dexto Polymer Co) using SAXS and rheological measurements. SAXS scattering profiles during heating and cooling showed the presence of different microdomain structures: from hexagonally packed to spherical microdomains in a cubic lattice and distorted lattice (179-185°C, two OOTs), and a disordered phase above 210°C. Rheological measurements confirmed these results. They conducted a dynamic temperature sweep under isochronal conditions, and a dynamic frequency sweep at various temperatures. From the first test G' was plotted against temperature for which the minimum identifies OOT, which was in the same range identified with SAXS. The minimum represents the competing effects of two events: softening of cylinders (decrease in G') and transformation into a cubic spherical phase, which corresponds to a higher contribution of the interphase to G' (increase in G'). They noticed that the same analysis conducted at higher frequency produced a less visible transition in the plot. Plots of log G' vs log G", obtained from the dynamic frequency sweep, showed a sharp slope inversion at the temperature corresponding to the OOT and confirmed the results for ODT obtained with SAXS measurements. Furthermore, they used TEM to determine the microdomain structures of quenched specimens at 170, 185, 200, 220°C. The images confirmed the hexagonally- packed cylindrical, cubic spheres and distorted cubic spheres structures respectively.

In this study both isochronal temperature ramps at low frequency and Han's method were applied to investigate the transition temperatures for the styrenic block copolymers. The determination of the two transitions is necessary to verify if the processing

temperature during manufacturing interfered with the shear alignment of the cylinders. Furthermore, if the material is processed above the T_{ODT} and quenched (as happens during compression moulding) the final structure could be distorted and distant from a uniformly aligned hexagonally packed cylinder structure.

Figure 2.30 shows the discontinuity in G' for SEPS22, determining the T_{ODT} to be at approximately 228°C. The shear oriented specimen shows a characteristic decrease in elasticity with increasing temperature, typical of an ordered BCP [60]. The sharp increase in the tanδ, represents a drop of strength which is proably correlated to phase mixing, *i.e.* disorder [75].

The Cole-Cole plot is represented in Figure 2.31. The frequency sweep was performed at 190°C, 210°C , 230°C and 250°C. The discrepancy between the results for 210°C and 230°C clearly indicates the presence of a transition between these temperatures. It has been shown that near the ODT, the disordered liquid-like phase develops transient composition patterns [41]. Furthermore, the curves for 230°C and 250°C are overlaid, indicating an independent behaviour of the moduli with respect to the temperature, which, according to Han's criteria, is indicative of the presence of a disordered phase. This result confirms the finding obtained from the temperature sweep at low frequency.

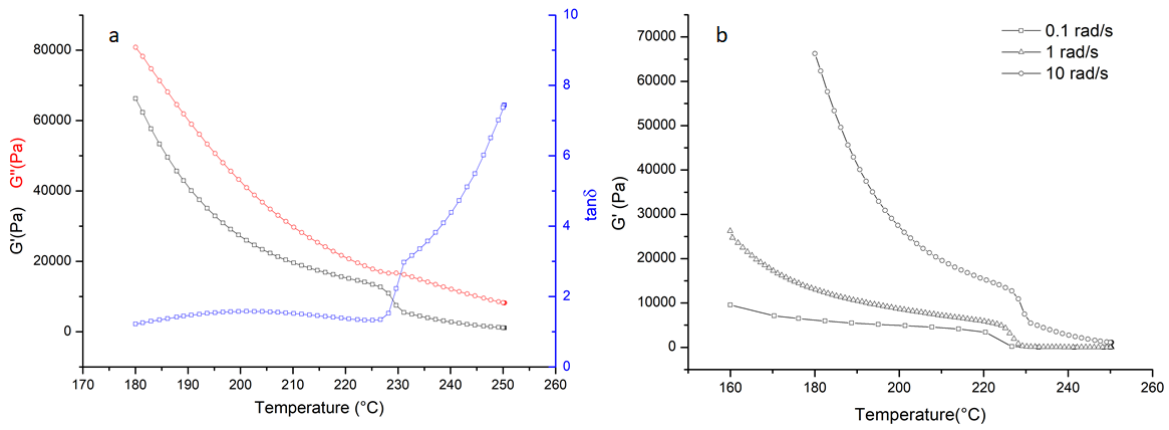

Figure 2.30: Temperature ramp for SEPS22 .a-the graph represents the loss and storage modulus on the left, and the tanδ on the righ axis. The temperature ramp was perferomed between 180°C and 250°C, 10 rad/s frequency and 1% strain; b-storage modulus versus temperature for 10, 1 and 0.1 rad/s at 1% strain for SEPS22 .

The presence of an order-order transition was not detected by these tests. If this transition was present, the loss modulus should have shown a minimum at a temperature below the T_{ODT}. However, it is not likely for the transition to happen if the

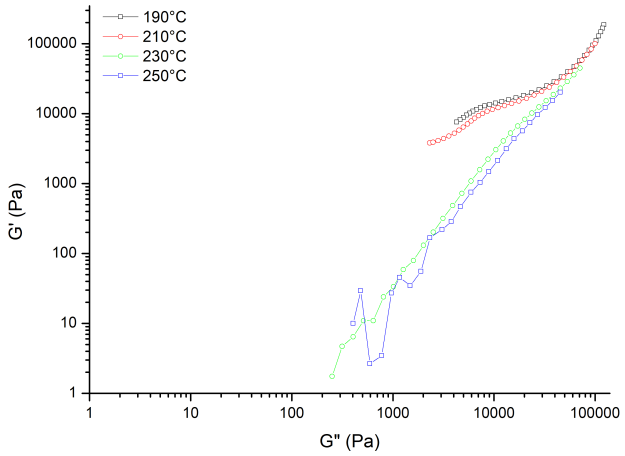

Figure 2.31: Plot of loss modulus versus storage modulus for SEPS22. The data were collected for frequency sweeps at different temperatures. The tests were performed at 190°C, 210°C, 230°C and 250°C at 1% strain. The frequency sweep started at 0.1 rad/s and reached 100 rad/s. The results idenitfy a order-disorder transition temperature at around 230°, where the log G'vs log G" behaviour starts to be independent from temperature.

composition is far from the border between two microstructure phases in the state diagram [82]. It is possible that a lower frequency test would better show this transition, if present. The transition from cylinders to spheres has been proven to go through a disordered state where the large scale mesostrucure is destroyed. The causes could either be a disordering process, drastic increase of fluctuations, or sudden increase in defect density and grains shrinking [44].

The plots in Figure 2.32 show the storage moduli and dynamic viscoleastic modulus trends at different temperatures during frequency sweeps. For each microstructure depicted in Figure 2.3 there is a characteristic frequency dependant response of the dynamic and loss moduli. In general, it has been demonstrated that viscoelastic properties for microphase separated copolymers are affected on time scales longer than the longest chain relaxation time. Therefore, the elastic modulus low frequency behaviour reflects the microstructure at a given temperature [83].

Graph 2.33, from the paper by Kossuth *et al.* [78] , shows a comparison of the different regimes at the terminal frequency regime. The cubic phase is the only one showing a plateau. Lamella and cylinders show an algebraic dependence on frequency at low frequencies. The decay is represented by: $G \propto t^{-\alpha}$, where t is time (s), α is 0.5 for lamella [51, 60] and 0.2 - 0.3 for cylinders [83]. The main explanation is that only

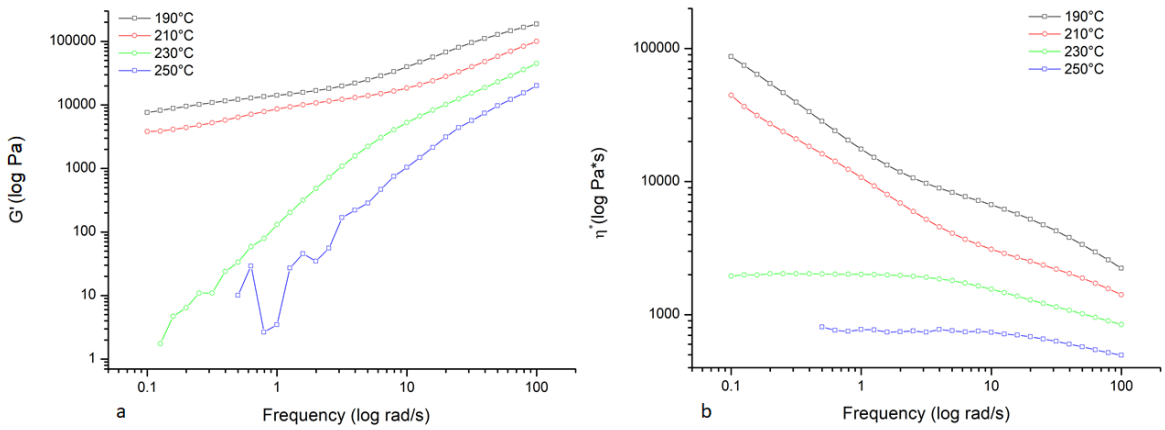

Figure 2.32: a- storage modulus vs frequency behaviour at 190°C, 210°C, 230°C and 250°C for SEPS22. Above 230°C the terminal behaviour indicates a shift towrds a disordered phase; b- dynamic viscosisty vs frequency at 190°C, 210°C, 230°C and 250°C for SEPS22, above 230°C the viscosity starts to become independet from frequency, representing a homogenoeus melt, *i.e.* a disordered phase.

the cubic phase has a 3D translational order (crystal like). An ideal periodic cubic crystal structure should exhibit a pure elastic response as frequency$\rightarrow$ 0, independent of the orientation of the crystal axis, which is represented for the cubic microstructure of the block copolymer by the plateau in graph 2.33. On the other hand, lamellar and cylindrical phases behave like liquid crystals: they should respond elastically or viscously to distortions in different directions. For these architectures, one of the directions will be more liquid and does not sustain static shear strain. In the disordered phase, the polymer behaves like a liquid at sufficiently low frequencies. From rheological and SANS analysis, they speculated that near T_{ODT} the instantaneous disordered morphology behaves similar to a spinodally decomposed binary fluid mixture, but still retaining terminal liquid like behaviour at low frequency measurements [41, 58]. At higher frequencies the elastic linear response of the chains dominates over the liquid or solid like behaviour and the plot converges in one curve [41].

In the case of SEPS22, Figure 2.32-a, the storage modulus behaviour shows a flatter profile at 190°C and 210°C for $\omega \rightarrow 0$, indicating a cylindrical microstructure. At higher temperatures the profile starts to decay faster, similarly to the disordered profile in Figure 2.33. Figure 2.32-b also shows that the dynamic viscosity at 230°C and 250°C has a Newtonian behaviour, more representative of the disordered phase.

Graphs in Figure 2.34 and 2.35 represent the results for SEBS20. No clear transitions are visible in the spectrum of frequency and temperatures investigated. The loss

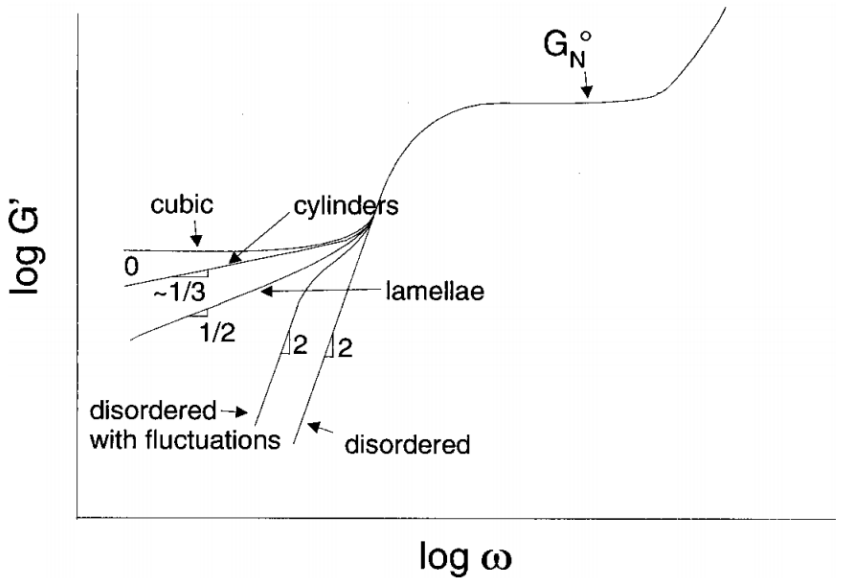

Figure 2.33: Low frequency behaviour of storage modulus for different types of ordered microstructure. The cubic spherical phase is frequency independent. The disordered phase has a rapid decay towards terminal behaviour. The figure was adapeted from reference [78].

modulus does not show any sharp discontinuity in the temperature ramp. Frequency sweeps at different temperatures show mild temperature dependance, excluding a transition or phase fluctuation . The T_{ODT} for SEBS20 is above 310°C. Similar findings were obtained for SEBS29, from the same polymer series [81]. For the purpose of this study, it is sufficient to demonstrate that the T_{ODT} is above 310°C for SEBS20.

It has already been pointed out that MED500400 has a spherical microstructure and a lower styrene content. Hence, a different rheological behaviour was expected. The temperature ramp performed shows a minimum between 140-160°C. After 220°C, G' goes through another minimum, this could be due to an error in the data collection, since it was towards the end of the run, or due to phase fluctuations near T_{ODT} (Figure 2.36-a). Moreover, in this range of temperature the contribution of the loss modulus is still much higher than the storage modulus, the material still performs like an elastic solid rather than a viscous liquid. The graph represents a rubbery plateau. Lower frequency tests were difficult to perform and the results were affected by noise, as shown in Figure 2.36-b.

The independence from temperature of the moduli in the temperature ramp in graph 2.36-a can be a consequence of the high molecular weight of the polymer. As explained in section 2.2.2, MED500400 did not dissolve in either THF and toluene and sothe molecular weight could not be measured by GPC.

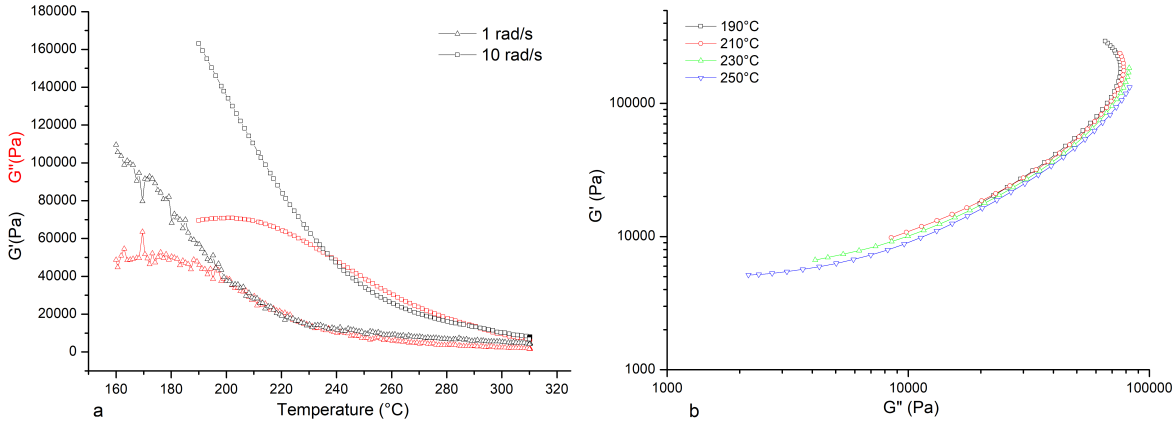

Figure 2.34: a-Temperature ramp for SEBS20, the graph represents the loss and storage modulus at 1% strain, 1 and 10 rad/s;b- logG" vs logG" Cole-Cole plot for SEBS20 from frequency sweep (0.1-100 rad/s) performed at 190°C, 210°C, 230°C and 250°C at 1% strain. No phase transition have been detected from these analysis.

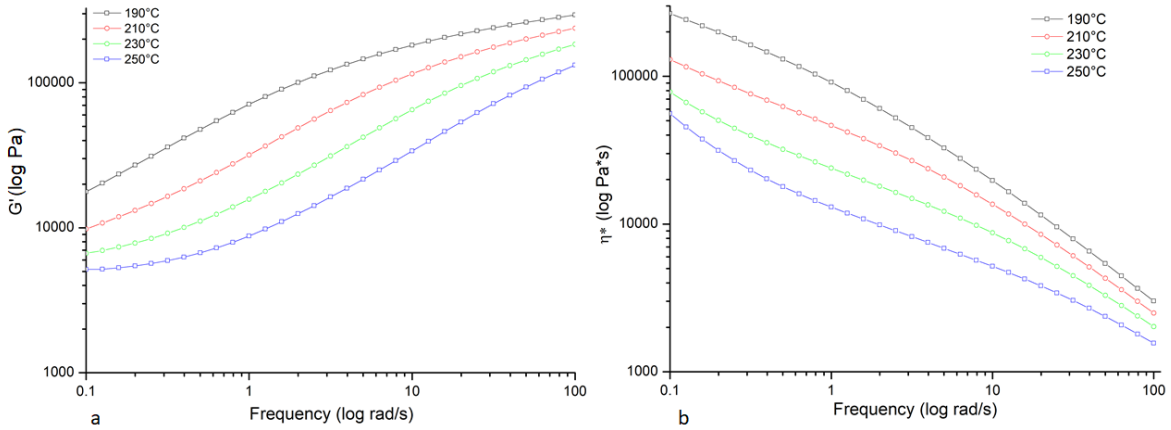

Figure 2.35: a- storage modulus vs frequency behaviour at 190°C, 210°C, 230°C and 250°C and 1% strain for SEBS20, the slight change of slope at low frequencies might indicate a change in microstructure configuration from cylinders to sphere; b- dynamic viscosity vs frequency at 190°C, 210°C, 230°C and 250°C at 1% strain for SEBS20. Shear thinning is shown for all temperatures investigated.

The results obtained from the frequency sweeps in graph 2.37-a are plotted according to Han's criteria in graph 2.37-c. The transition anticipated in graph 2.37-a is confirmed in the Cole-Cole plot. It is not possible to identify a order-disorder transition, however the change in rheological behaviour indicates a phase transition. Frequency sweeps at 160°C and 250°C show a change in terminal behaviour. At 160°C the slope

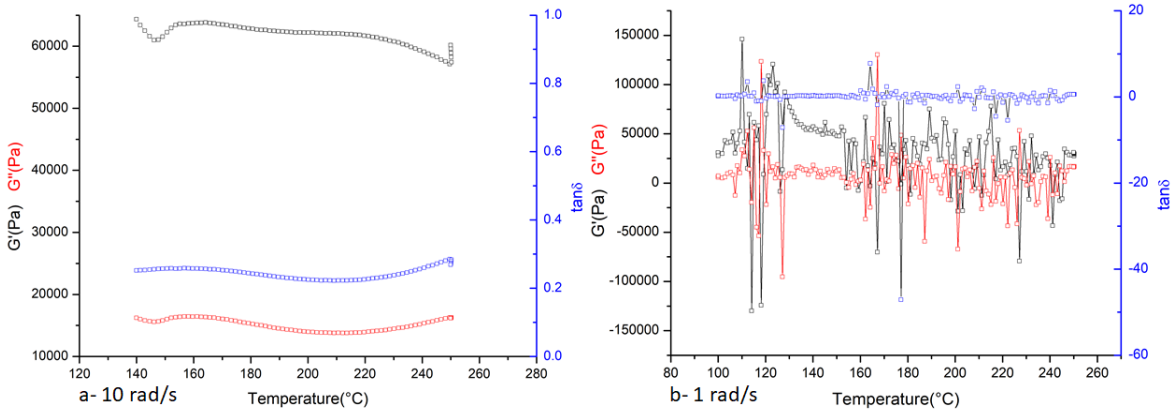

Figure 2.36: Temperature ramp for MED500400. The graph represents the loss and storage modulus on the left, and the tan δ on the righ axis. 10 The temperature ramp was perferomed at 10 (a) and 1 (b) rad/s frequency and 1% strain.

represents a BCC spheres pattern, while at 250°C the curve decays more rapidly as a disordered phase would behave. However, the decay of G' it is not as well pronounced as for SEPS22 and SEBS20, indicating that even lower frequencies are needed to properly investigate the phase transitions. The dynamic viscosity for the same test shows a temperature independent behaviour above 1 rad/s, confirming that the material is frequency sensitive. Shear thinning excludes the presence of a completely disordered phase.

2.3.6 Estimate of the microstructure dimensions

The main dimensions of the microdomain for the anisotropic block copolymers are d-spacing, diameter and length of the cylinders. The information on the d-spacing was obtained from SAXS pattern integration, as explained in section 2.2.2.

The diameter of the cylinders was assessed from known composition, d-spacing and measured hexagonal spacing. Keller *et al.* [84] compared this method with a different interpretation of the X-ray pattern. They interpreted the missing second order of the strong hexagonal spacing as coming from the first order Bessel function. They obtained the same values with both methods analysing SBS (Kraton 102, Shell Co.).

Fewer studies on length of cylindrical domains can be found in the literature. The main finding was reported by Cooney *et al.* [87]. They studied etching of polystyrene-polylactide (PLA) block copolymer (f_{PLA}= 0.325 Mw=33000 g/mol) to form a mesoporous structure. The PLA cylindrical domain was hydrolysed to create pores where the cylinders were. The samples were prepared with a shear alignment method. They

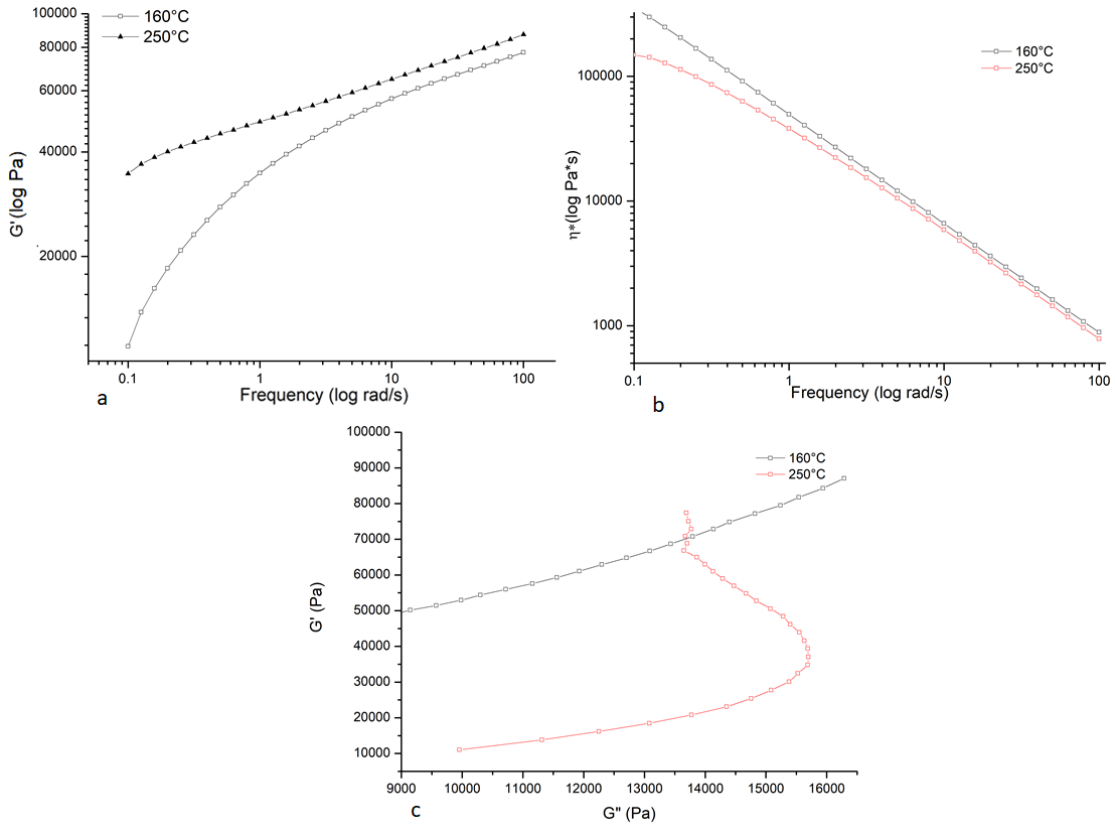

Figure 2.37: Frequency sweep for MED500400 at 1% strain. a- storage modulus vs frequency behaviour at 160°C and 250°C for MED500400, there is marked change towards disordered terminal behaviour from 160°C to 250°C; b- dynamic viscosisty vs frequency at 160°C and 250°C for MED500400,above 1rad/s the frequency is almost independet from temperature and shows a shear thinning behaviour; c- Cole-Cole plot for MED500400.

found that the cylindrical channels could reach up to 2.5 mm and that probably the cylindrical network was connected across the length of the sample (5 mm). It could not be confirmed that each channel corresponded to a single cylinder. It is also likely that the cylinders were connected by phase imperfections in the samples.

Previous related studies by Zalusky *et al.* [85] describe manufacturing and microstructure of a similar PS-PLA copolymer for the same application. The hexagonal pattern of cylinders was obtained with shear forces and analysed via SAXS. They also confirmed a long network of PLA in the PS matrix aligned in one direction. They assumed that the channels formed along the sample could be the connection of more cylinders, rather than a unique long cylinder.

Yamashita *et al.* [88] were able to fabricate an oriented lattice applying chemical epitaxy of PEO-b-PMA(Az) block copolymer. They could build 50 nm tall cylinders

using a chemical template of PMA(Az) with e-beam lithography.

Spontak *et al.* [89] studied SBS copolymer (30% styrene, Mw= 230000 g/mol) microstructure using TEM. They collected different projections at several angles, applied a filter back-projection reconstruction method and built a 3D map of the polymer structure. With this technique they could identify the hexagonal pattern of the cylinders' packing and showed that the height of the cylinders extended through the sample thickness (36 nm). The limitation of this technique is mainly the requirement that the film for the TEM imaging should be less than 100 nm.

Dr J. Stasiak used AFM to study the microphase structure of SI/BS19 (Kraton, Belgium) and SIBS30 (Innovia, Belgium), the images are showed in Figure 2.38. The microphases presented as worm-like cylinders, which were measured between 100-500 nm long. However, this measure does not consider the 3D path of the cylinders, which is not captured in the AFM image. The cylinder could be much longer than seen in the picture in Figure 2.38. However, the images show clearly that a different molecular weight (MwSI/BS19=180 kg/mol, MwSIBS30=102 kg/mol) and styrene fraction (19% and 30% for SI/BS19 and SISB30 respectively) produce different size and shape of microphases. SIBS30 seems to have shorter and more clustered segments, while SI/BS19 has longer, more uniformly distributed segments.

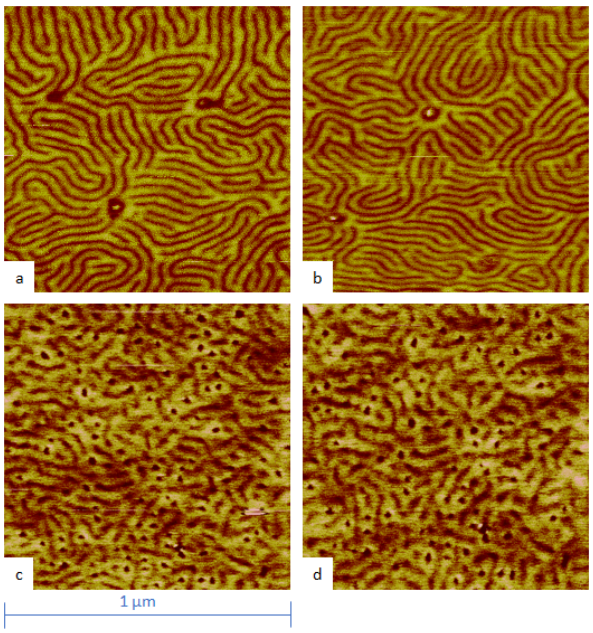

Figure 2.38: AFM images of SI/BS19 (a,b) and SIBS30 (c,d). The images show worm like cylinder microphase structures. The images were collected by Dr J. Stasiak.

The cylinder diameter was calculated using the information obtained from SAXS

analysis. The approach I took to calculate an estimate of a hypothetical height of the cylinders is to treat the material as a composite and use the Halpin-Tsai equation [93, 94]. Knowing the perpendicular and parallel values for Young's modulus, I reversed the equation and optimised a value for the height of the cylinders for SEBS20 and SEPS22. MED500400 is isotropic and has a spherical microstructure, hence no calculation was performed.

Cylinder diameter

In order to estimate the diameter of the cylinders, I considered the results obtained from SAXS, and followed a geometrical approach, similar to Helfand *et al.* [52, 53, 54] to calculate the average diameter of the cylinders.

SAXS analysis confirmed that the styrene cylinders are arranged in a hexagonal pattern and gave a d-spacing 30.5 nm and 23.3 nm for SEBS20 and SEPS22 respectively.

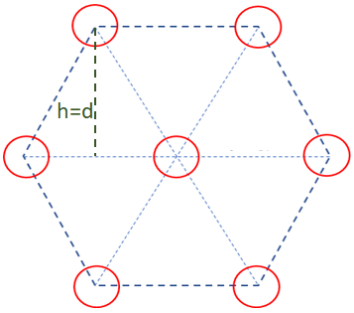

Figure 2.39: Schematic representation of the hexagonal pattern of the styrene cylinders divided in 6 equilater triangles. The red circles represent the cylinders. The height of the cylinder corresponds to the d-spacing.

The schematic drawing in Figure 2.39 shows the hexagonal pattern. The hexagon can be divided in 6 equilateral triangles and each triangle contains 1/2 a cylinder (3/6 of cylinders since every corner contains 1/6 of the cylinder). The d-spacing measured with the azimuthal integration of the SAXS scan is the perpendicular distance between planes, which corresponds to the height of the triangle.

Considering the volume occupied by the styrene and matrix within that triangular base, I can write:

$$Volume = Area * Height = \frac{\sqrt{3}}{4} l^2 H \tag{2.7}$$

The styrene volume is the total volume multiplied by the volumetric styrenic fraction. I converted the mass fraction of styrene to volumetric using equation:

$$\%v_{st} = \frac{\%m_{st}}{\%m_{st} + (1 - \%m_{st})\frac{\rho_{st}}{\rho_{matrix}}} \tag{2.8}$$

Where $\%v$ is the volumetric fraction and $\%m$ the mass fraction, ρ_{st} is styrene density and ρ_{matrix} the density of the matrix.

The value for styrene density was taken from the literature as 0.969 g/cm^3 [90]. The density of the matrix was estimated since there is no generic standard value in the literature, and the value depends on the fraction of the two components of the rubbery matrix (*i.e.* ethylene-butylene and ethylene propylene for SESB20 and SEPS22 respectively). I was not able to find or measure this information. I calculated a range for the density varying the fractions of the two components, the variation is considered in the final value of the cylinder diameter. The values for the single components' density were taken from the literature and are reported in Table 2.7 [100]. The styrene volume within the triangle is:

$$volumestyrene = \frac{\sqrt{3}}{4} l^2 H * \%v_{st} \tag{2.9}$$

From geometric analysis, the same styrene volume can be calculated as the cylinders half area multiplied by the height:

$$volumestyrene = \frac{\pi r^2}{2} H \tag{2.10}$$

Putting together 2.9 and 2.10, the radius of the cylinders can be calculated as:

$$r = \sqrt{\frac{\sqrt{3} l^2 \%v_{st}}{2\pi}} \tag{2.11}$$

where $l^2 = 4/3d^2$ and d is the d-spacing. Table 2.7 shows the results for the cylinders diameter of SEBS20 and SEPS22 considering the variation in the matrix composition. The mean value for the diameter will be considered in the second part of the microstructure size estimation.

Cylinders height

Estimation of the cylinders' height (or length) was calculated based on the hypothesis that the anisotropic material with small cylinders could be considered as a composite material composed of matrix and oriented fibres.

For these types of composite materials, the Young's modulus varies according to the stretching direction (as happens for anisotropic SBCs, see chapter 3) and with the

Table 2.7: Calculation of the matrix density (EB-ethylene butylene, EP-ethylene propylene), styrene volumetric fraction and cylinders diameter as a function of the matrix composition. The data shows the results for SEBS20 and SEPS22. The matrix density has been calculated using the rule of mixture : $\rho_{matrix} = \rho_1 \% m_1 + \rho_2 \% m_2$.

ρ_E (g/cm^3) 1.18	ρ_P (g/cm^3) 0.969	ρ_B (g/cm^3) 0.69	SEBS20			SEPS22		
E%	P%	B%	ρ_{EB} (g/cm^3)	$\%v_{st}$	D (nm)	ρ_{EP} (g/cm^3)	$\%v_{st}$	D (nm)
0.1	0.9	0.9	0.739	0.157	14.66	0.935	0.186	12.20
0.2	0.8	0.8	0.788	0.166	15.06	0.962	0.191	12.34
0.3	0.7	0.7	0.837	0.174	15.44	0.989	0.195	12.48
0.4	0.6	0.6	0.886	0.183	15.81	1.017	0.199	12.62
0.5	0.5	0.5	0.935	0.191	16.15	1.044	0.204	12.75
0.6	0.4	0.4	0.984	0.199	16.49	1.071	0.208	12.88
0.7	0.3	0.3	1.033	0.207	16.81	1.098	0.212	13.01
0.8	0.2	0.2	1.082	0.214	17.12	1.126	0.216	13.14
0.9	0.1	0.1	1.131	0.222	17.42	1.153	0.220	13.26
mean value					16.11			12.74
standard deviation					0.95			0.36

length of the fibres. The two most practical and commonly used models for Young's modulus prediction are the rule of mixture [91, 92] and the Halpin-Tsai equation [93, 94].

$$E_{par} = E_f v_f + (1 - v_f) E_m \tag{2.12}$$

$$E_{pepr} = \frac{1}{\frac{v_f}{E_f} + (\frac{1-v_f}{E_m})} \tag{2.13}$$

$$E_{par} = E_m \frac{1 + 2\frac{l}{d}\mu_L v_f}{1 - \mu_L v_f} \tag{2.14}$$

$$E_{perp} = E_m \frac{1 + 2\mu_T v_f}{1 - \mu_L v_f} \tag{2.15}$$

Where $\mu_L = \frac{\frac{E_f}{E_m} - 1}{\frac{E_f}{E_m} + 2\frac{l}{d}}$ and $\mu_T = \frac{\frac{E_f}{E_m} - 1}{\frac{E_f}{E_m} + 2}$ and E_f and E_m are the Young's modulus for

the fibres and matrix respectively.
Equation 2.14 and 2.15 are a simplification of the Halpin-Tsai equation for fibre composites. The factor $2\frac{l}{d}$ is taking into account the packing order and shape of the fibres. In the original equation the parameter is called ϵ and it assumes different forms according to the reinforcement nature [91].

Since the SBCs are not real composites and it is impossible to know the elastic modulus of the two domains independently, E_f and E_m are two unknown variables and I need two more equations to calculate the hypothetical length of the fibres. I used the rule of mixture to calculate E_f and E_m and applied equation 2.14 to estimate a value for the average length of the styrene cylinders. The results are shown in Table 2.8.

Table 2.8: Results for SEBS20 and SEPS22 of the estimation of Young's modulus of the two domains of the block copolymers considered as matrix and fibres of a composite system, using the rule of mixture [91, 92]. The last column on the right shows the calculation of the average length of a fibre according to the Halpin-Tsai equation [93, 94].

	E_{par} (MPa)	E_{perp} (MPa)	v_{st}	E_{st} (MPa)	E_m (MPa)	D_{st} (nm)	μ_L	length (nm)
SEBS20	4.99	2.25	0.1907	18.25	1.865	16.11	0.00036	171000
SEPS22	6.32	2.74	0.2036	22.32	2.237	12.74	0.00159	31150

The average length estimated is much larger than the diameter. However, it could represent the mechanical response of a network of cylinders, rather than the length of one. The different values obtained for the two materials could explain the different mechanical and rheological behaviour. More details on the discussion are presented in chapter 3.

With the information above, it was also possible to approximate the volume of one cylinder and give an estimation of the number of chains packed in it. Using the polystyrene density from the literature (ρ_{PS}=0.969 g/cm^3 [90]) I calculate the weight of one polystyrene cylinder. The weight of the PS in one chain is given by the molecular weight of the SBC multiplied by the mass fraction of PS. The molecular weight and mass fraction were obtained from the GPC analysis. Since the SBCs considered are triblock, it must be decided if there is a possibility that two blocks of the same chain could be part of the same cylinder or not. In the second case, the weight of PS measured in one chain should at least be divided by 2. I continued the approximation

considering that only one block, with half monomers of the styrenic fraction of the tri-block copolymer, is part of one cylinder.

The weight of the cylinders divided by the molecular weight of styrene gave the number of moles in one cylinder. This number was divided by the number of moles in one chain to give the total number of chains in one cylinder. The moles of styrene in one chain was given by the number of monomers in a chain (given by the molecular weight of the chain divided by the molecular weight of styrene) divided by Avogadro's constant. Hasegawa *et al.* [95] studied the lamella microstructure of polystyrene-polyisoprene diblock polymers coupling SAXS and SANS (deuterium labelling) techniques. They could demonstrate the perturbation of chains within the different microphases, in fact they argued that there were no unperturbed chains. The lateral contraction or expansion was related to the repulsive forces present between the different blocks. The centre of the chains in a domain space are confined in a space within narrow interphases which are much smaller than the polymer dimension. This factor should be considered when estimating the number of chains packed in a cylinder. The results are summarised in Table 2.9. They are a reasonable approximation considering that high chain perturbation has been proven for BCPs, hence we expect a large number of chains.

Table 2.9: Calculation of the number of chains per cylinder of styrene and number of chains per unit cylinder volume for SEBS20 and SEPS22. V_{cyl} is the volume of one styrene cylinder, w_{cyl} is the weight of one cylinder, $Mw_{st,ch}$ is the molecular weight of a chain block of polystyrene, N_{cyl} and N_{ch} is the number of moles for a single cylinder and in one chain block respectively. The constants used are $\rho_{st} = 0.9075\ g/cm^3$, Avogadro's number $Na = 6 * 10^{23}$, $Mw_{st} = 104.15\ g/mol$.

	V_{cyl} (nm^3)	w_{cyl} (g)	$Mw_{st,ch}$ (g/mol)	N_{cyl} (moles)	N_{ch} (moles)	chains	chains/ volume
SEBS20	3.48e7	3.16e-14	10926	2.89e18	1.68e-22	1.72e4	0.05
SEPS22	3.97e6	3.6e-15	6875	5.24e19	1.06e-22	4.94e3	0.08

The cylinders in SEBS20 are one order of magnitude larger than SEP22, however the number of chains per unit volume is higher in the latter , according to this approximation. The consequences of these properties will be further discussed in the mechanical tests section in chapter 3. No definitive conclusions can be drawn from this approximation; however, it could be a good indication for material's comparison.

2.4 Conclusions

This chapter presented a thorough investigation of material properties. It was possible to accurately measure the styrene mass fraction and molecular weight, the lattice configuration of the crystalline phase and the domain spacing (d-spacing), glass transition temperatures and to have a good approximation for the order-disorder transition temperature.

It was demonstrated that the manufacturing method applied for the unitensile and flat sample and valve prototypes succesfully produced the desired parallel orientation. The information gathered with the aforementioned analysis will be considered when analysing the results obtained for the fatigue life prediction model. The mechanical performances of block copolymers are very complex and many structural parameters such as domain size and orientation, interdomain distances and molecular weight can influence the final properties.

The measurements obtained from GPC and SAXS analysis of SEBS20 and SEPS22 were used to calculate an approximate value for the cylinder diameter of the polystyrene domain. Both d-spacing and diameter were found to be larger for SEBS20. There is no consensus on an approach to evaluate the height of the cylinders. In this chapter I considered the materials as a fibre reinforced composite and reversed the Halpin-Tsai equation. According to this approximation, SEBS20 has longer cylinders compared to SEPS22 (171 μm and 31.2 μm respectively). However, there is no confirmation that the value obtained corresponds to a real height or if it represents a network of cylinders. Finally, the number of chains packed in a cylinder gave another comparison between the two materials. SEPS22 is more densely packed than SEBS20, according to this approximation. Further investigations should be carried out on the determination of the height of the oriented cylinders. The available techniques are not accurate enough to determine its value.

Chapter 3

Fatigue Model

3.1 Introduction

Fatigue is the principal mode of failure of polymeric PHVs. Over the last 50 years several materials have been considered and tested for this application. However, the limiting factor for the successful design of a polymeric valve has been durability. The ISO 5840-2015 standard requires 200 million cycles lifetime, which corresponds to 5 years of opening and closing of the valve's leaflets. This milestone can be achieved by a synergistic combination of design and material. The most durable material has to be manufactured in a shape that minimises the strain energy density, while retaining the desired mechanical properties for the valve to function (*i.e.* satisfactory opening and closing as per ISO standard).

Successive iterations of valve prototypes can be long and expensive, if shortcuts are not taken. A specific machine was built by TA instruments, the DuraPulse (Figure 3.10), able to run the valve at up to 30 Hz, for an accelerated fatigue test. However, a complete understanding of the link between the material's characteristics and fatigue properties cannot be achieved through this test. The most rigorous method is to build a fatigue prediction model for the material.

The method applied in this work is based on fatigue properties collected at relatively high strain, and then extrapolated to the lower strains present in a working valve; this allows the analysis to be done within a reasonable time-frame. It is based on the combination of crack growth and crack nucleation experiments. The model was able to provide a tool for selecting the longest lasting material for a heart valve prosthesis (and indeed would be able to do so for other low strain, long durability requirement applications). I was also able to include consideration of the different orientation of

the styrene domain within the leaflet.

Baxter *et al.* [101] used crack propagation resistance as a selection criteria for materials for a PHV made of fibres embedded in an elastomeric matrix. They measured the crack propagation rate for EPDM, silicone rubber and polyurethane. The study showed that crack propagation is an accurate method for screening and highlighted PU as the most resistant to crack propagation of the materials investigated. This is consistent with recent studies on advanced PUs for medical applications [27, 28, 29]. This category of materials are the most promising on the market so far, thanks to the good biocompatibility and resistance to calcification, coupled with the desired mechanical properties described in the aforementioned study. The Foldax valve, for example, is made of a modified PU, as described in the introduction. Concerns remain, however, about the long term stability of PUs in the body.

Brubert *et al.* [64] used crack propagation as a selection criteria for a PHV candidate material. The results were incorporated in the definition of a performance index for the valve, as described in section 2.1.4. The results showed that styrenic block copolymers are competitive with PU materials in terms of durability.

Elastomer fatigue has been extensively studied for natural rubber, SBR rubber, with and without additives and fillers, modifying molecular weight and several other variations [101-125,129,130]. This study focused on the validation of the unified Mars-Fatemi model [102] for anisotropic and isotropic styrenic block copolymers. The model was applied to simple standard geometries, such as the pure shear specimen and uniten-sile specimen, as well as the valve prototypes. The results presented in this chapter are divided according to individual factors affecting fatigue life.

3.1.1 Fatigue prediction models

Elastomers as well as TPEs are highly non linear elastic materials with large deforma-tions. Therefore, linear elastic and small strain assumptions typically used for metals do not apply to elastomers. With regards to fatigue failure, literature mainly refers to strain energy density, tearing energy and crack growth rate as driving parameters and these will be described in the following study .

Strain is the preferred choice for elastomers since is easily determined from dis-placements. Moreover, when defining the strain energy density, a hyperelastic SED function is often used, which is also defined by strain [103].

Rubber-like components subjected to fluctuating loads often fail due to the nucle-ation and growth of defects or cracks. The fatigue failure of rubber is thought to be

essentially a crack growth process from small flaws that nucleate in the bulk [104]. Thus, material deformation and fatigue characterisation including both crack nucleation and crack growth are typically required for fatigue analysis and prediction of fatigue life [103].

There are two main approaches to the prediction of the fatigue lifetime of elastomers. Crack nucleation is based on stress and strain quantities at a material point, according to continuum mechanics. The crack growth approach uses the initial geometry and energy release history of the crack to predict the lifetime [103].

Crack nucleation approach

This approach is based on the concept that the stress and strain history of the material at a point determines its intrinsic life. The crack nucleation life is determined by the number of cycles required for the growth of the crack up to a certain critical size. This method is particularly favourable for applications where the intrinsic flaw is significantly smaller (several order of magnitudes) than the component size. The fatigue life parameters used in this approach are maximum principal strain and strain energy density [103].

The first studies correlating experimental results on components' life to a strain energy density based model were performed by Gent Lindley and Thomas [104, 105, 106], followed by Lake and Lindley [109, 110, 112]. SED was defined as the measure of the energy release rate of a naturally occurring flaw. Researchers and engineers followed up applying such theories to different components and materials' life times. Mars [103], in his review , describes the main applications of the model in the last 60 years. The main focus was on tyre and car components. The main users of these models were in the rubber industry.

A big limitation for this approach is that the location and state of the critical crack should be known. This information is usually difficult, if not impossible, to obtain.

Crack growth approach

The crack growth approach was first developed and studied by Inglis (1912) and Griffith (1920). Inglis proposed a quantitative correlation between the geometry of the defect and the stress-state around it. He analysed a flat sheet with an elliptic crack under unidirectional stretch parallel to the main crack dimension. He predicted an infinite stress at the tip of a sharp crack, independent of the stress applied. Griffith looked to overcome the limitation of Inglis theory by solving the infinite-stress prediction with

an energy-based failure criterion [107, 139].

However, both their studies considered metals. It was Rivlin and Thomas in 1950s [106], who started to apply these theories on rubber materials. They focused on vulcanized rubber and three different types of specimen: edge-cracked sheet, centre-cracked sheet and trouser specimens. Their aim was to derive an energy criterion for rubber tearing that was independent of the test specimen used. They based their considerations and mechanical model on the Griffith's criterion.

Griffith stated that a cut of length a will increases by da at a determined overall deformation only if the decrease of elastic stored energy $-dW$ is greater than the increase in surface free energy due to the formation of new surface. The concept is represented in the equation:

$$-\left(\frac{dW}{da}\right) > T\left(\frac{dA}{da}\right) \tag{3.1}$$

Where dA is the area of the new surface, T is the surface free energy per unit volume and a is the crack size.

Griffith's approach implied that the quasi-static propagation of the crack could be considered a reversible process from the thermodynamic point of view [107]. However, Rivlin and Thomas [106] argued that the decrease of elastic stored energy with the creation of new surface for the increase in the cut length can also be balanced by other forms of energy instead of solely the increase in free-surface energy. The change of this energy has to be proportional to the length of cut growth and primarily determined by the state of deformation around the crack tip during tearing.

The state of deformation is dependent on the shape of the crack tip and the extension ratio. For these assumptions they considered a thin sheet of material where the crack length is large compared to its width and to the specimen thickness. In this way, the energy will be independent of the shape of the test-piece and of the deformation mode and can be considered a characteristic energy for tearing. Using this tearing energy (T) variable they defined the following energy balance. For a crack to grow by da, an amount of work $Tt * da$ must be done (where t is the thickness in the undeformed state). No extra work is done by external forces, which leads to the following free-energy balance:

$$-\left(\frac{dW}{da}\right)_l = Tt \tag{3.2}$$

Where l indicates that the differentiation is happening at constant displacement. The equation is similar to Griffith's criterion, except that T is not a surface-free energy.

In their paper [106], Rivlin and Thomas tried to validate the criterion for natural vulcanized rubber. They observed that even a small strain would make the cut grow by a noticeable amount from its tip and after a few hundredths of a millimetre catastrophic rupture will occur, making the crack grow by a few millimetres. They also defined that the point for measuring tear should be when catastrophic rupture occurs, and not before, since it is difficult to compare behaviour of different rubbers in the latter phase. Using this convention it is also possible to compare different test pieces.

They compared different specimen shapes of similar thickness for which they measured $\left(\frac{dW}{da}\right)_l$ and they found good agreement for different shapes of the same material, proving that tearing is a material property independent of shape.

I present here their analysis on the pure shear specimen, as shown in Figure 3.1 , where the length l_0 between the clamps is substantially smaller then the width of the specimen and also the cut is significantly larger than l_0.

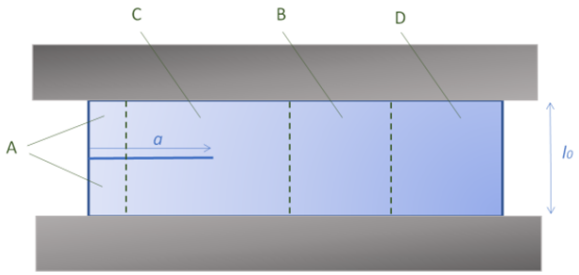

Figure 3.1: Schematic of pure shear test specimen adapted from reference [106].

When the specimen is deformed parallel to l_0, the region A remains undeformed, B is in pure shear and the region in between, C, is characterized by a complex strain state. D is not considered pure shear because it is close to the free-edge. For a fixed displacement λ, the cut grows by da causing the region A to increase at the expense of B. The respective volume transfer is calculated as $l_0 t * da$, where t is the thickness measured in undeformed state.

In the three principal directions, the extension ratio for the pure shear specimen are λ, 1 and $1/\ \lambda$; as a consequence the first and the second invariants are:

$$I_1 = I_2 = \lambda^2 + 1 + (1/\lambda^2) \tag{3.3}$$

And the change in stored elastic energy dW with da is given by $-W_0 l_0 t * da$, where W_0 is the elastic energy stored per unit volume in a state of pure shear given an extension ratio λ. W_0 was calculated using the stored energy function in terms of I_1 and I_2, but in general it can be obtained by graphical integration under the stress-strain curve for

the pure shear specimen. The final equation for this specimen is then:

$$\left(\frac{dW}{da}\right)_l = -W_0 l_0 t \tag{3.4}$$

The simplified version putting together equation 3.2 and 3.4 is:

$$T = W_0 l_0 \tag{3.5}$$

As part of their study, they considered a specimen with a small cut, as shown in Figure 3.2.

Figure 3.2: Schematic of unitensile specimen with small crack adapted from reference [106].

The specimen is designed with length much larger than width and the crack much smaller than the latter. If the cut was not present, the central part of the specimen would be in simple extension. With a small cut the region around it has a complicated strain state, while the central region away from the crack is still in simple extension. Furthermore, the area between the crack and the free edge is unstrained.

By dimensional analysis with an ideally sharp crack, they observed that the variation of the stored elastic energy caused by the presence of the crack is proportional to a^2. Moreover, if the classical elasticity theory is valid for the specimen tested, for each point the deformation has to be proportional to $(\lambda - 1)$ and dW to $(\lambda - 1)^2$ or W_0,which is the stored elastic energy in simple extension. These considerations lead to the equation:

$$W' - W = ka^2 t W_0 \tag{3.6}$$

Where W' is the energy without crack and W the energy after the formation of a crack a. k is a constant of proportionality and t is the thickness of the test piece. Even if for large strain the assumptions of classical elasticity theory are not valid, they found it convenient to use equation 3.6 and define k as a function of λ. They defined a criterion for T using equation 3.2, which gave:

$$T = 2kWa \tag{3.7}$$

The relationship between k and λ can in principle be found mathematically, but Rivlin and Thomas proved that the problem was intractable. Experiments, on the other hand, could not be accurate enough, since it would involve calculating k while measuring W and λ at various a, with a having only a few percentage variation with W, due to the assumption that the crack should be much smaller than the specimen width. This fact added to the small irreversibility of rubber elasticity made it very difficult for them to measure k accurately. They identified an interval of $2 < k < 3$ for the rubber [106].

Greensmith [108] developed a method to measure k involving only elastic properties. He measured k based on extension tests from 5 to 200% strain on vulcanized and cured rubber. The result is represented in Figure 3.3. The graph is used as an accurate guideline to determine values of k in this report.

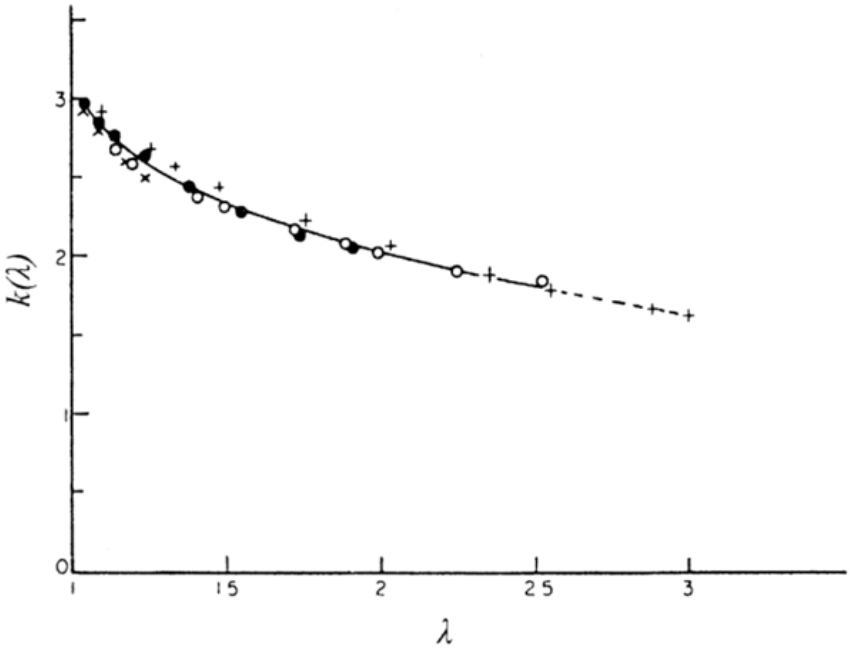

Figure 3.3: Values of k(λ) plotted against extension ratio. The results are for different types of vulcanized rubber. Picture taken from reference [108].

The data were approximated in terms of engineering strain (ϵ) [109]:

$$k = \frac{2.95 - 0.08\epsilon}{(1+\epsilon)^{1/2}} \tag{3.8}$$

The definition of J-integral by Rice [118] in 1968 gave another perspective on how to study the local crack tip conditions. Rice calculated the integral as the energy balance on a volume around the crack tip. He demonstrated that the integral calculation is independent of the integration path so the volume can be chosen close to the crack tip

or along the boundaries of the specimen. Hence, the J-integral can be both equivalent to the measure of the local crack tip conditions and to the energy release rate. This proved once again that the energy release rate is the measure of the intensity field surrounding the crack tip.

A significant study for the development of the crack growth approach was developed by Lake and Lindley [110] in 1965. They identified 4 different regimes for crack growth rate versus maximum tearing energy (T) for R=0, where R is the ratio of minimum to maximum strain. They tested natural rubber and SBR, as shown in their graph in Figure 3.4.

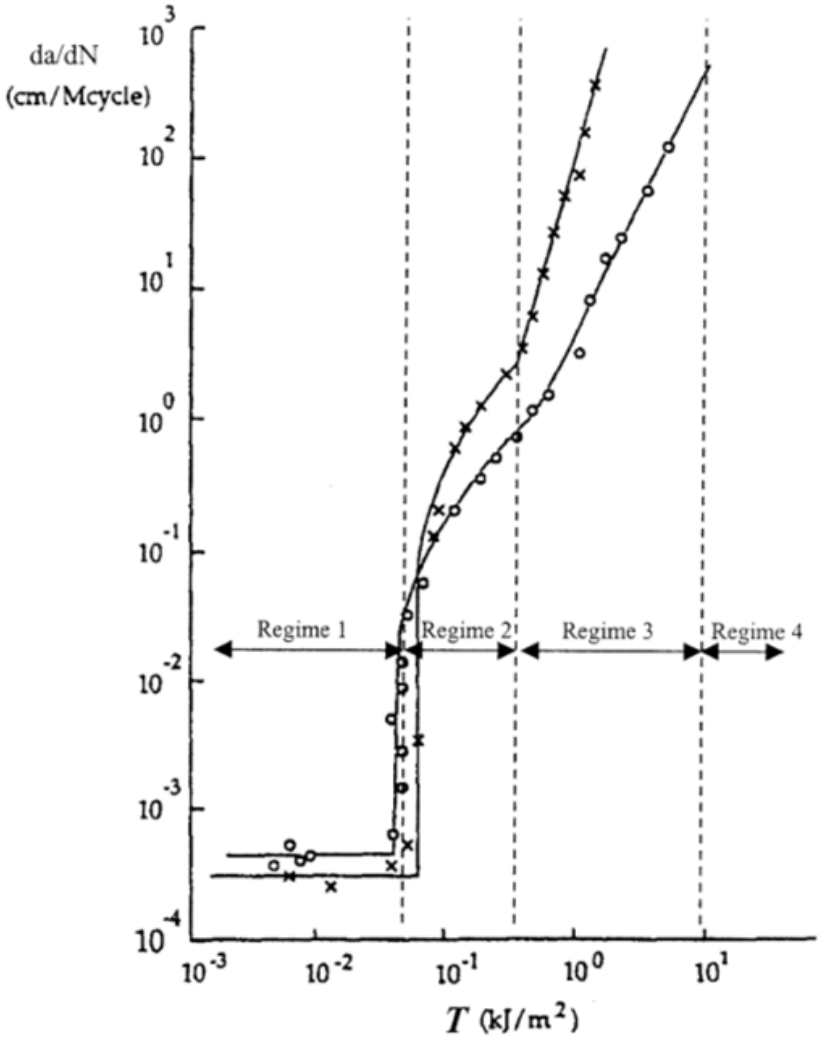

Figure 3.4: Regimes of fatigue crack growth behaviour in unfilled styrene-butadiene (x) and natural rubber (o) under R=0. Plot from reference [110].

They showed that below a certain threshold (T_0) the crack grows only because of environmental attack, independent of the mechanical loading, at a constant crack

growth rate. This is denoted Regime 1.

$$\frac{da}{dN} = r \qquad T < T_0 \tag{3.9}$$

Above T_0, three regimes were identified. The transition regime (2), between T_0 and T_t, where t signifies transition, over which there is a drastic change in the crack growth rate. The transition is described by the following relationship, in which A is a material property.

$$\frac{da}{dN} = A(T - T_0) + r \qquad T_0 \leq T \leq T_t \tag{3.10}$$

After the transition there is a range between T_t and T_c (critical tearing energy), over which the relationship between the fatigue crack growth rate and the energy release rate obeys a power-law. This is denoted Regime 3, where B and F are the fatigue power-law coefficient and exponent for R=0 condition, respectively.

$$\frac{da}{dN} = BT^F \qquad T_t \leq T \leq T_c \tag{3.11}$$

Finally, beyond T_c, unstable crack growth ensues. This is Regime 4 and it is where the crack growth rate is essentially infinite.

$$\frac{da}{dN} = \infty \qquad T = T_c \tag{3.12}$$

Crack growth threshold T_0

Lake and Thomas (1967) [111] further investigated calculation of the T_0 threshold, below which no crack propagation occurs in the absence of chemical attack. Their calculation gave a T_0 of 50J/m^2. They also showed that the value for T_0 varies only slightly with chemical composition and does not depend on the viscoelastic properties of the materials or strain crystallization.

This value for T_0 suggested that the energy was mainly determined by primary bonds. They observed, however, that the energy required to break the bonds across the crack plane is much lower than experimental values they found in the literature for different rubber samples. For natural rubber, the energy to break a single bond, considering a cross sectional area of 2*10^{-16} cm^2 and C-C dissociation energy is 5*10^{-19} J, is around 2 J/m^2 which is less than 1/20 of the experimental value.

They argued that this calculation is too simplified for complex cross-linked materials. When considering highly elastic materials, one has to consider that the plane

of the crack growth in front of the crack tip is going to be crossed by several chains crosslinked at different sides of the plane. They described the situation around the crack tip with a schematic showed in Figure 3.5 where L is the displacement vector between two crosslinked chains and n is the number of monomer units contained in that part of the polymer chain.

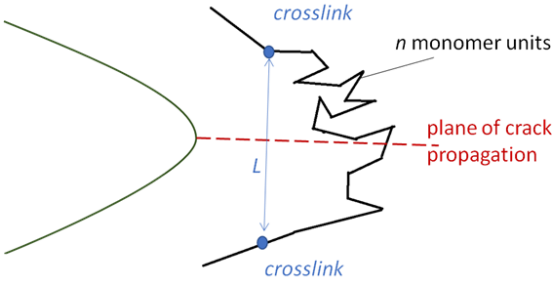

Figure 3.5: Diagram representing a polymer chain of n-monomer lying across the crack propagation plane. Schematic adapted from reference [111]

Considering that forces are transmitted mainly through the crosslinking network, for one single bond to break all the other bonds lying in the same chain must be subjected to the same force. Hence, the total mechanical breaking energy will be greater than that required for a single bond. If U is the energy for single bond rupture, then nU is the energy required to break a chain of n monomers. They suggested the following equation for T_0:

$$T_0 = \frac{1}{2}\bar{L}N\bar{n}U \tag{3.13}$$

Where L is the average vector, n the average number of monomers in the chain considered and N is the number of chains per unit volume.

They compared the value for their theoretical result for T_0 (see paper for accurate calculation) with experiments on natural rubber and found reasonable agreement for the cases analysed. The small discrepancy between the values is explained by neglecting the secondary forces and to the relaxation of deformed chains. They also argued that the theoretical value takes into account the sharpest possible tip, while in real experiments "the tip can become rough". The real value of T_0 can also be higher due to the breakage of the chain before the main crosslinks, followed by an increase in the tip diameter.

Flaw growth model for crack nucleation

An integrated approach was studied by Mars and Fatemi [102] who used a power law model to describe nucleation and growth of the crack. The crack growth model was applied to predict fatigue lifetime of unitensile samples. The model works very well if small defects are considered, where it is possible to assume that the energy release rate is proportional to strain energy density and crack size.

This unified approach is based on the integration of the power-law equation, considered as a good shortcut for the entire life of the flaw, for the fastest growing crack from its initial to final size. They used unitensile and pure shear specimens for crack nucleation and crack growth respectively. They decided to focus on unitensile specimens since these are designed such that once the crack reaches ca 1 mm there would be little life remaining until complete failure.

For crack growth tests they used the energy release rate as the parameter driving crack propagation, since it better correlates the general specimen loading conditions with the strain field at the local crack tip for elastomers. The pure shear specimen is a practical choice for the experiment since the tearing energy is independent of crack length and it has a simple relationship with SED (equation 3.5). SED is calculated as the integral of the stress-strain curve of an uncracked specimen; the calculation is done taking into account Mullins effect (transient softening), hence the integral is measured after more than 100 cycles.

Mullins effect, also known as preconditioning or initial softening, happens because of breakage of linkages between chains within the material. The effect is transient and after several stress-strain loops (approx. after 30 cycles for most elastomers) the non-linear elastic response stabilises [113]. The combination of equation 3.7 and 3.11 gave:

$$\frac{da}{dN} = f[T(a,W)] = BT^F = B(2kWa)^F \tag{3.14}$$

which was integrated from the initial (a_0) to the final (a_f) crack size:

$$N_f = \int_0^{N_f} dN = \int_{a_0}^{a_f} \frac{1}{f[T(a,W)]} da = \int_{a_0}^{a_f} \frac{1}{B(2kW)^F} a^{-F} da \tag{3.15}$$

$$N_f = \frac{1}{F-1} \frac{1}{B(2kW)^F} \left[\frac{1}{a_0^{F-1}} - \frac{1}{a_f^{F-1}} \right] \tag{3.16}$$

From the first integration, considering that the final crack size is much larger than the

initial size, the following simplification is applicable:

$$N_f = \frac{1}{F-1}\frac{1}{B(2kW)^F}\left[\frac{1}{a_0^{F-1}}\right] \tag{3.17}$$

Furthermore, by integrating expression 3.11 the maximum permitted strain energy density to avoid failure, W_{max}, can also be obtained:

$$W_{max} = \left[\frac{1}{F-1}\frac{1}{BN_f}\left(\frac{1}{a_0^{F-1}} - \frac{1}{a_f^{F-1}}\right)\right]^{\frac{1}{F}}\frac{1}{2k} \tag{3.18}$$

Mars and Fatemi [102] assumed a_0=0.02 mm, k=2, with B and F obtained from the crack growth rate experiment to calculate the number of cycles to failure according to equation 3.17. The value was compared to the results from the nucleation test and good agreement found between the two methods. Another paper from Zarrin-Ghalami and Fatemi [113] reports the same analysis technique and good agreement is again reported.

3.1.2 Unified fatigue model for the PHV application

There is no study in the literature concerning the application of the unified Mars-Fatemi model, or any other fatigue approach, to intrinsically anisotropic materials, or styrenic block copolymers. The literature focuses on the fatigue life prediction and crack growth propagation of fiber reinforced materials, which is the closest case to that of the block copolymer anisotropy [114]. However, further investigations on anisotropic block copolymers are needed in order to have a robust fatigue life prediction for these materials and extend this knowledge to the prediction of the valve lifetime.

If the TPEs are considered as two-phase nanocomposite, as suggested by Buckley *et al.* [115], it means that the mechanical behaviour should be determined by three factors: the dispersed volume fraction of the hard phase, the mechanical coupling of the phases and their individual mechanical properties. The mechanical coupling of the phases happens at a nm scale and leads to a complex 3D stress distribution. Moreover, anisotropic materials will have a different behaviour and phase mechanical interaction according to the strain direction with respect to the domain orientation. This effect is difficult to capture in a macroscopic model without conspicuous simplifications. Experimental data can be used as guidance to adapt the model applied for isotropic rubber materials to the more complex multiphase block copolymer systems.

The model has been applied on standard samples, as per the Mars and Fatemi

method [102] described in the previous section, and transferred to predictions for the valve geometry. This was possible thanks to several simplifications valid for the valve application. Firstly, the main principal strain direction is circumferential in the valve leaflet system, which is comparable to uniaxial loading studied by Mars [102]. Secondly, the loading ratio R (*i.e.* the ratio of the minimum and maximum loads) can be considered 0 for the valve, since there is complete relaxation of the leaflet during closing at the end of the strain cycle . An R ratio different than zero can imply several other mechanism affecting fatigue, which have been extensively studied in the literature for rubber material [102, 113, 116]. Strain crystallizing polymers have beneficial effects on lifetime with increasing minimum load, while non crystallizing material often have the opposite [116]. Mars and Fatemi [113] studied a modified power-law equation which takes into account the R-variation.

$$\frac{da}{dN} = r_c \left(\frac{T_{max}}{T_c} \right)^{F(R)} \tag{3.19}$$

where the power-law parameters depend on R and there is a reference value of critical tearing based on Lindley's estimation for fatigue crack growth in natural rubbers (T_c=10 kJ/m^2). It was not necessary to use a similar equation for the valve application. Hence, crack growth and uniaxial crack nucleation were also performed at R=0 load ratio. This allowed characterization of the materials and comparison with the findings of Lindley *et al.* [109]. Moreover, the study of the fatigue behaviour of this group of materials concentrates on low strain fatigue, since the valve runs at very low strain (maximum of 20% [16]). This excludes effects like strain crystallisation.

Other factors affecting lifetime

As Mars presented in his review [116], there are several factors influencing the lifetime, which make it difficult to find a general method for the life time prediction of TPEs and rubbers in general.

Load history is one of the most important aspects to take into consideration. Complex load histories are difficult to represent with a single set of parameters. For the valve prediction method, we can assume a simple mechanical load mode that works until valve failure. The valve runs continuously for an indefinite number of cycles, so it is not necessary to consider down time for the fatigue for this application. Even the variations of heart beat rate and volume are quite limited and can be neglected. There are no static loads involved in the valve fatigue life. I can also exclude the effect of strained rest periods from the mechanical modelling. Internal stresses derived from

injection moulding can be present though and these would fall into the category of prior load history. At this stage of the model design, this aspect has been neglected.

The waveform of the stress cycle was a sinewave for all the tests, in order to approximately mimic the actual opening and closing of the valve.

It is well known that frequency can have an effect on fatigue life, depending on the type of polymer. It has been shown [116] that frequency has a larger effect on amorphous rubber, while for strain crystallizing rubber it has been observed to have less effect. Hertzberg *et al.* [117] demonstrated that frequency sensitivity is higher in polymers with crazing tendency. The crazing phenomenon is characteristic of glassy polymers, such as PMMA or PS, and it leads to the formation of microvoids, especially on the surface, that can precede failure. They reported that polystyrene showed a significant improvement in fatigue resistance with increasing frequency. Most of the tests performed on the materials are at 1 Hz. However, the accelerated durability test for the valve prototypes (see section 3.2.2) runs at 30 Hz to achieve hundreds of millions of cycles in a reasonable amount of time. Only tests performed at the same frequency were compared. Further study should follow to investigate this aspect.

Environmental conditions can influence the performance of the polymers under fatigue loading. Temperature and chemical reactants play both a crucial role in the life time of the material. It is well known that high temperatures are detrimental for TPEs [116]. In this study all the tests have been performed at 37°C, the average body temperature, in order to better represent the condition inside the human body. Hence, a temperature factor was not included in the mechanical model for the fatigue life prediction.

The valve is exposed to the chemicals contained in blood, among them are calcium and oxygen. It is difficult to accurately estimate the concentration of these, since it is patient specific. Mechanisms such as oxidation and calcification should be considered when selecting a material for the valve application. Oxidative aging causes polymers to become brittle and reduces their resistance to crack growth. Oxidation of SBCs will be considered in future studies.

This thesis focuses only on calcification, which is performed in a blood simulating calcium solution (more details in chapter 4). However, the prediction and the mechanical model do not include this factor, since the mechanical test set up for both valve and standard samples included only RO water and air respectively. Moreover, a standard procedure for calcification experiments is still lacking, making it very complicated to include such factors in a mechanical model. It is also not clear if mechanical failure in the valve is enhanced by polymer calcification or calcium deposits. This topic is

discussed in detail in chapter 4.

Finally, a heparin coating was applied on the valve prototypes and standard specimens. The coating has the property of improving the blood compatibility of the material, a very important requirement to avoid platelet activation and coagulation. When blood comes into contact with synthetic or biomaterial surfaces, multiple reaction mechanisms are triggered. The reaction cascade can lead to severe consequences for the patient, such as thrombosis, thromboembolic complications and inflammation [127].

Bernacca *et al.* [128] reported that heparin surface modification improved the durability of two polyurethane valves (PEU and PEUE) without compromising leaflet thickness and hydrodynamic function. In this study, I investigated whether the same effect applies to the SBCs considered in this work. A set of coated samples and valves was compared to uncoated specimens, in terms of durability, by applying the unified prediction model described above.

Initial crack size

The most critical parameter of the prediction model in equation 3.17 is the initial crack size a_0. Its value is calculated as a fitting parameter for the crack growth and crack nucleation experimental results for each material and orientation. The initial crack size is intended to correspond to the size and shape of a naturally occurring flaw [103]. The nature of the flaws is not always well identified; they can derive from fillers, agglomerates, manufacturing techniques, voids, mould lubricant, imperfections in the mould surface, or a combination of these factors.

Lake and Lindley [112] studied different polymer types and various fillers and compounds to measure the initial flaw size; they found that their pool of materials had an initial flaw size in the range of 0.02 and 0.06 mm. However, it has been shown that the life time of the polymer is not only influenced by the flaw size, but also by the number of flaws per volume, their density and distribution, as reported by Abraham [130].

He defines a Effective Flaw Size (EFS), which combined with the stress concentration factor and strain energy density was used to simulate fatigue. The EFS is calculated from fatigue data and fracture mechanics where a stress intensity factor and dynamic strain energy density were defined to simulate both relaxing and non-relaxing test condition of rubber materials for high and low strain [130]. Micro CT before testing gave shape, size and distribution of naturally occurring flaws. During testing the CT showed that the cracks initially grow independent of each other, until they cross

paths and start interacting and combining into a bigger crack. In the light of this fact, when calculating or measuring the initial flaw size, it would not be accurate to simply use the largest flaw. In fact, the relevant size would be the one in the most highly stressed volume element where fewer smaller flaws in proximity can act as if they were a bigger flaw. For fatigue life analysis it is also fundamental to consider other factors regarding the flaws, such as their geometry, distribution and number [130].

A complete flaw size/distribution analysis makes the mechanical fracture simulation impossible, since it would be necessary to know the 3D description of all flaws at a micrometre level in the whole test part. Even if there was a straightforward method to collect all these data, the simulation of the fracture mechanism would be extremely time intensive. Taking this approach would lead to a very expensive and impractical method. A simpler method is necessary to calculate the effective flaw size.

In order to address this problem, Kingstone *et al.* [131] introduced a reference tearing energy in equation 3.17. In this way, the other material parameters took a simple dimension of length increment per cycle. They picked T_{ref} as 1 kJm^{-2} since it is an average value for most rubbers in the middle of the crack growth regimes. They found that filled natural rubber has higher a_0 (as expected since filler clusters and agglomerates can act as crack initiators) and more scatter in the results. Furthermore, the effective flaw size seemed to be dependent of the strain amplitude and they suggest taking the fit to the flaw size from low-strain fatigue measurements.

In conclusion, the definition of the initial crack size is still not fully understood. Values obtained from fitting to experimental fatigue results do not directly represent the size of a naturally occurring flaw, but a group of factors influencing the lifetime of the material. Not only the source of the defects, but also their location has an impact on durability. The orientation of the styrenic domain is also expected to strongly influence the value of this parameter.

3.1.3 Finite element model for anisotropic block copolymers

Finite element modelling simulations have been used to map the strain distribution in the valve leaflet and to calculate the maximum strain energy density as an input to the lifetime prediction model of equation 3.17.

The mechanical behavior of TPEs is described by a hyperelastic constitutive law. In the case of rubber-like material, the incompressibility condition is assumed, which means:

$$J = det(\mathbf{F}) = \lambda_1\lambda_2\lambda_3 = 1 \tag{3.20}$$

Under this condition, the strain energy density can be written as:

$$W = W(\mathbf{C}) - p(J-1) \tag{3.21}$$

where $\mathbf{C}$ is the right Cauchy–Green tensor, and p is the hydrostatic pressure. Serrani *et al.* [67] further divided the strain energy density into isotropic and anisotropic contribution:

$$W = W_{iso}(\mathbf{C}) + W_{aniso}(\mathbf{C}) \tag{3.22}$$

The isotropic part was described by a Mooney–Rivlin stress– strain relationship and is represented in terms of $\mathbf{C}$ invariants as:

$$W_{iso}(\mathbf{C}) = c_1(I_1 - 3) + c_2(I_2 - 3) \tag{3.23}$$

where c_1 and c_2 are the material parameters to be identified experimentally. The anisotropic part was defined by:

$$W_{aniso}(\mathbf{C}) = W_{aniso}(I_4) = k_4(log\sqrt{I_4})^2 \tag{3.24}$$

where k_4 is a material's parameter obtained from mechanical tests on unitensile samples. Serrani [67] defined I_4 as a pseudo-invariant of $\mathbf{C}$ which reproduces the cylinders' orientation through the unit vector $\mathbf{u}$.

$$I_4 = \mathbf{u}_0 \cdot \mathbf{C}\mathbf{u}_0 = \mathbf{u}^T \cdot \mathbf{u} \tag{3.25}$$

where $\mathbf{u}_0$ and $\mathbf{u}$ represent the cylinders' direction in the undeformed and derformed configuration respectively. This make I_4 the measure of the square of the stretch along the cylinders' direction.

Equation 3.23 and 3.24 together give the strain energy density for anisotropic materials:

$$W = c_1(I_1 - 3) + c_2(I_2 - 3) + k_4(log\sqrt{I_4})^2 - p(J-1) \tag{3.26}$$

Dr M. Serrani performed the simulations of the valve reported in this study using ABAQUS. The constitutive law was implemented in the software using the UANISOHYPER subroutine. To simulate isotropic materials the anisotropic contribution was dropped.

3.2 Materials and Methods

3.2.1 Materials

The materials studied for fatigue performances and modelling are described in chapter 2. In addition to the list of materials for leaflet applications, I also measured the fatigue prediction equation for natural rubber. I used this result as a basis for comparison, since most of the research on fatigue has been developed for rubber materials. The natural rubber was provided by Tun Abdul Razak Research Centre.

The unitensile and pure shear specimen samples and polymeric PHV prototypes were manufactured according to the procedure described in chapter 2. Samples were coated with two different heparin coating technologies, described in the section below.

Heparinisation

Polymeric samples (both valve and unitensile specimen) were coated with two different coating technologies: CHC™ Corline Heparin Conjugate kit (Corline®,Uppsala, Sweden) and ASTUTE®Advanced Heparin Coating (BioInteractions Ltd.,Reading, UK). The CHC™ Corline Heparin Conjugate is a pre-assembled aggregate of heparin molecules. The coated surface is formed of macromolecular heparin covalently attached via a heterobifunctional crosslinker to an inert polyamine carrier chain.

The surface heparinisation of the samples was done in the CEB laboratory following the procedure given with the do-it-yourself coating kit. The main steps are summarised in Figure 3.6. The coating process involves first surface preconditioning to form a cationic layer on top of the uncharged synthetic material using PAV (polyallylamine). The heparin complexes were then coupled to the polyamine through ionic interaction by contact with the water based CHC coating formulation (60 minutes). The ratio of heparin to polyamine chain is 70/1. These two steps were repeated and followed by acetylation. The samples were rinsed in MQ-water and dried in air before further testing.

The ASTUTE® coating was done by BioInteractions Ltd. in Reading, UK. It is composed of a hydrophilic priming layer where the sulfonate bearing groups (PEG) and the heparin molecules are covalently attached. The priming layer consist of a modified polyethyleneimine [127]. Their coating protocol is not publicly available.

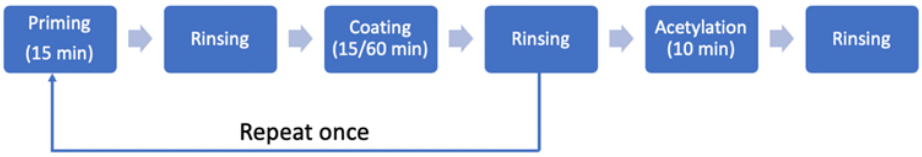

Figure 3.6: Schematic process overview of CHC™ Corline Heparin kit (Corline®,Uppsala, Sweden) coating process. The procedure was supplied by the manufacturer.

3.2.2 Methods

The mechanical tests on the different types of prototypes were all conducted at 37°C to simulate average body temperature. Furthermore, a load ratio R=0 was applied to crack growth and crack nucleation tests.

Planar mechanical test

A cyclic incremental test on a pure shear specimen (Figure 3.7) was performed to obtain the cyclic stress-strain curve ($\sigma(\epsilon)$) and the strain energy density function (SED(ϵ)). The tests were performed using Stable Microsystems Texture Analyser (Stable Microsystems, UK) in displacement control with a sinusoidal waveform at 1 Hz using a 30 kg load cell. The specimen was positioned between the two clamp fixings, with 10 mm of material within each clamp. Because of Mullins effect stabilized cycle data were used for each strain level (*i.e.* after 40 cycles) and the incremental steps were performed from 10% to 100% strain and reverse, for 200 cycles at each step. The

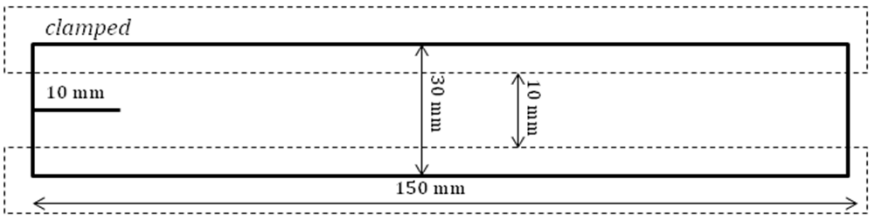

Figure 3.7: Pure shear specimen geometry.

applied displacement was then converted into gauge section strain and the measured load from the load cell was used for stress calculation. A MATLAB (MATLAB, The MathWorks, Inc.) routine was used for post processing of the data. To calculate the Young's modulus (E) the stress-strain curve was fitted with a second order polynomial equation (hyperelastic model). The slope of the initial linear part of the curve is the

elastic modulus, which is represented by the parameter relating to the second term of the equation.

The SED was calculated as the integral under the engineering stress-strain curve. The strain energy density function was obtained fitting the data of SED plotted against strain with a quadratic equation. The function was then used to calculate the SED from strain measurements for the crack growth test. For every material at least six tests were performed and the final values were taken as the mean value of all tests.

Crack growth test

A precracked planar tension specimen (Figure 3.8 and 3.7) is typically used for fatigue crack growth tests since energy release rate is independent of crack length for this specimen geometry [103]. In this experiment the crack growth rate was measured against the tearing energy at different strain levels.

The crack growth test was performed in the Stable Microsystems Texture Analyser (Stable Microsystems, UK) in displacement control, with a sinusoidal waveform at 1 Hz. The specimen was positioned in the same manner as for the planar mechanical test and pre-cut with a razor blade, as shown in Figure 3.8. The cut had to be sharp and parallel to the clamp.

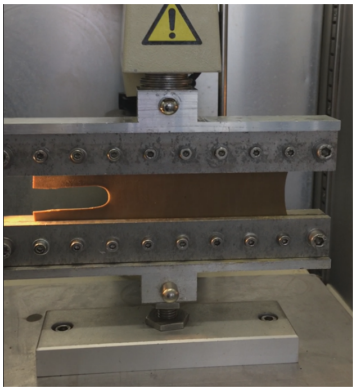

Figure 3.8: Stable Microsystem Texture Analyser during crack growth test.

A single specimen can produce results for multiple crack tests at different loading conditions since tearing energy is independent of crack size for the pure shear specimen geometry. This is valid as long as the crack length and remaining specimen length are sufficiently longer than the specimen height. If the crack grew irregularly or at an inclined angle, re-cutting was performed by a razor blade, followed by some initial cycles to initiate a natural crack tip.

A 110% maximum strain was implemented as preconditioning for 300 cycles at each strain level in order to produce a natural crack tip as well as to minimise the transient deformation response. Because of transient softening, tests on each specimen were conducted in ascending order of strain levels.

For each material, different strain levels and cycles were used in the experiments, the detailed protocol depending on the material behaviour: the general guideline was to apply a number of cycles sufficient to produce significant crack growth, so for lower stresses a higher number of cycles was required.

A camera was used to measure the growth of the crack tip along the crack line. A collection of 10 pictures was taken every 100 seconds, so when analysing the data the number of the pictures could be assigned to the number of cycles.

Fatigue crack growth rate (da/dN) is obtained by fitting a linear relationship to the crack length versus cycles data and determining the slope of the linear fit. Numerical integration methods can be used to calculate the area under the stress-strain curve from the experimental data. For a constant displacement or strain, strain energy density is constant and so the crack growth rate would be constant with repeated cycles of the same amplitude [103].

The test conditions used for the constant amplitude fatigue crack growth experiments produced crack growth rates in the region that can be characterized by a power-law relation (equation 3.11) and linear relation (equation 3.10) The materials' parameters of the two relationships (B, F and A) were calculated fitting all the results at different strain levels of crack growth rate versus tearing energy with the respective functions. Matlab (MATLAB, The MathWorks, Inc.) was used for the data processing.

Crack nucleation test

Uniaxial tensile specimens were used for crack nucleation tests. Multiple samples were clamped in the Stable Microsystems Texture Analyser (Stable Microsystems, UK) (Figure 3.9) and stretched at 1 Hz with sinusoidal waveform to complete failure. The criterion for defining fatigue nucleation life in the test is the number of cycles at which the specimen breaks completely according to ASTM standard D 4482. Preconditioning cycles ($\sim$40) were conducted to account for the transient softening effect. Tests were performed in displacement control and different levels of maximum strain were chosen for testing. Since each material behaves differently, different number of cycles were chosen for each test in order to reach failure in a reasonable time.

For each specimen the SED at fracture was calculated as the integral of the engineer-

Figure 3.9: Unitensile samples mounted on the Stable Microsystem TA for crack nucleation test.

ing and real stress-strain curve. The nucleation points (Nf vs SED) were used as fitting parameters for equation 3.17 to obtain the initial defect value a_0. Matlab (MATLAB, The MathWorks, Inc.) was used for the data processing. The test was performed on SEBS20, SEPS22 and MED500400 for different thicknesses, coatings, geometries and orientations. The anisotropic samples were tested in parallel and perpendicular cylinder orientation with respect to the principal strain direction.

Valve accelerated fatigue test

An accelerated fatigue test was performed on the valve prototypes to calculate the number of cycles to failure. Figure 3.10 illustrates the instrument used for the test. The ElectroForce® DuraPulse™ (TA instruments, DE, USA) is an instrument specific for prosthetic heart valve durability test and complies with ANSI/AAMI/ISO Standard 5840. Three stations were used for the test allowing 6 valves to be tested at the same time since every station has 2 valve chambers. Each chamber is independently controlled and fully see-through to allow the user to control the test valve. The valves were mounted in the chamber with a silicone ring to set the valve in position. The chamber was filled with distilled water to reduce impurities in the instrument.

An extra rigid ring (Figure 3.11) was mounted on the valve prototypes used for the rigid stent experiment described in section 3.3.4. The ring was 3D printed (Form 2, Formlabs, USA) with a hard resin. The valve posts were inserted into specific compartment in the ring in order to block their bending during fatigue cycles.

The test conditions were set up using the WinTest® software package (included with the instrument). The same software was used for data acquisition and continuous

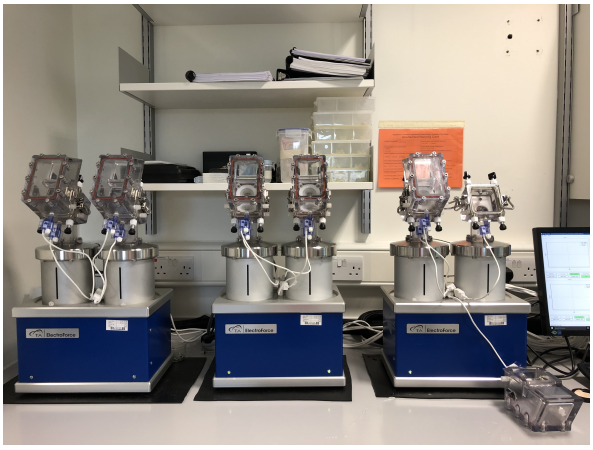

Figure 3.10: ElectroForce® DuraPulse™ (TA instruments, DE, USA). A total of 6 valves could run at the same time.

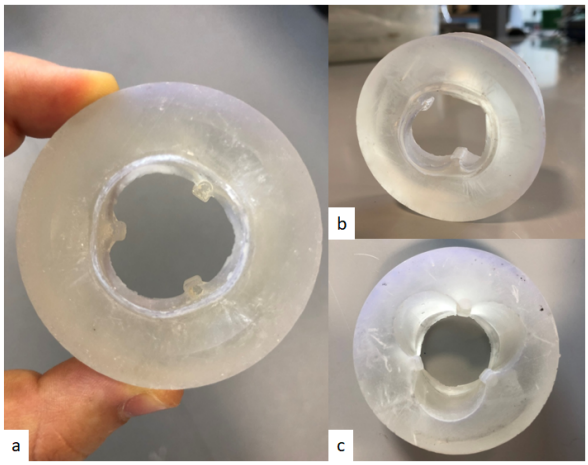

Figure 3.11: 3D printed rigid ring for valve rigid stent experiment. a- bottom view, where the post inserts are visible;b- side view; c- top view showing extra cavity to allow the opening of the leaflets.

monitoring of the test parameters. The software records the number of cycles performed by the valve.

The test was run according to the requirement of the ISO 5840:2015. The target pressure was set at 100 mmHg difference across the closed aortic valves for a minimum of 5% of every cycle, maintained for more than 95% of the total number of cycles. Temperature was set at 37°C to simulate the condition of the human body. The high-frequency testing capabilities of the instrument allowed testing to be run at 30 Hz.

Valve failure was determined by visual inspection with a stroboscope or by monitoring abnormal proximal and distal pressure traces.

Pulse Duplicator

The pulse duplicator is the most used *in vitro* cardiovascular hydrodynamic testing system to assess the performance of cardiovascular devices and prosthetic heart valves.

The system in Figure 3.12-a was built by De Gaetano [176, 137] in the laboratory of the Department of Chemical Engineering and Biotechnology (University of Cambridge, UK). The instrument replicates the physiological pressure, stroke volume and flow of the left ventricle in the human heart. It consists of a servo-electrically controlled pump, an aortic valve housing, a ventricular chamber, a systemic impedance simulator and a mitral valve housing.

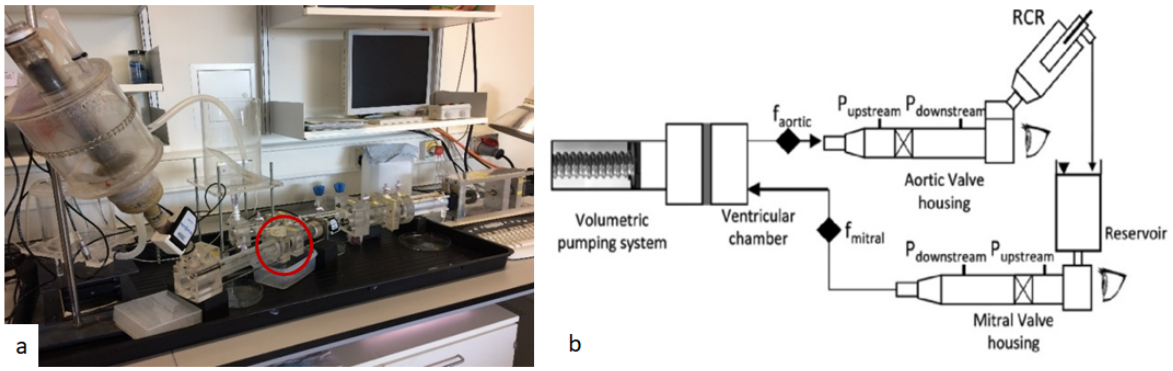

Figure 3.12: a- photo of the Pulse Duplicator of the Department of Chemical Engineering and Biotechnology (University of Cambridge, UK), the red circle indicates the polymeric valve housing; b- schematic representation of the pulse duplicator.

As illustrated in Figure 3.12-a and b, the polymeric valve was placed in the aortic position, while a tilting disc bileaflet mechanical valve was mounted in the mitral position. The aortic and the mitral valve housing were connected with straight Perspex tubing (35 mm diameter) to the systemic impedance simulator and to the ventricular element respectively. A thin silicone membrane (0.3 mm thickness) was positioned between the pump and the loop to isolate the piston and prevent damage to the mechanical system, while the rest of the instrument was filled with water.

The pumping system was set with a systolic flow rate replicated by the Swanson and Clark waveform [140] and a modified Talukder and Reul [141] flow rate waveform for diastolic flow rate.

The test conditions were set at 70 bpm frequency, 5 l/min simulated cardiac output and 35% systolic duration at normotensive conditions, conforming to ISO 5840:2015 requirements.

Flow and pressure measurements were recorded upstream and downstream from

the tested valve. A transit-time ultrasound flowmeter (HT110 series, Transonic System Inc, Ithaca, NY, USA) measured the flow rate in two different positions. A large probe positioned downstream of the valve measured the systolic peak flow (ca 25 l/min), a small probe (maximum volume 20 l/min) upstream measured the backflow to calculate the valve regurgitation.

Pressure ports were positioned 35 mm upstream and 105 mm downstream from the aortic housing (140PC pressure sensors, Honeywell Inc, Freeport, IL, USA). The instrument had transparent viewpoints which allow direct visual observation of the valve during the test.

Polivalve prototypes were tested at different flow rates and back pressures, as required by the UNI EN ISO 5840 Standard. Transvalvular pressure drop was measured at variable flow rates (2 l/min, 3.5 l/min, 5 l/min and 7 l/min) and constant frequency (70 bpm). Regurgitation volume was calculated at a mean flow rate of 5 l/min at three different frequencies (45 bpm, 70 bpm, 120 bpm). At each frequency, three backpressures were tested (80 mmHg, 120 mmHg, 160 mmHg) [6].

3.2.3 Finite element modelling

Finite element modelling simulations were implemented to calculate the maximum strain energy density for the valves tested in the Dura Pulse (TA instruments, DE, USA). An example of unitensile oriented sample was also simulated to verify the optimisation of the model parameters. Dr Marta Serrani ran the valve simulations on ABAQUS.

Experimental data for the model implementation, as described in section 3.1.3, were obtained from uniaxial tensile tests (Stable Microsystem TA, UK) on unitensile samples (Figure 2.11-b). Samples were tested up to 100% strain at 1 Hz, according to the ASTM standard D882. A minimum of 1000 cycles were performed to reach a reproducible stress–strain behaviour between two subsequent cycles. The anisotropic materials were tested in both parallel and perpendicular directions with respect to strain. At least three samples were tested for each material and orientation. Sample manufacturing is described in chapter 2.

As described in equation 3.26, three material parameters have to be identified for the anisotropic case (c_1, c_2, and k_4) and two parameters for the isotropic case (c_1 and c_2). Serrani *et al.* [67] wrote a MATLAB (MATLAB, The MathWorks, Inc.) routine to optimise the parameters using a nonlinear least-square algorithm to match data from experimental mechanical tests. The parameters were input in the ABAQUS

nonlinear implicit FE algorithm to solve the numerical problem. A separate subroutine was used to define the material's equation for the anisotropic material, which included parameters k_4 for the two main directions.

For the anisotropic case, the vector $\mathbf{u}_0$ defined the cylinders' orientation in the reference configuration. We were already in possession of detailed mapping of orientation, hence $\mathbf{u}_0$ was defined according to the SAXS pattern described in chapter 2. The orientation of the cylinders was assigned at the centre of each element of the mesh. Since the number of elements was much greater than the number of points scanned on the leaflets, the orientation was assigned with a proximity criteria.

3D models of the PHV leaflet and unitensile sample were designed by CAD software RHINOCEROS 5 (Rhinoceros, Robert McNeel and Associates, Seattle, WA). For the valve the rigid stent was assumed, as simulated in the experimental results in the Dura Pulse. In the FE simulation, the rigid stent effect was set with a boundary condition of no displacement at the commissural surface of the leaflet. The simulation consisted of closing of three leaflets, which also allowed verification of the correct representation of the contact of the leaflets at the free edge.

The pressure load was set as uniform on the leaflet surface and two different back pressures were modelled (100 and 70 mmHg). For the unitensile sample I set a 50% elongation to match the experimental results. A quasi-static loading condition was assumed [**?**].The leaflet geometry was discretized in up to about 60,000 hexahedral linear elements to perform the FE analyses. Specifically, three elements were placed across the leaflet's thickness to correctly model the structure bending. The unitensile sample mesh consisted of up to about 5500 hexahedral linear elements. The final outcome of the FE simulation was the nodes' locations and the value of maximum strain energy density.

3.3 Results and Discussion

3.3.1 Planar mechanical test

The results from the planar mechanical test are summarised in Table 3.1. The anisotropic materials SEBS20 and SEPS22 have parallel and perpendicular orientations reported separately, as the mechanical properties significantly change from one direction to the other. This is confirmed by the values obtained for the Young's Modulus. The perpendicular orientation of both SEPS22 and SEBS20 are much softer compared to the parallel counterpart, as expected. A similar situation is seen in fibre composite mate-

rials: when the strain is parallel to the fibre the material is stiffer [114, 132].

The ratio of Young's modulus is 2:1 between parallel and perpendicular orientations and both orientations are stiffer than isotropic SEBS (*i.e.* MED500400). Natural rubber and MED500400 have comparable values. The strain energy density function also varies significantly according to orientation. This is reflected in the calculation of the SED for the crack growth test at different strain levels and the definition of the parameters B and F of the power law equation.

Table 3.1: Strain energy density function defined by second order equation experimental parameters and Young's modulus E (MPa) for SEPS22, SEBS20, MED500400 and Natural rubber.

	SED function			E
	a	b	c	(MPa)
SEPS22 parallel	1.426	0.723	-0.032	6.32
st.dev.	0.144	0.249	0.006	0.70
SEPS22 perpendicular	0.841	0.175	-0.008	2.75
st.dev.	0.103	0.151	0.007	0.41
SEBS20 parallel	1.419	0.280	-0.010	4.99
st.dev.	0.238	0.215	0.011	0.78
SEBS20 perpendicular	0.615	0.167	-0.009	2.23
st.dev.	0.061	0.021	0.001	0.17
MED500400	0.406	0.079	-0.002	1.07
st.dev.	0.073	0.020	0.001	0.01
Natural rubber	0.325	0.088	-0.003	1.07
st.dev.	0.005	0.002	0.001	0.01

3.3.2 Crack growth test

The parameters for the lifetime prediction equation (3.17) B and F were obtained from linear fitting of the crack growth data at different strain levels. The results for the tested materials are plotted in the graphs of Figure 3.13. The anisotropic material SEPS22 and SEBS20 were tested with the cylinders oriented parallel and perpendicular with respect to the strain direction. The fitting produced the values for F and B listed in Table 3.2, the errors are represented in the confidence and prediction band plotted in Figure 3.13.

Table 3.2: Experimental results of the power law fitting to the crack growth results for SEPS22, SEBS20, MED500400 and natural rubber.

	B	F
SEPS22 parallel	3.57e-5	1.464
SEPS22 perpendicular	1.37e-5	2.064
SEBS20 parallel	2.29e-5	2.852
SEBS20 perpendicular	3.63e-4	1.759
MED500400	3.15e-4	3.278
Natural rubber	8.65e-5	1.322

In order to understand the distinct behaviours of the materials tested, I plotted selected examples of the materials' slopes in different groups. For the valve application, the more suitable materials should have a steep slope and minimise the value of crack growth velocity at low tearing energy, at which the valve will function.

Figure 3.14 shows a group of isotropic materials. The values for SEPS22 comes from reference [133]. The isotropic samples for SEPS22 were obtained via solvent casting in THF.

MED500400 has a higher molecular weight than SEPS22, and a predicted spherical microstructure. The result is a steeper slope. On the other hand, higher styrene content and lower molecular weight for SEPS22 resulted in lower crack growth velocity for the same tearing energy levels. Which of the two factors have more influence on the crack growth cannot be easily determined from this comparison. Moreover, the two materials have a different rubber matrix. It can be hypothesised, at this stage, that the higher fraction of styrene constitutes a bigger impediment for the crack growth. All three materials seem to converge at low tearing energy, possibly indicating the beginning of the transition regime. It is known from the literature that the transition tearing energy threshold for natural rubber is approximately 50 J/m^2 [111]. The natural rubber tested in this work has an intermediate behaviour in terms of crack growth velocity, but shows a flatter slope than the SBCs. The effect of physical crosslinking of styrene is comparable to the chemical crosslinking of vulcanization for the natural rubber, which can explain why the SBCs show a similar behaviour. Figure 3.15 and 3.16 show the crack profile at the end of the test. Both natural rubber and MED500400 show a linear smooth profile.

In Figure 3.17 I compare MED500400 with SEBS20 and SEPS22 with cylinders oriented parallel to strain. The two latter materials have very similar styrene fraction

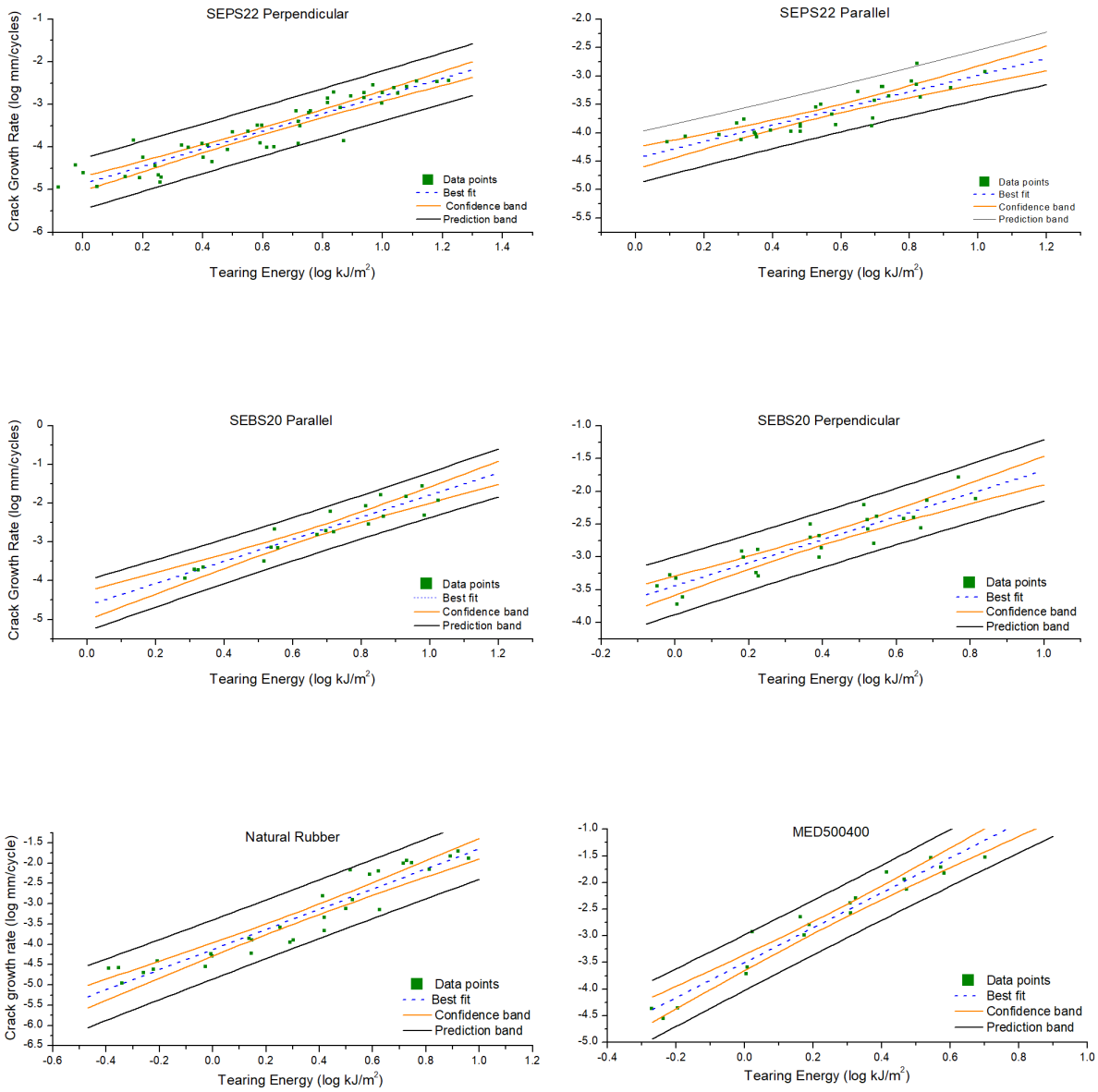

Figure 3.13: Tearing energy (kJ/m^2) versus crack growth rate (mm/cycle) for SEBS20 and SEPS22 parallel and perpendicular, MED500400 and Natural rubber. The plot for each material show the experimetnal points, the best fit, the 95% confindence band and the prediction band.

but SEBS20 has higher molecular weight. The two SEBS materials (SEBS20 and MED500400) have almost identical slopes: however MED500400 has higher molecular weight, lower styrene fraction and spherical morphology. It is clear that increasing styrene fraction moves the slope to the right and increasing molecular weight might shift the slope up and left. I represented this trend in the scheme in Figure 3.18. SEPS22 presents a very different slope compared to SEBS20, a combined effect of

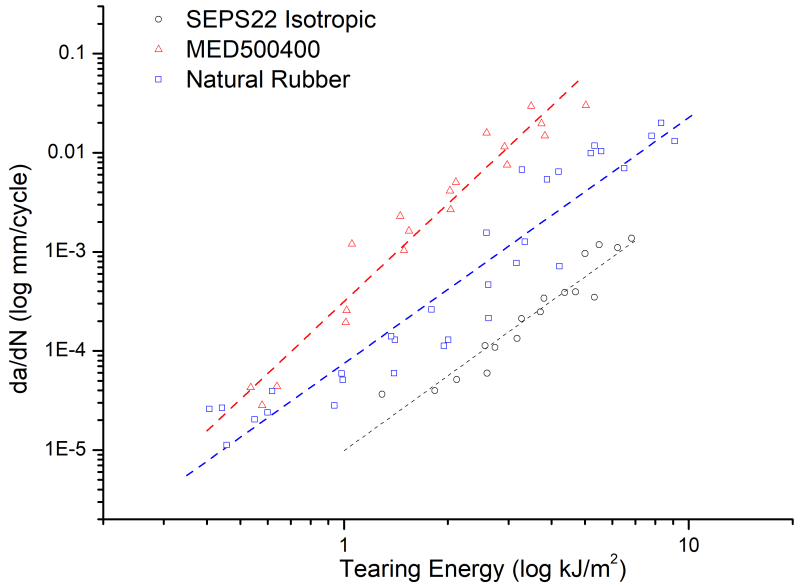

Figure 3.14: Crack growth slope for isotropic materials SEPS22, MED500400 and natural rubber. The dashed line represents the best fit for the experimental points.

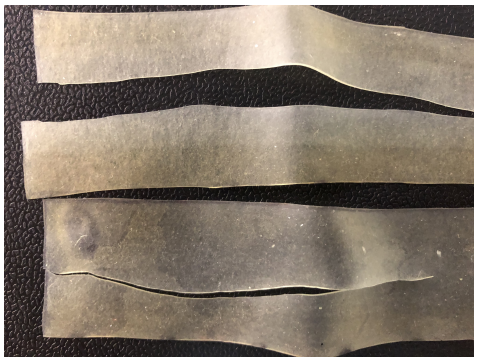

Figure 3.15: MED500400 compression moulded pure shear samples after crack growth test. The material is isotropic and shows a smooth linear crack path profile.

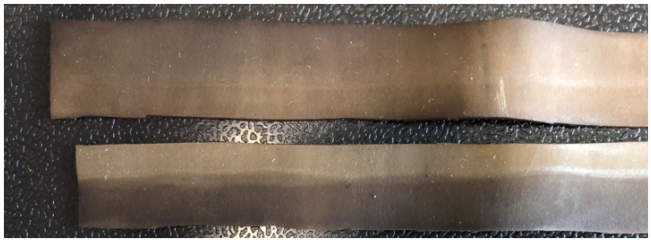

Figure 3.16: Natural rubber compression moulded pure shear sample after crack growth test.

different molecular weight and chemical composition of the rubber matrix (-EP- vs -EB-). However, they meet at T 1.5 kJ/m^2, a tearing energy that produces a similar behaviour for both materials.

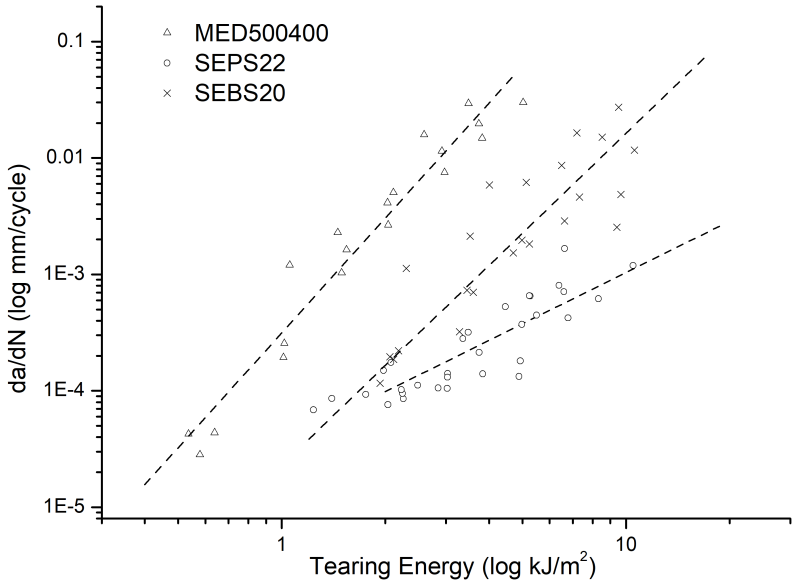

Figure 3.17: Crack growth slope for parallel oriented SEPS22 and SEBS20 and isotropic MED500400. The dashed line represents the best fit for the experimental points.

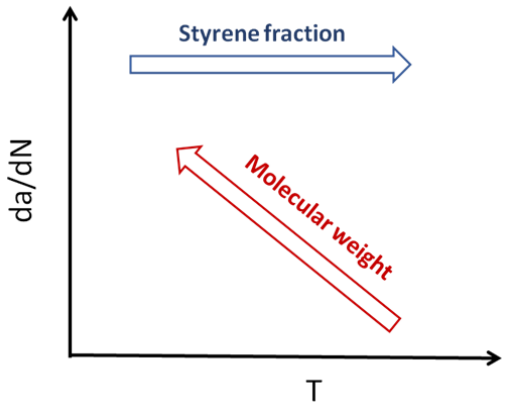

Figure 3.18: Schematic representation of the effect of molecular weight and styrene fraction on the position of the crack growth slope for styrenic block copolymers.

The effect of styrenic cylinder orientation is better represented in Figures 3.19 and 3.21. The graph in Figure 3.19 shows the comparison between parallel and perpendicular orientation of the cylindrical domain for SEBS20 and SEPS22. The slopes for each

material are quite close to each other, more so for SEPS22 than SEBS20. The main difference between the two opposite orientations is the slope of the crack growth versus tearing energy. It is also noticeable that the slopes for both perpendicular orientations are almost parallel to each other. The crack growth rate seems to differ more between the two materials when considering the parallel orientation of the cylinders.

The SBCs can be compared in this case to short fibre reinforced composites. For this class of material, crack growth rate and path are influenced by fiber orientation. It was found that the rate of crack propagation perpendicular to aligned fibers is much slower than that parallel to fibers when compared at the same energy range. The fibers perpendicular to the crack propagation direction block crack growth. On the other hand, fibres parallel to the crack path assist crack propagation as reported in several studies [134]. Tanaka *et al.* [134] also demonstrated that for short fibre reinforced polymers, the crack growth prediction of different orientation angle for the fibres fell on the same line when crack growth velocity was plotted against intensity factor (K) over Young's modulus ($\Delta K/E$) instead of only ΔK, as was done in previous studies. This underlines the fact that the crack velocity is strongly correlated with stiffness, which is connected to orientation as shown in Table 3.1 This is consistent with what I found for parallel and perpendicular orientations.

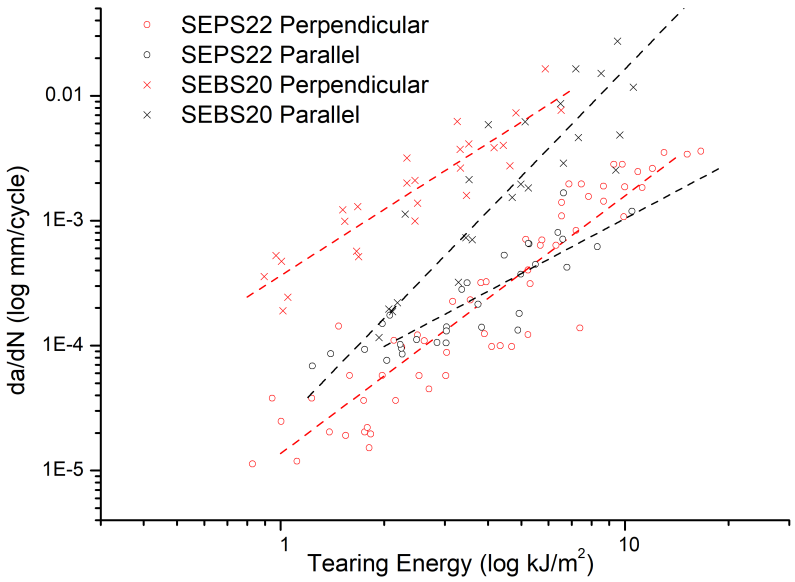

Figure 3.19: Crack growth slope for parallel and perpendicular orientation of SEPS22 and SEBS20. The dashed line represents the best fit for the experimental points.

In the perpendicular case, the crack propagates along the plane of the initial crack,

which mainly involves the rubbery matrix. The cylinders (*i.e.* fibres) are not stretched and the matrix is subjected to elongation. This determines the crack path, which as shown in Figure 3.20-b, follows a smooth linear profile across the matrix. This leads to the hypothesis that the slope of the crack growth is less influenced by the matrix composition, since they are parallel to each other in Figure 3.19. However, the chemical composition can still influence the position of the data points in the graph.

The crack path for the parallel orientation has two options: crossing the cylinders or going around them . Figure 3.20-a shows the crack profile of SEBS20 at the end of the test. It looks like the crack grows along the initial crack plane at the beginning and then starts bending in a curved line. The crack path is blocked by the cylinders and changes direction every few millimetres to go around them. The result is an irregular saw-tooth profile. However, at higher tearing there could be enough energy to break the cylinders: in fact, at the end of the crack in Figure 3.20-a, highlighted in red, which corresponds to higher strain, the "tooth" is less pronounced and the profile becomes more linear.

For composite materials, the crack path is highly influenced by the volume ratio of fibre: below a certain threshold the crack follows the initial crack plane direction, while for higher ratios the crack follows the orientation of the fibres [135]. In this case the crack does not regularly follow the path of the cylinders and changes direction. Increasing styrene fraction and molecular weight could lead to this effect also in the SBCs.

In the case of cylinder forming SBCs, the crack growth velocity is much more influenced by the length, size and packing of the cylinders, which are also dependent on the molecular weight and styrene fraction of the two materials. The value for the cylinder's length has been estimated in chapter 2. Nevertheless, the possibility that all cylinders are interconnected over long distances cannot be excluded. This aspect should be investigated further in future.

SEBS20 has a larger d-spacing and cylinder diameters, according to the results obtained in chapter 2, which could explain why SEBS20 has a higher crack velocity. According to the findings for short fibre reinforced composites, the crack is slowed down by the cylinder barriers parallel to the crack front. Hence, the crack should grow faster if there is more space for the crack to grow between cylinders. As is clear for SEBS20, where all the data collected for the perpendicular orientation sit at higher crack velocity values, after a critical tearing energy the cracking of the parallel orientation starts to move faster, potentially representing a faster fragile fracture of the glassy polystyrene domain. We can imagine that SEBS20 slopes for the parallel

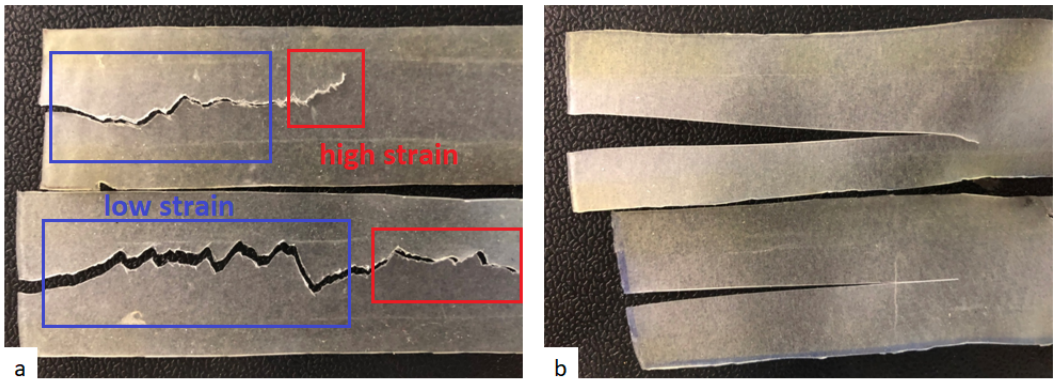

Figure 3.20: Pure shear specimen samples after crack growth test, after stretching at increasing strain levels. The samples are compression moulded and cut SEBS20. a) SEBS20 with cylinders parallel to the strain direction, the blue square highlights the saw-tooth profile at low-medium strain (up to 70%) and the red square represent the higher strain (up to 100%) for which a more linear profile is noticeable; b) SEBS20 with cylinders perpendicular to the strain direction, represented by a smooth crack line.

and perpendicular orientation will intersect at the "fast-fracture" tearing energy level.

The behaviour for SEPS22 is inverted; at lower tearing energy the perpendicular orientation crack proceeds at a slower velocity. The trend changes at a lower tearing energy compared to SEBS20 and there is a large area of the graph where the crack growth behaviour is similar for both orientations. For SEPS22 the orientation influence is more obvious at high or low tearing energy level. At tearing energy in the interval 2-7 kJ/m^2, the crack velocity is similar for isotropic, parallel and perpendicular oriented cylinders, as shown in Figure 3.21. If the application of the Halpin-Tsai equation (chapter 2) to calculate the length of the cylinders represents a realistic approximation of an average length, then the shorter SEPS22 cylinders could be the explanation of the similar behaviour for the three orientations: the path around the cylinders is similar for all directions of crack growth.

Crack growth velocity was measured at low strain for the parallel orientation of SEBS20 and SEPS22. This energy range is modelled by the transition regime, which is reported in the literature as:

$$\frac{da}{dN} = A(T - T_0) + r \tag{3.27}$$

where the parameters A and T_0 are characteristic of the material and, where present, orientation. The last parameter r represents a constant value of crack growth rate accounting for environmental factors. Theoretically, below a certain level of tearing

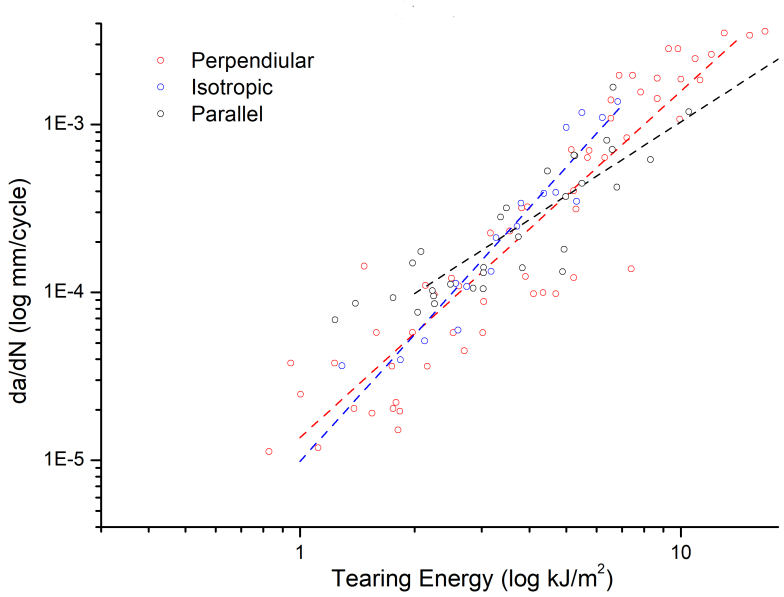

Figure 3.21: Crack growth slope for parallel, perpendicular and isotropic SEPS22. The dashed line represents the best fit for the experimental points.

energy the crack will stop growing, however in real life, environment always plays a role in the growth of the crack (oxygen or ozone attack for example). For the purpose of our application and the derivation of the life time prediction, the value of r has been neglected. The calculation of r requires long tests and specific equipment. Moreover, the aortic valve environment is very complex. Correct measurement of r for the PHV application purpose would require a specifically designed test. The parameters are summarised in Table 3.3.

Table 3.3: Parameters A and T_0 of the transition law for SEBS20 and SEPS22 parallel oriented.

	A	T_0
SEPS22 parallel	1.2e-5	0.15
SEBS20 parallel	9e-6	0.02

The grey area in Figure 3.22 marks the transition tearing energy, where both materials' slopes converge. Crack velocity decreases faster and from higher T for SEBS20, which is consistent with the power law behaviour. The SEPS22 profile is flatter throughout the transition regime, confirming the hypothesis of shorter paths around the cylinders, which is not strongly influenced by the change in tearing energy.

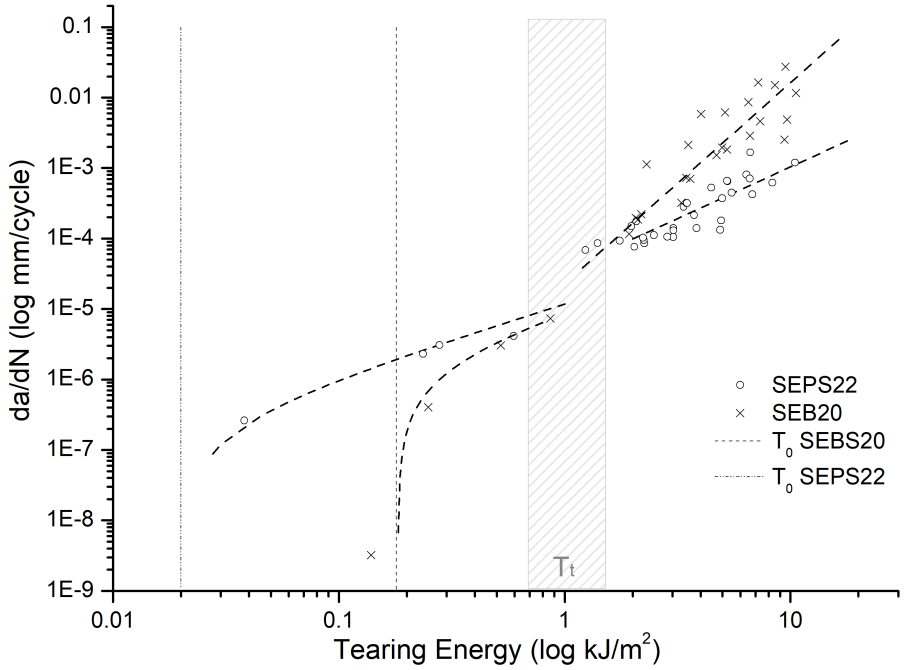

Figure 3.22: Crack growth versus tearing energy profile of transition and power low regime for SEPS22 and SEBS20 parallel oriented. The vertical dashed line on the low tearing end are the calculated T_0 values, the grey box at 1 kJ/m^2 is the predicted transition tearing energy, a precise value was not calculated. The dashed line is the best fit for the experimental points.

T_0 is predicted to be an order of magnitude different between the two materials, which could be the effect of molecular weight and cylinder spacing. The T_0 can be theoretically calculated as the energy to break the bonds in an n-monomer chain between two crosslinks, as described in section 3.1.1. Hence, if the molecular weight is higher also T_0 is expected to increase.

From the above consideration for the calculation of T_0, one would expect that, when the energy for the complex bond-crosslinks to break is reached, the crack should grow indefinitely. However, catastrophic fracture occurs at much higher tearing energy. Lake and Thomas [111] pointed out that catastrophic crack growth is governed by the mechanical hysteresis properties of rubbers. A hypothetical rubber with no hysteresis should have a vertical relationship between T and da/dN. In reality, every rubber undergoes hysteresis to different extents. They explained that, once T_0 is reached the crack growth is governed by the extension stress-strain relationship for the material. As the crack grows, the area surrounding the tip undergoes relaxation, which in turn follows the retraction stress-strain curve. High hysteresis can lead to lower strain at the crack tip compared to the case of perfectly elastic materials, meaning that it will be

more difficult to grow a crack. Thus the hysteresis properties of the material directly influence the crack propagation rate compared. SEBS20 has lower hysteresis than SEPS22 and hysteresis also depends on the orientation of the cylindrical domain.

In order to collect more data points at lower strain, the use of a traveling microscope would be required; for this reason these data have not been acquired in this study.

3.3.3 Crack nucleation test

This section presents the application of the prediction model to unitensile specimens and valve prototypes. The initial crack size parameter is calculated by fitting equation 3.17 to crack nucleation points in the number of cycles to failure versus strain energy density plot.

As explained in section 3.1.1, parameter k is calculated from equation 3.8. The average value for the unitensile specimen was kept at 2.4, while for the model application to the valve geometry k=2.8.

The prediction line has the slope fixed by F, while the intercept is changed by both B and the initial crack size a_0. As explained in the introduction, the initial crack is the defect that initiates the failure and has a specific size for each material tested. I will demonstrate in this work that other factors influence the value of the initial crack size of the material. Changing the position of the intercept in the graph significantly affects the predicted number of cycles to failure. Hence, it is of paramount importance to verify which material and geometry variables to consider when applying the model. This section describes the effect of orientation of the styrenic cylindrical domain, thickness, geometry, manufacturing technique and heparin coating on the final calculated value of the initial crack size. Finally, I compared the result for the different materials to establish which is the best candidate for the valve application.

Parallel versus perpendicular

The graphs in Figure 3.23 show the comparison between parallel and perpendicular orientation of the styrenic domain with respect to the strain direction for SEBS20 and SEPS22. For both materials, the lines for the two orientations cross at a specific SED level (100 MPa and 2 MPa for SEPS22 and SEBS20 respectively). Below a certain SED, one orientation is predicted to last longer than the other. If we consider the SED range for PHVs simulated with finite element modelling for our designs and materials (0.02-0.06 log MPa) [6], the predicted durability differs up to two orders of magnitude between the two orientations. These results must be taken into account in the valve

design process. For example, a valve made of SEBS20 should have the styrene cylinders predominantly parallel to the strain direction. This test has been performed only on 1 mm thick specimens, the initial crack size and consequently the crossing point of the two lines might shift for different thicknesses, as will be explained in the following section. However, we can be confident with this conclusion, since it would take an unreasonable a_0 value to move the crossing point below the calculated SED value for PHVs.

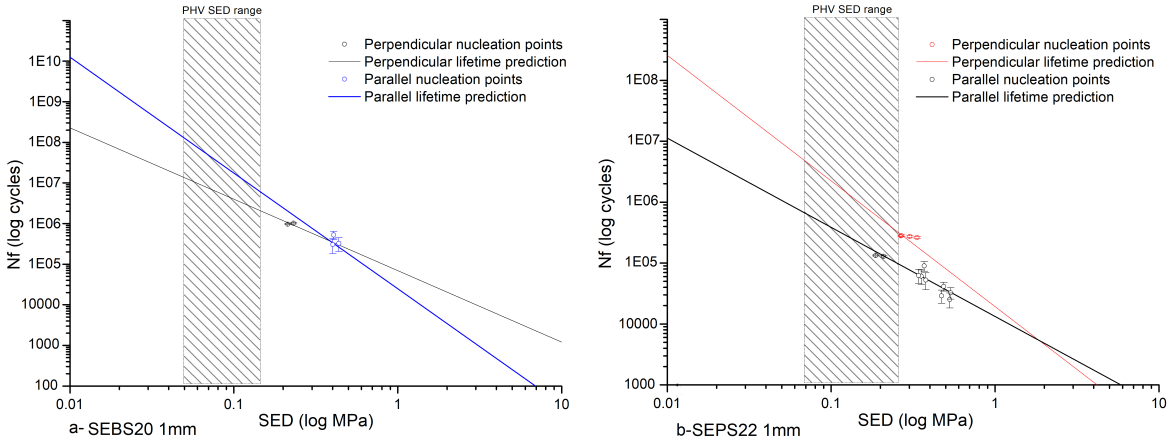

Figure 3.23: Lifetime prediction model for unitensile samples with cylinders parallel and perpendicular to the strain direction. The grey box represent the SED range for the valve made of the respective material. The samples were cut with a die from an injection moulded sheet. (a)SEBS20, (b)SEPS22. Error bars represent standard deviation.

Table 3.4: Initial crack size values for parallel and perpendicular orientation of SEPS22 and SEBS20.

a_0 (mm)	SEPS22	*st. dev.*	SEBS20	*st. dev.*
Parallel	0.184	0.02	0.087	0.004
Perpendicular	0.149	0.013	5.3e-4	6e-5

For this test I used die-cut specimens taken from the same injection moulded sheet for both orientations, in order to minimize the factors influencing the initial crack size. The correct orientation was confirmed by SAXS imaging. In this case, we can assume uniform defect sizes and distributions for both orientations. However, the results for a_0 differs substantially for the two orientations in both materials. When the SBC is

stretched with the styrene parallel to the strain, the stress concentrates on the styrene cylinders and fatigue failure is driven by flaws in this phase. In the perpendicular case, the load is supported by the rubber matrix, for which a different intrinsic flaw size is expected. This result is confirmed by the a_0 value reported in Table 3.4. The initial crack size values obtained for SEBS20 differ two order of magnitude from one direction to the other. The parallel orientation has a much larger a_0, indicating that the styrenic domain constitutes a larger source of defects and more brittle material. A similar trend is observed for SEPS22, albeit the difference is much smaller. The fact that the first material had a more pronounced discrepancy between the two directions can be related to the size of the styrenic glassy domain. The smaller SEPS22 cylinders had less impact in the anisotropic performance in terms of defect size and concentration. Moreover, the prediction line is steeper for the parallel direction in SEBS20, while it is the opposite for SEPS22.

Figure 3.24 shows SEBS20 specimens after the test. The crack for both orientations and the secondary cracks on the edge are identical for the two materials.

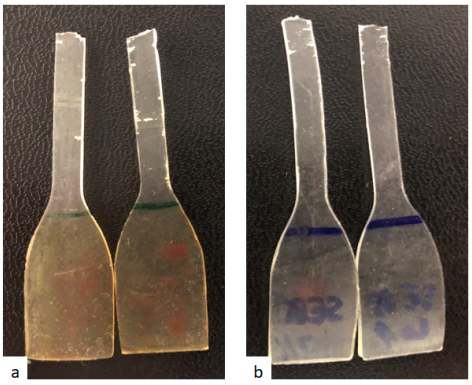

Figure 3.24: SEBS20 broken unitensile samples; the samples were cut from an injection moulded sheet with a ISO37-type 2 sharp cutting die. a- samples with styrene cylinders perpendicular to the strain direction b- injection moulded samples with styrene domain parallel to the strain direction.

Thickness effect

The effect of specimen thickness on the initial crack size was investigated by testing unitensile specimens of different thicknesses. The most commonly used thickness for standard specimens is 2 mm. However, a polymeric valve leaflet should not be thicker than 0.45 mm, even with the softest material (see section 3.3.7). Hence, the prediction model had to be validated with varying specimen thicknesses.

Figure 3.25 shows the comparison between 1 mm and 2 mm specimen thicknesses with the styrenic domain parallel to the strain direction for SEPS22. There is enough difference in SED and number of cycles to failure for the different thicknesses to justify separate fitting of the power law equation for the two sets of samples. The calculated values of a_0 for 1 mm are almost half of the values for 2 mm, as shown in Table 3.5. This is consistent with defining a_0 as the representation of the probability of a flaw of a particular size being present in the volume of sample experiencing the maximum strain energy density. If we assume a uniform distribution of defects in a small hypothetical layer, adding up layers increases the probability of a defect being present . Moreover, a larger volume allows for larger defect formation.

Table 3.5: Initial crack size values for 2 mm, 1 mm and 0.7 mm thickness specimen for SEPS22, SEBS20 and MED500400.

a_0	SEPS22	*st. dev.*	SEBS20	*st. dev.*	MED500400	*st. dev.*
2 mm	0.387	0.009	0.133	0.01	-	-
1 mm	0.184	0.02	0.087	0.004	-	-
0.7 mm	-	-	0.038	0.005	0.22	0.003

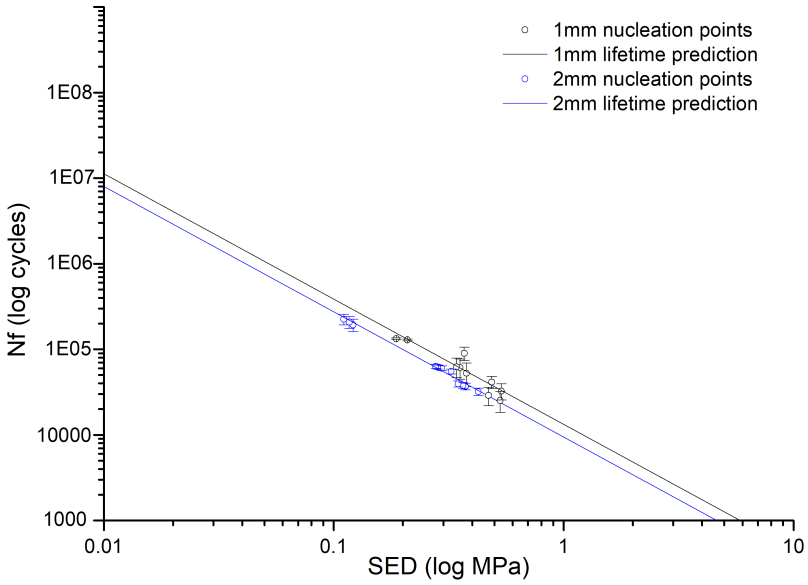

Figure 3.25: Lifetime prediction for 1 mm and 2 mm thickness unitensile specimens made of SEPS22 with cylinders oriented parallel to strain direction. Error bars represent standard deviation.

The effect is even more evident when decreasing thickness down to 0.7 mm, as

shown in Figure 3.26 for parallel oriented SEBS20. The calculated initial crack size decreases with a similar trend to SEPS22. Further discussion of this point is given in section 3.3.5. In order to assess if thickness also influences parameters B and F (as well

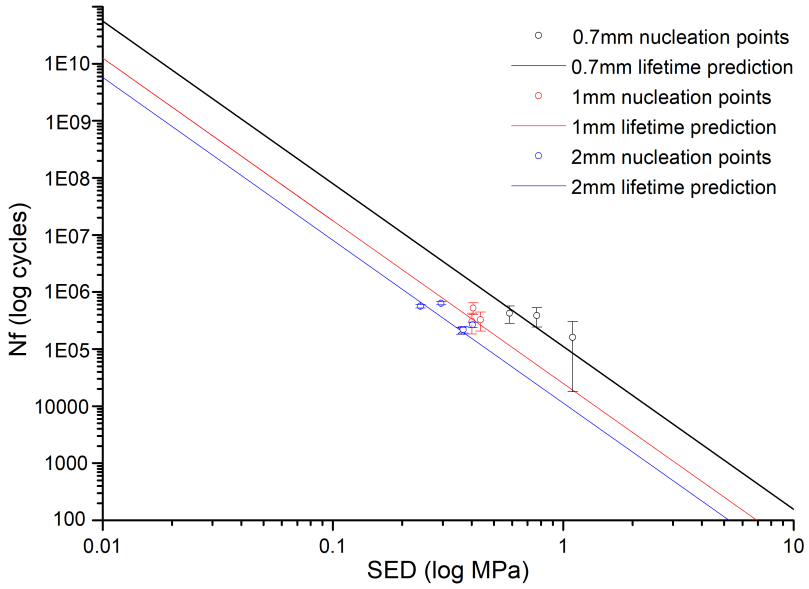

Figure 3.26: Lifetime prediction for 0.7 mm, 1 mm and 2 mm thickness unitensile specimens made of SEBS20 with cylinders oriented parallel to strain direction. The nucleation test for 0.7 mm samples was performed by R.Patel. Error bars represent standard deviation.

as a_0) used in the lifetime prediction equation 3.17, I plotted the crack growth points distinguishing samples of different thickness for parallel oriented SEBS20 and SEPS22. It has been reported in the literature that a change in the crack tip roughness can take place with thickness variation. For a rough tip, a stick-slip crack growth effect occurs, and a thickness effect can be observed [103]. Crack growth test on natural rubber showed little influence below 0.5 mm and above 5 mm, but between these values changes of crack growth rate of more than on order of magnitude were observed, with crack growth being higher for thinner specimen [103]. Figure 3.27-a and b show no systematic variation of crack growth rate (and hence B and F) with sample thickness. The variation in thickness in this case is limited to ± 0.25 mm; however a similar difference in the unitensile samples significantly changes the number of cycles to failure (as a result of a_0 being affected by thickness). Based on these experimental results, a thickness effect on B and F has been excluded. The nucleation data points collected at different strains all fall on the same material line prediction for the same thickness. This suggests that the parameters obtained from the crack growth model for different cylinders orientations are an accurate fit. Thinner uniaxial tensile specimens, with

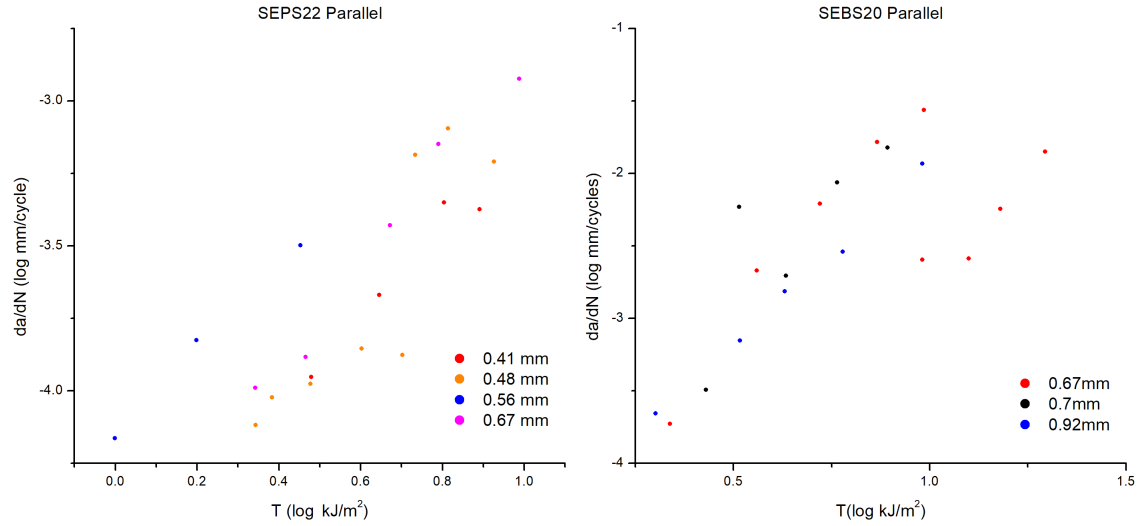

Figure 3.27: Left: Crack growth data for SEPS22 parallel separated in different samples thicknesses of 0.41 mm, 0.48 mm, 0.56 mm and 0.67 mm. Right: Crack growth data for SEBS20 parallel separated in different samples thicknesses of 0.67 mm, 0.7 mm and 0.92 mm. The data points fall in the same area of the plot for both cases.

different orientation, should be tested in the future to better support the hypothesis suggested in this study.

Compression versus injection moulding

I compared the nucleation results for unitensile samples manufactured via injection moulding (results presented in section 3.3.3) and unitensile samples cut from compression moulding sheets. Figure 3.28 and Table 3.6 show the results for both parallel and perpendicular orientation of SEPS22.

Table 3.6: Initial crack size value for compression and injection moulded SEPS22, both parallel and perpendicular. The injection moulded samples were 1 mm thick, while the compression moulded 0.55 mm thick.

a_0 (mm)	Compression	*st. dev.*	Injection	*st. dev.*
Parallel	7.29	1.82	0.184	0.02
Perpendicular	3.41	2.75	0.149	0.013

The resulting initial crack size is significantly larger for both orientations for the

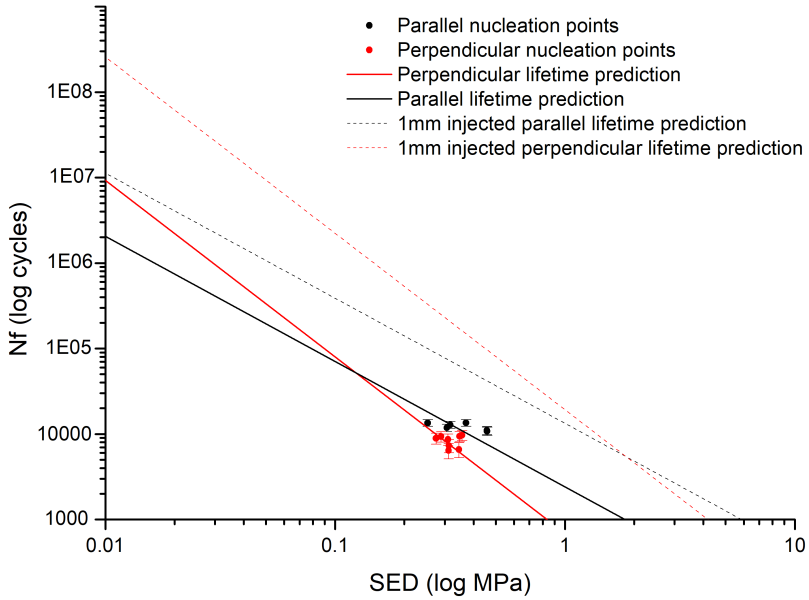

Figure 3.28: Lifetime prediction for compression and injection moulded parallel and perpendicular SEPS22. The dashed lines represent the injection moulded prediction. Error bars represent standard deviation.

compression moulded samples compared to injection moulded ones. The compression moulded samples lasted for a significantly shorter time. They are very well oriented (see Figure 2.22), meaning that the degree of orientation is not the limiting factor for durability. In this case, the thickness of the compression moulded samples was around 0.55 mm, which should have resulted in longer durability than the 1 mm injection moulded samples, according to the results presented in section 3.3.3. It is likely that compression moulding manufacturing introduced more and larger defects into the samples. It is also noticeable that a 7.2 mm defect size should be easily visible and would also be larger than the sample width. This confirms that the initial crack size does not simply represent a physical length or size.

During compression moulding, pressure on the mould was applied only after the desired temperature was reached. However, this might not have been sufficient to guarantee even temperature distribution in the melt. This could result in voids and cavity formation. Furthermore, the initial packing of the pellets or fluffy powder could have left some trapped air, which is difficult to remove. The samples with larger bubbles were rejected, but smaller, invisible to the eye, bubbles could be trapped in the final sheet.

The difference between parallel and perpendicular orientation for compression moulded samples is similar to the injection moulded ones, except for the cross-over point, which

occurs at higher strain energy density. More samples should be tested to give a definitive explanation on the matter, since the number and size of defects could influence the statistical significance of this result.

Geometry

The life time prediction model was validated for different unitensile specimen geometries. The geometries showed in Figure 2.11 were injection moulded and tested under the same conditions. The crack nucleation points for parallel SEPS22 are plotted in Figure 3.29. It is evident that, for the same thickness, short and long unitensile samples with the same orientation fall on the same prediction line. This result demonstrates that orientation and thickness are the fundamental factors in the definition of the prediction model parameters, which seems to be independent from geometry .

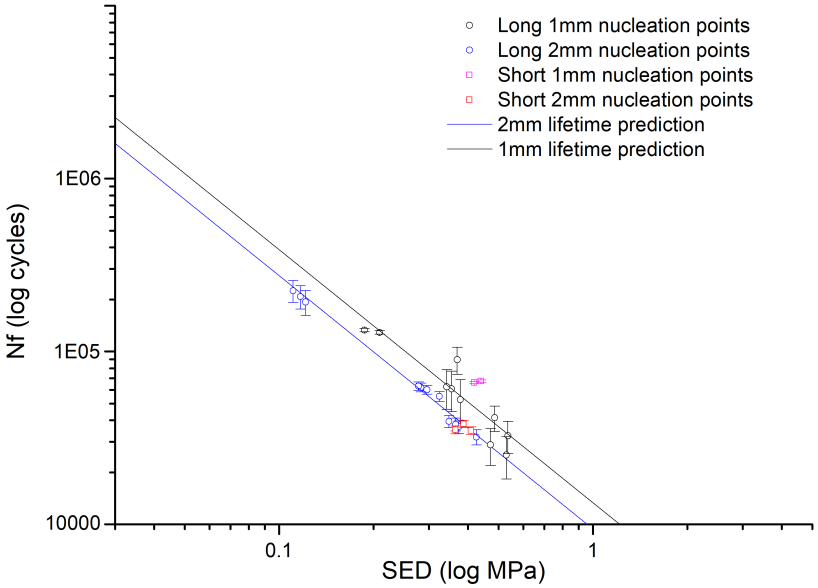

Figure 3.29: Lifetime prediction of 1 mm and 2 mm thick parallel oriented SEPS22 specimens. The nucleation points for short and long geometry from ISO37 type 2 and ASTM D638 type v specimen fall on the same line for the same thickness. The short 1 mm points are within the error of the prediction.

Mixed orientation

This section considers the case where bi-directionality or deviation from simple parallel or perpendicular alignment is present in the specimens tested. Unitensile samples were cut from the injection moulded sheet described in section 2.1.5 and 2.2.2, for both

SEBS20 and SEPS22. Crack nucleation test were performed on specimens cut from the centre of the sheet, where the majority of cylinders are aligned parallel to strain, and from the two edges of the sheet, where orientation deviates significantly from parallel. The specific orientation of the set of bi-directional sample is shown in Figure 3.30. The central specimen (NS) has a high percentage of parallel cylinders, while the left and right cut specimen have specular orientation. The edge samples' orientation was governed by a radial flow, which imparted a 45° and 30° angle for SEBS20 and SEPS22 respectively. The central layer is perpendicular to the outer layer, which is maintained even when the angle of the cylinders is intermediate between 0 and 90°.

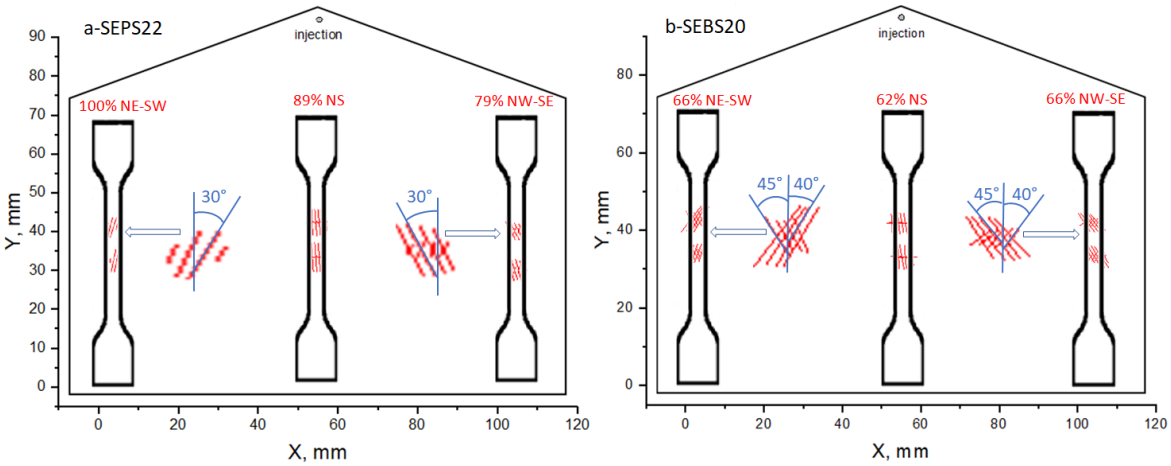

Figure 3.30: Orientation map and angle measurement of specimen cut form injection moulded sheet. a- SEBS20 specimens have 66% of cylinders oriented at 40° on the left, and 45° on the right, the central specimen has 62% of cylinders oriented parallel to strain; b- SEPS22 specimens have 100% cylinders oriented at a 30° angle on the left hand side, 89% parallel in the centre and 79% at a 30° angle on the right edge.

The central cut specimens for both SEBS20 and SEPS22 have bi-modal orientation of the cylinders in directions parallel and perpendicular to strain. In this case one can consider use of a mixture rule to build the prediction line for fatigue. The nucleation points are plotted with the prediction line obtained from the unidirectional injection moulded samples. The new slope for the central cut bi-modal oriented sample was calculated with equations 3.28 and 3.29.

$$B_{bi} = x_{NS}B_{NS} + x_{EW}B_{EW} \tag{3.28}$$

$$F_{bi} = x_{NS}F_{NS} + x_{EW}F_{EW} \tag{3.29}$$

where x_{NS} and x_{EW} are the fraction of parallel (NS) and perpendicular (EW) oriented cylinders, and B_{NS}, B_{EW},F_{NS} and F_{EW} are the respective power law parameter from Table 3.2.

For SEPS22 the parallel layer constitutes 89% of the cylinders, which (unsurprisingly) proved to give very similar results to the injection moulded unitensile specimen of graph 3.23. Two different tests proved the accuracy of the slope prediction. The same procedure was applied to SEBS20 central cut samples, which had a higher fraction of perpendicular cylinders (62% parallel-36% perpendicular). The result for the initial crack size of SEPS22 is consistent with the thickness trend for parallel specimens described in section 3.3.3. Since the injection cut sample is 1.6 mm thick, the a_0 is larger than the 1 mm injection moulded result.

On the other hand, the initial crack size for the bi-modal orientated SEBS20 has a smaller value compared to the 1 mm injection moulded samples. This can be explained as a combined effect of the change in the parameter B, which has to be proven to be a correct prediction by further nucleation tests on the same type of samples, and sample thickness.

Table 3.7: Initial crack size for central injection cut specimen. The samples are cut from the centre of the injection moulded sheet.

	a_0	*st.dev.*
SEPS22	0.22	0.006
SEBS20	0.038	0.009

The samples cut from the left and right side of the injection moulded sheet are not fitted a prediction line. If the prediction lines are close to the data points in these cases is just by coincidence, since the rule of mixtures could not be applied in this case because none of the styrenic cylinders are aligned parallel or perpendicular with respect to strain. It is likely that the prediction line will have a slope intermediate to the cases of parallel and perpendicular orientation. Specific tests should be run to verify this hypothesis. However, it is noticeable that the left-cut sample in Figure 3.34, which shows unidirectionality at a 30° angle with respect to the parallel axis, lasted a significantly shorter time compared to the 1 mm and 2 mm crack nucleation points predicted in the slope plotted in the graphs in Figure 3.25.

On the other hand, samples that showed bi-modal orientation with both layers of cylinders aligned at 45°, or 30°, angles with respect to the parallel axis (Figure

3.33 and 3.34), had superior durability at a similar strain energy density level. This result applies to both SEPS22 and SEBS20 and proves the importance of optimising orientation during manufacturing to enhance durability. It is of particular interest because such bimodal orientation is present in the polymeric valve leaflets.

The samples after testing (Figure 3.31 and 3.32) do not show crack profile features specific to the different orientations.

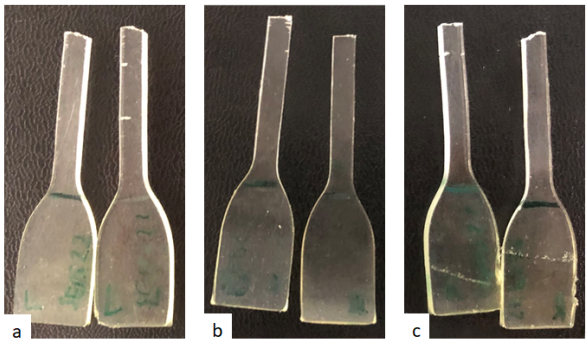

Figure 3.31: SEPS22 broken unitensile samples. The samples were cut with a ISO37 type 2 sharp cutting die from the injection moulded sheet . The samples are cut from specific area of the sheet to obtain different orientation of the styrene domain. a) left cut samples with unidirectional 30° orientation; b) central cut samples with bimodal styrene cylinders orientation 89% parallel and 11% perpendicular; c) right cut samples with bimodal styrene cylinders orientation 79% at 30° angle.

Finally, thickness played a different role for the highly bi-modal samples. The average thickness for SEBS20 and SEPS22 injection moulded sheet was 1.5±0.05 mm and 1.64±0.06 mm respectively. For central-cut SEPS22 the results match the findings presented in section 3.3.3: the thinner the sample the higher the durability, which is consistent with the prediction line and data points sitting between the 1 mm and 2 mm lifetime prediction. When the proportion of the central perpendicular layer increases the thickness effect is not reproducible, not even compared to the 1 mm perpendicular lifetime prediction. The higher durability of the bimodal 45° samples is an interesting aspect to investigate. Similar orientation is found in the bottom part of the valve leaflet, as shown in Figure 2.17, which rarely shows crack formation during accelerated fatigue tests. More studies investigating this aspect are required for a complete understanding of the potential of bimodal cylinder orientation.

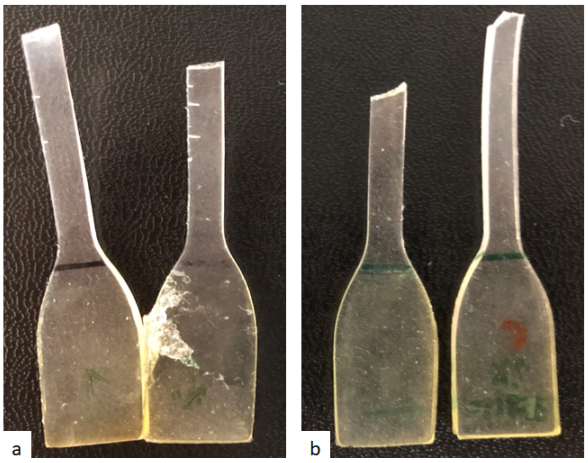

Figure 3.32: SEBS20 broken unitensile samples. The samples were cut with a ISO37-type 2 sharp cutting die from the injection moulded sheet shown in Figure 2.11. The samples are cut from specific area of the sheet to obtain different orientation of the styrene domain. a) left cut samples with bimodal styrene cylinders orientation 66% at 45° angle; a) central cut samples with bimodal styrene cylinders orientation 62% parallel and 36% perpendicular.

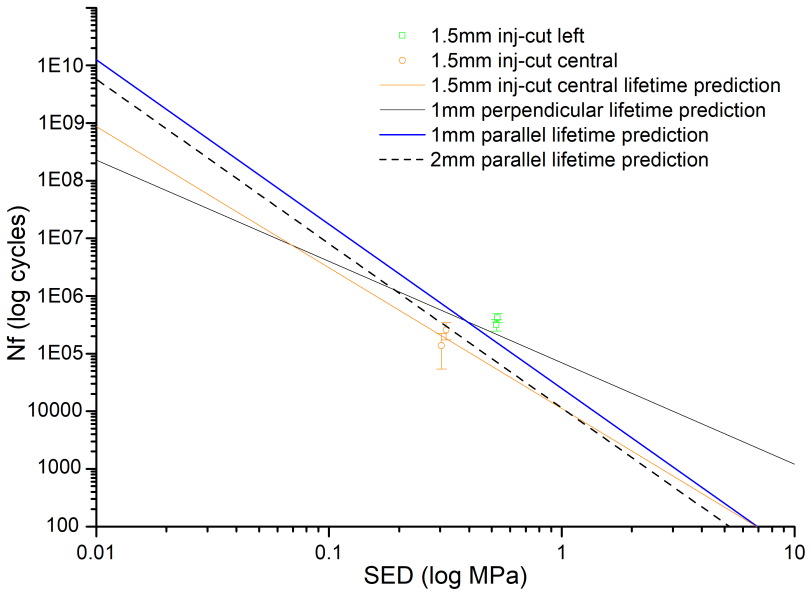

Figure 3.33: Lifetime prediction for central injection cut specimen of SEBS20. The prediction is compared to the cases of 1 mm, 2 mm parallel and 1 mm perpendicular samples for the same material. Error bars represent standard deviation.

Heparin coating effect

As mentioned in the introduction, heparin coating improves the hemocompatibility of the material [127]. Bernacca *et al.* [128] concluded that the coating could also

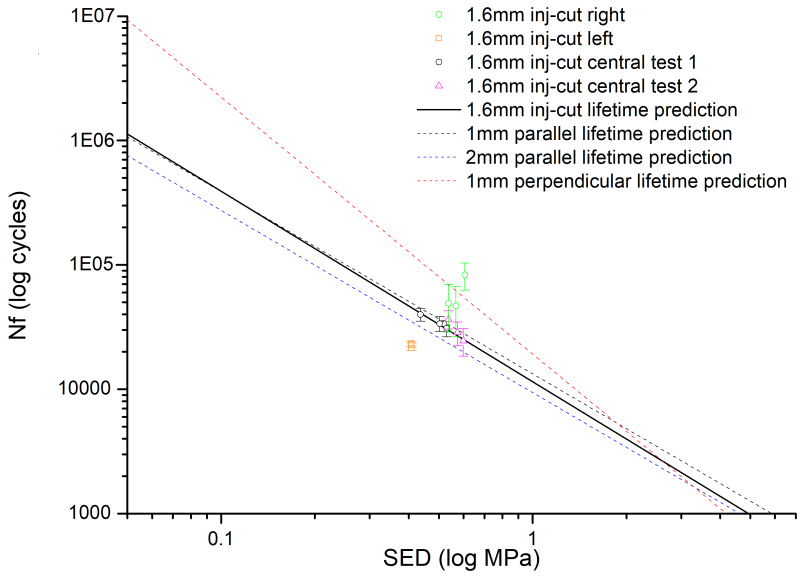

Figure 3.34: Lifetime prediction for central injection cut specimen of SEPS22. The prediction is compared to the cases of 1 mm, 2 mm parallel and 1 mm perpendicular samples for the same material. Error bars represent standard deviation.

have a beneficial impact on the durability of the polymers they tested. In my experiment, I coated uniaxial tensile specimens with CHC™ Corline Heparin Conjugate kit (Corline®,Uppsala, Sweden) and ASTUTE® Advanced Heparin Coating (BioInteractions Ltd.,Reading, UK) for the crack nucleation test of parallel oriented SEPS22 and SEBS20 to verify the effect on fatigue life. The parallel orientation was chosen as it is the desired orientation in the valve leaflets.

The results demonstrated that there is a small improvement in durability for both materials in the 2 mm thick samples (Figure 3.35-b and 3.36-b). As a consequence, the value of the initial crack size calculated for the coated samples is smaller than for the uncoated case (Table 3.8). We can explain this phenomenon with the hypothesis that the coating is filling surface defects and delaying the growth of these flaws. The 1 mm sample results shown in Figure 3.35-a and 3.36-a demonstrated that both coatings techniques have no discernible effect on the fatigue performance of the material. This coincides with the fact that uncoated 1 mm initial crack size is smaller than the 2 mm counterpart for both material parallel oriented. It is likely that less large defects are present on the surface of the 1 mm sample . This hypothesis is supported by the crack growth test on the coated pure shear samples, results for which are shown in graphs 3.37.

Table 3.8: Initial crack size for 2 mm thick SEBS20 and SEPS22 parallel oriented samples Corline®coated and uncoated.

a_0 (mm)	SEPS22	*st. dev.*	SEBS20	*st. dev.*
uncoated	0.3887	0.009	0.133	0.01
Corline®coated	0.03	0.004	0.098	0.011

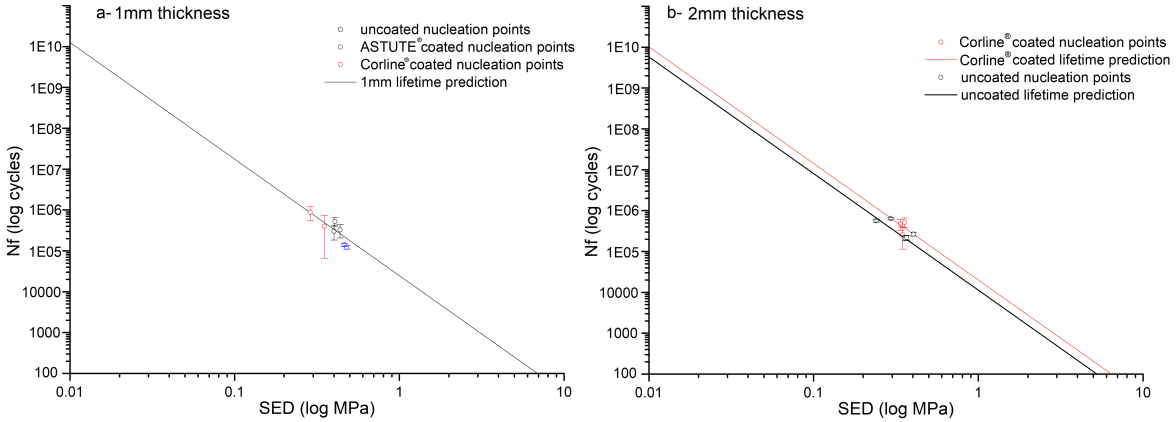

Figure 3.35: Lifetime prediction of coated with Corline®and ASTUTE®and uncoated SEBS20 parallel oriented samples;a- 1 mm specimen thickness;b-2 mm specimen thickness. Error bars represent standard deviation.

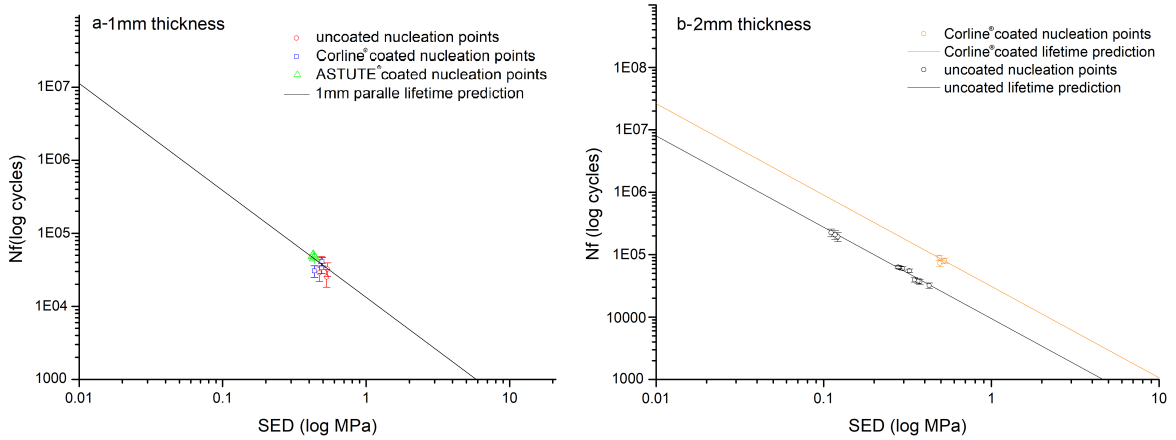

Figure 3.36: Lifetime prediction of coated with Corline®and ASTUTE®and uncoated SEPS22 parallel oriented samples; a- 1 mm specimen thickness;b-2 mm specimen thickness. Error bars represent standard deviation.

Corline®coated parallel oriented SEBS20 pure shear specimens were tested in the crack growth experiment. The data did not show any change in the material response

(identical values of B and F) with coating, which implies that the crack propagation and material structure has not been affected by the coating. Similarly, the stress-strain curve for uncoated and coated materials show the same behaviour for real and engineering strain (Figure 3.38), demonstrating that the mechanical response is not affected by the coating.

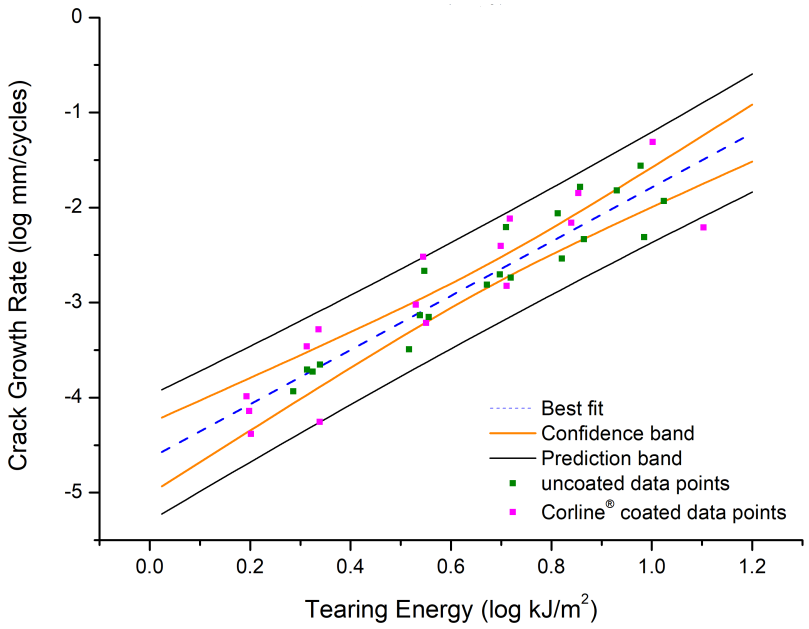

Figure 3.37: Crack growth results for SEBS20 parallel oriented. The experimental points for the Corline®coated samples are plotted with the results obtained from crack growth of uncoated samples. The coated data points lay withing the same prediction band.

Brubert [5] showed that in a three point bending test on parallel oriented SEPS22, heparin coated samples (with CHC™ Corline®) survived the test in a higher proportion than uncoated ones. The samples were immersed in calcifying and not calcifying solution and stretched at 1 Hz for 12 days continuously. In both cases heparin enhanced the material durability. The strips of material in Brubert's study were 0.5 mm thick. His findings imply that heparin can have a beneficial effect on surface cracks or defect propagation. More details on the calcification and heparin effect are presented in chapter 4.

Dr J. Stasiak performed fatigue tests in DuraPulse on polymeric PHV prototypes made of SEPS22 (durability results shown in Figure 3.39). JA and JB are the name given to different valve geometries. The valve prototypes coated with CHC™ Corline Heparin Conjugate kit (Corline®,Uppsala, Sweden) showed a significantly longer durability in comparison to uncoated valves for the JA prototype, while similar durability

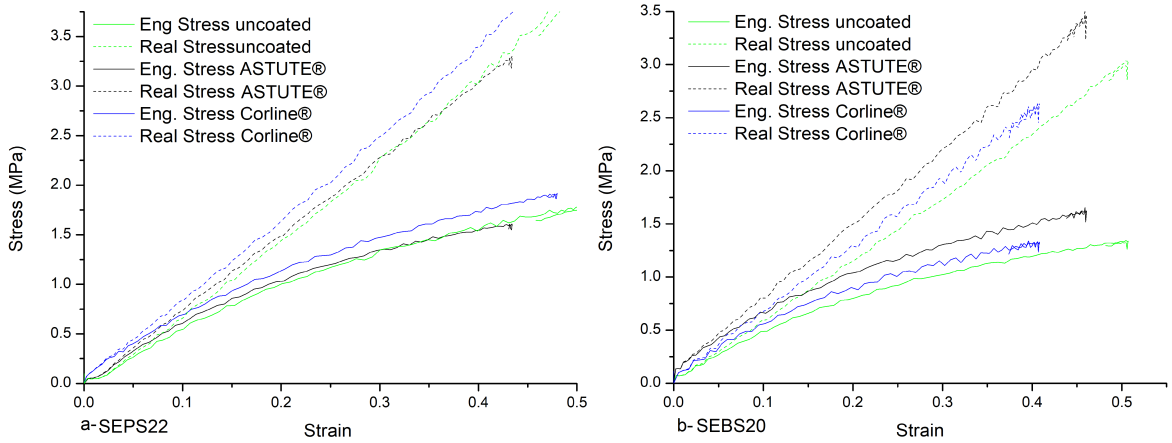

Figure 3.38: Stress strain curve of parallel oriented SEPS22 (a) and SEBS20 (b) uncoated, Corline®coated and ASTUTE®coated. The plot shows engineering and real stresses. Data collected by E. Okafor, J. Allford and V. Manhas.

was measured for the JB valve design. The large error bar for the heparin coated JA valve suggests that the results are influenced by the defects introduced by manufacturing, however none of the uncoated valves reached durability similar to the coated JA valves. A larger number of tests and detailed manufacturing quality control should be carried out to prove the coating effect on the valve leaflet durability.

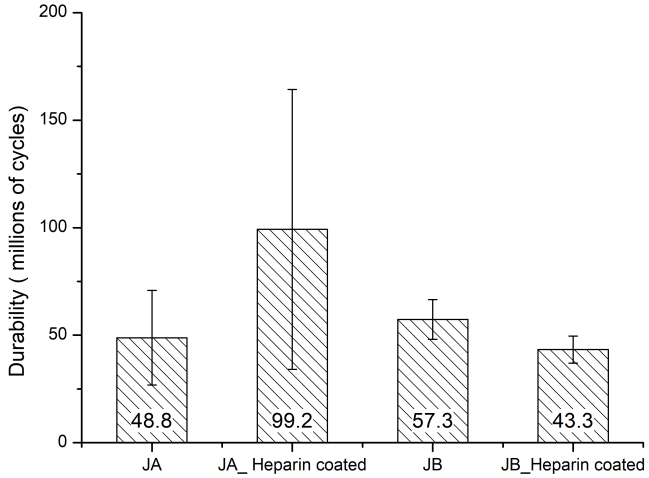

Figure 3.39: Valve durability for prototype JA and JB [6] uncoated and Corline®heparin coated. Error bars represent standard deviation. Data collected by Dr J. Stasiak.

In conclusion, the heparin coating does not show any detrimental effect on the durability properties of the materials tested in this study. Fatigue lifetime improvement

due to heparin coating is more difficult to prove from this data, differences generally lying within experimental error. However, there does appear to be a pattern over several different experiments (including those of Bernacca *et al.* [128]) that heparin coating imparts a durability benefit to polymeric samples. It can be hypothesised that the coating works as a barrier for surface defects propagation.

Materials comparison

The durability prediction model developed in this work is used for material selection for the valve application by comparing their fatigue performances. The parallel orientation of the cylinders have been demonstrated to be the optimal orientation distribution according to the model of Serrani *et al* [67]. Figure 3.40-b compares the parallel orientation fatigue life prediction for SEBS20 and SEPS22, the two anisotropic materials considered in this work.

Figure 3.40-b shows that SEBS20 samples had a longer lifetime compared to SEPS22. The initial crack size is also significantly smaller (see Table3.4 and 3.5). The slope for SEBS20 is much steeper too, which as a result predicts an higher number of cycles to failure at the SED levels present in the PHV (area highlighted in Figure 3.40). This effect can be explained by the molecular weight and cylinder dimension, both of which are larger for SEBS20. Molecular weight could also be a determinant factor in the comparison of perpendicular orientation of the cylinders, shown in Figure 3.40-a. SEBS20 performs better than SEPS22 also for the perpendicular orientation, where the size of the cylinders has less influence on the mechanical response, since it is the rubbery matrix which sustains the strain and where the crack propagates. The comparison of the perpendicular orientation in Figure 3.40-a demonstrates that the different matrix compositions, together with molecular weight, influences the durability and crack velocity propagation of the materials. SEBS20 has a higher molecular weight and a more branched chemical structure than SEPS22. This could explain why SEBS20 lasts longer than SEPS22. SEBS20 is likely to be more entangled and so will require higher strain to propagate the crack.

Figure 3.41 shows a comparison of parallel orientations of the 0.7 mm SEBS20, MED500400 and 1 mm SEPS22. The oriented SEBS20 shows superior durability compared to the isotropic MED500400. Anisotropy and styrene content seem to matter more than molecular weight when chemical composition is similar. SEPS22, which has the lowest molecular weight among the three, shows the lowest durability. Finally, prediction for oriented and isotropic SEPS22 is plotted in Figure 3.42. The isotropic

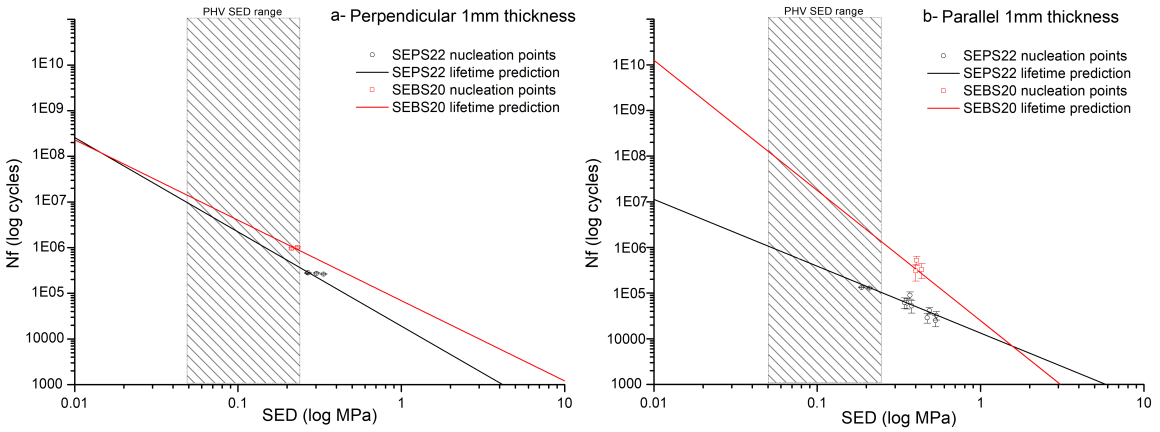

Figure 3.40: Lifetime prediction of 1 mm thick SEBS20 and SEPS22 specimens.(a) perpendicular, (b) parallel orientation of the styrene domain respect to the principal strain direction. The grey box indicates the SED range for a prosthetic valve made of these materials.Error bars represent standard deviation.

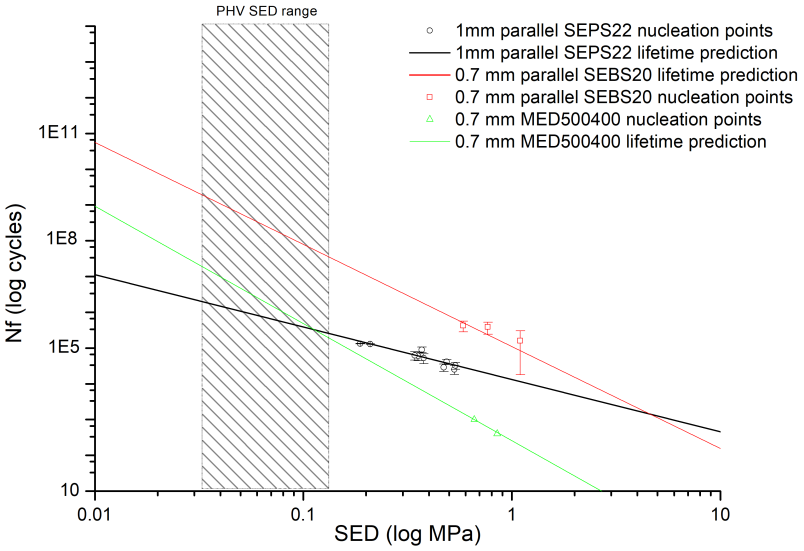

Figure 3.41: Lifetime prediction of 1 mm thick parallel oriented SEPS22 , 0.7 mm parallel SEBS20 and 0.7 mm MED500400 specimens. The grey box indicates the SED range for a prosthetic valve made of these materials. Error bars represent standard deviation.

unitensile samples were solvent casted in THF and the specimen was 0.34 mm thick. The slope for the isotropic material predicts a longer lifetime . However, a valve with leaflets of 0.34 mm thickness would be predicted to last only for few millions cycles. The slope for isotropic SEPS22 is similar to that for MED500400 and the predicted durability is also similar. However, if I account for the thickness effect, a 0.7 mm thick

isotropic SEPS22 sample would be predicted to have a shorter lifetime than 0.7 mm MED500400. Table 3.9 shows the comparison of the initial crack sizes for SEPS22. Despite the steeper slope, the initial crack size is larger for the isotropic case compared to the anistropic parallel and perpendicular cases. This suggest that solvent casting could increase the number and density distribution of defects.

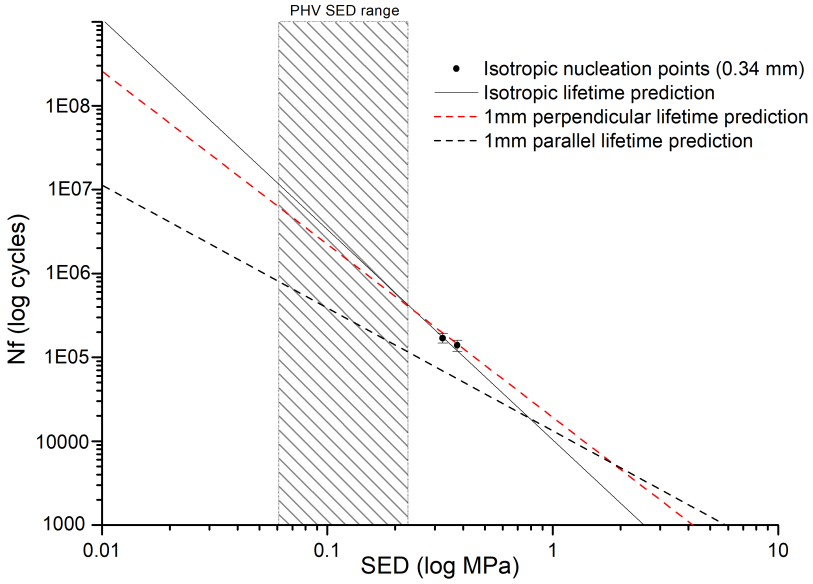

Figure 3.42: Lifetime prediction of 0.34 mm isotropic SEPS22 compared with prediction of anisotropic parallel and perpendicular 1 mm thick specimens. The grey box indicates the SED range for a prosthetic valve made of these materials.Error bars represent standard deviation.

Table 3.9: Initial crack size values for parallel, perpendicular and isotropic SEPS22 specimen. The parallel and perpendicular value refer to 1 mm thick samples. The isotropic case is calculated based on solvent casted 0.34 mm specimen.

SEPS22	a_0	*st.dev.*
Parallel	0.184	0.02
Perpendicular	0.149	0.01
Isotropic	0.29	0.01

In conclusion, the best candidate material according to this analysis is SEBS20 with cylinders oriented parallel to strain.

3.3.4 Rigid stent experiment

The ultimate goal of the study of a fatigue life model prediction is to calculate the number of cycles to failure of a polymeric PHV prototype, based on known material properties. These properties are the parameters of the power law equation obtained from the crack growth test and the initial crack size a_0. I demonstrated that the value B and F vary with orientation of the anisotropic material with respect to the strain direction. The initial crack size is also strongly influenced by orientation, as well as thickness and, possibly, coatings. The average thickness of the valve leaflets vary between 0.25 mm to 0.45 mm, depending on the material's stiffness: a softer material needs higher thickness to sustain the closing pressure without collapsing, but is also able to open fully during systole.

According to the consideration on the effect of thickness presented in section 3.3.3, a unitensile sample of the same thickness as the valve leaflet should be used to provide nucleation data points to fit to the prediction model to obtain an a_0 value for the valve. In theory this option should be viable; however the injection moulding instruments I used were not suited for injecting planar samples of such low thickness, and compression moulding proved to give unsatisfactory results in terms of durability (see section 3.3.3).

An alternative method to calculate the initial crack size was therefore designed. The valve geometry in Figure 2.15 was modified by adding an extra 4 mm height to the valve posts. The posts were inserted into a 3D printed holder (Figure 3.11) able to fit the posts and block their bending during opening and closing in the durability test. The effect was to produce a valve with a rigid stent, which increases the maximum strain energy density, and hence shortens the lifetime of the valve. This is convenient for the measurement of a_0 because it means that tests to failure of the valves can be carried out within a reasonable time frame (unlike the case of flexible posts, where failure takes months to achieve, even in the accelerated tester at 30 Hz). The data for the number of cycles to failure (N_f) could be combined with a FE simulation of the valve closing, which gave the value of the maximum SED within the leaflet. Data points for N_f obtained in this way, at relatively high strain energy density, were combined with the slope of the predicted line for the relevant material and orientation, obtained via crack growth experiments. This allowed life time prediction at lower strain energy density (relevant to practical heart valve prototypes) and calculation of the initial crack size for the valve. The prediction gives the number of cycles to failure for identical valve geometries with the same leaflet thickness but with reduced SED values relative to the rigid post valve. It is the objective of the valve design to optimise orientation and

geometry features, such as leaflet thickness, curvature or shape, to minimise the SED and maximise the number of cycles to failure. This prediction methods makes such iterative design improvements possible, without the requirement of testing to failure each successive prototype.

Using the real valve geometry for the initial crack size calculation has the advantages of taking into account the direction of the cylinders in the area of maximum strain energy density and the possible deviations from unitensile strain during the operationg of the valve .

The rigid stent experiment was also used to confirm the hypotheses investigated in the previous sections. Valve durability was compared as a function of material, orientation, thickness and coatings. Figure 3.43 shows valve prototypes made of SEBS20, SEPS22 and MED500400 from left to right.

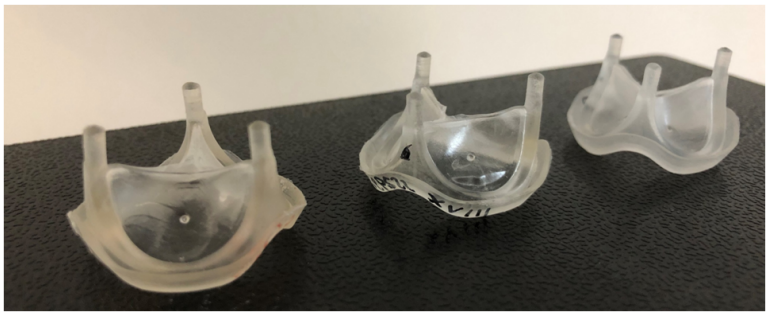

Figure 3.43: Rigid stent valve prototypes made of SEBS20, SEPS22 and MED500400 from left to right.

The FE model was applied to unitensile samples with parallel orientation of the cylinders. Figure 3.44 shows the SED map along the sample, with 50% strain applied. The strain energy density is uniformly distributed in the thin section of the sample, where the cylinders are highly aligned. The simulated SED matched the experimental results obtained from the same cyclical test on SEPS22 specimens. The values are compared in Table 3.10. The simulation proved that the experimental values of SED used in the simulation are accurate.

The FE model takes into account the three main strain direction when integrating the SED. This could result in a discrepancy when comparing experimental results for unitensile samples with the valve simulation. However, Figure 3.45, obtained from the simulation, demonstrates that this is not the case. The maximum principal strain aligned in the cylinder direction proved to be by far the largest contribution to the SED calculation in the element having the maximum SED. This also confirmed that the deformation in the valve leaflet is mainly unidirectional.

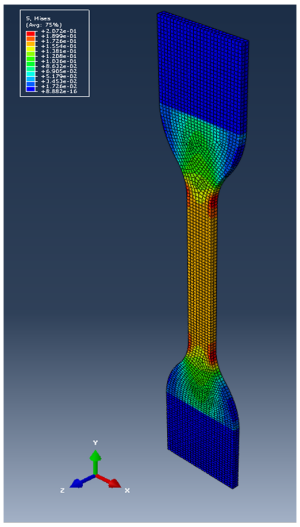

Figure 3.44: SED map of the ISO37-type 2 specimen stretched at 50% strain. The figure was obtained from ABAQUS software output.

Table 3.10: Experimental and finite element values of SED (MPa) for a unitensile sample (ISO37-type 2) stretched at 50% strain.

	SED max
FEM	0.364
experimental	0.378±0.03

The lifetime prediction model was validated by testing rigid stent valves made of SEPS22 at different strains. The back pressure in the DuraPulse was changed from 100 mmHg to 70 mmHg, giving a lower strain level and consequently lower SED. The results for both 100 mmHg and 70 mmHg are represented in the graph in Figure 3.46-a. The data points lie on the same prediction line, giving an a_0 of 0.0017 mm and demonstrating the efficacy of the model applied to a complex geometry, but with same thickness and orientation. The a_0 value is substantially lower than that obtained from the unitensile sample; a thorough discussion of this aspect is presented in section 3.3.5.

The effect of thickness shows an opposite trend to the (thicker) unitensile samples. Thinner valves have shorter lifetime and higher initial crack size. It is expected that, below a certain thickness, it becomes very difficult to inject leaflets with precision and manufacturing defects are almost inevitable, explaining why thinner samples have larger a_0 for very thin samples. This is shown also for valves made of SEBS20, presented in Figure 3.46-b.

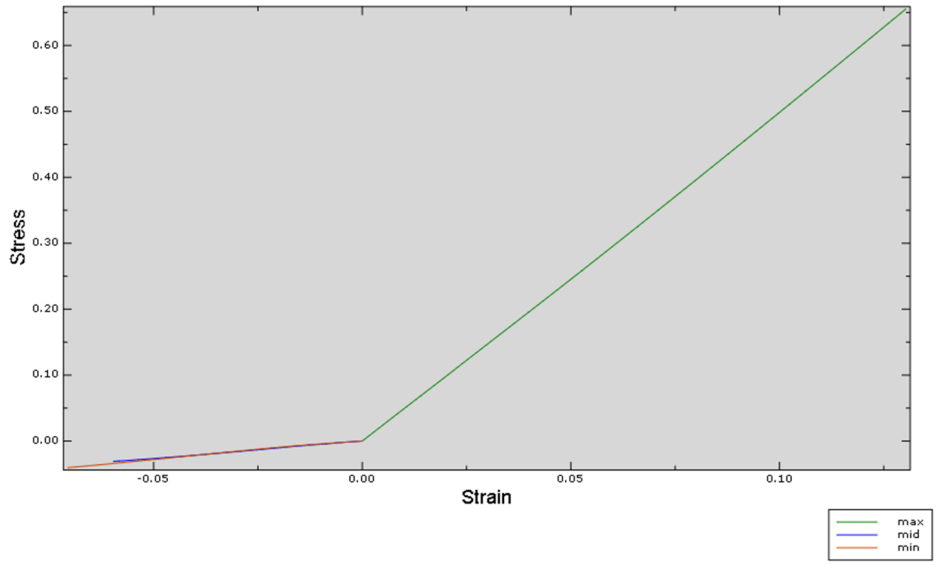

Figure 3.45: Comparison of maximum, medium and minimum principal stress/strain in the element with maximum SED in the valve leaflet simulation.

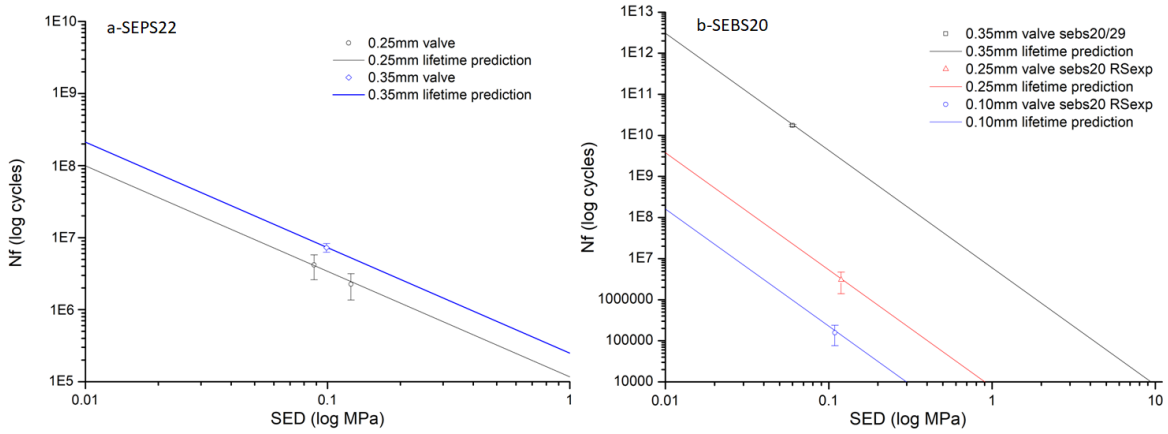

Figure 3.46: Lifetime prediction of the rigid stent experiment for a-0.25 mm and 0.35 mm SEPS22 valves ,b-0.1 mm, 0.25 mm and 0.35 mm SEBS20 valves. Error bars represent standard deviation.

Valves usually start to fail on the edge of the leaflets where SED is maximum, as shown in the FE simulation of Figure 3.49. However, for the 0.1 mm SEBS20 valve the crack started and propagated in the red area indicated in Figure 3.48, which corresponded to the region of lowest leaflet thickness.

Among the three materials, SEBS20 showed the best performance also in the rigid post valve geometry, which supports the use of the model based on crack growth and nucleation on standard samples as a screening method for valve leaflet materials. The leaflet thickness for the valves made of the three materials selected was mapped with

Table 3.11: Initial crack size value for valve made of SEPS22 and SEBS20. Thicknesses of 0.35 mm, 0.25 mm and 0.1 mm of the leaflets were tested.

a_0 (mm)	SEPS22	*st. dev.*	SEBS20	*st. dev.*
0.35 mm	3.32e-4	1e-4	0.0045	2e-4
0.25 mm	0.0017	1.59e-4	0.16	0.056
0.1 mm	-	-	0.916	0.268

Figure 3.47: Schematic representation of the leaflet indicating where the thickness measurements were taken.

Table 3.12: Thickness values of the leaflet (mm). The numeration respect the scheme on the left. Measurements were taken with a micrometer.

Material	1	2	3	4	average
SEPS22	0.296	0.25	0.248	0.192	0.246
st.dev.	0.021	0.019	0.014	0.015	
SEBS20	0.312	0.259	0.252	0.208	0.258
st.dev.	0.024	0.021	0.021	0.019	
MED500400	0.3	0.25	0.247	0.203	0.251
st.dev.	0.016	0.013	0.011	0.013	

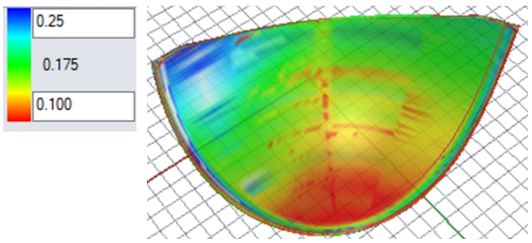

Figure 3.48: Thickness map in mm of the valve leaflet for the rigid stent experiment. Image produced by Dr. M. Serrani.

4 different measurements according to Figure 3.47. The values are reported in Table 3.12.

It is possible that, by tuning the thickness of MED500400, a longer lifetime could be achieved, since this is a softer material (lower styrene content). A thicker leaflet could

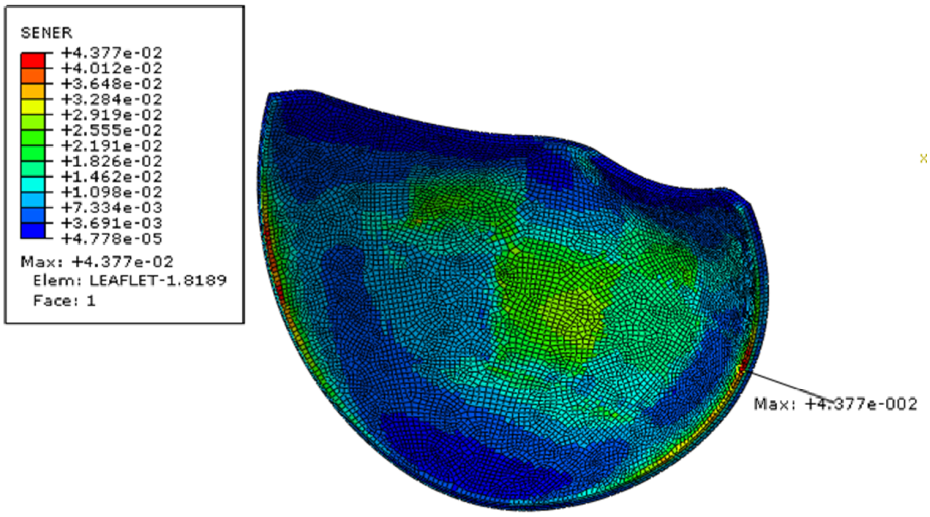

Figure 3.49: SED map of the 0.25 mm valve leaflet 3.48 for the rigid stent experiment. Image produced by Dr. M. Serrani.

be manufactured from MED500400 still maintaining sufficient opening and closing of the valve. Future studies will investigate this possibility.

The heparin coated valves tested in the DuraPulse gave mixed results (Figure 3.50) and no clear trend could be identified. The durability results for coated SEBS20 show an improvement in durability with both coatings technologies (Corline®and ASTUTE®). However, this was not confirmed for the other materials: SEPS22 valves showed no significant difference in durability, while MED500400 coated valves had a minor reduction in lifetime. The number of samples tested are not sufficient to draw definitive conclusions. Nevertheless, it is possible to confirm the comments made on the coated unitensile samples, that the coating is, at least, not detrimental for the lifetime of the materials.

XPS data were collected (by Dr J Stasiak) to establish the stability of the coating on the surface over a long period of time (Figure 3.51). Sulfur was identified as a marker for the presence of heparin coating. After 200 millions cycles the peak for sulphur decreased by 36%. This analysis shows that only a relatively minor erosion of the coating layer took place on the valve leaflet.

3.3.5 Effect of thickness on the initial crack size

Variation of thickness in both unitensile samples and valves prototypes proved to have a significant effect on predicted durability. This behaviour has been demonstrated to be independent of the material tested. In order to try to quantify this effect and include

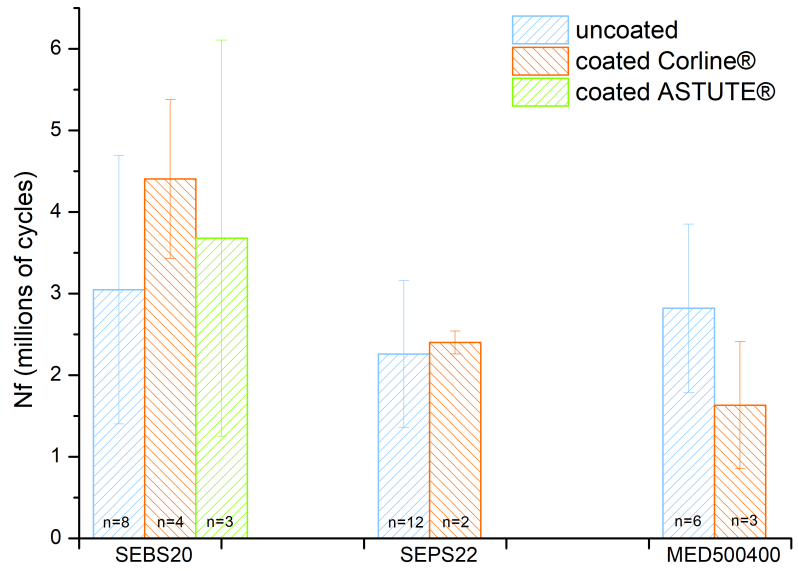

Figure 3.50: Number of cycles to failure for the rigid stent experiment valve made of SEBS20, SEPS22 and MED500400 both uncoated and coated with Corline®and ASTUTE®coatings.Error bars represent standard deviation.

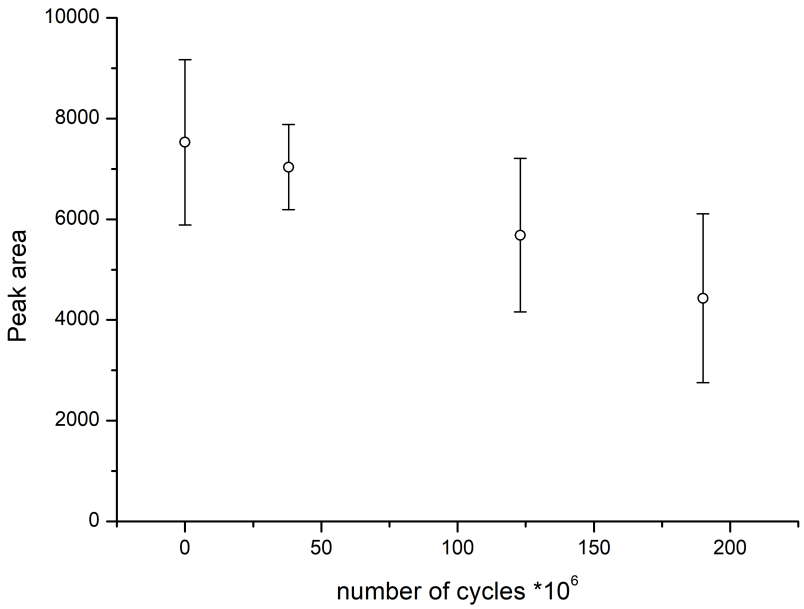

Figure 3.51: XPS data for a valve that underwent fatigue testing. The measurements were taken at different time for the duration of the valve. The peak area is related to the concentration of sulfur on the surface. Data collected by Dr J. Stasiak.

this factor in the model, identification of a relationship between the initial crack size and thickness was attempted in this section.

From the results obtained in this work, it is possible to speculate that the initial crack size diminishes linearly with thickness and that the slope should go through the origin, since it is physically impossible to have a defect with zero thickness. Based on these assumptions I plotted the results for SEBS20 and SEPS22 with parallel orientation (Figure 3.52 and 3.53). The linear relationship is remarkably precise for SEBS20 and reasonable for SEPS22.

It is plausible that, in practice, below a certain thickness, the material will be difficult to manufacture, with the result that the initial crack size will increase and the lifetime will become shorter for thinner samples in this very thin sample regime. This was observed for the rigid post valve durability test: thinner valves had a shorter lifetime and the initial crack size obtained from the crack growth prediction fitting gave a larger a_0 (see section 3.3.4). Hence the linear relationship will shift towards an asymptote at the (0,y) axis. This is visible in Figure 3.53, where the scale of the initial crack size changes makes it more evident. SEBS20 initial crack size also increases (Table 3.11) at thicknesses below 0.35 mm, but it is not so noticeable on the scale of the graph.

The minimum of the curve before the asymptote should give the thickness minimum initial crack size which can be achieved for a particular material (and manufacturing method). This can be an indicator for optimisation of manufacturing of thin parts, although the steep upward trend of a_0 below the optimum thickness make it sensible to error on the side of a thickness just above this minimum in practical applications. However, the initial crack size obtained for the valves at 0.35 mm are far from the prediction line. Figure 3.52 and 3.53 also show the prediction of the initial crack size value for a 0.35 mm thickness sample according to the linear relationship. For example, with an a_0 of 0.071 for SEPS22, the number of cycles to failure for the same SED obtained from the simulation should be 612000 instead of the experimental 7.2 M value.

There could be a combination of factors responsible for this. Firstly, the valve runs at 30 Hz frequency, while the unitensile samples are tested at 1 Hz. Adiabatic hysteretic heating due to higher frequency is very unlikely to increase the temperature up to the glass transition of styrene (approximately 110°C) to soften the physical crosslinking of the glassy domain. In general, the literature shows that polymeric materials which are strongly influenced by frequency in terms of durability are those having a crazing tendency, which is not the case for the materials considered in this work [123]. Further study should investigate the effect of frequency on durability, using unitensile samples, since the DuraPulse is not designed to run at 1 Hz frequency. Some

effect of frequency on durability is expected, but it should not account for the couple of orders of magnitude decrease/increase in number of cycles to failure observed.

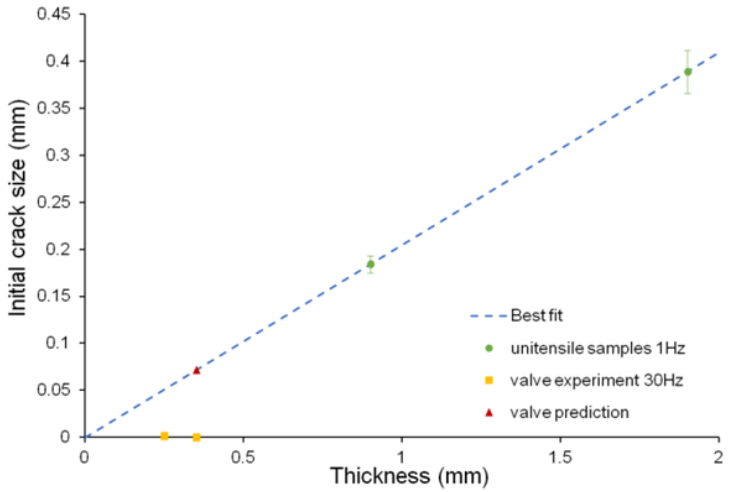

Figure 3.52: Relationship between initial crack size and part thickness for SEBS20 parallel oriented. The dashed line represent the best fit of the experimental points. Both results for unitensile samples and rigid stent experiment valve are plotted. The red triangle represent the initial crack size prediction for a 0.35 mm thick part with cylinders oreinted parallel to main strain direction.

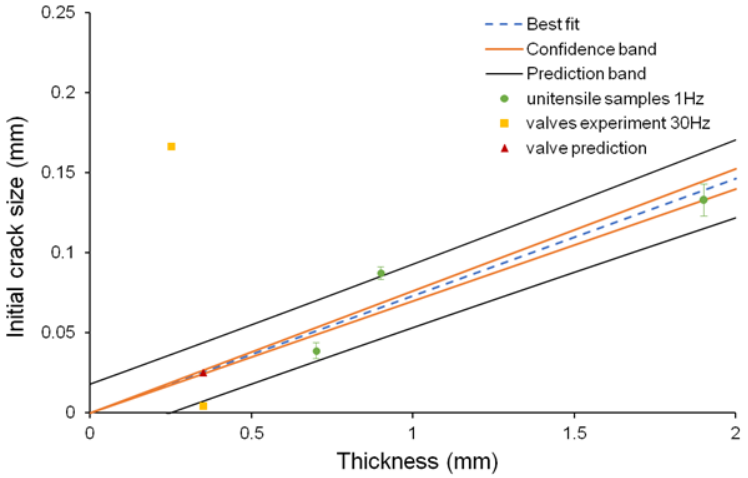

Figure 3.53: Relationship between initial crack size and part thickness for SEPS22 parallel oriented. The dashed line represent the best fit of the experimental points. Prediction and 95%confidence band are also reported. Both results for unitensile samples and rigid stent experiment valve are plotted. The red triangle represent the initial crack size prediction for a 0.35 mm thick part with cylinders oreinted parallel to main strain direction.

On the modelling side, the prediction discrepancy could be accounted for by the local orientation and thickness variation in the area of maximum strain energy density. Both of these factors can significantly affect SED calculation and durability. In the injection moulding of the leaflet, the melt front expands circumferentially from the central injection point and later starts to fill the thicker posts. SAXS measurements, shown in Figure 2.17, demonstrated that at the interface between the thicker post and thin leaflet the cylinders rotates towards a radial orientation. The transition from circumferential to radial and from a thin to thick part represents the weak point of the leaflet. This effect has to be accurately captured when calculating SED in the FE model. Since the simulation uses material parameters for a specific orientation, a mixed orientation parameter should be defined. It could be possible that the parameters for the bi-modal orientation at 45°, would better represent the mechanical response in this region. This could account for the discrepancy between the valve and unitensile specimen predictions . However, the prediction model based on unidirectional B and F worked well for the SEPS22 valve of the rigid stent experiment (Figure 3.46).

The meaning of the initial crack size has proven to be far from simply representing the actual size of the defect. If that was the case, some of the defects, especially in compression moulded samples, should have been visible to the naked eye or even cut across the section of the sample. This study shows that a_0 accounts for a combination of factors influencing fatigue life prediction. This could apply specifically to thin parts, such as the valve leaflets. While the effect of anisotropy is captured in the performance of crack growth and crack nucleation tests, thickness, coating and manufacturing quality are certainly represented by the initial crack size.

3.3.6 Transition law

The standard approach takes the power law regime as the total life approach for polymeric applications. However, for the prosthetic valve case, the working SED is very low and precision in the prediction of cycles to failure is vital for the use of the device in patients. If the SED level of the valve falls within the transition regime, there could be a significant variation in the lifetime prediction by using the equation derived from the power law. Furthermore, there is no data available in the literature that can confirm below which SED level the prediction is better represented by the transition regime; hence the lifetime prediction for unitensile specimens could also be inaccurate for the same reason.

The rest of this section will focus on the derivation of lifetime prediction from the

transition regime law and the fitting of this to experimental points. These points derive from nucleation tests of unitensile specimens and fatigue durability of prosthetic heart valve (PHV) prototypes for SEPS22 and SEBS20 with styrene cylinders aligned parallel to the strain direction.

The derivation steps are the following:

$$\frac{da}{dN} = A(T - T_0) \tag{3.30}$$

$$T = 2kWa \tag{3.31}$$

$$\frac{da}{dN} = A(2kWa - T_0) \tag{3.32}$$

$$\int_{a_0}^{a_f} \frac{da}{(2kWa - T_0)} = A \int_0^{N_f} dN = AN_f \tag{3.33}$$

Solve the integral by substitution:

$$u = (2kWa - T_0) \qquad du = 2kWda \tag{3.34}$$

$$\frac{1}{2kW} \int \frac{1}{(u)} du = \frac{1}{2kW} lnu = \frac{1}{2kW} ln(2kWa - T_0) \tag{3.35}$$

Integrate from initial to final crack size:

$$N_f = \frac{1}{2kWA} ln \left(\frac{2kWa_f - T_0}{2kWa_0 - T_0} \right) \tag{3.36}$$

with the condition:

$$a_0 > \frac{T_0}{2kW} \tag{3.37}$$

The values of k and T_0 are fixed by the strain and experimental fitting of the parameters to the crack growth curve, respectively. Hence, over a range of strain energy density we should be able to fit the relationship to the experimental points of the crack nucleation test and verify if they lie on a power law or transition regime. However, the prediction equation is expected to fail below a certain level of strain energy density, because of the logarithm's limit (eq 3.37). This limit does not necessary represent the point after which the crack stops growing, as will be demonstrated by the following results.

SEPS22

The first point to address for the application of equation 3.36 is the definition of a value for the final crack size (a_f). Since, by definition, the unitensile specimen will fail when the crack travels across the whole width, I take this as an approximation. The unitensile specimens are 4 mm wide; this value is also appropriate to represent a critical crack size for the failure of the valve.

In Figure 3.54, the nucleation points are plotted together with the power law and transition law prediction. The unitensile specimen nucleation points are separated between 1 mm and 2 mm thickness. It has already been demonstrated that the power law prediction is accurate for the SED range investigated. In the graph below, the transition law was plotted with the parameters listed in Table 3.13. Three cases are represented, as transition law I, II and III. I first assumed the initial crack size to be the same as that obtained from the power law prediction fitting. The transition line fits with good accuracy the set of point in the middle for the 2 mm case. If we were to assume that below that SED the transition regime would better represent the lifetime trend, then the nucleation points at lower SED should lie close to the transition line in the graph. However, the experimental points are still better predicted by the power law and would be underestimated by the transition regime.

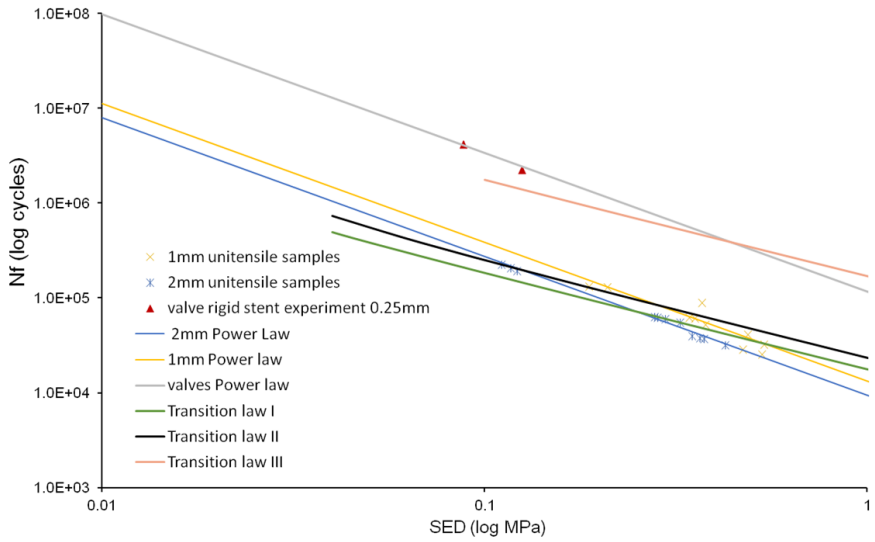

Figure 3.54: Lifetime prediction based on power law and transition law for SEPS22 parallel oriented. The plot includes nucleation points for unitensile samples 1 and 2 mm thick and rigid stent valves.

From this, I conclude that the transition regime starts at a lower SED and the transition line should be moved higher changing the initial crack size to fit the points

Table 3.13: Transition law prediction parameters for SEPS22 parallel oriented. Three cases represented in Figure 3.54 are summarised.

SEPS22	A	T_0 (kJ/m^2)	a_f (mm)	a_0 (mm)
I	1.2e-5	0.02	4	0.3887
II	1.2e-5	0.02	4	0.184
III	1.2e-5	2e-10	4	7e-10

at lower SED.

The same initial crack size value fits perfectly the nucleation points for the two different thicknesses and it also matches the value obtained from the fitting of the power law prediction to the 1 mm thick samples. One could assume, shown as prediction II, that the transition regime is not affected by the thickness of the samples. However, I do not have experimental points for unitensile samples below that SED level to prove that the transition regime modelling works better than the power law regime at such low SEDs. It is evident however that the power law prediction is still accurate for the low SED points. I can only assume that for that SED level we may be close to a transition point and for the valve lifetime calculation we should consider both predictions.

The triangles in Figure 3.54 represent experimental points for rigid stent experiments using valve prototypes (see section 3.3.4). The experimental points for the valves can be used as a test to verify the effect of the different predictions on lower SED. Figure 3.54 shows the fitting of the two predictions to those points. The grey line is the power law prediction, which works very well at lower strain. Both points lie on the same slope and the fitting gives an initial crack size value of 0.0017 mm. On the other hand, the transition law could not fit the data well. The transition line, in all three cases plotted, stops at a certain minimum level of SED because of the inequality required for equation 3.37. Decreasing the initial crack size moves the limit towards higher SED. There is no value of a_0 able to move the slope towards the experimental points of the valve.

At this point, I considered the hypothesis that the calculation of the parameter T_0 could be inaccurate since I did not collect a large number of experimental points for low tearing energy in the graph in Figure 3.22. I tried then to fit the valve's points by changing both a_0 and T_0 of equation 3.36. Table 3.13 shows the parameters of transition line III plotted in Figure 3.54. The values obtained are not realistic since we are not dealing with a quantum physics problem! The transition law is not able to

account for the valves' experimental points.

The fact that the prediction law derived from the transition regime does not work for thin small samples poses a limitation to its application. It is also arguable whether the results obtained for the unitensile samples are legitimate. Moreover, the fact that the limit of equation 3.36 varies with the initial crack size and strain energy density, makes it difficult to believe that it represents the tearing energy level after which there is no crack propagation.

SEBS20

The same analysis was performed on unitensile samples of SEBS20 with parallel orientation and rigid stent valves.

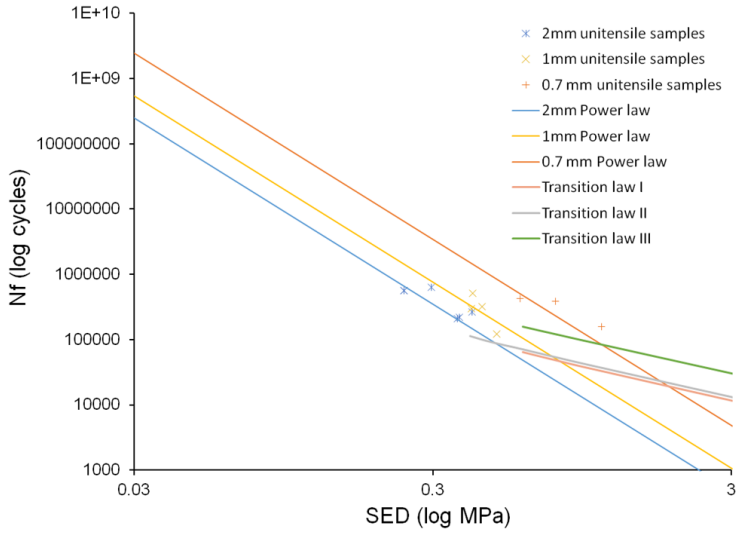

Figure 3.55: Lifetime prediction based on power law and transition law for SEBS20 parallel oriented. The plot includes nucleation points for unitensile samples 0.7,1 and 2 mm thick.

Table 3.14: Transition law prediction parameters for SEBS20 parallel oriented. Three cases represented in Figure 3.55 are summarised.

SEBS20	A	T_0 (kJ/m^2)	a_f (mm)	a_0 (mm)
I	9e-6	0.1	54	0.133
II	9e-6	0.08	4	0.087
III	9e-6	0.0005	4	5e-4

Power law and transition law predictions are plotted in Figure 3.55. The transition law parameters have been calculated in order to fit the nucleation points and are summarised in Table 3.14. The crack nucleation test on SEBS20 has been performed for 3 different unitensile specimen thicknesses: 2 mm, 1 mm and 0.7 mm. For the three cases the power law prediction worked accurately.

The transition law I prediction is plotted using the initial crack size obtained from the power law equation for 2 mm samples and the values of A and T_0 from the crack growth experiment. The transition line prediction stops at a higher SED than was used to measure the nucleation points. This is due to the limit imposed by the logarithm in equation 3.37. Following this result, I changed T_0 to a reasonable value, considering some inaccuracy in its calculation due to lack of experimental points (transition law II). The value of a_0 was changed to the one calculated for 1 mm samples . However, the line still lay distant from the experimental points and the limitation of the logarithm was not resolved. If this limit represented the energy threshold for crack propagation, it would contradict the fact that the power law prediction still works well at lower energy for the unitensile samples.

Finally, transition law III is an attempt at fitting by changing both a_0 and T_0. There was no set of parameters able to predict the points. The values in Table 3.14 produced the closest fitting to the nucleation points of 0. 7mm thickness. However, the value for T_0 would not represent the experimental data of the crack growth test in Figure 3.22.

Changing A or the final crack size does not influence the position of the slope. It can be concluded from this preliminary analysis that the lifetime prediction equation derived from the transition law regime is not applicable to the range of SEDs relevant to heart valve leaflets. On the other hand, the power law equation is an accurate instrument for lifetime prediction for the materials considered in this work.

3.3.7 Polivalve

The design and manufacture of a clinical valve, known as the Polivalve, was carried out in the Structured Material group in collaboration with Prof. R. Ascione.

Iterative improvement to the valve design over the past 4 years led to the latest prototype J6. Various testing of leaflet shapes and heights, moulding methods and block copolymers resulted in a potentially clinically effective PHV. The Polivalve mould is shown in Figure 2.16. The valve is manufactured by over-moulding of SEBS20 leaflets onto a previously fabricated SEBS29 stent. The microstructure orientation present in

a J6 leaflet is shown in Figure 2.17. The optimisation of cylinder orientation was consistent with the prediction of Serrani *et al.* [67] represented in Figure 2.7.

The material selection tool presented in this chapter and optimisation of the injection moulding process were critical to the improvement of the valve durability which have been achieved, as shown in Figure 3.56. The durability of PHV prototypes was tested according to ISO standard 5840:2015 in the DuraPulse. The designs from B to J3 had injection points at the top of each leaflet on the free edge, a soft material stent with concomitantly larger posts, and were made of SEPS22. Prototypes J5 and J6 were made of softer SEBS20, had injection points at the centre of each leaflet, and an over-moulded rigid stent made of SEBS29, allowing smaller posts. The central injection point improved the orientation distribution in the leaflet. SEBS20 was found to be more durable, as predicted from the fatigue model in section 3.3.3. Finally, between J5 and J6 there was an optimisation of leaflet thickness, as represented in Figure 3.56-b. Higher thickness resulted (unsurprisingly) in longer lifetime, which is consistent with the findings of the rigid stent experiments described in section 3.3.4. J6 had optimised leaflet thickness, based on the maximum thickness consistent with adequate hydrodynamic performance (if the leaflets are made too thick, the effective orifice area starts to drop because the leaflets cannot open fully during systole). Two sizes of J6 were manufactured to guarantee good size matching to the aortic anulus of a 70-80 kg adult sheep, used for preliminary *in vivo* short-term evaluations.

Four valves of the J6 prototype (two 19 mm and two 21 mm internal diamater) have been tested for durability in the DuraPulse and for hydrodynamic performance in the Pulse Duplicator, described in methods section. According to the standard, the opening and closing of the valves are assessed by the effective orifice area (EOA) and regurgitation fraction (REG), respectively. Calculation of these two parameters are described in chapter 4. The minimum EOA required by ISO standards is 0.85 cm^2 for 19 mm and 1.05 cm^2 for 21 mm internal diameter valves. The maximum regurgitation fraction allowed by ISO standard is 10% for surgical valves.

The valves' performances were measured before the fatigue test and, after 500 millions cycles, every 100 millions cycles until failure. The measurements of EOA and REG are presented in Figure 3.57 -a and b, respectively. After 500 million cycles the opening area started to decrease (minus 10-15%), however the EOA remained well above the minimum required by ISO standards until the end of the tests.

Regurgitation worsened after 500 millions cycles for 3 out of 4 valves, gradually exceeding the 10% regurgitation limit. This corresponded to the valves showing damages on the free edge of the leaflets, which clearly increased regurgitation. Nevertheless the

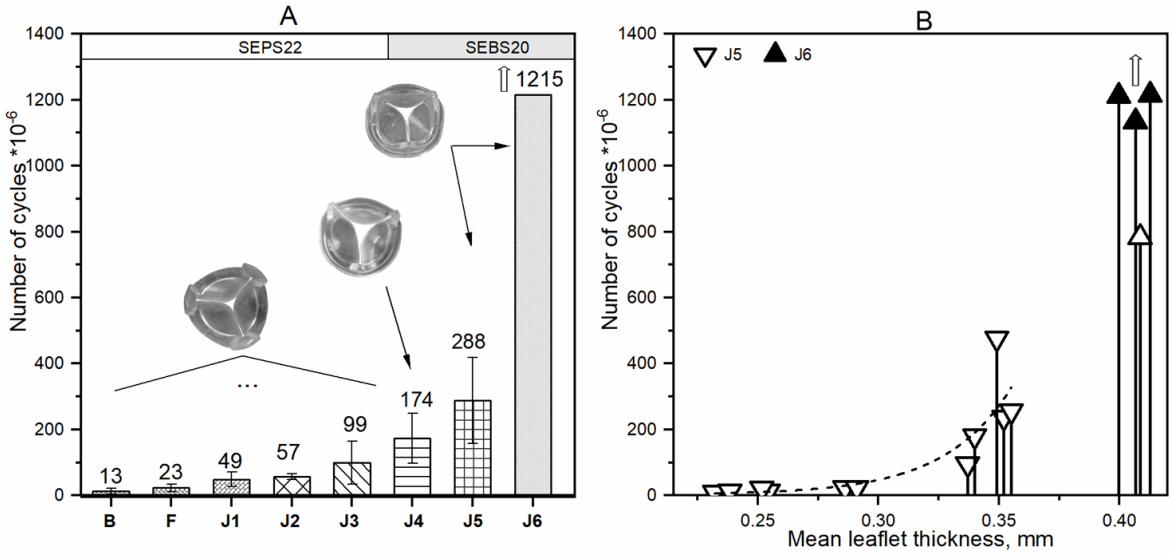

Figure 3.56: Bench durability testing: A: durability of PHV prototypes with leaflets made from SEPS22 and SEBS20. Error bars represent one standard deviation. Data for J6 valves does not show any variation and represents the actual state of ongoing test. B: Durability as a function of mean leaflet thickness for J5/J6 design. Ongoing durability testing of the J6 prototype is shown by shaded markers, while finished tests are represented by unfilled markers. Figure sourced from reference [6].

regurgitation fraction remained well below 20%, which is the maximum allowed by ISO standards for transcatheter valves. Hence, with these performances, the valves would not significantly compromise the health of a patient. Furthermore, the ISO standards only require testing to 200 million cycles and it is not clear what the status of the 10% limit is beyond the required cycles.

Figure 3.58 compared to behaviour of J6-Polivalve prototypes with different leaflet thicknesses and the best-in-class clinical valve made from fixed biological tissue (Carpentier-Edwards Perimount Pericardial Bioprosthesis). Photos of the PHV and the Edwards Perimount at peak diastole and systole are shown in Figure 3.58-a. The polymeric J6 prototype showed a 15% larger geometric opening area at peak systole than the Edwards Perimount reference valve, and a more circular orifice. Figure 3.58-b shows the pressure and flow waveforms acquired during pulsatile testing (5 l/min, 70 bpm) of the J6-Polivalve. The measurements of EOA, REG and mean systolic pressure difference are reported in Figure 3.58-c-e. The graphs compare the behaviour of different leaflet thickness PHVs with the Edwards Perimount reference valve. Sets of aluminium moulds were used to manufacture different leaflet thickness valves of 0.24 mm, 0.30 mm, 0.35 mm, 0.40 mm and 0.46 mm for the same valve geometry (prototype J6). All

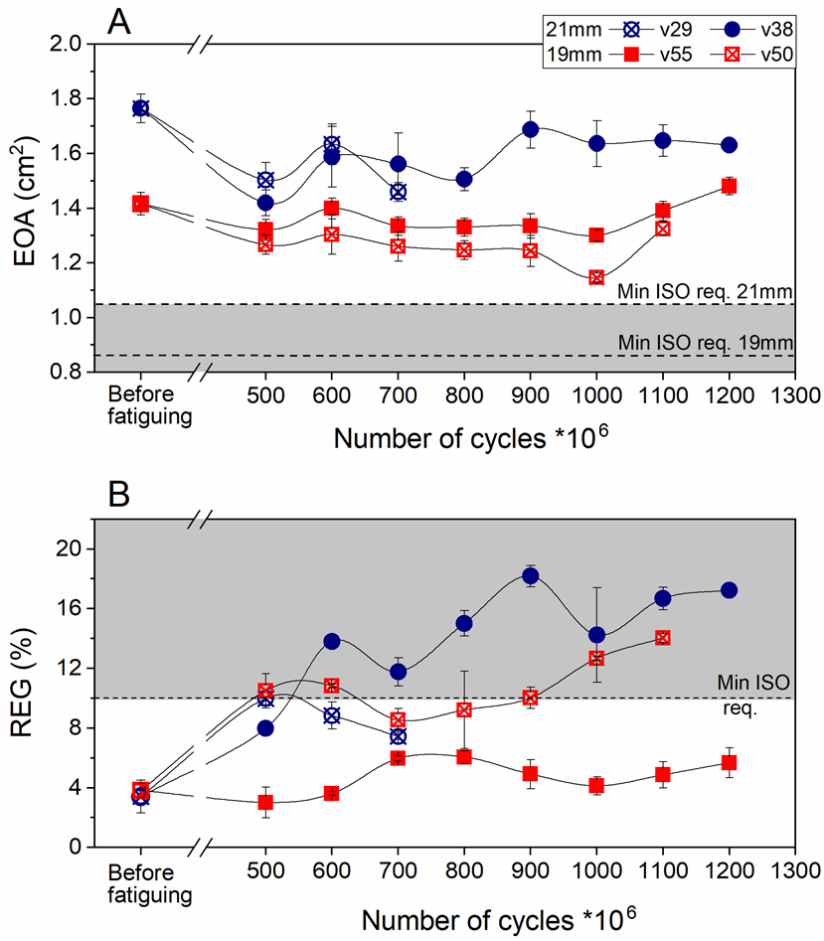

Figure 3.57: Hydrodynamic performance of fatigued J6 valves. A Effective Orifice Area (EOA); B Fractional Regurgitation (REG). Error bars indicate variation between repeated measurements of the same valve. Figure sourced from reference [6].

valves exceeded the minimum ISO standard requirements. As expected, decreasing the thickness improved the effective orifice area and mean pressure gradient across the open valve. Increasing the thickness of the leaflet resulted in reduced EOA and regurgitation fraction (Figure 3.58C-D) and, at the same time, increased durability. A compromised was made to optimise the leaflet thickness of the J6 prototype. The graph highlights the selected leaflet thickness (0.40 mm) for the *in vivo* trials, based on matching the effective orifice area of the same diameter Edwards Perimount valve.

Preliminary clinical feasibility evaluations consisted of *extra-vivo* (porcine/sheep hearts, animal cadavers), and *in vivo* (sheep) and bench-based evaluations. The animal procedures took place at the University of Bristol Translational Biomedical Research Centre (TBRC). All procedures were approved by the University of Bristol Research

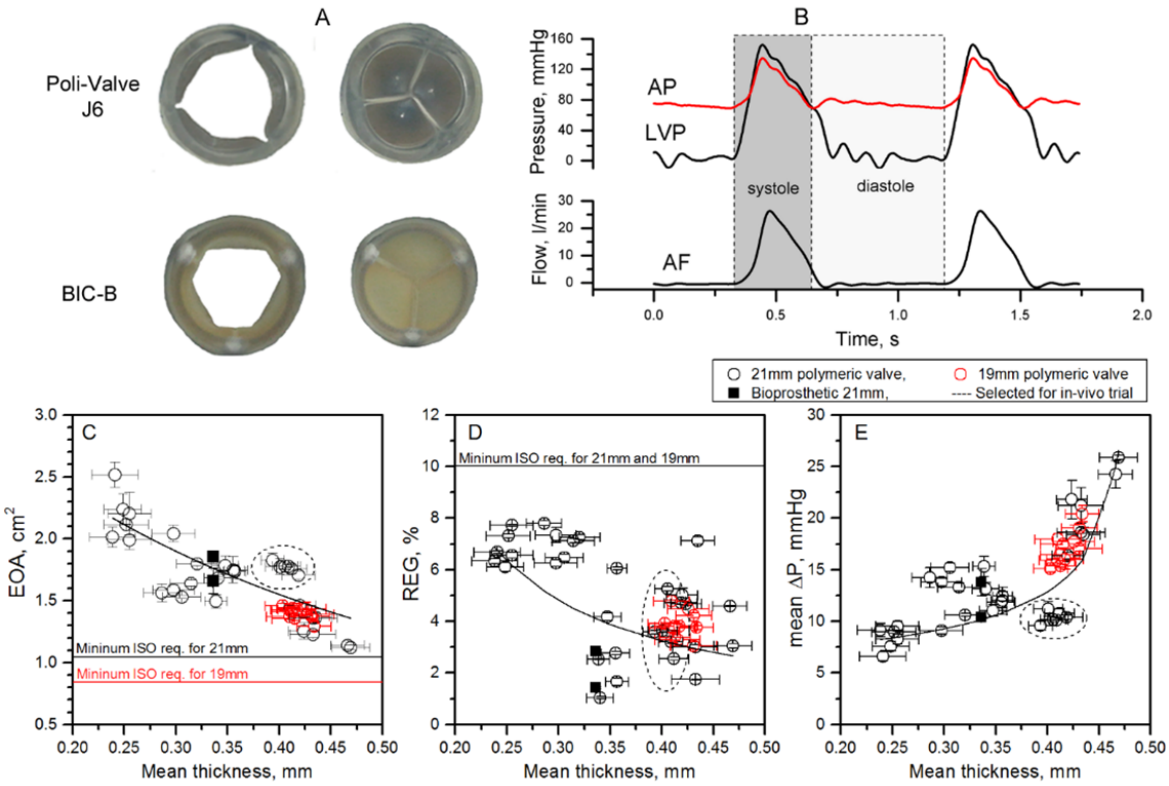

Figure 3.58: Measurements of hydrodynamic performance: A: Prototype J6 21 mm and Edwards Perimount 21 mm valve at peak systole (left) and diastole (right); B: Pressure and flow waveforms acquired during pulsatile tests of J6 valve: AP is aortic pressure, LVP left ventricular pressure, and AF aortic flow; C: Effective Orifice Area (EOA); D: Regurgitant fraction (REG); E: mean systolic pressure gradient ΔP. Error bars represent one standard deviation. The trend line catches the effect of leaflet thickness on hydrodynamics of 21 mm polymeric valves. Results for the J6 valve (21 mm) are circled by a dashed line; the 19 mm J6 valve selected for *in vivo* testing is represented by red markers. All data are prior to fatiguing. Figure sourced from reference [6].

Ethics committee and performed in accordance with the Guide for the Care and Use of Laboratory Animals and the United Kingdom Animal (Scientific Procedures) Act, 1986, under Home Office Project Licence PPL 7008975. The experiments were directed by Prof R. Ascione and surgery was carried out by Prof R. Ascione and Dr V.D. Bruno.

The *in vivo* short-term (1-24 hours post-operation) feasibility study (n=3) was carried out in 75-80 kg sheep: details of the procedure are reported in the paper [6]. Implanted valves showed no evidence of peri-valvular or trans-valvular regurgitation. Moreover, measurements of the average trans-valvular peak gradient during the test

matched those measured *in vitro* using the pulse duplicator. Post-*mortem* examination confirmed the structural integrity of the PHVs, with no evidence of any acute valvular clot/thrombus after 1-24 hr without anticoagulation.

It has been demonstrated that Polivalve J6 comfortably exceeds ISO standards for *in vitro* testing, has exceptional *in vitro* durability (the best reported for any polymeric valve); and showed encouraging preliminary acute *in vivo* feasibility/safety testing in sheep without anticoagulation.

3.4 Conclusions

The main goal of the fatigue study was to create a tool for material selection for the PHV application; with the potential also for use in other applications where long term, low strain durability is required. The long lifetime requirements for the valve called for a practical, reliable and quick assessment method - compared to the much longer iterations (many months) required is new valve geometries, materials or processing conditions were assessed by direct accelerated durability testing.

This study presents a series of novel conclusions on the appropriate factors to take into account in the design and durability prediction of polymeric heart valves. A model based on the power-law equation successfully predicted the lifetime of the material for a given orientation, thickness and manufacturing technique, in both valve prototypes and unitensile specimens. Geometry does not seem to be a limiting factor, which is encouraging for the application of the model to valve lifetime prediction (or in future perhaps to other applications). Orientation was demonstrated to be a key aspect to consider when modelling fatigue for anisotropic materials.

Reduction of specimen thickness was demonstrated to improve lifetime for unitensile sample (at constant strain). On the other hand, the rigid stent experiment for the valve demonstrated that below a certain thickness threshold, which is material (and probably processing method) dependent, the lifetime of prototypes worsen, probably due to the difficulty of accurately manufacturing to high quality very thin samples. This information is fundamental to valve design. The effect of leaflet thickness suggests that MED500400 valve should be manufactured at higher thicknesses, since the softness of this material would make this possible whilst maintaining adequate hydrodynamic performance. SEBS20 has been demonstrated to be the best material of those tested for the heart valve application. Prototype SEBS20 valves have been manufactures and tested (following ISO standard protocols) *in vitro* and in an acute feasibility study in sheep; and shown to be promising for surgical application. A chronic trial in sheep is

about to commence as the next step in progressing towards first in human testing.

The transition regime failed to predict the lifetime of the tested specimen. The power-law equation was confirmed to be the appropriate tool for total-life prediction in the range of SED relevant to polymeric heart valves.

The results of this study showed that there are still aspects of the fatigue properties of TPEs that should be investigated. Firstly, bi-modal and 45° degree orientation should be investigated to improve the FE model and the prediction of SED in valves. The effect of testing frequency and thickness should be investigated under different circumstances, such as different degrees of anisotropy, molecular weight and styrene fraction. The latter aspects should be separately studied to define a criteria to identify long lasting materials.

A thorough investigation of all the aspects presented in this study could allow the application of the model based on crack growth and nucleation of standard specimens to other applications.

Chapter 4

Calcification

4.1 Introduction

Calcification is responsible for the majority of bioprosthetic heart valve (BHV) failure and has also been shown to affect cardiovascular polymeric implants, such as blood pumps, cardiovascular grafts, artificial hearts and polymeric prosthetic heart valves (PHV) [142]. The mechanisms behind this phenomenon have been extendedly studied. However, because of the problem complexity, the topic still requires further understanding.

Clinical data show that less than 1% of porcine aortic bioprostheses suffer from disfunction before 5 years after implantation in adults. However, after 10 years 20-30% of the implanted valves fail and more than 50% after 12-15 years post implantation [149]. The 50% valve failure within 15 years after implantation is mainly related to cuspal calcification and secondly tears and regurgitation. Calcification is also responsible for stenosis, related to the stiffening of the leaflet, and calcific deposits embolization [143].

The calcification process consists in the nucleation and growth of calcium phosphate crystals on substitute material. Physiological calcification is the crystallisation of calcium phosphate for the growth of healthy bone. Pathological calcification refers to mineralisation of tissues or surfaces that would not normally have calcium salt depositions. For the BHV, this leads to leaflets stiffening which can cause stenosis or tearing of the valve. Calcification of porcine and bovine BHV is considered their principal mode of failure. Other complications are vascular obstruction and embolization of calcific deposits [149].

The calcification process in a tissue valve starts from the residual devitalised cells. The mechanism consists of the reaction of the calcium, rich in the extracellular fluid,

and phosphorus within the membrane, yielding calcium phosphate mineral deposits [143].

The variables involved in the process, such as patient age, immune system, mineral levels in blood, make it very difficult to predict when calcification and failure will occur. The current scientific community focus is to find strategies to prevent calcification in the first place. Therefore, a fundamental step for the design of a prosthetic valve is to verify if the material is prone to calcification. The ISO 5840 requires *in vitro* testing to assess the physical and chemical stability of the materials, as well as biocompatibility (see chapter 5 for discussion on the latter).

So far, animal trials have proven to be an effective way to model the calcification performance of substitute implant materials. The morphology of the deposits resembles that observed in clinical specimens. BHV have been mounted in sheep or calves and tissue samples have been implanted subcutaneously in young mice, rats and rabbits. The advantages of *in vivo* testing (*i.e.* animal valve replacement) are the ability to evaluate the performance of the design, look into the process and account for clinical failure, study blood/material interaction and finally collect data for regulatory agency approval to move into clinical trials [143].

Although animal trials are indispensable for the development and design of a PHV, *in vitro* experiments can elucidate the calcification performances of materials and provide a comparison and threshold for material selection.Above all, they are a cheaper and quicker method, able to be performed in any laboratory setting [143]. However, there is no consensus on a standard method for calcification experiments on substitute valve materials.

This chapter reviews the main mechanism responsible for calcification in BHV and PHV, anticalcification techniques, some of the methods used for *in vitro* calcification testing, and finally experimental *in vitro* calcification assays are reported, to study the performance of the SBCs shortlisted for the valve application in this work.

4.1.1 Mechanism of calcification for soft tissue and failure of BHV

Calcium salt deposition in the matrix of specialised tissues is a vital process for living beings. The main examples are bone and teeth, which protect soft tissues (ex: heart, brain, lung), support the body and constitute a mineral reservoir. Indeed, calcium is taken as a food supplement in many diets. However, calcium deposits are also responsible for severe pathological complications, such as stones' formation and, most

importantly, vascular lesion [146].

The pathogenesis of tissue calcification is deposition of calcium phosphate (hydroxyapatite, HAP is the predominant form). The nucleation of the crystals is regulated by the interaction between the calcium, present in blood and interstitial cell fluid, and phosphorus, largely present in cell membranes. The first deposits enlarge and coalesce until large mineralized nodules stiffen and damage the tissue dissecting between its planes and often ulcerating and deforming the structure [143].

Native living cells have very high gradients of calcium concentration between internal and external fluids, with the intracellular concentration being 10,000 times smaller than the extracellular one (0,1 mM inside, 1000 mM outside the cell) [143, 142, 144]. The gradient of calcium across the cell membrane is maintained by several active pumping mechanisms, regulated by an ATP-dependent calcium ion exchange system and the intracellular calcium buffering mechanism. The two main mechanisms responsible for Ca^{2+} extrusion are the Ca^{2+}ATPase plasma membrane pump and the Na^{+}/Ca^{2+} plasma membrane exchanger [144].

However, necrotic or devitalised cells in the substitute tissue of the BHV no longer have these removal mechanisms, and passive entrance of calcium happens unimpeded. Calcification in BHV starts mainly from nonviable connective tissue cells that have been devitalized or damaged by glutaraldehyde pre-treatment. The mechanism is believed to be analogous to natural tissue mineralization. The membranes of the cells are rich in phosphorus and serve as sites for the nucleation of crystals. Rat subdermal implants showed that the calcium influx reacted with the phosphorous within the first 48 hr to form calcium phosphate [145, 147].

Collagen also act as nucleation sites for calcium phosphate minerals independent of cellular calcification, glutaraldehyde or formaldehyde cross-linking enhances calcification. Elastin calcification occurs independently of any pre-treatment [143]. The degree of calcification and the morphology of the deposits are similar for both bovine pericardium and porcine aortic valve, which confirms the fact that the mechanism for calcification is the same.

The incidence and rate of calcification in BHV is caused and related to several factors. The main determinants for implanted material calcification are host metabolism, material structure and chemistry, and mechanical factors. It has been shown that the calcification process is accelerated in young patients, by glutaraldehyde fixation and high mechanical stress [143, 146].

Rat subdermal implants of porcine bioprosthetics showed early calcific deposits on cells devitalised by glutaraldehyde pre-treatment, which later extended to collagen fib-

rils. Butany and Leask reported that glutaraldehyde fixation on the tissue valve led to severe alteration of the surface which resulted in cross-linking of collagen, providing favourable sites for calcification [147]. The hypothesised mechanism concern the cross-linking properties of glutaraldehyde, which stabilises the material but also creates nucleation sites by modifying the phosphorus rich structure in the tissue.

The immune system has been demonstrated to have a key role in the initiation of calcification. The residual antigens in the implanted tissue generate an immune response: the IgM/IgG antibodies entering the valve matrix cause the formation of macrophage deposition on the tissue surface, the deposits break the collagen and initiate the calcification process. This is one of the reasons why in young patients with strong immune systems the rate of calcification is much higher (50% failure within 3 years for children) [149].

Finally, calcification at every level is accelerated in areas of high stress, such as the flexion point in the valve. Prosthesis calcification often occurs at the leaflet's commissure and basal area of the cups, where stress aggregation is higher. The consequence is localized tearing and stiffening in these sites, which leads to failure through stenosis or regurgitation [148].

Calcification is also one of the factors associated with infective endocarditis. In the area where calcification or tear occurs there is a higher degree of mononuclear cell infiltration, responsible for the infection [149].

4.1.2 Polymer calcification

The application of polymers in prostheses has raised the concerns over material compatibility and stability. The mechanisms for polymer blood contact calcification are still unclear. Few hypotheses have been postulated after *in vivo* and *in vitro* tests on medical grade polymer, such as polyurethane, PTFE and SIBS, on blood pumps, trileaflet valves and vascular grafts. Several hypotheses have been proposed to explain the mechanism and factors causing the calcification of the polymeric materials. This section summarises the main studies and findings on polymer calcification mechanisms.

Levy *et al.* [142] in their review presented some findings on PU properties after *in vivo* tests. The tests showed that PU undergoes a similar pathophysiology for calcification for both blood pumps and valve prostheses. SEM images showed that the HAP deposits consist of irregular and slightly elevated plaque areas. The proposed mechanisms are direct adsorption of calcium and phosphate in PU, and nucleation of calcium in adherent degraded cells (platelets, inflammatory cells or erythrocytes)

or entrapped cells within deposited fibrin thrombus. Furthermore, several *in vivo* experiments on blood pump and trileaflet valves demonstrated that the areas with higher stress showed plaques of calcium, regardless of the material tested. According to the authors, this might be caused by high haemodynamic forces able to traumatize the cells and lead to further deposition of blood cells and platelets.

Park *et al.* [150] investigated the calcification properties of PTFE (Teflon), PU (Pellethane) and silicone (Sewoon medical Co.) *in vitro*. The experiment consisted of a continuous supply of calcium solution (see section 4.1.4 for details) to sterilized polymeric films over 21 days. The calcification profile was similar for all the samples; however, PTFE showed a greater absolute value of calcium compared to the other two materials. This phenomenon was explained considering the effect of the rough surface of Teflon. The Teflon graft consists of nodes and fibres which confer a certain porosity to the material. Permeation of calcium and phosphorous is believed to increase because of the formation of biological lining on the porous PTFE graft. On the other hand, PU and silicone presented a soft and smooth surface which could be the reason for the reduced extent of calcification.

Coleman *et al.* [151] proposed that biological components absorption (such as lipids) could alter the physical and mechanical properties of the polymer and create nucleation sites for HAP. They also stressed the importance of hydrophilicity of the material, which was shown to significantly influence the calcification rate. They gave the example of poly(hydroxyethyl methacrylate), a hydrogel with about 40% water, reported to calcify in different biological environments. The gel permeability to ion diffusion was identified as the main cause for precipitation and crystallization in the bulk. They also reported a second mechanism related to porosity, since they showed that porous gels calcify faster than the homogenous one.

Coleman [152] also studied PU artificial blood pumps. He studied non textured Biomer, Avcothane and Pellethane mineralization, which he related to presence of microbubbles and cracks, but also to the capability of PU to selectively extract ions, especially calcium ones, through cation and soft segment interactions.

Bernacca *et al.* [153, 156] tested PEU and PEUE flexible-leaflet PHVs for fatigue and calcification. The prototypes underwent both *in vitro* and *in vivo* tests (*i.e.* subdermal rat implant). The PEUE valves were fabricated with a PEU frame and dip-coated in PEUE since the polymer cannot be melt processed. They found small calcific deposits in the coaptation area and along the leaflet free edges, mainly close to the position of maximum bending. The fatigue tested PEU valve analysed post failure showed calcific deposits on the cracked sites of the leaflets and nothing in the

rest of the valve, but it could not be concluded if the calcification was the cause of the crack formation or a post event. For PEUE valves, which lasted longer, the calcium deposits developed in areas of high mechanical strain but not associated with cracks. FTIR spectroscopy on the calcified PEUE leaflets showed an alteration in the bonded carbonyl peak, which suggests that the hard block of the copolymers was involved in the calcification process. The opposite was proved for PEU, where the soft segments more likely calcified. They argued that the urea links in PEUE, rather than the urethane ones in PEU, created preferentially available binding sites for calcium, despite the higher fraction of soft segments in the first polymer. Subdermal and *in vitro* test did not show a significant difference between the two materials' calcification performances, and in general little calcification compared to bovine pericardium.

Baloori *et al.* [154] investigated the effect of flow shear rate and surface roughness on polyurethane (Angioflex) leaflets and polycarbonate. They proved that rough or cracked-roughened surfaces are more prone to calcification. Moreover, calcification was even more pronounced when the samples were exposed to low shear rate for both smooth and rough surfaces. According to the authors, calcium and phosphorus would be trapped in the surface irregularities, which would act as nucleation sites in the case of low shear rate. With higher shear rate, the elements would be washed away by the flow. EDX analysis of the calcified samples also showed that there was no subsurface diffusion of the calcification deposits and no trace of calcium or phosphorous was detected beneath the surface. This proved that PU calcification is a surface dominant mechanism. Moreover, a peeling test demonstrated the presence of a weak bond (Van der Waals force) between the PU surface and the HAP layer. The comparison between PC and PU showed that the PC, independent of crack presence on the surface and shear rate, was less calcified.

In a later study, Baloori *et al.* [155] studied the performance of a trileaflet polyurethane valve (Angioflex) in an accelerated fatigue tester in calcification solution. Calcium deposits were found only on the leaflets' surface, while they also observed crack formation which were not present in the static *in vitro* calcification test previously performed by the authors. They also investigated the effect of bisphosphonate treatment on Angioflex, which was supposed to inhibit calcification but failed to do so in their *in vitro* experiment.

Wheatley *et al.* [156] implanted PU valves in the mitral position in growing sheep for a 6-month trial. Their main finding was some minor focal calcification correlated to the previous attachment of fibrous and thrombotic material on the leaflet surface. The calcification was only extrinsic and some early penetration on the polymer surface

was detected due to material deterioration. The intact area of the surface did not show any intrinsic calcification.

Imachi *et al.* [157] advanced a new hypothesis to explain the calcification mechanism of blood-contacted polymers. An artificial heart was attached to a goat for 532 days, made with a segmented polyurethane coated pump, jellyfish valves and thin PU based membrane polymeric valve. The PU used for the valves and coating was a copolymerized polyether-polyurethane with polydimethylsiloxane (KIII, Nippon Zeon Co.Ltd., Japan). Calcification was concentrated on the portion that sustained the higher stress, no deposits were found on the compressed side and or the static parts of the valves. They hypothesized that the stretching of the material would create microgaps and loosening of the polymeric chains, which would give space for biological molecules to penetrate in the surface and to attract Ca ions, followed by the mineralization reaction with phosphate ions.

Hilbert *et al.* [158] evaluated explanted polyurethane (Biomer, Ethicon Inc, USA) trileaflet valves after up to 21 weeks in juvenile sheep in the mitral position. The leaflets calcified and the valve became stenotic. They observed two types of calcification: the first type was on the surface of the material or at the interface between the surface and microthrombi or fibrous sheets; the second type was associated with the presence of degenerated cells within the thrombotic and fibrous materials. Calcium plaque like deposits were observed both at the inflow and outflow of the leaflets and an increased presence of those was found on the free-edges and near the posts. They correlate the presence of these deposits with surface modifications on the PU introduced during manufacturing, processing, or mechanical stress. The alteration of the physicochemical properties of the polymer was identified as the most plausible cause of calcification.

Golomb *et al.* [159] investigated the effect of porosity, thickness, and incubation time of polyurethane (Pellethene, Dow Chemicals, USA) during *in vitro* calcification. They observed that: longer incubation time lead to higher HAP levels; thicker samples were more calcified; higher porosity significantly increased calcification levels for both thin and thick films. The increase in volume and surface area with higher thickness lead, according to the authors, to more calcium phosphate solution absorption, hence higher calcification. The same goes for higher porosity. However, they showed that some calcific deposits were found in the non- porous material cross-section. The mechanism involved in their experiments is not correlated to any cellular involvement, which suggests an intrinsic calcification is happening on PU surfaces.

In a different study, Golomb *et al.* [160] focused on the effect of the hydrophilicity relationship with calcification of PU foam (Hypol FHP 2002, Grace,USA) and PU films

(HEPB, Norwich Eaton, USA) comparing *in vitro* and *in vivo* (subdermal rat implant) results. Marked calcification was detected in both experimental environments. Only PU films had very low amount of HAP on the surface *in vivo*. They suggested that the water capacity of the material directly correlates with the bulk calcification level and it is enhanced by the affinity of the sites of the material with Ca cations. In particular, the affinity of the material with the metal ions generates the calcification cascade and the absorbed water facilitates the supply of calcium and phosphate ions. Also voids and pores were identified as facilitators of water absorption and accelerators of the latter mechanism. The same findings were confirmed *in vivo* on a subdermal rat implant model [161].

Kekec *et al.* [162] tested calcification resistance *in vitro* with simulated body fluid of polyisobutylene (PIB) and PIB-based materials. They investigated the performances of PIB, PIB based polyurethanes such as PIB-PU and PIB-PUU, PIB-PU containing S atoms (PIBs-PU), SIBS and reinforced PU-based PIB with organically modified montmorillonite. These materials were compared with a commonly used PU for medical application, Elast-Eon. They pointed out that polyether-based PU containing ether oxygen atoms are more prone to calcification and they demonstrated that the PIB on the surface highly improves their HAP resistance. According to their studies, the chemical structure of high molecular weight PIB gives great resistance from immune system attack, enzymes and prevent small molecules diffusion. Thanks to the densely packed inert repeat unit -CH2C(CH3)2-, PIB based materials are considered the most biocompatible and biostable elastomer available. They observed extensive calcification on Elast-Eon, which they correlated to the chelation of Ca^{2+} at oxygen sites in the soft segments.

PIB and PIB-PU had no HAP deposits, while PIB-PUU showed encrustation on the surface. The latter polymer has higher nitrogen content on the surface and bifurcated hydrogen bonds, which were identified by the authors as the potential causes for the increase of calcification deposits, since they provide binding sites for Ca and P. PIBs-PU showed less calcific deposits than PIB-PUU, probably because S sites for chelation were less then N sites in PIB-PUU, but it could also be because of sulphur oxidation due to oxygen presence in the SBF, according to the authors. Sulfone groups were, in fact, proved to promote calcification [163]. Since the mechanical strength of PIB-PU is reduced by a high fraction of PIB, they tried to reinforce the material with montmorillonite nanolayers and this was shown not to modify the original calcification resistance properties. SIBS was demonstrated to be very lightly encrusted, they correlated the HAP deposits to the polystyrene presence.

However, Wang *et al.* [164] implanted SIBS trileaflet valves in sheep and demonstrated that the valve failed due to deformation and cracking on the leaflets, with severe blood reaction. They found extrinsic calcification on the leaflets around surface cracks.

Liu *et al.* [165] investigated the effect of neutral, positively and negatively charged functional group with similar density on the HAP growth mechanism on their surfaces. They deposited on a gold coated silicon wafer –COOH, -NH_2 and –CH_3. *In vitro* tests after 14 days showed inhibition of crystallization on the -CH_3 surface and promotion of calcification for the charged surfaces. The negatively charged surface absorbed Ca^{2+} ions, which than attracted $PO_4{}^-$ and formed the initial crystal layer. The effect of the functional group appeared to grow weaker as the crystallization proceeded. However, the supersaturated solution simultaneously showed homogeneous nucleation which formed the upper layers of the HAP crystals. According to the authors, the latter phenomenon explains the adsorption of the HAP in the positively charged solution. Since the electrostatic interaction between -NH_2 and $PO_4{}^-$ was considered too weak, they hypothesized that the small nuclei cluster in the supersaturated solution were negatively charged, due to unbalanced ions gatherings, and were adsorbed on the surface. The neutral functional group showed fewer crystals, probably formed by adhesion due to the long immersion. However, compared to the hydrophilic control surface, the -CH_3 surface showed even fewer crystals thanks to its hydrophobicity. This indicated the importance of interface affinity as a key factor in the adsorption and nucleation of HAP.

Brubert [5] studied the *in vitro* calcification performances of SBCs for PHV application. He designed a novel device to simulate *in vitro* calcification, where both static and dynamic test could occur for a large number of samples. He tested SIS18, SIBS30, SEBS20, SI/BS19, SEPS22 and heparin coated SEPS22 comparing them with treated pericardium tissue (the numbers on the polymer name represent the styrenic fraction). The samples that were dynamically strained registered a higher calcification rate. He also proved that pericardium samples calcified more than the polymeric ones. Heparin coatings had slightly lower calcium levels. In general, the samples were mechanically stiffer at the end of the calcification cycles, which, according to Brubert, was correlated to the filling of the surface defects with the deposits. SEM analysis showed that calcium was not deposited on the sites were micro-crack were present. The material tested are hydrophobic and the surface roughness was identified as the main feature influencing static calcification. Lower styrene fraction corresponded to lower calcium level, which seemed in agreement with the theory that PS is prone to calcification [163].

The phenomena influencing the calcification mechanism of polymeric materials are

likely to be a combination of various biochemical and mechanical factors. Summarised below are the main mechanisms causing polymer mineralisation according to literature studies:

- Water capacity, hydrophilicity
- Surface porosity and roughness
- Volume and surface ratio (thickness related effect)
- Low shear rate
- Mechanical stress concentration and loosening of the polymeric chain
- Surface modification (other polymers or coatings)
- Chemical affinity with Ca^{2+} cations of the polymer chain on the surface
- Microcracks and defects due to manufacturing and processing.
- Extrinsic calcification due to biological material deposition and calcium binding protein absorption (only detectable for *in vivo* experiments)

It is unclear which factors influence the calcification rate. Not all of them were noticed in every experiment and every material tested. It can be intuitive to think that if the material is prone to calcification because of its chemical structure, every test should show regardless some calcification, and that other factors can only influence its level. In this case, a simple *in vitro* test could screen qualitatively the calcification potential of the material. However, it could also be that other factors such as mechanical stress, defects or extrinsic calcification would trigger calcification despite the poor affinity of the chemical structure. Further investigations are needed on the topic to successfully apply polymers in cardiovascular implants.

4.1.3 Anticalcification techniques and treatments

The scientific response to tackle the calcification problem for BHV and PHV has resulted in a quest for an anti-calcification treatment. There is no effective therapy available to remove the calcific deposits already formed on implanted prostheses. The aim therefore is to find a material treatment or a localized drug delivery to inhibit calcification.

Systemic therapy with anti-calcification agents (calcium chelators) can directly affect calcium metabolism and inhibit bone formation. That is why localized drug delivery has been studied as a preferred means to deliver the anti-calcification treatment to the prosthesis. Animal models showed that EHBP (ethane-1-hydroxy-1,1 bisphosphonate) incorporation in polymers such as ethylene vinyl acetate, silicone and PU is an effective strategy. Bisphosphonate is a well-known HAP growth inhibitor and it is approved by the Food and Drug Administration (FDA) as a hypercalcemia of malignancy treatment or to stabilize osteoporosis [143, 166].

Alferiev *et al.* [167] demonstrated that bisphosphonate derivatised PU did not calcify in circulatory sheep model implants after 90 days. They modified polyurea PU (Biospan, Polymer Technology Group Medical LLC, USA) and polycarbonate PU (Bionate 80A, Polymer Technology Group Medical LLC, USA) performing hard segment alkylation followed by covalent binding of a thiol-bisphosphonate. They carried out rat subdermal implants for 60 days and sheep cusps replacement for 90 days for both derivatised and underivatised materials. The covalently bonded bisphosphonate did not dissociate during the test and caused an increase in water capacity in both PUs. The experiments showed marked differences between the modified and unmodified PUs, since no calcification in derivatised PUs was found while some deposits formed in the original PUs. Bisphosphonate acts by disrupting calcium phosphate crystals, specifically poisoning the crystallization of calcium phosphate mineral phases. It is also believed to inhibit alkaline phosphatase, hence reducing calcification through devitalized adsorbed cells, especially important for BHVs [143, 166, 167, 142].

Degeratu *et al.* [168] investigated the influence of aluminium depositions of carboxymethylated poly(2-hydroxyethyl-methacrylate), a biomimetic polymer able to mimic the mineralisation process happening in bone. They incubated the polymer pellets in a Simulated Body Fluid (SBF) solution with addition of Al^{3+} or aluminium foil and measured concentration of Ca^{2+}, $PO_4{}^{-}$ and Al^{3+} in the mineral deposits dissolved in HCl. The results demonstrated that high concentration of Al inhibits HAP growth and low concentration reduces crystal diameter. Aluminium was incorporated into the forming minerals and led to disruption and structural modification of the deposits by complexing with the phosphate [166]. Only mineral plates were found on the polymer surface instead of a calcospherite shape deposits.

PU modification was studied also by Ghanbari *et al.* [171], who produced a novel nanocomposite polymer polyhedral oligomeric silsesqioxane- poly(carbonate-urea)urethane (POSS-PCU). *In vitro* accelerated pulsatile pressure test in SBF solution for up to 31 days showed a considerably lower amount of calcium on the modified PU compared

to the unmodified version (p=0.015) and glutaraldehyde treated bovine pericardium (p=0.008). The material showed great tear resistance and no cracks or holes on the surface after the tests, suggesting that the lack of this possible nucleation sites protected the material. Furthermore, POSS-PCU is more hydrophobic and the surface nano-architecture positioned the POSS rich hard segment closer to the surface (soft segments of PU seemed to calcify more [153]). Both mechanisms were proved to lower the chances of HAP nucleation.

Bernacca and Withley [128] studied the effect of surface modification of PEU and PEUE on the calcification behaviour with heparin, taurine, 3-aminopropyltriethoxysilane and polyethylene oxide (PEO). The different types of surface modification did not show a significant alteration of the materials investigated towards calcification, except for PEO which had greatly increased calcification.

Vyavahare *et al.* [166] synthetised a series of PUs which proved to be calcification resistant. They covalently bonded EHBP, heparin or both, to the hydroxy terminus of the PU through polyepoxidation. After 60 days in a rat subdermal study, the modified PU showed insignificant calcification while the unmodified one was significantly calcified.

Chanda *et al.* [170] tested heparin bonded substitute tissues subcutaneously in rat for 5 months. Jugular veins coated with heparin did not show any improvement. However, both porcine thoracic aorta and pulmonary artery had significantly lower calcium contents than the glutaraldehyde-cross-linked versions.

Brubert [5] also coated SEPS22 with heparin (Corline ®, Corline Systems, Sweden) and performed dynamic *in vitro* test with SBF. The heparin coated samples showed lower calcium level compared to the uncoated counterpart. Preliminary evidence of heparin coating inhibiting calcium crystal growth on polymeric surfaces, in addition to the already proved blood compatibility improvement (see chapter 5), motivated further investigation of the effect of heparin on the SBCs considered in this work. *In vitro* tests were performed on CHC™Corline Heparin Conjugate kit (Corline®,Uppsala, Sweden) and ASTUTE®Advanced Heparin Coating (BioInteractions Ltd.,Reading, UK), as explained in the following sections.

4.1.4 Method for calcification tests

The validation of an *in vitro* model to evaluate calcification performances of implanted substitute materials has been the focus of research for several years. *In vivo* models are very expensive and time consuming. Moreover, the criterion of repeatability is not

often met for animal trials and a large number of subjects is usually needed.

To overcome this issue, the scientific community has been developing *in vitro* models, both static and dynamic, to simulate human blood plasma and physiological mineralisation conditions. The synthetic solutions are designed to obtain hydroxyapatite precipitation in the solution and different studies have come up with different solution compositions.

Golomb *et al.* [159] showed that the HAP concentration deposited in their *in vitro* model was comparable to *in vivo* experiments in sheep. While the sheep experiment took up to 21 weeks, the *in vitro* model could simulate the same deposition mechanism in 30 days.

Baloori *et al.* [155, 154] compared the Golomb *et al.* [159] solution with Starcher *et al.* [173] in accelerated tests of PU heart valves. They concluded that the first one is more representative of the calcium content present in HAP formed *in vivo*. The composition of the two solutions are shown in Table 4.1.

Table 4.1: Metastable calcifying solution compositions from Golomb *et al.* [159] and Starcher *et al.* [173] (mM).

	$CaCl_2$	K_2PO_4	Ca/PO_2	KCl	pH	buffer
Golomb *et al.* [159]	3.87	2.32	1.67	/	7.4	Tris
Starcher *et al.* [173]	1.5	1.25	1.2	55	7.41	Barbital

Bernacca *et al.* [169] studied three different calcifying solutions in dynamic *in vitro* test (Rowan Ash fatigue tester) of glutaraldehyde fixed bovine pericardium valves. The compositions of the three solutions are listed in Table 4.2. They kept to simple solutions in order to minimize the number of parameters, whilst still achieving calcification using close to physiological concentrations of Ca and P. The most reliable solution was number 3, which showed consistent calcification. Solutions 1 and 2 only minimally and inconsistently calcified the valves. They traced back the reason to the lack of buffer, which led to a pH 5-6 environment. These levels of pH kept calcium and phosphate ions in solutions, preventing precipitation and calcification. Only solution 3 was considered for further calcification studies.

Extensive studies have explored Simulated Body Fluid (SBF). Kokubo *et al.* [172] reviewed SBF development history and trials. SBF was initially designed as a prediction tool to simulate apatite crystal formation as a confirmation that the synthetic material could bind to living bone. The idea was to replicate the ion concentration

Table 4.2: Calcium, phosphate and buffer composition of Bernacca *et al.* [169] study on *in vitro* dynamic calcification of bovine pericardium valves.

Solution	Calcium (mmol/l)	Phosphate (mmol/l)	buffer
1	2.5	none	none
2	3.0	2.25	none
3	2.0	1.2	MOPS (pH 7.4)

of human blood plasma (HBP). The first solution lacked SO^{4-}, which was corrected in the current SBF version (see Table 4.3 for complete compositions). A revised version adjusted the value of Cl^- and $HCO_3{}^-$ to better replicate HBP values. However, it showed calcium carbonate precipitation and was not considered suitable. A newly improved version of SBF (n-SBF) changed the level of Cl^- and proved to have very similar performances to the previous SBF. The authors proved that SBF experiments on a glassy material (P_2O_5-free Na_2-CaO-SiO_2 glass) gave very similar apatite value compared to the results from rabbit tibia implantation of the same material for the same period. These results showed that SBF can simulate calcification, both qualitatively and quantitatively.

Table 4.3: Ion concentration (mM) of SBF solutions compared to human blood plasma values according to Kokubo *et al.* [172].

	Na^+	K^+	Mg^{2+}	Ca^{2+}	Cl^-	HCO_3	$(HPO_4)^{2-}$	$(SO_4)^{2-}$
Human blood plasma	142	5	1.5	2.5	103	27	1	0.5
Original SBF	142	5	1.5	2.5	148	4.2	1	0
Corrected c-SBF	142	5	1.5	2.5	147.8	4.2	1	0.5
Revised r-SBF	142	5	1.5	2.5	103	27	1	0.5
Newly improved n-SBF	142	5	1.5	2.5	103	4.2	1	0.5

Another indication that *in vitro* tests using SBF have the same mechanism of calcium deposits formation as the *in vivo* test was provided by Park *et al.* [150] . During the *in vitro* test they analysed the [Ca]/[P] ratio, which rapidly decreased after the 7th day of testing. This suggests that the onset of calcification is governed by calcium ion accumulation, later followed by phosphorous ions, similarly to the natural mineralisation mechanism. Kekec *et al.* [162] used c-SBF to successfully compare the calcification performances of PIB, PIB-based PUs and SIBS.

Brubert [5] modified the original SBF using HBP concentration except for Cl-, for which he picked an intermediated value between SBF and HBP (see Table 4.4). Calcification deposits were easily detectable in all the samples after 8 days of testing.

Nogueira *et al.* [175] performed calcification tests on bovine pericardium using 1.5*SBF ion concentrations to accelerate calcification. The solution was changed every 2 days for a total of 7 days of sample immersion. At the end of the test, severe calcification was visible on the pericardium surface, while it was not detectable on the biopolymer coated tissue (silk fibroin, chitosan coatings were investigated). They identified this *in vitro* method as an effective screening tool to verify if a material is suitable for application where calcification must be avoided. However, they pointed out the limitation of not being able to predict the effect of cellular or enzymatic interactions.

With a similar purpose, Liu *et al.* [165] used a supersaturated solution containing 1.5 times higher concentration of $Ca_2{}^+$ and $PO_4{}^-$ ions. Their study involved three different charged surfaces to investigate the effect of functional groups on mineralisation. They saw dramatically different amounts of HAP crystals on the three surfaces using the *in vitro* method. Details of the compositions used by these authors are listed in Table 4.4.

Table 4.4: Ion concentration (mM) of modified SBF solutions by various authors. For all the solutions a Tris buffer was used, except Brubert [5], which used MOPS buffer.

	Na^+	K^+	Mg^{2+}	Ca^{2+}	Cl^-	HCO_3	$(HPO_4)^{2-}$	$(SO_4)^{2-}$
Kekec *et al.* [162]	142	5	1.5	2.5	147.8	4.2	1	0.5
Park *et al.* [150]	140	5	1.5	2.5	148.8	4.2	10	0
Liu *et al.* [165]	142	5	1.5	3.8	147	4.2	1.5	0.5
Nogueira *et al.* [175]	213	7.5	2.25	3.75	221.7	6.3	1.5	0.75
Brubert [5]	142	5	1.5	2.5	128	27	1	0

The lack of consensus about an appropriate *in vitro* calcification protocol makes the direct comparison of all reported polymer performances impractical. To compare the results for the SBCs tested by Brubert [5], the same ion concentrations was used in this work.

4.2 Materials and Methods

Polymeric samples and pericardium tissue were calcified in SBF solution for 8 days and tested for residual calcium deposit concentration and variation of mechanical properties. Briefly, the calcification experiment was conducted on two samples types with different techniques. Firstly, unitensile specimens were calcified by immersion in the solution and by stretching with a three-point bending device. Secondly, PHV prototypes (see chapters 2 and 3 for details on geometry) were both immersed in the solution and agitated to simulate a turbulent system. The calcifying solution was placed in a tank in which the samples were immersed using the rig in Figure 4.1.

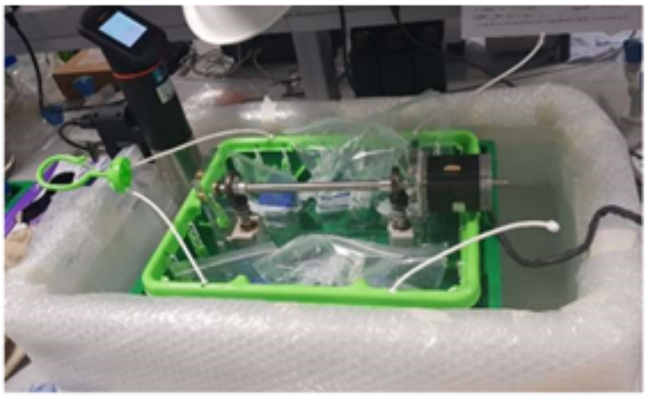

Figure 4.1: Complete testing apparatus for the calcification test. The big outer tank is filled with water and covered with bubble wrap to insulate the system. The instrument on the top left is the ANOVA heater set at 38°C. The inner green tank contains the calcifying solution, the green plastic stand where the static samples are hung, the bending device and some weights to prevent the floating of the green tank in the water. Picture collected by E. Okafor and J.Allford.

The tank was placed in a water bath to maintain 37°C temperature within the solution. The water was heated with an ANOVA heater at 38°C. On top of the tank some bubble wrap was used to insulate the system. The calcifying solution was prepared with reverse osmosis water and the reagents listed in Table 4.5. The reagents were dissolved individually in a volumetric flask a few hours before the start of the experiment.

The calcifying solution was changed every two days for a total of 8 days to maintain the ion concentrations and the pH within the desired range. Temperature and pH were monitored at the beginning and end of each day and solution cycle (Jenway probe). With the same frequency, solution samples were taken to measure the change in calcium ion concentration over time, both with and without mixing the solution in the tank

Table 4.5: Ion concentration (mM) of modified SBF solution. Resulting calcium concentration is equal to 100 ppm.

Na^+	K^+	Mg^{2+}	Ca^{2+}	Cl^-	HCO_3	$(HPO_4)^{2-}$
142	5	1.5	2.5	126	27	1

before collecting the sample. The calcium ion conductivity was measured in a water bath at 25°C using a Jenway calcium ion probe and adding Calcium ISAB following the manufacturer's instructions (EDT directION).

After discarding every solution, the tray and the test apparatus were washed with RO water, HCl and acetone to avoid residual calcium deposits on the experiment setup.

At the end of the 8th day, the samples were rinsed with RO water to remove loose deposits and dried in an oven at 40°C for 24h.

4.2.1 Unitensile samples

Two different experiments were performed on the unitensile samples manufactured by injection moulding. The materials calcified in the experiments are: SEBS0, SEPS22, MED500400 and pericardium tissue. SEBS20 and SEPS22 were injection moulded, and hence had anisotropic mechanical properties (chapter 2 for details). Only the orientation direction parallel to the strain is reported in this work, since it is the one applied in the valve leaflet design. The SBCs were also tested with heparin coating, both CHC™Corline Heparin Conjugate kit (Corline®,Uppsala, Sweden) and ASTUTE®Advanced Heparin Coating (BioInteractions Ltd.,Reading, UK) (see chapter 3 for more details on the coatings).

The pericardium tissue was pre-washed in buffered solution and fixed in glutaraldehyde (0.4% for 48h followed by 0.2% for 1 week).

For every material and coating, the samples were tested both statically and under stress. In the first case, the specimens were hung as shown in Figure 4.1 on the side of the solution tank on the light green stand suspended from clips. The other set of samples were fixed in the instrument in Figure 4.2-a, where they underwent a bend test up to 11% strain at 65rpm, to simulate calcification under stress.

The bending device (Figure 4.2) was fabricated in the Department of Chemical Engineering and Biotechnology (University of Cambridge) by Brubert [5]. The rig can accommodate a maximum of 9 samples per run, which were fixed with a double layer of

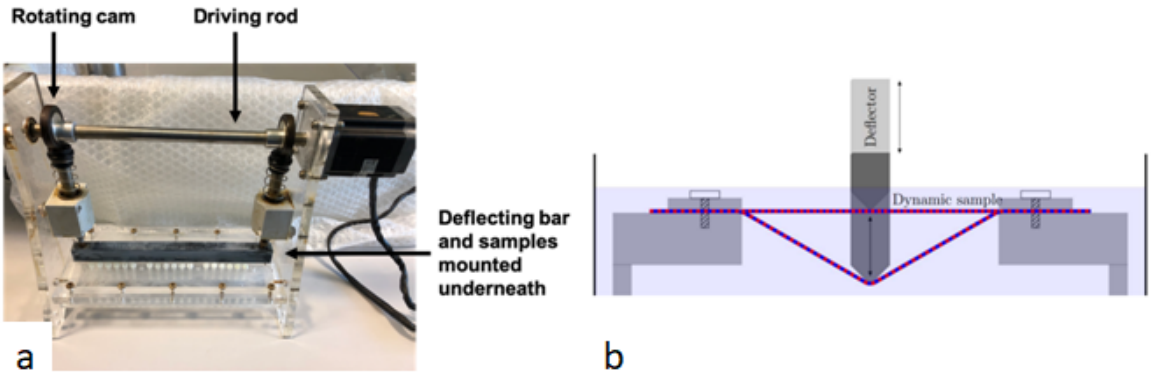

Figure 4.2: a- Picture of the bending device (collected by V. Manhas), the arrows point out the rotating cam and driving rod that move the deflector bar; b- schematic drawing of the rig showing the deflector tensile test on the unitensile samples depicted in blue-red lines (picture adapted from Brubert [5]).

PMMA clamps. The samples were also secured with a PMMA washers and polystyrene screws. The deflector is driven by a rotating cam and could only move to one specific minimum and maximum position.

4.2.2 PHV samples

The calcification experiment was also performed on valve prototypes made via injection moulding. The geometry of the valve is the same described in chapter 2. The materials are the ones considered for the unitensile samples, except for the pericardium. The valves were both calcified in a static and dynamic system. For static calcification, the prototypes were positioned in the same way as the unitensile samples, hanging from the clips. While in the dynamic calcification case, the valves were immersed in the solution and agitated continuously to simulate a dynamic flow system around the valves. To do so, a set of 3 stents was 3D printed (Form 2, Formlabs, USA) with a hard resin as shown in Figure 4.3. The stents were then positioned on top of the deflector.

The displacement of the latter gave enough agitation to consider the system dynamic, although the turbulence was not comparable to that produced by the closing and opening of the valve, since the leaflets were not moving to that extent. Moreover, the leaflets were not stretching as much as they would have under working conditions. However, it was a useful comparison with the static test.

After 8 days in the SBF fluid, the valve prototypes were tested for hydrodynamic performance in the Pulse Duplicator and for fatigue performances in the Dura Pulse

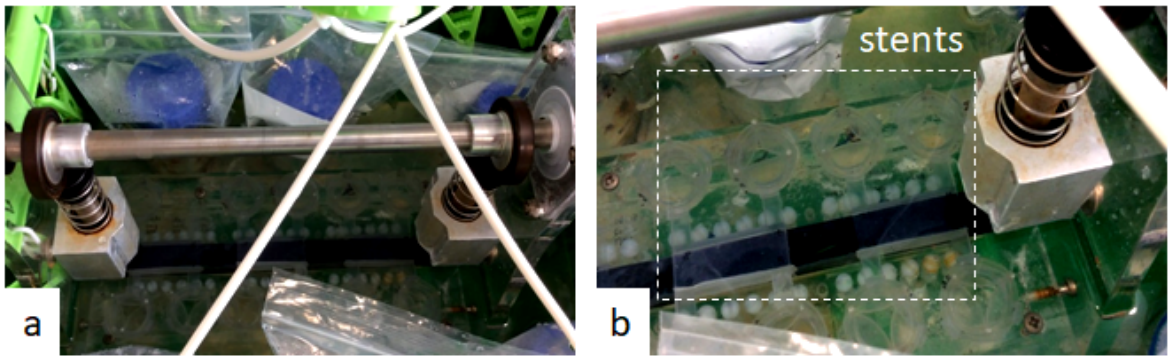

Figure 4.3: a- Picture of the bending device immersed in the calcifying solution with the set of 3 stents with the valves prototypes mounted on top of the deflector; b- zoom of the picture a on the valves on attached to the stents.

(described in chapter 3). The results were compared with the uncalcified valves prototypes.

4.2.3 Calcium Analysis

The calcified samples and valve prototypes were analysed with Atomic Absorption Spectroscopy (AAS, Varian AA 240 & Spectra AA v.5.1, air/acetylene flame) to calculate the calcium concentration. Only the central narrow part of the unitensile sample was used for the analysis, while for the valve only one leaflet was cut out and analysed at a time. The samples were left in a 1 M HNO_3 solution for 24 h to completely dissolve the calcium phosphate deposits. The solutions were syringe-filtered (0.22 μm filter) before analysis.

Calcification on unitensile sample and respective AAS analysis was performed by Emmaline Okafor, Julia Allford and Varun Manhas, during their Masters projects, under my supervision.

4.3 Results and Discussion

4.3.1 Atomic absorption spectroscopy

Analysis of the AAS data gave the amount of calcium retained on the materials during testing. The graphs in Figure 4.4 shows a comparison of the performance of the SBCs with the pericardium tissue. These results are obtained from a static test, where the samples are simply immersed in the solution (as explained in the experimental section). The level of calcium in the tissue is roughly 26.5 times higher compared to

the polymers. The calcification of the leaflets is one of the most critical failure modes for the bioprosthetic valve made of pericardium, as documented in the introduction. The amount of calcium found on the SBCs after the test suggests that calcification represent a less relevant threat for the polymeric materials considered in this work. Figure 4.5 shows the calcified unitensile samples after the test: it is evident that calcification took place at least on the surface. Based on these results, it is reasonable to conclude that a SBCs valve could potentially suffer less from calcification than the tissue valves. However, an *in vivo* test would be necessary to confirm this theory since the working and calcifying conditions in the human heart are difficult to replicate *in vitro*.

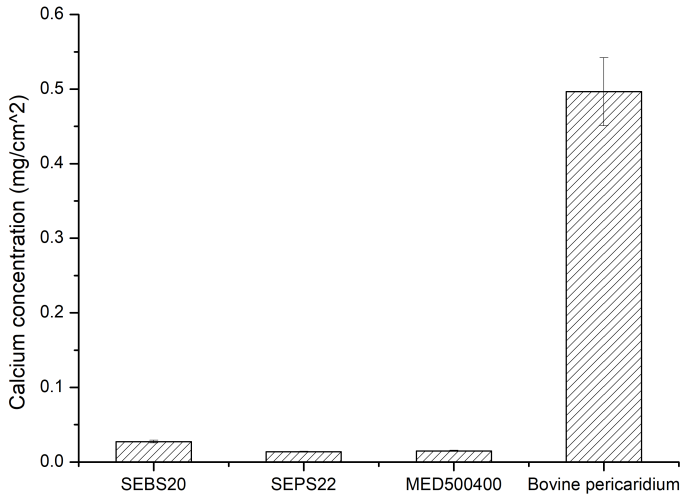

Figure 4.4: Calcium concentration on SEBS20, SEPS22, MED500400 and Bovine pericardium tissue measured with AAS (Varian AA 240 & Spectra AA v.5.1, air/acetylene flame) after static calcification test on unitensile samples. Error bars represent standard deviation. Data collected by E. Okafor, J. Allford and V. Manhas.

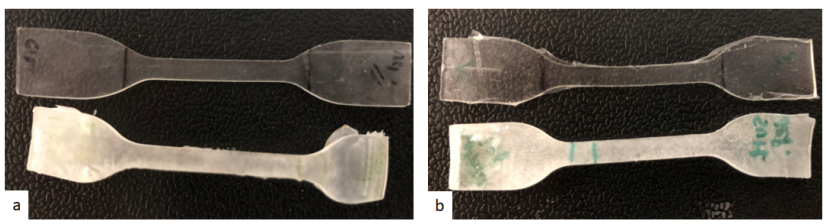

Figure 4.5: Comparison of injection moulded samples uncalcified and samples that underwent static calcification; (a) SEPS22, (b) SEBS20.

The effect of heparin coating on the calcification process was also evaluated, considering both Corline®(Corline®,Uppsala, Sweden) and ASTUTE®(BioInteractions Ltd.,Reading, UK) coatings. The unitensile samples coated and uncoated were calcified in static and under-stress condition (stretching device). The graph in Figure 4.6 shows the results for MED500400. It is evident that the heparin increased the level of calcium deposited on the polymer for both static and stretched condition (static: + 208% Corline, +246% Astute, stretched: + 326% Corline, +989% Astute). This result was expected since the heparin molecule has the highest negative charge density among known biological molecules. The negative charge on the surface covered by the coating promotes Ca^{2+} ion adsorption.

The mechanisms involved in the significant increase in calcium concentration for the under-stress condition could be two. The first one is the stretching of the samples that increases the dimension of microcracks and loosen up the polymeric chain which, as reported in the literature [155, 157, 153, 152], could increase the adsorption of the calcific solution. The second hypothesis is an increase in calcium supply due to local recirculation of the solution around the stretched sample produced by the bar movement . The recirculation of the solution provided higher calcium supply compared to the static one, resulting in higher calcium adsorption.

The same tests performed on MED500400 was also replicated for SEBS20 and SEPS22. However, the samples mounted in the stretching device failed before the end of the 8 days and started floating in pieces in the solution. Only the samples coated with heparin lasted for the duration of the calcification test and the results are shown in the graph in Figure 4.7. These results give some support to the suggestion of Bernacca *et al.* [128] that heparin coating increases the lifetime of polymers.

Figure 4.7 shows that the stretching test resulted in significantly higher calcium level than the static test, for all the three materials and both coatings (SEPS22: + 531% Corline®, +507% ASTUTE®, SEBS20: + 1316% Corline®, +774% ASTUTE®; MED500400: + 304% Corline®, +779% ASTUTE®). Differences between the two coatings in Figure 4.6 and 4.7 can be explained by the coating technology and its interaction with the polymer.

ASTUTE ®coating consists of a hydrophilic priming layer (modified polyethyleneimine), that allows surface adsorption, to which PEG chains, sulfonate bearing groups and heparin molecules are covalently attached. Corline ®coating is made of macromolecular complexes of unfractionated heparin that are covalently attached to polyamine carrier chains via heterobifunctional crosslinkers [127].

However, there is no clear trend across the three materials on which coating cal-

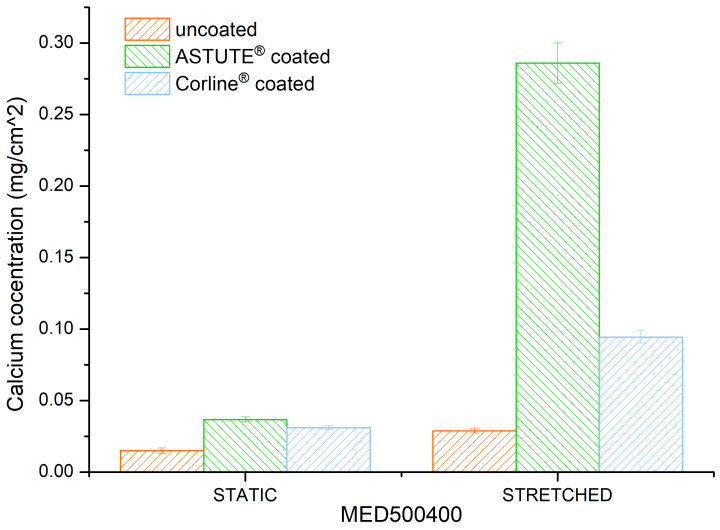

Figure 4.6: Calcium concentration on unitensile samples of MED500400 uncoated, Corline®and ASTUTE®coated measured with AAS (Varian AA 240 & Spectra AA v.5.1, air/acetylene flame) after static and under-stress calcification. Error bars represent standard deviation. Data collected by E. Okafor, J. Allford and V. Manhas.

cifies more, which makes it impossible to draw any conclusion regarding which is the most suitable coating technology, and which calcifies less. The results could also be influenced by how well the coating is distributed on the surface.

The calcification experiment was also performed on valve prototypes made of the same SBCs. Figure 4.8 shows a comparison between static and dynamic experimental conditions for SEBS20 and MED500400 valve prostheses. Even if the valve leaflets were not stretched, the turbulent flow was enough to increase the level of calcium concentration in the tested prototypes (SEBS20: + 154% dynamic; MED500400: +444% dynamic). The valves after the test are showed in Figure 4.9, where the different amounts of calcium deposited is visible to the naked eye. It was not possible to compare the dynamic test to the experiment designed by Baloori *et al* [154] to study the effect of shear on calcification. They concluded that lower shear gave higher calcium ion concentration since there was more time for the ions in solution to get trapped on the surface. In my case, the solution was merely agitated. However, it was possible to visibly identify small vortices in the solution around the valves. This test demonstrated that it is possible that calcification (crystal growth in specific) is a diffusion limited phenomenon.

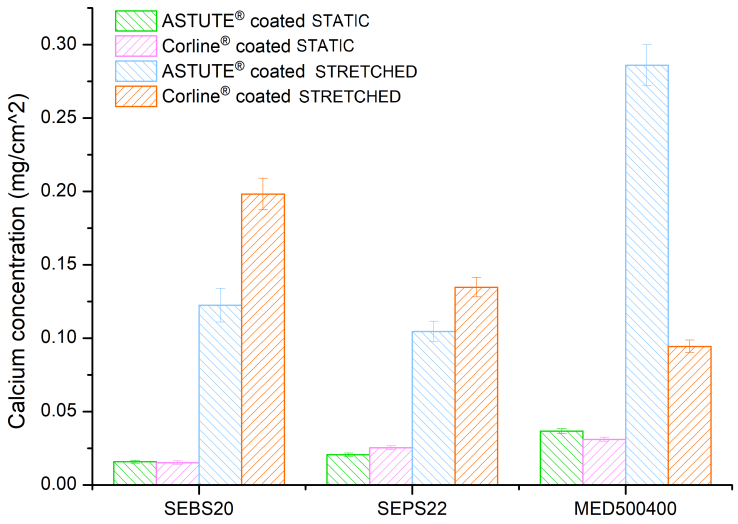

Figure 4.7: Calcium concentration on unitensile samples of SEBS20, SEPS22 and MED500400 Corline®and ASTUTE®coated measured with AAS (Varian AA 240 & Spectra AA v.5.1, air/acetylene flame) after static and understress calcification. Error bars represent standard deviation. Data collected by E. Okafor, J. Allford and V. Manhas.

After this comparison, I focused only on dynamic tests since they are closer to flow around the implanted valve. The dynamic test was able to give a comparison between the shortlisted materials, both coated and uncoated. The graph in Figure 4.10 shows the results obtained from the test. As expected, heparin coating increases the level of calcium (SEPS22: + 179% Corline®; SEBS20: + 180% Corline®; MED500400: + 134% Corline®). However, the value is still lower than the concentration measured for the pericardium tissue (approximately 0.5 mg/cm^2). This confirms the positive results obtained from the unitensile samples.

SEBS20 and SEPS22 have similar calcium concentration levels when comparing both their coated and uncoated versions. The results obtained for MED500400 differ from the other two materials.

The mechanism of polymeric surface calcification is still poorly understood and there is agreement only on some general mechanisms (see section 4.1).

The increase in calcium level for MED500400 can be related to surface and material's properties or due to error in the measurements of calcium level. The small difference between MED500400 can be due to a small loose deposit that was not de-

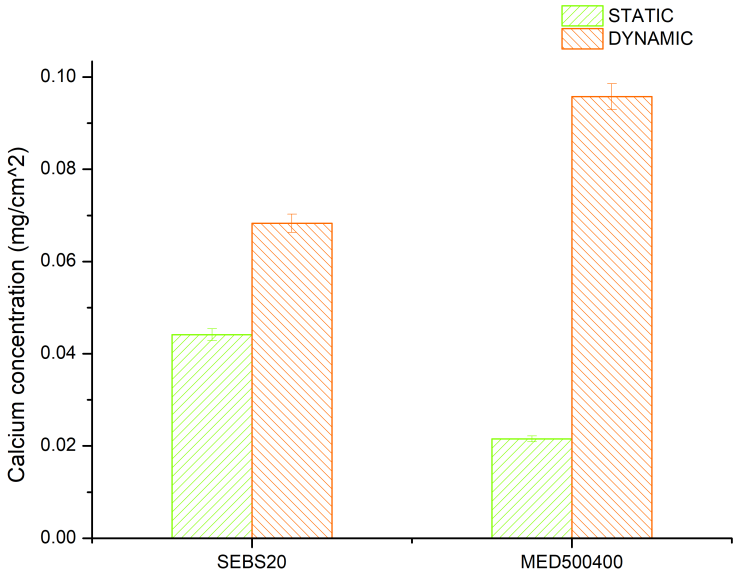

Figure 4.8: Calcium concentration on polymeric valve leaflet of SEBS20 and MED500400 measured with AAS (Varian AA 240 & Spectra AA v.5.1, air/acetylene flame) after static and dynamic calcification. Error bars represent standard deviation.

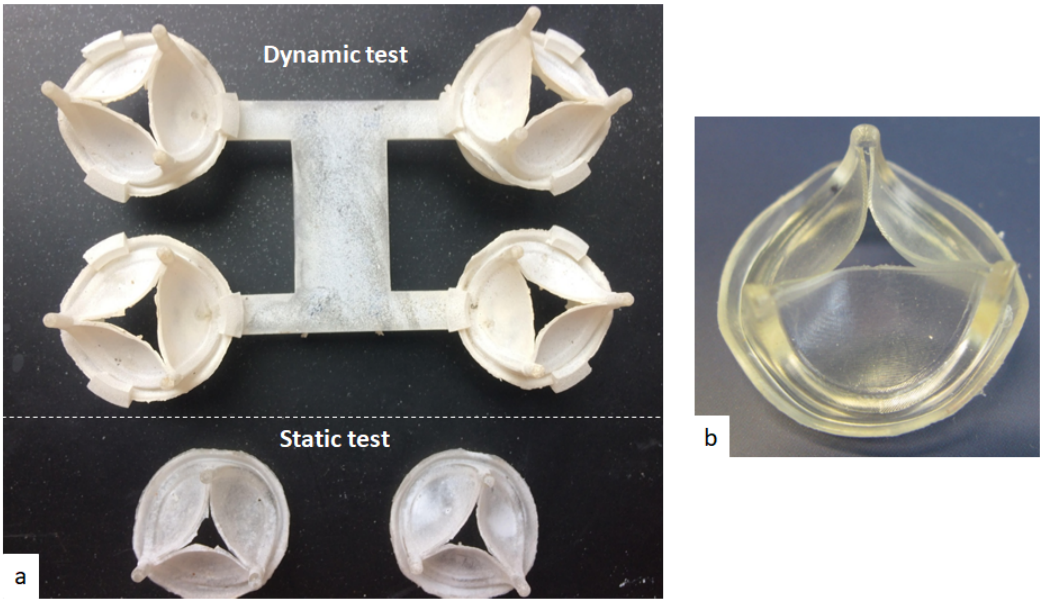

Figure 4.9: a-Comparison between SEBS20 PHVs calcified dynamically and statically; the level of calcium is visibly higher for the dynamic test; b-valve prototype uncoated and not calcified.

tected when preparing the sample for AAS, which could be enough to increase the concentration from 0.10 to 0.18 mg/cm^2.

MED500400 does not differ significantly from the other two materials in terms of surface roughness, porosity and hydrophobicity (contact angle measurements proved the latter [174]). Even considering the results in Figure 4.7, it was not possible to identify a specific trend or a cause for the increase in calcium of MED500400.

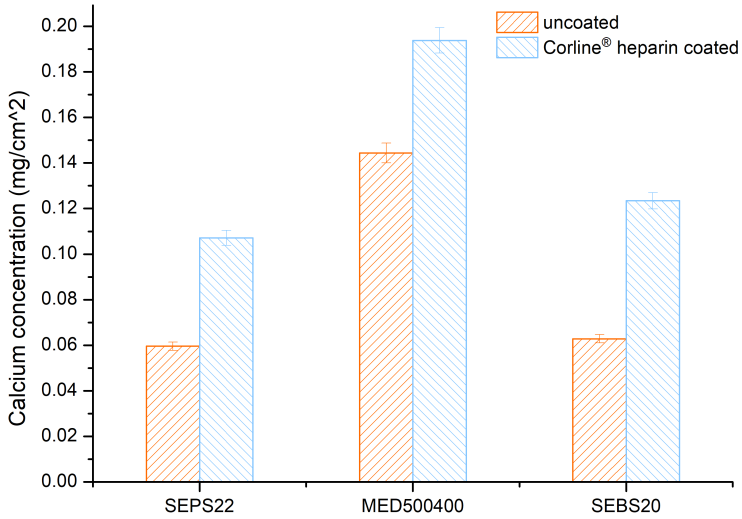

Figure 4.10: Calcium concentration on polymeric valve leaflet of SEBS20, SEPS22 and MED500400 Corline coated and uncoated measured with AAS (Varian AA 240 & Spectra AA v.5.1, air/acetylene flame) after dynamic calcification. Error bars represent standard deviation.

The level of calcium for all polymers tested is acceptable for valve applications and, at this stage of material shortlisting and valve design, MED500400 can be discarded based on hydrodynamic performances and durability (see following section and chapter 3 respectively).

4.3.2 Results from hydrodynamic test

The calcified PHV prototypes, as explained in methods, were tested to compare their hydrodynamic performances with standard uncoated valves.

Hydrodynamic performance was tested using the Pulse Duplicator (see chapter 3), with the valve placed in the aortic position. Water was added in the circuit and pumped

to opend and close the valve. One parameter calculated to quantify performance is the effective orifice area (EOA), a standard parameter for the area through which blood can flow when the valve is open during systole [6]. EOA is calculated according to equation [176, 177]:

$$EOA = \frac{Q_{RMS}}{51.6\sqrt{\frac{\Delta p}{\rho}}} \tag{4.1}$$

where Δp is the mean pressure difference in mmHg during systole, ρ is the density of the test fluid in grams per cubic centimetre, and Q_{RMS} is the root mean square of forward flow in millilitres per second given by equation:

$$Q_{RMS} = \sqrt{\frac{\int_{t_1}^{t_2} Q(t)^2\, dt}{t_2 - t_1}} \tag{4.2}$$

where Q(t) is the instantaneous flow at time t, and t_1 and t_2 are the time at start and end of the forward flow, respectively. According to UNI EN ISO 5840 standard, for a 19 mm valve the EOA must be minimum of 0.85 cm^2.

The graph in Figure 4.11 shows the results for the three materials for the three test conditions: uncoated, calcified, calcified and coated.

For each material, the difference between the three test conditions is within experimental error. The effect of the coating and calcification on the mechanical properties of the leaflet materials is negligible. Moreover, values of EOA all lie well above the minimum of the ISO requirements. This is a promising result for the application of the SBCs considered to valve design. Among the three materials, SEBS20 performed best in terms of leaflet opening, considering that the average thickness of the leaflets was the same for all the valves, as shown in Table 4.6. The effect of thickness on opening is explained in more detail in chapter 3. Briefly, it has been proven that a thinner leaflet is more easily opened [6].

The second hydrodynamic parameter calculated from pressure and flow measurements in the Pulse Duplicator is regurgitation. The design of the valve tested in the calcification experiment is not optimised for regurgitation. Regurgitation is the fraction of backflow while the valve is closed during diastole. A valve that shows high level of regurgitation is considered a "leaky" valve. Regurgitation is given by equation [176, 177]:

$$REG = \int_{t_3}^{t_4} Q(t)^2\, dt \tag{4.3}$$

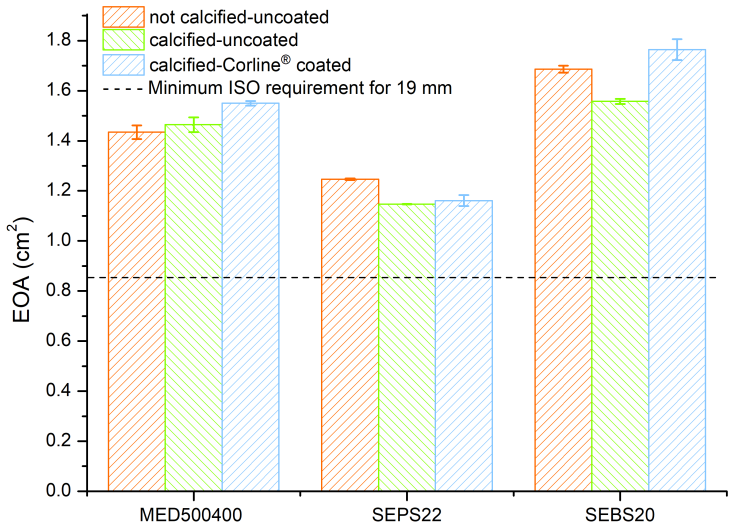

Figure 4.11: Effective orifice area for MED500400, SEPS22 and SEBS20 uncoated and not calcified, uncoated and calcified, calcified and Corline® coated. The dashed line represents the minimum ISO 5840 requirements for a 19 mm valve. The measurements of pressure and flow were taken according to the instruction in section 3.2.2 for the Pulse Duplicator. Error bars represent standard deviation.

Table 4.6: Average leaflet thickness measured for valve prototype made of SEPS22, MED500400 and SEBS20. The valve geometry is the one for the rigid stent experiment described in chapter 2 and 3. The thickness was measured in 4 different points within one leaflet and averaged with the results for the three leaflets. A digital micrometre was used.

Material	Average leaflet thickness (mm)	standard deviation
SEPS22	0.25	0.02
SEBS20	0.26	0.02
MED500400	0.25	0.01

where t_3 and t_4 are time at start and end of the backward flow, respectively.

Regurgitant fraction REGF(%) is calculated by equation:

$$REGF(\%) = \frac{REG}{SV} * 100 \tag{4.4}$$

where SV is the stroke volume [176, 177].

The results obtained from the tests are summarised in Figure 4.12.

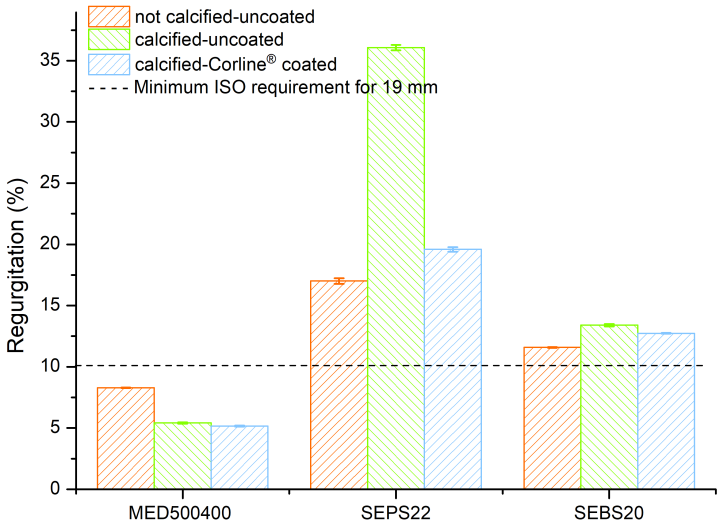

Figure 4.12: Regurgitation fraction for MED500400, SEPS22 and SEBS20 uncoated and not calcified, uncoated and calcified, calcified and Corline® coated. The dashed line represents the minimum ISO 5840 requirements for a 19 mm valve. The measurements of pressure and flow were taken according to the instruction in section 3.2.2 for the Pulse Duplicator. Error bars represent standard deviation.

Regurgitation should be below the ISO minimum. However only MED500400 stayed below the standard. The main reason is due to the geometry of the valve prototype: the rigid posts prevented the extra bending that is necessary to seal the leaflets. Creating such rigid posts was a strategy to increase the SED in the leaflet and shorten the lifetime for practicality of durability testing (as explained in chapter 3). Figure 4.13 shows the opening and closing of the valve for four prototypes tested. On the right-hand column, I have highlighted the area that remains open even during diastole; it is visibly much larger for SEPS22, identical for calcified an uncalcified SEBS20 and non-existent for MED500400. For the EOA, it is reasonable to assume that flexibility is the key parameter for the opening; however, regurgitation is influenced by a combination of the mechanical properties of the material and the leaflet geometry. To be consistent with the results obtained for the EOA, within the same material the regurgitation is expected to be similar for the three conditions. This is the case for MED500400

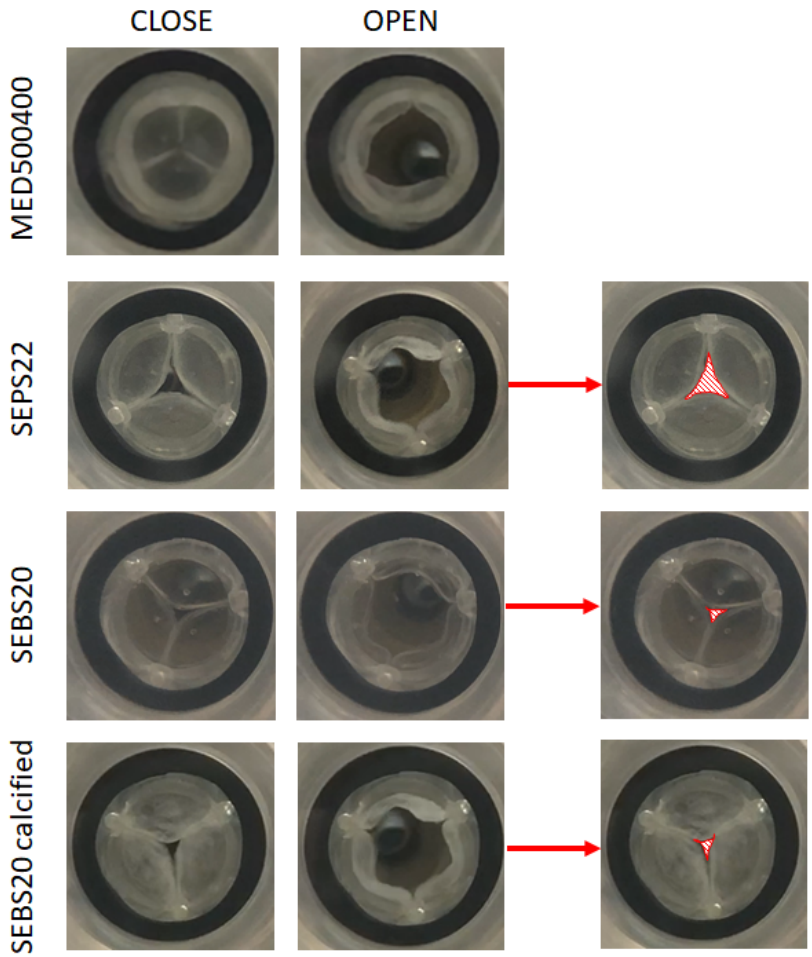

Figure 4.13: Images taken from the Pulse Duplicator test during opening and closing of the valve prototypes made of MED500400, SEPS22 and SEBS20. The last line represents an SEBS20 tested after calcification. The right-hand column has highlighted in the pictures the area that remains open for the fluid to pass through during diastole.

and SEBS20. SEPS22 shows a much higher value for the calcified valve without the coating. The result can be considered an outlier for the test since the same trend is not seen in the EOA measurements, nor for the calcified coated valve, for which higher calcification occurred. The calculation of the regurgitation can be strongly influenced by details of valve mounting, which may explain this anomaly.

4.3.3 Results from durability test

The batch of dynamically calcified valves was tested and compared with uncalcified valves with and without coating in the Dura Pulse. As explained in section 3.2.2, the

accelerated durability test was performed at 30 Hz. The valves durability was below 6 millions cycles, which significantly reduced the time to test a large batch of valves required for the comparison. As discussed in chapter 2 and 3, the prototype for the rigid stent experiment was designed with thin leaflets and rigid posts to increase strain energy density and reduce the lifetime. Reaching the ISO standard for durability was not the goal of this experiment. The results are shown in Figure 4.14 .

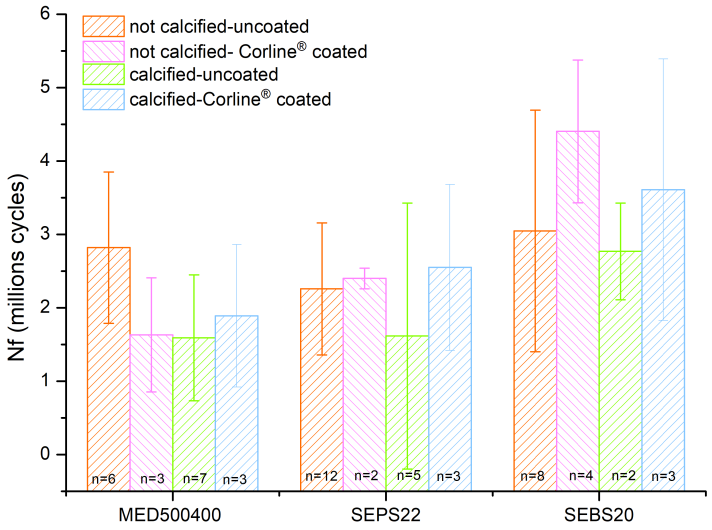

Figure 4.14: Number of cycles to failure for MED500400, SEPS22 and SEBS20 uncoated and not calcified, Corline®coated and not calcified, uncoated and calcified, calcified and Corline®coated. The valves were calcified dynamically. The value n indicates the number of samples tested for each condition. The results are obtained from durability test run at 30 Hz on the Dura Pulse (TA instruments, DE, USA). Error bars represent standard deviation

The variability in the results is quite large and the main conclusion is that the coating and the calcification do not have a negative effect on the valve lifetime for any of the materials tested. The early failure of some of the valves cannot be related to higher calcium levels and it is probably due to material's properties and manufacturing.

4.4 Conclusions

The effect of calcium deposits on polymeric surfaces was analysed for both unitensile and PHV samples, with and without heparin coating. The SBCs shortlisted for the PHV application and pericardium tissue were tested.

The tests performed on uni-tensile samples showed that the level of calcium for the polymers, both coated and uncoated, was significantly lower than that obtained for the pericardium tissue. Even though *in vitro* experiment conditions differ from the *ex vivo* test in human body, these results are very promising for the application of these materials in prostheses, especially where calcification is a serious issue.

The effect of heparin was not in agreement with the findings of Brubert [5] and Chanda *et al.* [170]. It is likely that the negative charge of the molecule played a significant role in attracting the positive Ca2+ ions and starting crystal nucleation and growth. However, the use of heparin should not be considered entirely detrimental from the calcification point of view. The primary benefit of heparin is to improve blood compatibility and inhibit thrombus formation, which have been shown to be one of the primary vehicles of calcification *in vivo* [127]. For this reason, *in vivo* tests should clarify the effect of heparin.

Moreover, the experiments performed on the valves showed that the coating and the calcium do not affect the hydrodynamic and durability performances of the prostheses. The EOA, measured in the Pulse Duplicator, was consistent for calcified and uncalcified prototypes, with and without heparin coating. Complete opening of the valve requires stretching of the leaflets because of the difference in pressure before and after the valve. The fact that the open area remains the same even after calcification suggests that the elastic properties are unchanged. For durability, there was no evidence of reduced lifetime due to coating and/or calcification. This shows that *in vitro* calcification did not damage the materials to the point of increasing the number of defects responsible for a shorter life-span . Bernacca *et al.* [128] reported increased durability in PEU and PEUE valve coated with heparin. There is a suggestion that the same phenomenon was shown for heparin coated SEBS20 valves.

Finally, the test showed that simulating a turbulent flow around the valve and stretching the uni-tensile samples increased the level of calcium in the materials. This suggests that the design of the calcification experiment is crucial for effective comparison of materials' performances. In order to better simulate the condition inside the human body, the PHV could be calcified in the Pulse Duplicator or DuraPulse, while the valve is properly opening and closing. However, the instruments were not built to

contain liquid with high calcium levels and could be permanently damaged by it. The dynamic test gave a good understanding of the materials can withstand calcium deposits, without compromising material properties. A more accurate test would require *in vivo* experiments.

Chapter 5

Ex vivo hemocompatibility

5.1 Introduction

The path to the clinical use of a polymeric PHV requires assessment of the biocompatibility of the material. The concept of biocompatibility is complex and covers many aspects of the interaction between the host body and the implanted material. A long term implant, such as the valve, requires careful analysis of the blood's reaction to the prosthesis. The effect of blood-polymer interaction can lead to severe inflammatory response, often resulting in thrombosis and tissue growth on the surface, which can ultimately lead to valve failure and embolic complications [179].

The immediate response of the biological system to the foreign material is rapid adsorption of blood serum proteins (within seconds) onto the surface. The protein layer acts as the substrate for the subsequent platelet and leukocyte adhesion. Platelets can be activated by several molecules, the most potent being thrombin. Activation triggers a change of shape, promoting platelet-platelet adhesion and further recruitment. On the other hand, leukocyte (immune cells) activation induces the release of inflammatory mediators. The mediators can attract more leukocytes, promote endothelial cells adhesion and platelet activation, as well as releasing oxidants. The reaction cascade that follows ultimately leads to thrombus and fibrin formation [179, 180, 181]. A detailed discussion of the biological phenomena is beyond the scope of this work and it is discussed in references [179, 190, 191]

For many years, research has been focused on the identification and development of a non-thrombogenic surface, but the ideal material is yet to be found [193]. Although full biocompatibility has not been achieved, many cardiovascular devices function with low or acceptable risks of complications. At the moment, surface modification seems to

be the most promising route to reducing the inflammatory response [179, 180, 188, 189]. It has been demonstrated that grafting of water soluble polymers, such as polyethylene oxide (PEO), albumin, and heparin, reduced thrombogenicity of biomaterials. Amiji *et al.* [182]showed that biomaterials grafted with one of these resisted plasma protein adsorption and platelet adhesion, predominantly by a steric repulsion mechanism. Kim *et al.* [183] demonstrated that immobilising heparin or PEO onto polyurethane (PU) produced superior blood compatibility both *in vivo* and *in vitro*.

Brubert *et al.* [184] tested a series of nano-cylinder forming block copolymers (SEPS22, SIBS30, SI/BS19) for hemocompatibility according to ISO 10993:4. The SBCs were compared to ePTFE, which is considered an excellent biocompatible material [16, 19], and bovine pericardium tissue, which is used in bioprosthetic heart valves, such as the Edwards Perimount. The effect of heparin coating was assessed on SEPS22, one of the materials considered in this thesis (chapter 2). They used a modified Chandler's loop to simulate the conditions experienced by blood and cells around prosthetic heart valves. The instrument consists of a tube filled with human blood, containing a strip of test material, which rotates at 30rpm in a water bath at 37°C. Thrombin concentration was used as a marker for the coagulation cascade activation by measuring thrombin-antithrombin-III complex (TAT) level before and after material contact. Heparin coated SEPS22 showed the lowest level of TAT, followed by bovine pericardium, ePTFE and the uncoated SBCs. SEM analysis of the surface after the test did not show any thrombus formation; however, a protein layer was adsorbed. Heparin coated samples showed sparser protein adsorption. In terms of inflammatory reaction, heparin coated SEPS22, followed by uncoated SEPS22, SIBS30 and SI/BS19 performed better than ePTFE and bovine pericardium. The promising performances of coated SEPS22 opened new possibilities for the application of cylinder forming styrenic block copolymers to PHVs.

This work covers an *ex-vivo* hemocompatibility test performed on SEBS20 uncoated and coated with heparin (both Corline®and ASTUTE®technology). The results of the test are an important step in the route towards Polivalve's FDA approval and commercialisation. The tests were performed in a Badimon perfusion chamber (Figure 5.1). The instrument allows assessment of the thrombogenicity of blood in humans. The use of anticoagulants, typical of most platelet function testing methods, is avoided in this test, giving a significant advantage in the unperturbed assessment of the thrombogenicity performances. Blood type, flow and endothelial wall can be simulated in the model, which has been used to assess the effects of various diseases (*e.g.* diabetes, HIV) and pathological states (arterial wall injury, atherosclerotic plaques, diesel exhaust in-

halation, etc.) , as well as several pharmacological interventions (*e.g.* anticoagulants, antiplatelet drugs, direct thrombin inhibitors) [185, 186].

The perfusion model is based on unaltered blood exposure to the material's surface at controlled flow rates, in order to mimic human (or animal) *in vivo* conditions. The flowing blood activates platelets on the surface and starts the coagulation cascades, resulting in the formation of fibrin and thrombus on the surface [187]. A more detailed explanation of the instrument is described in the following section.

5.2 Materials and Methods

The tests were conducted in collaboration with Professor Azfar Zaman in the Clinical Research Facility at Royal Victoria Infirmary in Newcastle (UK). A total of 10 subjects were recruited based on their health conditions. The volunteers, aged between 20 and 50, had no known history of coronary artery disease, diabetes mellitus, haematological dyscrasias and were not on blood thinning medications.

Figure 5.1 shows the Badimon chamber[187] used for the test. The system usually consists of a pump and three chambers connected in series and positioned in a water bath kept at 37°C. In Figure 5.1-a the connection to the pump is represented by the tube on the right of the chambers, while the tube on the left side was connected to the antecubital vein of the patient to draw blood.

For each experiment, three 14x20 mm rectangles of injection moulded polymeric film were positioned in three different chambers to act as the thrombogenic substrate (only two in this picture because in that specific run one chamber was leaking due to excessive thickness of the polymeric sample). The three perfusion chambers have a small channel crossing the middle of the polymer sample surface. The channels are designed to mimic the flow in a coronary artery and are positioned in series. The first one has low shear (shear rate approximately 500 s^{-1}, Reynolds number=30, inner diameter 2 mm), representing the flow in a healthy coronary artery. The second and third ones have higher shear (shear rate approximately 1920 s^{-1}, Reynolds number = 60, inner diameter 1 mm) to simulate the conditions of a mildly stenosed coronary artery. The combination of the different conditions in series gives a deep coronary arterial injury model [187]. The pump was set at a constant flow of 10 ml/min. The instrument was first washed with PBS to initiate the system and then connected with a syringe to the patient's arm to extract the blood. The pump was stopped after 5 minutes, allowing 50 ml of blood to run over the samples. For every material, the two different conditions were tested on both heparin coated and uncoated samples.

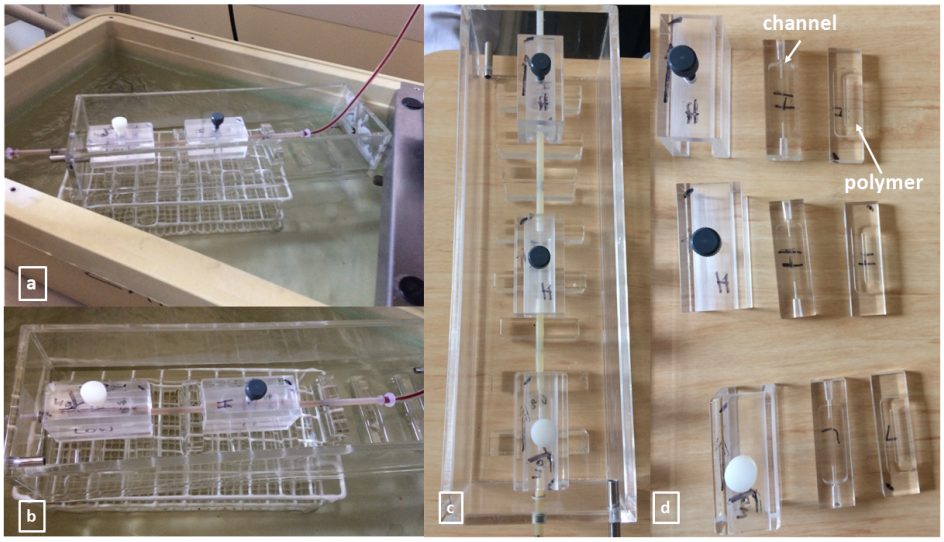

Figure 5.1: Badimon chamber instrument: a- high and low shear chambers connected in series and positioned in a water bath at 37°C, the right side tube connects to the pump while the left one is connected to the vein of the patient to withdraw blood; b- close up from the top, showing the blood crossing the chambers; c- close set up of the three chambers in series; d- open chambers showing the channel size and the area where the polymeric sample is positioned, the two pieces on the right are closed on top of each other and inserted in the cover on the left.

The same chamber was used for all subjects and the same operator (Samantha Jones) performed the tests. At the end of the study, the polymeric samples were removed from the chambers and fixed in 4% paraformaldehyde for storage. The tested materials were then fixed with 10% neutral buffered formalin, which inhibits cracking of the clotted blood layer and gives better retention on the polymer, compared to washing the sample with 99% alcohol.

Next, the samples were stained with Masson Trichrome (water-based reagents) to mark the fibrin. The staining procedure was as follows:

1 Chromium trioxide – 60 mins

2 Bleach in sodium metabilsulphate - 1 min

3 Weigerts haematoxylin – 15 mins

4 Blue in Scott's tap water

5 Ponceau-Acid fuchsin – 3 mins

6 Differentiate in Phosphomolybdic acid – 10-20 mins

7 0.25% Light green – 10-20 mins

The samples were handled with forceps and rinsed in running water between each step of the staining process. Furthermore, the reagents were added directly into the pot containing the polymer rather than fixing the polymer to a slide, to avoid damage to the deposited clotting material. After staining, the specimens were dehydrated in graded alcohols and dried in air.

Histological analysis was performed (by Thomas Ness) with an Olympus BX51 optical microscope with a Nikon DS-Fi2 microscope camera. The samples were mounted on a plain glass slide with a cover slip on top.

5.3 Results and Discussion

The analysis of the images obtained from the Badimon chamber, both in low and high shear conditions, showed no thrombus formation. Hence, no quantitative analysis was possible. The results were compared to porcine aorta, a thrombogenic substrate, of the type typically studied by the same test, shown in Figure 5.3. The images only show a thin layer of fibrin and red cells, highlighted in red/pink by the stain. The Corline®coated samples lack the fibrin layer, only the red cells were visible. The images in the right hand column (5.2-e-f-k-l) refer to the sample coated with the Bionteractions ASTUTE®coating; the pictures show a more distinct pink colour because the coating itself was stained by the dye. Nevertheless, the pictures do not show the thrombus formation that is present in Figure 5.3 below. This is characterised by irregular granular outgrowths on the surface. The pictures on the right show a SEM micrograph of the fibrous nature of the thrombus.

5.4 Conclusions

SEBS20 showed good hemocompatibility performance and no thrombus formation. The coating seemed to marginally improve the blood reaction to the surface, but quantitative data to prove this could not be obtained from this test because no samples, coated or uncoated, resulted in thrombus formation. It was demonstrated that SEBS20 is a good potential candidate for a polymeric PHV, from the perspective of blood compatibility.

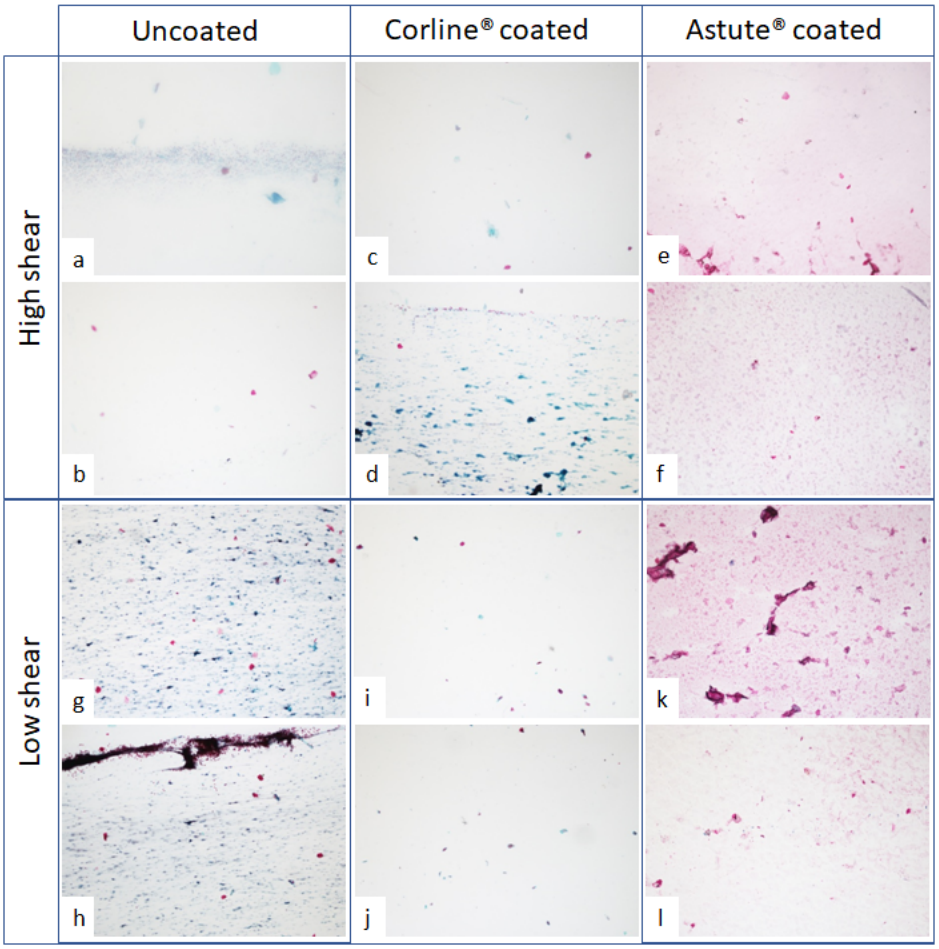

Figure 5.2: Images obtained from the samples after blood contact in Badimon chamber, fixation and staining. The columns group, from left to right, uncoated, Corline®heparin coated and ASTUTE®heparin coated SEBS20 injection moulded samples. a-f samples subjected to high shear blood flow; g-l samples subjected to low shear blood flow.

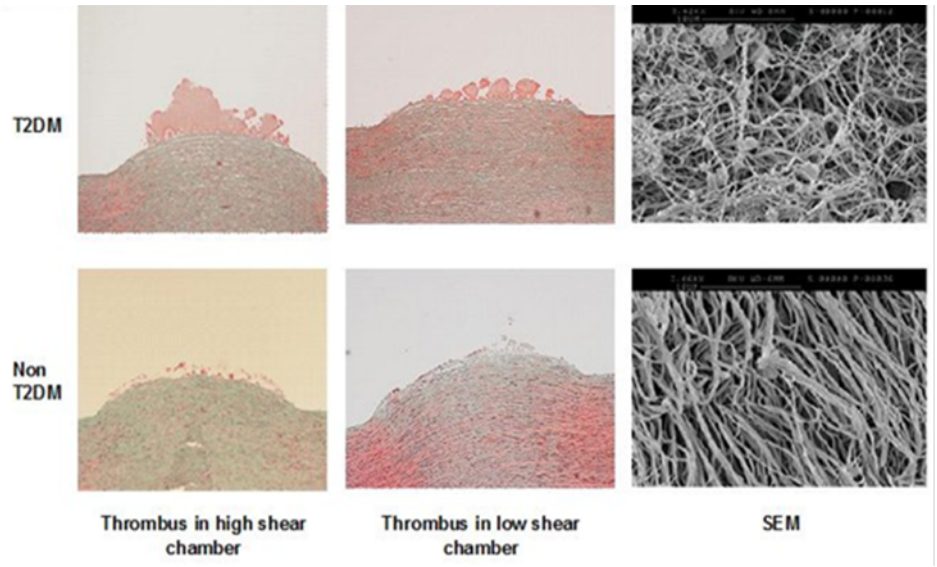

Figure 5.3: Thrombus of patients obtained from Badimon chamber experiment at high (left column) and low shear (central column). Platelet rich thrombus was stained in pink and the tunica media of the aortic tissue stained in green.The images on the top row are from a patient suffering from diabetes (T2DM) while the second row is from an healthy subject. The SEM micrographs show the respective fibre mesh of the thrombus.Images adapted from reference [186].

Chapter 6

Conclusions and future work

6.1 Conclusions

The design of a polymeric valve prosthesis requires careful consideration of many aspects of the material. The most critical are durability, calcification and biocompatibility. This dissertation describes investigations of the first two aspects.

The valve is required to reach only 200 million cycles durability *in vitro* to meet the ISO 5840-2015 standard. However, in order to be competitive with bioprostheses available on the market, the real durability target is at least 800 million cycles, the equivalent of 20 years. This goal can be achieved by a combination of material and geometry. Accelerated fatigue testing on the valve prototypes is able to speed up durability assessment: however 800 million cycles at 30 Hz still takes almost a year. In the design and material selection stage, this length of time for testing makes it almost impossible to progress by iterative prototype testing. This is the reason why identification of a good fatigue prediction model for the material is of the utmost importance.

The materials selected for the valve are cylinder forming styrenic block copolymers, in particular poly(styrene-b-butadiene-b-styrene) (SEBS) and poly(styrene-b-propylene-b-styrene) (SEPS). The cylinders form an anisotropic microstructure, which is predicted to improve the durability and to strengthen the valve leaflet. The orientation pattern can mimic the native valve structure, which remains the gold standard.

There is no fatigue model in the literature for anisotropic thermoplastic elastomers, such as the SBCs studied in this work. Hence, the focus of the research has been the validation of a fatigue model for the shortlisted materials for the valve. The approach I took was based on the unified model described by Mars and Fatemi [113, 102].

As described in chapter 2, the materials SEPS22, SEBS20 and MED500400 were characterized by measuring the styrene mass fraction and molecular weight, glass transition temperatures and order-disorder transition temperature. The analysis confirmed that the block copolymers self-assemble into cylindrical styrene microstructures for SEPS22 and SEBS20, and spherical ones for MED500400, according to the established block copolymer phase diagram. Injection and compression moulded samples were X-rayed using SAXS, which confirmed that unidirectional or bi-directional orientation of the domain was achieved on both standard specimens (pure shear and unitensile specimens) and valve leaflets.

As part of the analysis, the lattice configuration and domain spacing (d-spacing) were measured. The d-spacing and molecular weight are larger for SEBS20 compared to SEPS22. This was reflected in the estimation of the average cylinder diameter, which was also larger for SEB20.

In an attempt to measure the height, or length, of the cylinders, I applied the Halpin-Tsai equation for fibre reinforced material based on known material properties and Young's modulus in the two opposite orientation of the cylinders. There is no consensus on an approach to measure the height of the cylinders, and it is not possible to exclude the possibility that they might form a connected network of cylinders. According to my approximation SEBS20 has longer cylinders compared to SEPS22 (171 μm and 31.2 μm respectively).

The information gathered with the aforementioned analyses were used in the comparison of the results of the mechanical tests for the two materials. The mechanical response of block copolymers is complex and many structural parameters such as domain size and orientation, interdomain distances and molecular weight can influence macroscopic properties.

The fatigue model, described in chapter 3, is based on a power-law equation for crack growth versus tearing energy, which is integrated from the initial to the final crack size to give the lifetime prediction model (equation 3.17). The model is based on experimental results from crack growth and crack nucleation tests on standard pure shear and unitensile specimens. In order to capture the effect of anisotropy, the materials were tested with the styrenic domains both parallel and perpendicular to the strain direction. It was demonstrated that orientation strongly influences fatigue properties. When the cylinders are parallel to the strain the material is stiffer and the glassy domain sustains most of the applied stress; the opposite happens for the perpendicular orientation, where deformation mainly affects the elastomeric matrix and the elastic modulus is smaller (1:2 ratio with respect to the parallel orientation).

This behaviour was reflected in the calculation of the initial crack size (a_0). The latter parameter was calculated as the fitting parameter between crack growth and crack nucleation results. Parallel SBCs had a higher calculated value of a_0 compared to the perpendicular orientation, meaning that the styrene domain is a larger source of defects.

Crack nucleation tests were performed on different thicknesses, geometries and with different manufacturing techniques. Thickness reduction resulted in improved durability (at constant strain) and reduced initial crack size for parallel oriented unitensile samples. The model accurately predicted the lifetime of different geometries of unitensile samples with the same thickness. Geometry does not seem to be a limiting factor, which is encouraging for the application of the model to valve lifetime prediction. Compression moulded samples showed significantly lower durability than injection moulded ones.

The rigid stent experiment described in chapter 3 was the first step towards applying the fatigue model to valve design. Thinner leaflets were demonstrated to have very limited durability, which set a threshold for the valve leaflet thickness for each material.

It can be concluded that the model based on the power-law equation successfully predicted the lifetime of the materials for a given orientation, thickness and manufacturing technique in both valve prototypes and unitensile specimen shape. On the other hand, application of the transition law to the unitensile specimens or valves did not work.

The physical meaning of the initial crack size was also questioned based on the results of this study. The a_0 cannot be considered as a simple measure of a natural occurring flaw size, but it is should represent size and distribution of defects, as well as microstructure orientation and thickness.

The material fatigue performances highlighted the best candidate for the valve: SEBS20 oriented parallel to strain. However, a thicker MED500400 valve should be tested to verify the effect of thickness and durability of this material. The reasons behind the superior durability of SEBS20 compared to SEPS22 were hypothesised to be higher molecular weight, different elastomeric matrix and longer predicted cylinders formed in SEBS20.

The effect of heparin coating and calcium on fatigue for the shortlisted materials was described in chapters 3 and 4. Heparin did not have any detrimental effect on the mechanical properties, which was demonstrated in the experiment for both valves and unitensile samples. A marginal improvement was observed for 2 unitensile sample lifetime, probably due to the filling of surface defects, and on the coated valve of the

rigid stent experiment made of SEBS20.

On the other side, heparin increased the calcium level for all the material tested. The heparin coated valves underwent an *in vitro* calcification test for 8 days, both with and without coating. Durability and hydrodynamic tests of these valves showed no significant effect on the number of cycles to failure, effective orifice area and regurgitation compared to uncoated uncalcified valves.

The three materials showed similar calcium levels, but significantly lower than pericardium tissue tested in the same batch. To date, the mechanisms behind polymeric calcification are not well understood and only a few hypotheses were advanced. The most relevant for this case are surface roughness and porosity, microcracks and defects, chemical affinity to calcium ions of styrene and heparin. It is likely that the highly negatively charged heparin molecules attract positive Ca^{2+} ions and start crystal nucleation. However, the main benefits of heparin are the improved haemocompatibility and inhibition of thrombi formation, which were proved to be one of the primary vehicles of calcification *in vivo* [127]. For this reason, *in vivo* tests should clarify the effect of heparin on calcification and durability.

Even though this *in vitro* experiment did not include leaflet stretching or blood, these results are promising for the application of these materials in prostheses, since calcification is a major cause of valve failure *in vivo*.

The haemocompatibility test described in chapter 5 demonstrated that SEBS20 did not show any thrombus formation when in contact with human blood. This further confirmed the suitability of the material for the valve application.

The material analysis described in this dissertation assisted in the design of Polivalve, a tri-leaflet flexible prosthetic valve made of anisotropic SEBS20. Bench *in vitro* tests on the valve gave excellent results in terms of durability and hydrodynamic performance. The valve prototype has undergone a successful animal feasibility study and FDA feedback on a pre-submission for a clinical feasibility study has been received, which will guide the parameters of a chronic (3-6 months) animal trial which is about to commence.

This research demonstrated that building a fatigue prediction model is an important tool in designing a successful polymeric prosthetic heart valve.

6.2 Future work

The findings presented in this thesis raise additional questions regarding the fatigue behaviour of anisotropic block copolymers and their lifetime prediction. The results

discussed in chapter 3 highlighted the need for a deeper understanding of the relationship between molecular weight, d-spacing, orientation and fatigue properties. These aspects should be considered separately since each of these factors can have a complex effect on material behaviour. It would be of great interest to perform crack growth and nucleation tests on the same material with varying molecular weights.

This dissertation mainly focused on parallel orientation of the styrenic domain with respect to strain. Similar tests investigating the effect of varying sample thickness and dynamic mechanical analysis are required also for the perpendicular orientation. The same goes for orientation angles between 0 and 90° reported in section 3.3.3. Bidirectional intermediate angles should be further studied to explore the possibilities of anisotropy and to improve and optimise durability. Moreover, the effect of test frequency on mechanical performance was not investigated in this dissertation. Literature has no guidelines on whether higher frequency can improve the fatigue lifetime of the SBCs. These materials are likely to have a more complex response to frequency variations compared to pure polystyrene or pure rubbery materials. The effect of the increase of frequency on fatigue tests will most certainly depend on the polymer's composition, in this case of the polystyrene fraction, molecular weight and elastomeric matrix composition. It is possible that certain directions are more sensitive to frequency changes. Mechanical fatigue tests should be conducted at various frequencies to understand if the results from the accelerated test at 30 Hz on the valves are realistic, or if the number of cycles to failure must be adjusted to account for the effect of elevated frequency. Furthermore, in order to close the gap between the unitensile sample and valve predictions, injection moulded samples of thickness identical to the leaflet should be tested to verify if the nucleation points fall on the same prediction line. Considering the multiaxiality contribution in the stretching of the leaflet would represent a further step towards improving the prediction. The effect of multiaxial loadings on elastomers it is still not fully understood at present. Although a realistic multiaxial loading history can be calculated with FEM, the prediction models able to process this data are still lacking, especially for anisotropic materials [116, 120, 122].

For valve prototypes, and Polivalve in particular, there are a few tests that should be carried out to progress towards approval for a clinical trial. Firstly, as indicated by the results in chapter 3, it would be interesting to investigate MED500400 as a possible candidate material, by increasing thickness in the valve leaflet. Secondly, the materials' chemical stability inside the human body has to be thoroughly investigated, in particular oxidation resistance. Finally, materials' aging should be assessed, mainly because the valve must remain intact for a minimum of 15 years, but also for the

purpose of defining shelf-life.

A test protocol should be designed to investigate these aspects also for future materials considered for polymeric valves, as well as for calcification. A more accurate test should include stretching of the leaflet in a calcifying solution, to better simulate the real service conditions of the valve. Stretching has been proposed as one of the potential causes of calcification in polymers [152, 153, 155, 157]. To conclude, *in vivo* experiments could clarify many of the aspects regarding the body's reaction to a device made of styrenic block copolymers and its durability. A chronic (3-6 months) trial of heparin coated and uncoated Polivalves is about to commence, under the supervision of Professor Ascione at the Translational Biomedical Research Centre of the University of Bristol.

References

[1] G. Friedland, *Discovery of the function of the heart and circulation of blood*, Cardiovascular journal of Africa 20 (2009) 160.

[2] M.Loukas, P.Youssef, J. Gielecki, J. Walocha, K. Natsis, R. Tubbs, . *History of cardiac anatomy: A comprehensive review from the Egyptians to today.* Clinical anatomy (New York, N.Y.) 29 (2016)

[3] https://www.ottocentenariouniversitadipadova.it/en/storia/william-harvey/

[4] http://gomerpedia.org/wiki/Harvey%E2%80%99s_De_Motu_Cordis

[5] J.Brubert, *A novel polymeric prosthetic heart valve: design, manufacture, and testing*, PhD thesis, University of Cambridge, Cambridge (2015).

[6] J.Stasiak, M.Serrani, E.Biral, J. Taylor, A. Zaman, S. Jones, T.Ness, F. De Gaetano, M.Costantino, V. Bruno, M.S. Suleiman, R. Ascione, G. Moggridge, *Design, development, testing at ISO standards and in vivo feasibility study of a novel polymeric heart valve prosthesis.* Biomaterials Science 8 (2020).

[7] F.H. Martini, E.F. Bartholomew, J.L. Nath, *Fundamentals of Anatomy & Physiology, 9th edition*, Benjamin Cummings, San Francisco (2012).

[8] https://medlineplus.gov/

[9] K. Maganti, V.H. Rigolin, M.E. Sarano, R.O. Bonow, *Valvular Heart Disease: Diagnosis and Management*, Mayo Clinic proceedings 85 (2010) 483–500.

[10] https://www.mayoclinic.org/diseases-conditions/aortic-stenosis/symptoms-causes/syc-20353139#dialogId62474880

[11] M.H. Yacoub, J.J.M. Takkenberg, *Will heart valve tissue engineering change the world?*, Nature clinical practice: Cardiovascular medicine 2 (2005) 60-61.

[12] P. Bloomfield, *Choice of heart valve prosthesis*, Heart 87 (2002) 583–589.

[13] A.P. Yoganathan, Z. He, S.C. Jones, *Fluid mechanics of heart valves*, Annual review of biomedical engineering 6 (2004) 331-62.

[14] C.A. Hufnagel, W.P. Harvey, P.J. Rabil, T.F. McDermott, *In the beginning. Surgical correction of aortic insufficiency. 1954*, The Annals of thoracic surgery 47 (1989) 475-476.

[15] P. Symersky, R.P.J. Budde, P. Westers, B.A.J.M. de Mol, M. Prokop, *Multidetector CT imaging of mechanical prosthetic heart valves: quantification of artifacts with a pulsatile in-vitro model*, European radiology 21 (2011) 2103-2110.

[16] F. Oveissi, S. Naficy, A. Lee, D.S. Winlaw, F. Dehghani, *Materials and manufacturing perspectives in engineering heart valves: a review*, Materials Today Bio 5 (2020) 100038.

[17] P. Zilla, J. Brink, P. Human, D. Bezuidenhout, *Prosthetic heart valves: Catering for the few*, Tissue Engineering and Biomaterials 29 (2008) 385–406

[18] D. Bezuidenhout, P. Zilla, *Flexible Leaflet Polymeric Heart Valves*, Tissue Engineering and Biomaterials 15 (2013) 93-129.

[19] D. Bezuidenhout, D.F. Williams, P. Zilla, *Polymeric heart valves for surgical implantation, catheter-based technologies and heart assist devices*, Biomaterials 36 (2015) 6-25.

[20] T.C. Flanagan, A. Pandit, *Living artificial heart valve alternatives: a review*, European cells & materials 6 (2003) 28-45.

[21] J. Butany, C. Fayet, M.S. Ahluwalia, P. Blit, C. Ahn, C. Munroe, N. Israel, R.J. Cusimano, R.L. Leask, *Biological replacement heart valves. Identification and evaluation*, European Heart Journal 40 (2019) 414–421.

[22] M. Arsalan, T. Walther, *Durability of prostheses for transcatheter aortic valve implantation*, Nature reviews: Cardiology 13 (2016) 360-367.

[23] W. Wojakowski, H. Baumgartner, *The Year in Cardiology 2018: Valvular Heart Disease*, European Heart Journal 40 (2019) 414–421.

[24] F.B. Coulter, M. Schaffner, J.A.Faber, A. Rafsanjani, R. Smith, H. Appa, P. Zilla, D. Bezuidenhout, A.R.Studart, *Bioinspired Heart Valve Prosthesis Made by Silicone Additive Manufacturing*, Matter 1 (2019) 266-279.

[25] N.S. Braunwald, A.G. Morrow, *A LATE EVALUATION OF FLEXIBLE TEFLON PROSTHESES UTILIZED FOR TOTAL AORTIC VALVE REPLACEMENT: Postoperative Clinical, Hemodynamic, and Pathological Assessments*, The Journal of Thoracic and Cardiovascular Surgery 49 (1965) 485-496.

[26] H.-L. Leo, H. Simon, J. Carberry, S.-C. Lee, A.P. Yoganathan, *A comparison of flow field structures of two tri-leaflet polymeric heart valves*, Annals of biomedical engineering 33 (2005) 429-43.

[27] https://foldax.com/

[28] C. Jenney, P. Millson, D.W. Grainger, R. Grubbs, P. Gunatillake, S.J. McCarthy, J. Runt, J. Beith, *Assessment of a Siloxane Poly(urethane-urea) Elastomer Designed for Implantable Heart Valve Leaflets*, Advanced NanoBiomed Research 2000032 (2020) 2699-9307.

[29] L.S. Dandeniyage, R. Adhikari, M. Bown, R. Shanks, B. Adhikari, C.D. Easton, T.R. Gengenbach, D. Cookson, P.A. Gunatillake, *Morphology and surface properties of high strength siloxane poly(urethane-urea)s developed for heart valve application*, Journal of biomedical materials research: Part B, Applied biomaterials 107 (2019) 112-121.

[30] L. Pinchuk, G.J. Wilson, J.J. Barry, R.T. Schoephoerster, J.-M. Parel, J.P. Kennedy, *Medical applications of poly(styrene-block-isobutylene-block-styrene) ("SIBS")*, Biomaterials 29 (2008) 448-460.

[31] W. Yin, S. Gallocher, L. Pinchuk, R.T. Schoephoerster, J. Jesty, D. Bluestein, *Flow-induced platelet activation in a St. Jude mechanical heart valve, a trileaflet polymeric heart valve, and a St. Jude tissue valve*, Artificial organs 29 (2005) 826-831.

[32] A. A. H. J. Sauren, *The mechanical behaviour of the aortic valve*, PhD thesis, Technische Hogeschool, Eindhoven (1981).

[33] F.S.Bates ,G.H. Fredrickson, *Block copolymer thermodynamics:Theory and Experiments*, Annu. Rev. Phys. Chem. (1990) 525-57.

[34] F.S. Bates, G.H. Fredrickson, *Block Copolymers—Designer Soft Materials*, Physics Today 52 (1999) 32-38.

[35] Y. Mai ,A. Eisenberg , *Self-assembly of block copolymers*, Chem. Soc. Rev. 41 (2012) 5969-5985.

[36] Y. Zhao, N. Ning, X. Hu, Y. Li, F. Chen, Q. Fu, *Processing temperature dependent mechanical response of a thermoplastic elastomer with low hard segment*, Polymer 53 (2012) 4310-4317.

[37] F.S. Bates, M.F. Schulz, A.K. Khandpur, S. Forster and J.H. Rosedale, *Fluctuations, Conformational Asymmetry and Block Copolymer Phase Behaviour*, Faraday Discussions 98 (1994) 7-18.

[38] H. Feng, X. Lu, W. Wang, N.-G. Kang, J.W. Mays, *Block Copolymers: Synthesis, Self-Assembly, and Applications*, Polymers 9 (2017) 494-525.

[39] https://polymerdatabase.com/polymer%20chemistry/ALP.html

[40] S. Tomita, H. Urakawa, I. Wataoka, S. Sasaki, S. Sakurai, *Complete and comprehensive orientation of cylindrical microdomains in a block copolymer sheet*, Polymer Journal 48 (2016) 1123–1131.

[41] G.H. Fredrickson, F.S. Bates, G.H. Fredrickson *Dynamics of Block Copolymers: Theory and Experiment*, Annual Review of Materials Science 26 (1996) 501-550.

[42] T.H. Epps, R.K. O'Reilly, *Block copolymers: controlling nanostructure to generate functional materials – synthesis, characterization, and engineering*, Chemical Science 7 (2016) 1674–1689.

[43] T.H. Epps, R.K. O'Reilly, *Self-assembly of block copolymers*, Chemical Society Reviews 41 (2012)

[44] M.A. Modi, R. Krishnamoorti, M.F. Tse, H.-C. Wang, *Viscoelastic Characterization of an Order-Order Transition in a Mixture of Di- and Triblock Copolymers*, Macromolecules 32 (1999) 4088–4097.

[45] J.K. Kim, J.I. Lee, D.H. Lee, *Self-Assembled Block Copolymers: Bulk to Thin Film*, Macromolecular Research 16 (2008) 267-292.

[46] E. Helfand, *Block Copolymer Theory. III. Statistical Mechanics of the Microdomain Structure*, Macromolecules 8 (1975) 552–556.

[47] E. Helfand, Z.R. Wasserman, *Block Copolymer Theory. 6. Cylindrical Domains*, Macromolecules 13 (1980) 994–998.

[48] R.W. Richards, J.L. Thomason, *A small angle neutron scattering investigation of block copolymers of styrene and isoprene in the solid state*, Polymer 22 (1981) 581-589.

[49] E. Helfand, Z.R. Wesserman, *Block Copolymer Theory. 4. Narrow Interphase Approximation*, Macromolecules 9 (1976) 879-888.

[50] R.H. Colby, *Block copolymer dynamics*, Current Opinion in Colloid & Interface Science 1 (1996) 454-465.

[51] J.H. Rosedale, F.S. Bates, K. Almdal, K. Mortensen, G.D. Wignall, *Order and Disorder in Symmetric Diblock Copolymer Melts* Macromolecules 28 (1995) 1429-1443.

[52] E. Helfand, Z. R. Wasserman, *Statistical thermodynamics of microdomain structures in block copolymer systems*, Polymer Engineering & Science 17 (1977) 582-586.

[53] E. Helfand, Z. R. Wasserman, *Block Copolymer Theory. 6. Cylindrical Domains*, Macromolecules 13 (1980) 994–998.

[54] Q. Pan, S. Liu, J. Xie, M. Jiang, *Synthesis and Characterization of Block-Graft Copolymers Composed of Poly(styrene-b-ethylene-co-propylene) and Poly(ethyl methylacrylate) by Atom Transfer Radical Polymerization*, Journal of Polymer Science Part A: Polymer Chemistry 37 (1999) 2699-2702.

[55] L. Leibler, *Theory of Microphase Separation in Block Copolymers*, Macromolecules 13 (1980) 1602–1617.

[56] K. Almdal, K.A. Koppi, F.S. Bates, and K. Mortensen, *Multiple ordered phases in a block copolymer melt*, Macromolecules 25 (1992) 1743–1751.

[57] D.J. Meier, *Theory of block copolymers. I. Domain formation in A-B block copolymers* J. polym. sci., C Polym. symp. 26 (1969) 81-98.

[58] F.S. Bates, J.H. Rosedale, G.H. Fredrickson, *Fluctuation effects in a symmetric diblock copolymer near the order–disorder transition*, The Journal of Chemical Physics 92 (1990) 6255-6270.

[59] J.H. Rosedale, F.S. Bates, K. Almdal, K. Mortensen, G.D. Wignall, *Order and Disorder in Symmetric Diblock Copolymer Melts*, Macromolecules 28 (1996) 1429-1443.

[60] J.H. Rosedale, F.S. Bates, K. Almdal, K. Mortensen, G.D. Wignall, *Rheology of ordered and disordered symmetric poly(ethylenepropylene)-poly(ethylethylene) diblock copolymers*, Macromolecules 23 (1990) 2329–2338.

[61] F.S. Bates, *Block copolymers near the microphase separation transition. 2. Linear dynamic mechanical properties*, Macromolecules 17 (1984) 2607–2613.

[62] J.G. Kennemur, M.A. Hillmyer, F.S. Bates, *Rheological Evidence of Composition Fluctuations in an Unentangled Diblock Copolymer Melt near the Order–Disorder Transition*, ACS Macro Letters 2 (2013) 496-500.

[63] Y. Matsushita, K. Mori, R. Saguchi, Y. Nakao, I. Noda,M. Nagasawa, *Molecular weight dependence of lamellar domain spacing of diblock copolymers in bulk*,Macromolecules 23 (19),(1990), 4313-4316

[64] J.Brubert, G.Moggridge, *Material Selection and Performance Index for Polymeric Prosthetic Heart Valve Design*, Journal of Medical Devices 9 (2015).

[65] J. Stasiak, J. Brubert, Marta Serrani, S. Nair, F. de Gaetano, M.L. Costantino, G.D. Moggridge, *A bio-inspired microstructure induced by slow injection moulding of cylindrical block copolymers*, Soft Matter 10 (2014) 6077-6086.

[66] J. Stasiak, J. Brubert, M. Serrani, A. Talhat, F. De Gaetano, M.L. Costantino, G.D. Moggridge, *Structural changes of block copolymers with bi-modal orientation under fast cyclical stretching as observed by synchrotron SAXS*, Soft Matter 11 (2015) 3271-3278.

[67] M. Serrani, J. Brubert, J. Stasiak, F. De Gaetano, A. Zaffora, M.L. Costantino, G.D. Moggridge, *A Computational Tool for the Microstructure Optimization of a Polymeric Heart Valve Prosthesis*, Journal of Biomechanical Engineering 138 (2016) 061001.

[68] L. Fang, M. Wei, Y. Shang, L. Jimenez, D. Kazmer, C. Barry, J. Mead, *Surface morphology alignment of block copolymers induced by injection molding*, Polymer 50 (2009) 5837-5845.

[69] D.E. Angelescu, J.H. Waller, D.H. Adamson, P. Deshpande, S.Y. Chou, R.A. Register, P.M. Chaikin, *Macroscopic Orientation of Block Copolymer Cylinders in Single-Layer Films by Shearing*, Advanced Materials 16 (2004) 1736-1740.

[70] N. Yamashita, S. Watanabe,K. Nagai, M. Komura, T. Iyoda, K. Aida, Y. Tada, H. Yoshida, *Chemically directed self-assembly of perpendicularly aligned cylinders by a liquid crystalline block copolymer* J. Mater. Chem. C 3 (2015) 2837-2847

[71] N.P. Balsara, H.J. Dai, *A transition from shear-induced order to shear-induced disorder in block copolymers*, The Journal of Chemical Physics 105 (1996) 2942-2945.

[72] Zs. Fodor, Á. Fodor, J.P. Kennedy, *A GPC method to determine the composition of two component copolymers*, Polymer Bulletin 29 (1992) 689–696.

[73] S.S. Gupta, A. Meena, T. Parikh, A.T.M. Serajuddin, *Investigation of Thermal and Viscoelastic Properties of Polymers Relevant to Hot Melt Extrusion - I: Polyvinylpyrrolidone and related polymers*, Journal of Excipients and Food Chemicals 5 (2014) 32-45.

[74] A. Arevalillo, M.E. Muñoz, I. Calafell, A. Santamaría, L. Fraga, J.A. Barrio, *Thermo-mechanical properties linked to rheological features in high molecular weight SEBS copolymers: Effect of styrene content and ethylene/butylene proportion*, Polymer Testing 31 (2012) 849-854.

[75] C.A. Sierra, C. Galán, J.G. Fatou, M.D. Parellada, J.A. Barrio, *Thermal and mechanical properties of poly (styrene-b-ethylene-co-butylene-b-styrene) triblock copolymers*, Polymer 38 (1997) 4325-4335.

[76] N.S. Karode, A. Poudel, L. Fitzhenry, S. Matthews, P.R. Walsh, A.B. Coffey, *Evaluation of interfacial region of microphase-separated SEBS using modulated differential scanning calorimetry and dynamic mechanical thermal analysis*, Polymer Testing 62 (2017) 268-277.

[77] C.D. Han, S.B. Chun, S.F. Hahn, S.Q. Harper, P.J. Savickas, D.M. Meunier, L. Li, T. Yalcin, *Phase Behavior of Polystyrene/Polybutadiene and Polystyrene/Hydrogenated Polybutadiene Mixtures:Effect of the Microstructure of Polybutadiene*, Macromolecules 31 (1998) 394–402.

[78] M.B. Kossuth, D.C. Morse, F.S. Bates, *Viscoelastic behavior of cubic phases in block copolymer melts*, Journal of Rheology 43 (1999) 167-196.

[79] E.V. Gouinlock, R.S. Porter, *Linear dynamic mechanical properties of an SBS block copolymer*, Polymer Engineering & Science 17 (1977) 535-543.

[80] C.D. Han, J. Kim, J.K. Kim, *Determination of the order-disorder transition temperature of block copolymers*, Macromolecules 22 (1989) 383–394.

[81] S.B. Chun, C.D. Han, *The Role of the Order-Disorder Transition Temperature of Block Copolymer in the Compatibilization of Two Immiscible Homopolymers*, Macromolecules 32 (1999) 4030–4042.

[82] N. Sakamoto, T. Hashimoto, C.D. Han, D. Kim, N.Y. Vaidya, *Order-Order and Order-Disorder Transitions in a Polystyrene-block-Polyisoprene-block-Polystyrene Copolymer*, Macromolecules 30 (1997) 1621–1632.

[83] C.Y. Ryu, M.S. Lee, D.A. Hajduk, T.P. Lodge, *Structure and viscoelasticity of matched asymmetric diblock and triblock copolymers in the cylinder and sphere microstructures*, Journal of Polymer Science Part B: Polymer Physics 35 (1997) 2811-2823.

[84] A. Keller, E. Pedemonte, F.M. Willmouth, *Macro-lattice from Segregated Amorphous Phases of a Three Block Copolymer*, Kolloid-Zeitschrift und Zeitschrift für Polymere 238 (1970) 385–389.

[85] A.S. Zalusky, R. Olayo-Valles, C.J. Taylor, M.A. Hillmyer, *Mesoporous Polystyrene Monoliths*, Journal of the American Chemical Society 123 (2001) 1519–1520.

[86] A.S. Zalusky, R. Olayo-Valles, J.H. Wolf, M.A. Hillmyer, *Ordered Nanoporous Polymers from Polystyrene-Polylactide Block Copolymers*, Journal of the American Chemical Society 124 (2002) 12761–12773.

[87] D. Cooney, M. Hillmyer, E.Cussler, G. Moggridge, *Diffusion in nanoporous materials made from block copolymers* Crystallography Reviews 12 (2006) 13-24.

[88] N. Yamashita, S. Watanabe, K. Nagai, M. Komura, T. Iyoda, K. Aida, Y. Tada, H. Yoshida, *Chemically directed self-assembly of perpendicularly aligned cylinders by a liquid crystalline block copolymer*, Journal of Materials Chemistry C 3 (2015) 2837-2847.

[89] R.J. Spontak, M.C. Williams, D.A. Agard, *Three-dimensional study of cylindrical morphology in a styrene-butadiene-styrene block copolymer*, Polymer 29 (1988) 387-395.

[90] D.T. Cooney, M.A. Hillmyer, E.L. Cussler, G.D. Moggridge, *Diffusion in nanoporous materials made from block copolymers*, Crystallography Reviews 12 (2006) 13-24.

[91] D. Hull, T.W. Clyne, *An Introduction to Composite Materials*, Cambridge University Press, 2nd Edition, Cambridge (1996).

[92] B. Harris, *Engineering Composite Materials*, The Institute of Materials, London (1999).

[93] M.M. Shokrieh, H. Moshrefzadeh-Sani, *On the constant parameters of Halpin-Tsai equation*, Polymer 106 (2016) 14-20.

[94] M.M. Shokrieh, H. Moshrefzadeh-Sani, *The Halpin-Tsai equations: A review*, Polymer Engineering & Science 16 (1976) 344-352.

[95] H. Hasegawa, T. Hashimoto, H. Kawai, T.P. Lodge, E.J. Amis, C.J. Glinka, C.C. Han, *SANS and SAXS studies on molecular conformation of a block polymer in microdomain space*, Macromolecules 18 (1985) 67–78.

[96] E. Helfand, Z.R. Wasserman, *Block Copolymer Theory. 5. Spherical Domains*, Journal of mechanics in medicine and biology 11 (1978) 960–966.

[97] F. A. Morrison, J. W. Mays, M. Muthukumar, A. I. Nakatani, and C. C. Han, *Shear-induced morphological structures in triblock copolymers* Macromolecules 1993 26 (19), 5271-5273

[98] Peleg M, *A note on the tan $\delta(T)$ peak as a glass transition indicator in biosolids* Rheola Acta, 1995, 34, 215–220

[99] R.Popli , M.Glotin ,L. Mandelkern and R.S.Benson , *Dynamic mechanical studies of α and β relaxations of polyethylenes*. J. Polym. Sci. Polym. Phys. Ed.,1984,22, 407-448

[100] https://www.engineeringtoolbox.com/ethylene-ethene-C2H4-properties-d_2104.html

[101] S. Baxter, J.J.C. Busfield, T. Peijs, *Chapter 12 - Selection of Elastomers for a Synthetic Heart Valve*, Elastomers and Components, Woodhead Publishing (2006) 171-177.

[102] W.V. Mars, A. Fatemi, *Fatigue crack nucleation and growth in filled natural rubber*, Fatigue & Fracture of Engineering Materials & Structures 26 (2003) 779-789.

[103] W.V. Mars, A. Fatemi, *A literature survey on fatigue analysis approaches for rubber*, International Journal of Fatigue 24 (2002) 949-961.

[104] G.J. Lake, P.B. Lindley, A.G. Thomas, *Fracture mechanics of rubber*, Fracture 1969: Proceedings of the Second International Conference on Fracture (1969) 493-503.

[105] A.N. Gent, P.B. Lindley, A.G. Thomas, *Cut growth and fatigue of rubbers. I. The relationship between cut growth and fatigue*, Journal of Applied Polymer Science 8 (1964) 455-466.

[106] G.J. Lake, P.B. Lindley, A.G. Thomas, *Rupture of rubber. I. Characteristic energy for tearing*, Journal of Polymer Science 10 (1953) 291-318.

[107] A.A. Griffith, *VI. The phenomena of rupture and flow in solids*, Philosophical Transactions of the Royal Society of London. Series A, Containing Papers of a Mathematical or Physical Character 221 (1921) 163–198.

[108] H.W. Greensmith, *Rupture of rubber. X. The change in stored energy on making a small cut in a test piece held in simple extension*, Journal of Applied Polymer Science 7 (1963) 993-1002.

[109] P.B. Lindley, *Energy for crack growth in model rubber components*, Journal of Strain Analysis 7 (1972) 132-140.

[110] G.J. Lake, P.B. Lindley, *The mechanical fatigue limit for rubber*, Journal of Applied Polymer Science 9 (1965) 1233-1251.

[111] G.J. Lake, A.G. Thomas, *The strength of highly elastic materials*, Proceedings of the Royal Society of London. Series A, Mathematical and Physical Sciences 300 (1967) 108–119.

[112] G.J. Lake, *Fatigue and Fracture of Elastomers*, Rubber Chemistry and Technology 68 (1995) 435–460.

[113] T. Zarrin-Ghalami, A. Fatemi, *Material deformation and fatigue behavior characterization for elastomeric component life predictions*, Polymer Engineering and Science 52 (2012) 1795-1805.

[114] A. Bernasconi, P. Davoli, A. Basile, A. Filippi, *Effect of fibre orientation on the fatigue behaviour of a short glass fibre reinforced polyamide-6*, International Journal of Fatigue 29 (2007) 199–208.

[115] C. Buckley, D. Focatiis, C. Prisăcariu, *Unravelling the mysteries of cyclic deformation in thermoplastic elastomers*, Constitutive Models for Rubber VII, Proceedings of the 7th European Conference on Constitutive Models for Rubber (2011) 3-10.

[116] W.V. Mars, A. Fatemi, *Factors that Affect the Fatigue Life of Rubber: A Literature Survey*, Rubber Chemistry and Technology 77 (2004) 391–412.

[117] R.W. Hertzberg, J.A. Manson, M. Skibo, *Frequency sensitivity of fatigue processes in polymeric solids*, Polymer Engineering and Science 15 (1975) 252-260.

[118] J.R. Rice, *A Path Independent Integral and the Approximate Analysis of Strain Concentration by Notches and Cracks*, Journal of Applied Mechanics 35 (1968) 379-386.

[119] A.G. Thomas, *Rupture of rubber. VI. Further experiments on the tear criterion*, Journal of Applied Polymer Science 3 (1960) 168-174.

[120] R.J. Harbour, A. Fatemi, W.V. Mars, *Fatigue life analysis and predictions for NR and SBR under variable amplitude and multiaxial loading conditions*, International Journal of Fatigue 30 (2008) 1231-1247.

[121] F. Cosmi, A. Bernasconi, *Micro-CT investigation on fatigue damage evolution in short fibre reinforced polymers*, Composites Science and Technology 79 (2013) 70-76.

[122] T. Zarrin-Ghalami, A. Fatemi, *Multiaxial fatigue and life prediction of elastomeric components*, International Journal of Fatigue 55 (2013) 92-101.

[123] P. Beardmore, S. Rabinowitz, *Craze formation and growth in anisotropic polymers*, Journal of Materials Science 10 (1975) 1763–1770.

[124] P. Behroozinia, R. Mirzaeifar, S. Taheri, *A review of fatigue and fracture mechanics with a focus on rubber-based materials*, Proceedings of the Institution of Mechanical Engineers, Part L: Journal of Materials: Design and Applications 233 (2019) 1005-1019.

[125] N. Roche, L. Perier, *Influence of Elastomers Formulation on Fatigue Crack Growth Properties*, Procedia Engineering 66 (2013) 705-712.

[126] J.J.C. Busfield, V. Jha, H. Liang, I.C. Papadopoulos, A.G. Thomas, *Prediction of fatigue crack growth using finite element analysis techniques applied to three-dimensional elastomeric components*, Plastics, Rubber and Composites 34 (2005) 349-356.

[127] R. Biran, D. Pond, *Heparin coatings for improving blood compatibility of medical devices*, Advanced drug delivery reviews 112 (2017) 12-23.

[128] G.M. Bernacca, D.J. Wheatley, *Surface modification of polyurethane heart valves: effects on fatigue life and calcification*, The International journal of artificial organs 21 (1998) 814-819.

[129] E.M.E. Kristensen, R. Larsson, J. Sánchez, H. Rensmo, U. Gelius, H. Siegbahn, *Heparin coating durability on artificial heart valves studied by XPS and antithrombin binding capacity*, Colloids and surfaces B, Biointerfaces 49 (2006) 1-7.

[130] F. Abraham, *Definition and use of an Effective Flaw Size for the simulation of elastomer fatigue*, Constitutive Models for Rubber VII, Proceedings of the 7th European Conference on Constitutive Models for Rubber (2011) 331-335.

[131] J.G.R. Kingstone, A.H. Muhr, *Determination of effective flaw size for fatigue life prediction*, Constitutive Models for Rubber VII, Proceedings of the 7th European Conference on Constitutive Models for Rubber (2011) 337-342.

[132] B. Harris, *Engineering Composite Materials*, The Institute of Materials, London (1999).

[133] E. Biral, *Fatigue life prediction and performance index evaluation of SEPS block-copolymers and advanced TPU for the design of a trileaflet Prosthetic Heart Valve*, MEng Thesis, University of Padova, Padova (2016).

[134] K. Tanaka, K. Oharada, D. Yamada, K. Shimizu, *Fatigue crack propagation in short-fiber reinforced plastics*, Frattura ed Integrità Strutturale 34 (2015) 309-317.

[135] S. Keck, M. Fulland, *Effect of fibre volume fraction and fibre direction on crack paths in flax fibre-reinforced composites*, Engineering Fracture Mechanics 167 (2016) 201-209.

[136] J. Stasiak, S. Nair, G.D. Moggridge, *Mechanical strength of sutured block copolymers films for load bearing medical applications* , Bio-medical materials and engineering 24 (2014) 563-569.

[137] F. De Gaetano, M. Serrani, P. Bagnoli, J. Brubert, J. Stasiak, G.D. Moggridge, M.L. Costantino, *Fluid dynamic characterization of a polymeric heart valve prototype (Poli-Valve) tested under continuous and pulsatile flow conditions*, The International journal of artificial organs 38 (2015) 600-606.

[138] B.N.J. Persson, O. Albohr, G. Heinrich, H. Ueba, *Crack propagation in rubber-like materials*, Journal of Physics: Condensed Matter 17 (2005) 1071-1142.

[139] G.C. Sih, P.C. Paris, G.R. Irwin, *On cracks in rectilinearly anisotropic bodies*, International Journal of Fracture Mechanics 1 (1965) 189–203.

[140] WM Swanson, RE Clark, *A simple cardiovascular system simulator: design and performance.* J Bioeng.1(2) (1977) 135-145.

[141] N. Talukder, H Reul, *Fluid Mechanics of Natural Cardiac Valves.* In: Bauer RD, Busse R, eds. The Arterial System. Berlin, Heidelberg: Springer (1978) 269-274.

[142] R.J. Levy, F.J. Schoen, H.C. Anderson, H. Harasaki, T.H. Koch, W. Brown, J.B. Lian, R. Cumming, J.B. Gavin, *Cardiovascular implant calcification: a survey and update*, Biomaterials 12 (1991) 707-714.

[143] F.J. Schoen, R.J. Levy, *Calcification of tissue heart valve substitutes: progress toward understanding and prevention*, The Annals of thoracic surgery 79 (2005) 1072-1080.

[144] M. Brini, E. Carafoli, *The Plasma Membrane Ca^{2+} ATPase and the Plasma Membrane Sodium Calcium Exchanger Cooperate in the Regulation of Cell Calcium*, Cold Spring Harbor perspectives in biology 2 (2011) 004168.

[145] E. Jorge-Herrero, C. Fonseca, A.P. Barge, J. Turnay, N. Olmo, P. Fernández, M.A. Lizarbe, J.M. García Páez, *Biocompatibility and Calcification of Bovine Pericardium Employed for the Construction of Cardiac Bioprostheses Treated With Different Chemical Crosslink Methods*, Artificial Organs 34 (2010) 168-176.

[146] V.N. Bapat, T.A. Barker, G. El Khoury, M.I. Ionescu, P. Modi, M. M. Mokhles, S. Rekhraj, J.J.M. Takkenberg, M. Uzzaman, L. Williams, *The Pericardial Heart*

Valve, Society for Cardithoracic Surgery in Great Britain and Ireland, London (2014).

[147] J. Butany, R. Leask, *The failure modes of biological prosthetic heart valves*, Journal of long-term effects of medical implant 11 (2001) 115-135.

[148] P. Singhal, A. Luk, J. Butany, *Bioprosthetic Heart Valves: Impact of Implantation on Biomaterials*, ISRN Biomaterials (2013) 728791.

[149] R.F. Siddiqui, J.R. Abraham, J. Butany, *Bioprosthetic heart valves: modes of failure.*, Histopathology 55 (2009) 135-144.

[150] J.C. Park, M.J. Song, Y.S. Hwang, H. Suh, *Calcification comparison of polymers for vascular graft*, Yonsei medical journal 42 (2001) 304-310.

[151] D.L. Coleman, H.-C. Hsu, D.E. Dong, D.B. Olsen, *Polymer Properties Associated with Calcification of Cardiovascular Devices*, In: R.P. Rubin, G.B. Weiss, J.W. Putney Calcium in Biological Systems (1985) 653-659.

[152] D.L. Coleman, *Mineralization of blood pump bladders*, Transactions - American Society for Artificial Internal Organs 27 (1981) 708-13.

[153] G.M. Bernacca, T.G. Mackay, R. Wilkinson, D.J. Wheatley, *Polyurethane heart valves: fatigue failure, calcification, and polyurethane structure*, Journal of biomedical materials research 34 (1997) 371-379.

[154] P. Boloori-Zadeha, S.C. Corbett, H. Nayeb-Hashemi, *Effects of fluid flow shear rate and surface roughness on the calcification of polymeric heart valve leaflet*, Materials Science and Engineering: C 33 (2013) 2770-2775.

[155] P. Boloori-Zadeha, S.C. Corbett, H. Nayeb-Hashemi, *In-vitro calcification study of polyurethane heart valves*, Materials Science and Engineering: C 35 (2014) 335-340.

[156] D.J. Wheatley, L. Raco, G.M. Bernacca, I. Sim, P.R. Belcher, J.S. Boyd, *Polyurethane: material for the next generation of heart valve prostheses?*, European journal of cardio-thoracic surgery : official journal of the European Association for Cardio-thoracic Surgery 17 (2014) 440-448.

[157] K. Imachi, T. Chinzei, Y. Abe, K. Mabuchi, H. Matsuura, T. Karita, K. Iwasaki, S. Mochizuki, Y.-P. Son, I. Saito, A. Kouno, T. Ono, *A new hypothesis on the*

mechanism of calcification formed on a blood-contacted polymer surface, Journal of Artificial Organs 4 (2001) 74–82.

[158] S.L. Hilbert, V.J. Ferrans, Y. Tomita, E.E. Eidbo, M. Jones, *Evaluation of explanted polyurethane trileaflet cardiac valve prostheses*, The Journal of thoracic and cardiovascular surgery 94 (1987) 419-429.

[159] G. Golomb, D. Wagner, *Development of a new in vitro model for studying implantable polyurethane calcification*, Biomaterials 12 (1991) 397-405.

[160] G. Golomb, A. Barashi, D. Wagner, O. Nachmias, *In-vitro and in-vivo models for the study of the relationship between hydrophilicity and calcification of polymeric and collageneous biornaterials*, Clinical Materials 13 (1993) 61-69.

[161] G. Golomb, *Calcification of polyurethane-based biomaterials implanted subcutaneously in rats: role of porosity and fluid absorption in the mechanism of mineralization*, Journal of Materials Science: Materials in Medicine 3 (1992) 272–277.

[162] N.C. Kekec, M. B. Akolpoglu, U. Bozuyuk, S. Kizilel, N. Nugay, T. Nugay, J.P. Kennedy, *Calcification resistance of polyisobutylene and polyisobutylene-based materials*, Polymers for Advanced Technologies 30 (2019) 1836-1846.

[163] J.A. Benton, H.B. Kern, K.S. Anseth, *Substrate properties influence calcification in valvular interstitial cell culture*, The Journal of heart valve disease 17 (2008) 689-699.

[164] Q. Wang, A.J. McGoron, R. Bianco, Y. Kato, L. Pinchuk, R.T. Schoephoerster, *In-vivo assessment of a novel polymer (SIBS) trileaflet heart valve*, The Journal of heart valve disease 19 (2010) 499-505.

[165] Z.-X. Liu, X.-M. Wang, Q. Wang, X.-C. Shen, H. Liang, F.-Z. Cui, *Evolution of calcium phosphate crystallization on three functional group surfaces with the same surface density*, CrystEngComm 14 (2012) 6695-6701.

[166] N.R. Vyavahare, W. Chen, R.R. Joshi, C.H. Lee, D. Hirsch, J. Levy, F.J. Schoen, R.J. Levy, *Current Progress in Anticalcification for Bioprosthetic and Polymeric Heart Valves*, Cardiovascular pathology: the official journal of the Society for Cardiovascular Pathology 6 (1997) 219-29.

[167] I. Alferiev, N. Vyavahare, C. Song, J. Connolly, J.T. Hinson, Z. Lu, S. Tallapragada, R. Bianco, R. Levy, *Bisphosphonate derivatized polyurethanes resist calcification*, Biomaterials 22 (2001) 2683-2693.

[168] C.N. Degeratua, G. Mabilleau, C. Cincu, D. Chappard, *Aluminum inhibits the growth of hydroxyapatite crystals developed on a biomimetic methacrylic polymer*, Journal of Trace Elements in Medicine and Biology 27 (2013) 346-351.

[169] G.M. Bernacca, A.C. Fisher, T.G. Mackay, D.J. Wheatley, *A dynamicin vitro method for studying bioprosthetic heart valve calcification*, Journal of Materials Science: Materials in Medicine 3 (1992) 293–298.

[170] J. Chanda, R. Kuribayashi, T.Abe, *Heparin coupling in inhibition of calcification of vascular bioprostheses* Biomaterials 20 (1999) 1753-1757.

[171] H. Ghanbari, A.G. Kidane, G. Burriesci, B. Ramesh, A. Darbyshire, A.M. Seifalian, *The anti-calcification potential of a silsesquioxane nanocomposite polymer under in vitro conditions: Potential material for synthetic leaflet heart valve* Acta Biomaterialia 6 (2010) 4249–4260

[172] T. Kokubo, H. Takadama, *How useful is SBF in predicting in vivo bone bioactivity?* Biomaterials 27 (2006) 2907–2915

[173] B.C. Starcher, D.W. Urry, *Elastin coacervate as a matrix for calcification* Biochemical and Biophysical Research Communications 53 (1973) 210-216.

[174] E. Okafor, *Calcification of the polymeric heart valve prosthesis: A comparative study into the effects of calcification on the mechanical and surface properties of potential polymers for use in heart valve prosthesis*, MEng, University of Cambridge, Cambridge (2019).

[175] G.M. Nogueira, A.C.D. Rodas, R.F. Weska, C.G. Aimoli, O.Z. Higa , M. Maizato, A.A. Leiner, R.N.M. Pitombo, B. Polakiewicz, M.M. Beppu *Bovine pericardium coated with biopolymeric films as an alternative to preventcalcification: In vitro calcification and cytotoxicity results.* Materials Science and Engineering C 30 (2010) 575–582

[176] F.De Gaetano, *Design, manufacturing and in-vitro testing of an innovative biomorphic heart valve made of a new thermoplastic elastomeric biomaterial*, PhD thesis, Politecnico di Milano, Milan, (2017).

[177] F. De Gaetano, P. Bagnoli, A. Zaffora, A. Pandolfi, M. Serrani, J. Brubert, J. Stasiak, G.D. Moggridge, M.L. Costantino, *A Newly Developed Tri-Leaflet Polymeric Heart Valve Prosthesis*, Journal of mechanics in medicine and biology 15 (2015) 1540009.

[178] G.M. Bernacca, B. O'Connor, D.F. Williams, D.J. Wheatley, *Hydrodynamic function of polyurethane prosthetic heart valves: influences of Young's modulus and leaflet thickness* Biomaterials 23 (2002) 45-50.

[179] M.B. Gorbet, M.V. Sefton, *Biomaterial-associated thrombosis: roles of coagulation factors, complement, platelets and leukocytes*, Biomaterials 25 (2004) 5681-5703.

[180] E.J. Brisbois, H. Handa, M.E. Meyerhoff, *Recent Advances in Hemocompatible Polymers for Biomedical Applications*, in F. Puoci: Advanced Polymers in Medicine, Springer, Cham (2015) 481-511.

[181] J.M. Woodbury, *Hemocompatibility of polymeric materials for blood-contacting applications*, Master's thesis, Colorado State University Fort Collins, Colorado Spring, (2015).

[182] M. Amiji, K. Park, *Surface modification of polymeric biomaterials with poly(ethylene oxide), albumin, and heparin for reduced thrombogenicity*, Journal of biomaterials science: Polymer edition 4 (1993) 217-034.

[183] S.W. Kim, H. Jacobs, *Design of nonthrombogenic polymer surfaces for blood-contacting medical devices*, Blood purification 14 (1996) 357-372.

[184] J. Brubert, S. Krajewski, H.P. Wendel, S. Nair, J. Stasiak, G.D. Moggridge, *Hemocompatibility of styrenic block copolymers for use in prosthetic heart valves*, Journal of materials science: Materials in medicine 27 (2016) 32.

[185] M. Urooj Zafar, C.G. Santos-Gallego, L. Badimon, J.J. Badimon, *Perfusion Chamber: An Ex Vivo Model of Thrombosis*, Methods in molecular biology 1816 (2018) 161-171.

[186] G.N. Viswanathan, S.M. Marshall, K. Balasubramaniam, J.J. Badimon, A.G. Zaman, *Differences in thrombus structure and kinetics in patients with type 2 diabetes mellitus after non ST elevation acute coronary syndrome*, Thrombosis research 133 (2014) 880-885.

[187] L. Badimon, J.J. Badimon, A. Galvez, J.H. Chesebro, V. Fuster, *Influence of arterial damage and wall shear rate on platelet deposition. Ex vivo study in a swine model*, Arteriosclerosis 6 (1986) 312-320.

[188] K.S. Lavery, C. Rhodes, A. Mcgraw, M.J. Eppihimer, *Anti-thrombotic technologies for medical devices*, Advanced Drug Delivery Reviews 112 (2017) 2-11.

[189] M.F. Maitz, M.C.L. Martins, N. Grabow, C. Matschegewski, N. Huang, E.L. Chaikof, M.A. Barbosa, C. Werner, C. Sperling, *The blood compatibility challenge. Part 4: Surface modification for hemocompatible materials: Passive and active approaches to guide blood-material interactions*, Acta Biomaterialia 94 (2019) 33-43.

[190] M. Gorbet, C. Sperling, M.F. Maitz, C.A. Siedlecki, C. Werner, M.V. Sefton, *The blood compatibility challenge. Part 3: Material associated activation of blood cascades and cells*, Acta Biomaterialia 94 (2019) 25-32.

[191] J.L. Brash, T.A. Horbett, R.A. Latour, P. Tengvall, *The blood compatibility challenge. Part 2: Protein adsorption phenomena governing blood reactivity*, Acta Biomaterialia 94 (2019) 11-24.

[192] I.H. Jaffer, J.I. Weitz, *The blood compatibility challenge. Part 1: Blood-contacting medical devices: The scope of the problem*, Acta Biomaterialia 94 (2019) 2-10.

[193] M. Hedayati, M.J. Neufeld, M.M. Reynolds, M.J. Kipper, *The quest for blood-compatible materials: Recent advances and future technologies*, Materials Science and Engineering: R: Reports 138 (2019) 118-152.

[194] H. Yang, S. Luan, J. Zhao, H. Shi, X. Lia, L. Song, J. Jin, Q. Shi, J. Yin, D. Shi, P. Stagnaro, *Improving hemocompatibility of styrene-b-(ethylene-co-butylene)-b-styrene elastomer via N-vinyl pyrrolidone-assisted grafting of poly(ethylene glycol) methacrylate*, Polymer 53 (2012) 1675-1683.

[195] S. Fitzgerald, O.M. Mereuta, K.M. Doyle, D. Dai, R. Kadirvel, D.F. Kallmes, W. Brinjikji, *Correlation of imaging and histopathology of thrombi in acute ischemic stroke with etiology and outcome*, Journal of neurosurgical sciences 63 (2019) 292-300.